The effects of clouds on the reconstruction of gamma-ray-induced air showers observed with CTA telescopes

Pecimotika, Mario

Doctoral thesis / Disertacija

2024

UNIVERSITY OF RIJEKA
FACULTY OF PHYSICS

Mario Pecimotika

THE EFFECTS OF CLOUDS ON THE RECONSTRUCTION OF GAMMA-RAY-INDUCED AIR SHOWERS OBSERVED WITH CTA TELESCOPES

DOCTORAL THESIS

Rijeka, 2024

UNIVERSITY OF RIJEKA
FACULTY OF PHYSICS

Mario Pecimotika

THE EFFECTS OF CLOUDS ON THE RECONSTRUCTION OF GAMMA-RAY-INDUCED AIR SHOWERS OBSERVED WITH CTA TELESCOPES

DOCTORAL THESIS

Supervisors:
doc. dr. sc. Saša Mićanović
doc. dr. sc. Dario Hrupec

Rijeka, 2024

Supervisor:	doc. dr. sc. Saša Mićanović *Faculty of Physics, University of Rijeka*
Co-Supervisor:	doc. dr. sc. Dario Hrupec *Department of Physics, J. J. Strossmayer University of Osijek*

The doctoral thesis was defended on June XX, 2024 in Rijeka before a committee comprised of the following members:

1.
2.
3.
4.
5.

In memory of my beloved aunt Branka.

“You popped my heart seams
All my bubble dreams, bubble dreams”

Stefani Joanne Angelina Germanotta

Acknowledgments

I extend my deepest gratitude to all those whose support and encouragement contributed to the completion of this doctoral thesis. First and foremost, I would like to express my sincere appreciation to my supervisors, Dr. Saša Mićanović and Dr. Dario Hrupec, for their guidance, insightful feedback and continuous support along the way to this thesis. Their encouragement and patience have been invaluable and have shaped not only the outcome of this thesis but also my growth as a physicist.

My sincere thanks go to my dear colleagues from the University of Rijeka. I would like to thank the head of the Doctoral Study in Physics, Dr. Dijana Dominis Prester, for all the suggestions that improved the outcome of this thesis and for the hard and selfless work for the benefit of our research group, Lovro Pavletić for every cross-checked analysis, Gordan Janeš for all the help with the supercomputer Bura when I was an absolute beginner, and the rest of the UniRi crew for active participation in numerous seminars and constructive feedback on my work. I would also like to thank my colleagues from the Ruđer Bošković Institute.

I also owe a great debt of gratitude to my dear Polish colleagues, Dr. Julian Sitarek, Dr. Dorota Sobczyńska and Dr. Natalia Żywucka-Hejzner. The collaborative spirit and exchange of ideas were very enriching and broadened the scope of my work. Thank you very much for making my stay in Łódź such a wonderful journey. It was a pleasure to be your guest and to work with you on so many projects. I extend my gratitude to all those whose names may not appear here, but who have contributed to this work in various ways. Your support, whether big or small, is deeply appreciated.

Finally, I am indebted to my family for their unwavering support, understanding and encouragement during the ups and downs of this academic journey, and to Duje and Monika for the love and moments of respite when I needed it most. Their belief in my abilities has been a constant source of motivation.

Abstract

In the very-high-energy range, both the low flux of cosmic gamma rays and their inability to penetrate the atmosphere, limit direct observations of cosmic phenomena. Over the past three decades, the Imaging Atmospheric Cherenkov Technique has become a powerful tool in the very-high-energy gamma-ray astronomy. As their name implies, Cherenkov telescopes observe gamma rays indirectly by capturing short flashes of Cherenkov light produced in the cascade of secondary particles in the atmosphere. Although an integral part of the detector, the atmosphere is also a source of systematic uncertainties. The scattering and absorption of Cherenkov light by aerosols and clouds result in the loss of Cherenkov photons that would otherwise trigger the telescopes, reducing the Cherenkov light yield and effective area.

To investigate the cloud-related effects on the reconstruction of gamma-ray-induced air showers observed with the Cherenkov Telescope Array, the next-generation observatory for very-high-energy gamma-ray astronomy, an extensive database of dedicated Monte Carlo simulations was generated. The transmission profiles were obtained using the MODerate resolution atmospheric TRANsmission band model algorithm. The effects of clouds were evaluated by analyzing the simulated data and calculating the instrument response functions for two different analyses, depending on the Monte Carlo simulations used to build Random Forest models for classifying the parent particle of the detected air shower and estimating its energy and direction: the *adaptive* Monte Carlo simulations that include clouds and the *standard* Monte Carlo simulations for clear sky conditions.

The effects of clouds on performance parameters such as energy resolution and energy bias can be reduced to the level of standard systematic uncertainties for observations in a clean atmosphere using adaptive Monte Carlo simulations. At the same time, it is important to note that clouds inevitably increase energy threshold and degrade effective area and differential sensitivity. This cannot be corrected even by applying adaptive simulations, as it is impossible to reconstruct events that are not detected. Using standard Monte Carlo simulations in the sample to create Random Forest models further degrades the performance of the Cherenkov Telescope Array and leads to significant energy bias and poor energy resolution. In such cases, the effective area and differential sensitivity are further decreased (by up to 50% compared to adaptive Monte Carlo simulations). Nevertheless, for La Palma, where most clouds are located at an altitude of more than 8 km above sea level, their influence on the angular resolution is of minor importance ($\lesssim 10\%$), as no significant differences are observed between standard and adaptive Monte Carlo simulations.

The method of adaptive Monte Carlo simulations was also tested on the Crab Nebula data taken during the joint observations of the LST-1 and MAGIC telescopes in the presence of clouds. The results show that the method can reconstruct the spectrum of the Crab Nebula with an accuracy of $\lesssim 10\%$ above 100 GeV. By precise modeling of the atmospheric conditions and including them in the simulation chain, systematic uncertainties can be minimized to the level of clear sky observations.

Keywords:

Cherenkov Telescope Array; clouds; Crab Nebula; Imaging Atmospheric Cherenkov Technique; LIDAR; LST-1 Telescope; the MAGIC telescopes

Prošireni sažetak na hrvatskom jeziku

U području vrlo visokih energija, dva čimbenika ograničavaju izravna opažanja kozmičkih pojava teleskopima na površini Zemlje: niski tok kozmičkog gama-zračenja i nemogućnost prolaska gama-zračenja kroz cijelu atmosferu. Tijekom posljednja tri desetljeća atmosferska Čerenkovljeva tehnika pokazala se kao moćni alat u astronomiji visokoenergijskog gama-zračenja. Kao što samo ime govori, Čerenkovljevi teleskopi opažaju gama-zrake posredno, detektirajući kratke bljeskove Čerenkovljevog zračenja emitiranog u pljuskovima sekundarnih čestica u atmosferi nastalim pri interakciji primarnih gama-zraka i atmosferskih molekula. Kao sastavni dio detektora, atmosfera je također izvor sistematskih pogrešaka. Ekstinkcija Čerenkovljevog zračenja na aerosolima i oblacima vodi gubitku Čerenkovljevih fotona koje bi teleskopi detektirali u uvjetima čiste atmosfere, smanjujući prinos Čerenkovljeve svjetlosti i efektivnu površinu. Kao rezultat toga, rekonstruirana energija i tok gama-zračenja najčešće su podcijenjeni.

Kako bi se istražili učinci oblaka na rekonstrukciju pljuskova čestica induciranih gama-zračenjem teleskopima CTA, opservatorija za gama-zračenje vrlo visokih energija sljedeće generacije, generirana je opsežna baza podataka namjenskih Monte Carlo simulacija. Transmisijski profili u prisustvu oblaka potrebni za Monte Carlo simulacije modelirani su pomoću računalnog paketa MODTRAN. Učinci oblaka evaluirani su analizom simuliranih podataka i računanjem funkcija odziva instrumenta za dvije različite analize, ovisno o Monte Carlo simulacijama korištenim za izradu Random Forest modela (koji se koriste za klasifikaciju primarne čestice koja je inducirala detektirani pljusak sekundarnih čestica te procjenu njezine energije i smjera): *prilagođene* Monte Carlo simulacije koje uključuju oblake i *standardne* Monte Carlo simulacije za atmosferu bez oblaka.

Istraživanje je pokazalo da se u prisustvu oblaka broj detektiranih događaja smanjuje, napose u niskoenergijskom dijelu spektra (i do 90% u usporedbi s opažanjima u čistoj atmosferi), što značajno povećava energijski prag (za faktor 2 ovisno o karakteristikama oblaka i zenitnom kutu opažanja). Uporaba prilagođenih Monte Carlo simulacija u uzorku za generiranje Random Forest modela daje energijsku razlučivost usporedivu s onom za čistu atmosferu, što govori da se energija primarne gama-zrake u prisustvu oblaka može rekonstruirati s jednakom (ne)pouzdanošću kao pri visokoj atmosferskoj transparentnosti. Međutim, događaji koji nisu detektirani ne mogu se rekonstruirati niti oporaviti, tako da su efektivna površina, a time i diferencijalna osjetljivost teleskopa, neizbježno narušene čak i kada se koriste prilagođene Monte Carlo simulacije. Opažanja slabijih izvora postaju veći izazov kada se suočavamo s gustom (transmisija $< 75\%$) i niskom (≤ 9 km nadmorske visine) naoblakom. U takvim uvjetima, diferencijalna osjetljivost je smanjena da na faktor 4 u usporedbi s onom koja se postiže u uvjetima visoke atmosferske transparentnosti.

Uporaba standardnih Monte Carlo simulacija u uzorku za generiranje Random Forest modela degradira odziv CTA te uzrokuje znatno podcjenjivanje energije i smanjenu energijsku razlučivost. U takvim slučajevima dodatno se smanjuju efektivna površina i diferencijalna osjetljivost (čak i za dodatnih 50% u odnosu na slučaj prilagođenih Monte Carlo simulacija). Ipak, za La Palmu gdje se većina oblaka nalazi iznad 8 km nadmorske visine, oblaci nisu od velike važnosti kada je u pitanju kutna razlučivost budući da je utjecaj oblaka na rekonstrukciju smjera $\lesssim 10\%$, pri čemu nisu uočene značajne razlike između standardnih i prilagođenih Monte Carlo simulacija.

Možemo se zapitati do koje mjere je sigurno koristiti standardne Monte Carlo simulacije, a da bi se pritom postigle performance Random Forest modela na razini sistematskih pogrešaka pri čistoj atmosferi. Odgovor na ovo pitanje nije jednostavan s obzirom na veliki broj varijabli, ali se može dati uz određena ograničenja. Kako bismo odgovorili na ovo pitanje, procijenili smo kako se mijenja rekonstruirana energija istog detektiranog (simuliranog) događaja u ovisnosti o tome koriste li se standardne ili prilagođene Monte Carlo simulacije za produkciju Random Forest modela. Dobivena razlika u rekonstruiranoj energiji uspoređena je s CTA zahtjevom A-PERF-2050 koji navodi da sistematske pogreške u mjerenju apsolutnog intenziteta Čerenkovljevog zračenja moraju biti manje od 8%. Za niske oblake između 5 km i 7 km iznad razine mora, sistematske pogreške u mjerenju energije uvijek su iznad 8% za oblake s transmisijom nižom od 95%. U slučaju visokih oblaka ($\geq$ 13 km iznad razine mora), standardne Monte Carlo simulacije mogu se sigurno koristiti za energije iznad 150 GeV bez obzira na transmisiju oblaka te na cijelom energijskom rasponu za transmisije $\geq$ 80%. Ispod navedene energije učinci oblaka obično su jači, a sustavne nesigurnosti rastu iznad 8%. Što su oblaci viši, to se u više slučajeva mogu koristiti standardne Monte Carlo simulacije, naravno u ovisnosti o energiji gama-zrake. Tako se na primjer standardne simulacije mogu sigurno koristiti samo za energije iznad 1 TeV i 10 TeV za oblake na 11 odnosno 9 km iznad razine mora.

Metoda prilagođenih Monte Carlo simulacija testirana je na podacima Maglice Rakovica prikupljenima pri zajedničkim opažanjima teleskopa LST-1 i MAGIC u uvjetima slabe do jake naoblake, pri čemu su popratna LIDAR mjerenja korištena za identifikaciju oblaka i modeliranje atmosferskih profila potrebnih za Monte Carlo simulacije. Različiti parametri, uključujući osnovne parametre koji opisuju sliku u kameri, uspoređeni su između Monte Carlo simulacija i stvarnih podataka potvrđujući dobro slaganje. Također su izračunati osnovni parametri koji karakteriziraju odziv teleskopa. Studija je pokazala da se za opažanja pri niskom zenitu osjetljivost sustavno smanjuje pri energijama do 1 TeV - za faktor 3 na energijskom pragu ili manje pri višim energijama, u usporedbi s osjetljivošću u čistoj atmosferi. Unatoč tim učincima, odziv teleskopa ostaje na prihvatljivoj razini u skladu sa zahtjevima konzorcija CTA ili čak na razini usporedivoj s promatranjima za čistu atmosferu. Prilagođene Monte Carlo simulacije daju realistične spektralne parametre i dobiveni spektar dobro se slaže s referentnim spektrom. Naprotiv, u slučaju kada se standardne Monte Carlo simulacije koriste za generiranje Random Forest modela, spektar je značajno podcijenjen čak i pri najvišim energijama (do $\approx$ 40%).

Važno je napomenuti da ovakav pristup zahtijeva velike računalne resurse. U najboljem slučaju različite Monte Carlo simulacije moraju se generirati na dnevnoj bazi, a najčešće i na bazi jednog opažačkog ciklusa (u trajanju od 20 minuta). U mnogim slučajevima metode korekcije mogu dati usporedivu izvedbu te bi se trebale koristiti ako za to postoje indikacije. Međutim, prilagođene Monte Carlo simulacije nezaobilazan su alat u slučajevima kada se opažaju varijabilni izvori u uvjetima promjenjive naoblake, na primjer oblaci koji prolaze kroz vidno polje teleskopa čija je varijabilnost kraća od varijabilnosti vremenskih uvjeta. U takvim slučajevima teško je razlikovati učinke oblaka od intrinzične varijabilnosti izvora te se klasičnim metodama korekcije ne može rekonstruirati stvarni spektar. Zbog trajanja simulacija i ograničenih računalnih resursa prilagođene

Monte Carlo simulacije nisu zamišljene kao dio standardne analize, već bi se trebale izvoditi na zahtjev korisnika (voditelja opažačke smjene, osobe zadužene za analizu na licu mjesta, tzv. *onsite* analizu, ili drugih) u slučajevima kada se ocijeni da klasična metoda korekcije podataka nije primijenjiva. U takvom je slučaju jedini nestandardni ulazni parametar za Monte Carlo simulacije odgovarajući atmosferski profil izveden iz, na primjer, LIDAR mjerenja.

Ključne riječi:
atmosferski Čerenkovljevi teleskopi; CTA; LIDAR; Maglica Rakovica; oblaci; teleskop LST-1; teleskopi MAGIC

Contents

List of Figures

List of Tables

List of Acronyms

a.g.l.	above ground level
a.s.l.	above sea level
AGN	active galactic nucleus
BM	band model
CCD	Charge-Coupled Device
CHIMP	Convert Hessio Into Mars inPut
CMB	cosmic microwave background
CMOS	Complementary Metal-Oxide Semiconductor
CoG	Center of Gravity
CR	cosmic ray
CTA	Cherenkov Telescope Array
CTAO-N	Northern Cherenkov Telescope Array Observatory
DirLUT	direction lookup table
DM	dark matter
DRS4	Domino Ring Sampler 4th Generation
EAS	extensive air shower
EC	external Compton
FoV	Field of View
GRB	gamma-ray burst
HITRAN	HIgh-resolution TRANsmission molecular absorption database
HPD	hybrid photodetector
IACT	Imaging Atmospheric Cherenkov Technique
IC	Inverse Compton scattering
IR	infrared
IRF	instrument response function
LBL	Line-by-Line models
LC	light curve
LIDAR	LIght Detection And Ranging system
LST	Large-Sized Telescope
LUT	lookup table

MAGIC	Major Atmospheric Gamma Imaging Cherenkov Telescopes
MARS	MAGIC Analysis and Reconstruction Software
MC	Monte Carlo
MCP	magic-ctapipe
MODTRAN	MODerate spectral resolution atmospheric TRANsmittance
MST	Medium-Sized Telescope
NKG	Nishimura-Kamata-Greisen
NSB	night sky background
OD	optical depth
ORM	Roque de los Muchachos Observatory
OT	Teide Observatory
PMT	PhotoMultiplier Tube
PSF	Point Spread Function
PWN	pulsar wind nebula
RF	Random Forest
SBG	starburst galaxy
SED	spectral energy distribution
SNR	supernova remnant
SR	synchrotron radiation
SSC	synchrotron self Compton
SST	Small-Sized Telescope
TIB	Trigger Interface Board
US1976	U.S. Standard Atmosphere 1976
UV	ultraviolet
VHE	very-high-energy
WIMP	Weakly Interacting Massive Particle

Foreword

This thesis aims to quantify the effects of clouds on the Imaging Atmospheric Cherenkov Technique in general and the Northern Cherenkov Telescope Array, the future ground-based observatory for very-high-energy gamma-ray astronomy, in particular. In recent years, several research have been carried out to investigate the effects and role of the atmosphere in the Imaging Atmospheric Cherenkov Technique. A few studies have investigated the effects of clouds and aerosols on the performance of Cherenkov telescopes. However, the previous studies were mainly conducted with relatively crude and simple cloud models. While these models served as valuable tools for initial investigations, they lacked the comprehensive depth and precision required for a detailed understanding of the effects of clouds on the Imaging Atmospheric Cherenkov Technique. What distinguishes this work from others is the careful integration of clouds into the simulations of extensive air showers by precise modeling of atmospheric transmission profiles (including clouds) needed for Monte Carlo simulations, a valuable and unavoidable tool in the analysis of the Cherenkov telescope data. This approach not only refines the accuracy of the study but also extends the scope of our understanding and paves the way for a method that allows reliable reconstruction of data even in the presence of low cloud layers with low transmission. The Monte Carlo simulations and the transmission profiles can be tuned to realistic conditions during the observations if the observations are accompanied by appropriate atmospheric transmission measurements. Therefore, the performance of the joint observations of LST-1 and MAGIC telescopes in the presence of clouds is evaluated by analyzing the Crab Nebula data. For this purpose, dedicated transmission profiles were created based on the simultaneous measurements of atmospheric transmission with the Light Detection and Ranging system.

The thesis is structured as follows:

- **Chapter 1** briefly introduces the reader to the field of cosmic rays and ground-based very-high-energy gamma-ray astronomy. The detection technique used in the thesis is explained in detail and the instruments used for the observations on which the work is based are described.
- **Chapter 2** describes the atmosphere in general and its influence on the measurements with the Imaging Atmospheric Cherenkov Technique. The reader is introduced to the state-of-the-art band model algorithms and atmospheric profile modeling, presenting atmospheric conditions modeled for this work. An overview of previous studies on the influence of clouds

on the Imaging Atmospheric Cherenkov Technique is given.

- **Chapter 3** gives an introduction to the software used to produce Monte Carlo simulations of extensive air showers and telescope response and provides the specific parameters used for the simulations.
- **Chapter 4** provides a comprehensive overview of the analysis technique used and the results of the analysis aimed at investigating the influence of clouds on the reconstruction of the arrival direction and primary energy of gamma-ray-induced air showers detected by the Northern Cherenkov Telescope Array. The analysis is compared between two types of Random Forest models: one created with the standard Monte Carlo simulations (clear atmosphere) and the other created with the adaptive Monte Carlo simulations (including clouds).
- **Chapter 5** presents a comparative analysis between adaptive Monte Carlo simulations (generated based on the knowledge of atmospheric conditions from the Light Detection and Ranging system measurements) and the real data. The performance of the joint observations of LST-1 and MAGIC in the presence of clouds is evaluated by analyzing data from the Crab Nebula. The chapter concludes with a comprehensive spectral and temporal analysis of the Crab Nebula data taken in the presence of clouds.

CHAPTER 1

The atmosphere as a detector

The universe is a complex web of high-energy phenomena in which astrophysical sources release colossal amounts of energy that exceed the limits of conventional understanding of electromagnetic radiation. Gamma rays reaching into the teraelectronvolt and even petaelectronvolt range offer unique insights into the most extreme and cataclysmic events in our universe. In this opening chapter, we explore very-high-energy gamma rays and the Imaging Atmospheric Cherenkov Technique, which has revolutionized our understanding of these cosmic messengers.

1.1 Cosmic rays

In 1785, the French physicist Charles-Augustin de Coulomb presented a report on a series of experiments which proved that a spontaneous discharge of isolated electrified bodies was not due to poor insulation but to an external cause (de Coulomb, 1785). In 1879, William Crookes, a British chemist and physicist, observed that the rate at which an electroscope loses its charge decreases with decreasing pressure (Crookes, 1879). Later, at the beginning of the 20th century, radioactivity and its ability to ionize the air were discovered by Henri Becquerel, Marie Skłodowska Curie, and Pierre Curie (Becquerel, 1896; Sherman, 1970; Curie, Curie and Bémont, 1898). These groundbreaking discoveries prepared the base for a more detailed study of the conductivity of air, but also erroneously supported the view that ionizing radiation originates in the Earth's crust.

In 1901, Charles Wilson, a Scottish physicist, suggested that the origin of ionization might be extremely penetrating extraterrestrial radiation (Wilson, 1901). Although this idea was dropped for many years because Wilson's experiments failed, subsequent experiments by the Italian Domenico Pacini and the Austrian Victor Hess led to the discovery of the radiation now known as cosmic rays (CRs). Pacini investigated, among other things, the rate of ionization both on land and underwater. He shielded an electroscope in a copper box and submerged it 3 m under water. He found that the ionization rate decreased by 20% (Pacini, 1909, 1911, 1912). The result argued for an extraterrestrial origin. Between 1911 and 1913, Hess made a series of balloon flights and discovered that the ionization rate was many times higher at an altitude of several kilometers than on the ground. One particularly important flight took place on April 17, 1912, during a total solar eclipse, in the time of which the ionization rate did not decrease (Hess, 1912, 1913). Hess concluded that the radiation had to come from above. His discoveries were confirmed in 1925 by Robert Millikan, who coined the term cosmic rays.

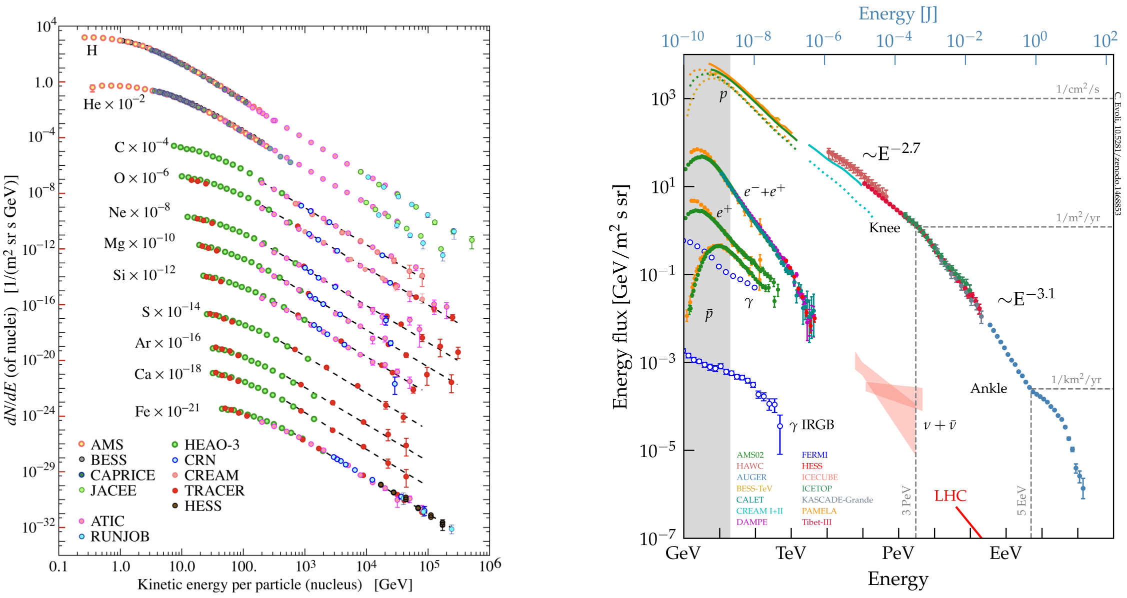

(a) **(b)**

Figure 1.1: a) The fluxes of the main primary CRs nuclei as obtained from different experiments (Beringer et al., 2012). b) The energy spectrum of cosmic rays. Credits: 10.5281/zenodo.2360277.

Since then, considerable progress has been made in understanding various properties of CRs such as their extensive energy range, composition, and flux. However, some questions remain unanswered or only partially answered, including the sources and origin of ultra-high-energy CRs and the acceleration mechanisms. Understanding the origin and acceleration mechanisms of CRs is important for expanding our knowledge of the universe and has practical implications, such as the development of new technologies for space exploration and radiation protection.

1.1.1 Spectrum and chemical composition

Cosmic radiation at the top of the atmosphere consists of primary and secondary particles. Primary CRs, such as protons, helium nuclei, electrons, and other nuclei produced in stars, e.g., carbon, oxygen, and iron, are the particles accelerated in astrophysical sources. In addition, CRs can interact in accelerating regions, producing secondary charged and neutral particles such as neutrinos, gamma rays, and nuclei such as lithium, beryllium, and boron (Figure 1.1a). A small fraction of antiprotons and positrons is probably of secondary origin as well. Electrons and positrons must be of galactic origin because they cannot reach intergalactic distances due to energy loss by Compton scattering. It is interesting to note that the measured positron-electron ratio (Figure 1.2a) increases at energies above 10 GeV. This ATIC peak (from Advanced Thin Ionization Calorimeter (Wefel, 2001)), observed between 0.1 TeV and 1 TeV, could possibly be explained by the presence of nearby pulsars or the decay of dark matter (Chowdhury, Vempati and Jog, 2011). A similar phenomenon is observed for the antiproton-to-proton flux ratio (Figure 1.2b): above 20 GeV a plateau is reached, which is difficult to explain with the currently available knowledge.

The relative abundance of CRs at the top of the atmosphere, which is remarkably similar to the chemical composition of the solar system but also has important differences, is shown in Figure 1.3.

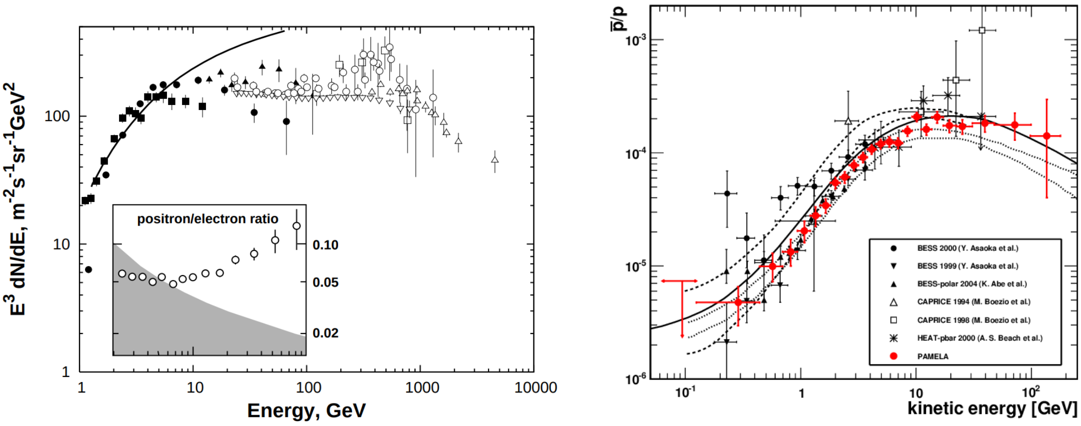

(a) **(b)**

Figure 1.2: a) The inset shows the positron-to-electron flux ratio measured at the top of the atmosphere (the PAMELA experiment) compared to the expected decrease (shaded area) (Beringer et al., 2012). The main plot presents the differential spectrum of electrons and positrons folded by E^3. b) The antiproton-to-proton flux ratio at the top of the atmosphere (Picozza and Sparvoli, 2011).

The peak in C, N, O, and Fe composition indicates that many of the CR nuclei must be of stellar origin. An even-odd effect related to the relative stability of the nuclei according to their atomic and mass numbers is visible in both the cosmic and solar chemical compositions. The excess of (Li, Be, B) and (Sc, Ti, V, Mn) in the chemical composition of CRs compared to their relative abundance in the solar system is due to the spallation of (O and N) and (Fe and Ni) nuclei, respectively. The relative underabundance of H and He is not yet fully understood, but it could either reflect the primordial composition of the sources of CR or be due to the fact that heavier elements are more readily ionized (Bergström and Goobar, 2006).

At energies up to ≈ 10 TeV, the flux of CRs is sufficient to perform direct observations. Above these energies, and especially above 1 PeV, the composition of CRs is determined by indirect observations. The flux of CRs decreases steeply with energy, ranging from 1 particle $\mathrm{m}^{-2}\,\mathrm{s}^{-1}$ at 10^9 eV to 1 particle $\mathrm{m}^{-2}\,\mathrm{yr}^{-1}$ at 10^{15} eV to 1 particle per century per km^2 at 10^{20} eV. The energy spectrum of CRs, which spans over 13 decades in energy, is described by a broken power law:

$$\frac{\mathrm{d}N}{\mathrm{d}E} \propto E^{-\alpha}, \tag{1.1}$$

with the spectral index α being dependent on the energy region:

$$\alpha = \begin{cases} 2.65, & E < 10^{16}\ \mathrm{eV}, \\ 3.10, & 10^{16}\ \mathrm{eV} < E < 10^{18}\ \mathrm{eV}, \\ 2.70, & E > 10^{18}\ \mathrm{eV}. \end{cases} \tag{1.2}$$

Different slopes indicate three distinct regions in the CRs spectrum, i.e., two transition points (Figure 1.1b): the first, called *knee*, at energies of ≈ 10^{15} eV, and the second, the *ankle*, at energies of ≈ 10^{19} eV. Particles with energies below and around the knee of the CR spectrum are thought to

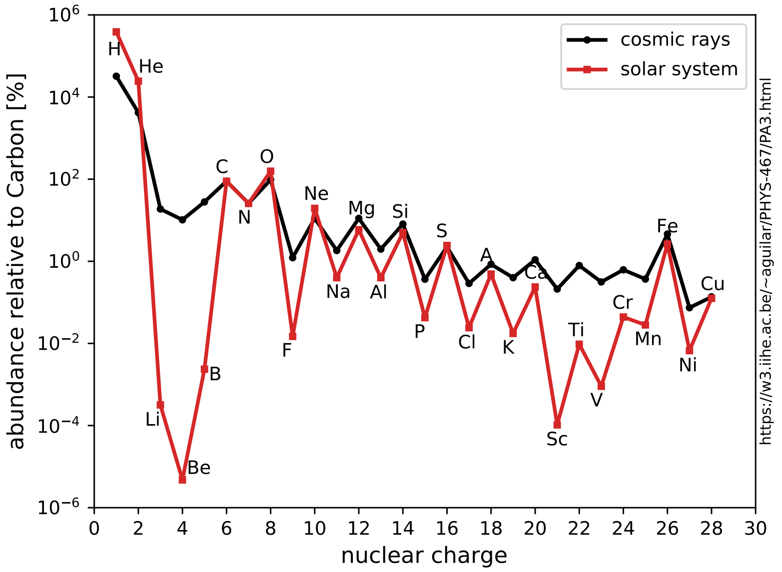

Figure 1.3: The relative abundance of CRs at the top of the atmosphere compared to the chemical composition of the solar system.

be accelerated primarily in astrophysical objects within our galaxy, such as supernova remnants (De Angelis and Mallamaci, 2018). The ankle, on the other hand, is considered a transition region between galactic and extragalactic acceleration sources. The changes in the spectral index in the knee region suggest that there are at least two distinct sources of cosmic rays. While it stands to reason that the bulk of the particles are galactic in origin, the particles with the highest energies must be extragalactic, since there are no such strong sources in the Milky Way galaxy and their arrival directions are highly isotropic. However, it is a puzzle how these particles can travel enormous distances without being subject to the Greisen-Zatsepin-Kuzmin cutoff (Greisen, 1966; Zatsepin and Kuz'min, 1966).

The chemical composition of the cosmic radiation of the highest energies (> 1 EeV) is almost completely unknown given the extremely low flux of only one particle per 100 km^2 per century. Low-energy CRs originating from outside the solar system are modulated by the solar wind, which slows them down and partially excludes them from the spectrum. Hence, CRs below 10 GeV must originate from the Sun. In addition, the flux of low-energy CRs is modulated by solar activity within the 11-year solar cycle and is affected by the geomagnetic field. Therefore, the intensity of the individual components of the CRs in the GeV range depends on both the location and the timing of the measurement. Above 30 GeV, where the influence of the geomagnetic and solar magnetic fields is small, due to diffusive propagation in the galactic magnetic field the CRs arrive isotropically to the Earth (Beringer et al., 2012).

1.1.2 Acceleration of cosmic rays

The characteristic shape of the CR spectrum associated with the extraordinary energies contradicts any explanation that these energies are due to thermal phenomena. This suggests that the observed cosmic rays have undergone an acceleration process. Most likely, CRs are accelerated in the electromagnetic fields surrounding astrophysical sources or the interstellar medium (Bell, 2013).

Second-order Fermi acceleration

In 1949, Enrico Fermi proposed a mechanism in which CR particles of mass m are scattered by randomly moving magnetic mirrors of mass $M \gg m$ (Fermi, 1949; Gaisser, Engel and Resconi, 2016; De Angelis and Pimenta, 2018). Magnetic mirrors correspond to irregularities in the galactic magnetic fields due to clouds of interstellar matter (i.e., plasma) whose density is greater than the density of the surrounding material. The particles gain energy in head-on interactions and lose energy in tail-on interactions. When a magnetic mirror moves isotropically with an average velocity v, the average energy gain per collision (in statistically more frequent frontal collisions) is:

$$\left\langle \frac{\Delta E}{E} \right\rangle \propto \left(\frac{v}{c} \right)^2, \tag{1.3}$$

where c is the speed of light in vacuum. The mechanism is known as second-order Fermi acceleration. Although the mechanism explains well the power-law shape, the predicted energy gain is slow ($\frac{v}{c} < 10^{-4}$ typically), and the mean free path length is of the order of 0.1 pc[1], too small to explain the observed CR spectrum.

First-order Fermi acceleration

An inherent limitation of Fermi's initial concept lay in the gradual and inefficient acceleration it offered, providing only $O(v^2)$ energy gains at each collision, which hindered its effectiveness. A more efficient mechanism, the first-order Fermi acceleration or diffuse shock acceleration, was introduced by Fermi in 1954 and discussed by many other authors (Gaisser, Engel and Resconi, 2016; De Angelis and Pimenta, 2018; Axford, 1981). The acceleration is based on the propagation of strong shock waves through the interstellar medium at supersonic speeds. Two regions are considered: the *upstream region*, which is the medium ahead of the shock front that is not perturbed by the shock, and the *downstream region*, which is a perturbed region behind the shock front. Due to accretion in the upstream region, the shock front is faster than the downstream region.

The particles are accelerated when they cross the shock front. Suppose the shock front is moving through the medium with velocity v. In the rest frame of the shock front, the upstream gas moves toward the shock front with velocity $v_1 = |v|$, while the downstream gas recedes with velocity v_2. The relationship between these two velocities is $v_2 = 0.25 \cdot v_1$. When observed from reference frames in which either the upstream or downstream gas is at rest, the gas in the opposite region appears to be moving toward the shock front with a velocity of $0.75 \cdot |v|$. After a charged particle from the upstream region enters the shock and passes the shock front, it is scattered by the magnetic field inhomogeneities in the downstream region. The particles leaving the downstream region also leave the acceleration process and contribute to the CR spectrum. Particles that re-cross the shock front experience further acceleration. In the rest frame of the particle, as the particle crosses the shock front from downstream to upstream, it approaches the upstream region with a velocity of $0.75 \cdot |v|$. Consequently, the particle always gains energy as it crosses the shock front.

---

[1] The parsec (pc) is the distance at which 1 astronomical unit (au) subtends an angle of one arcsecond.

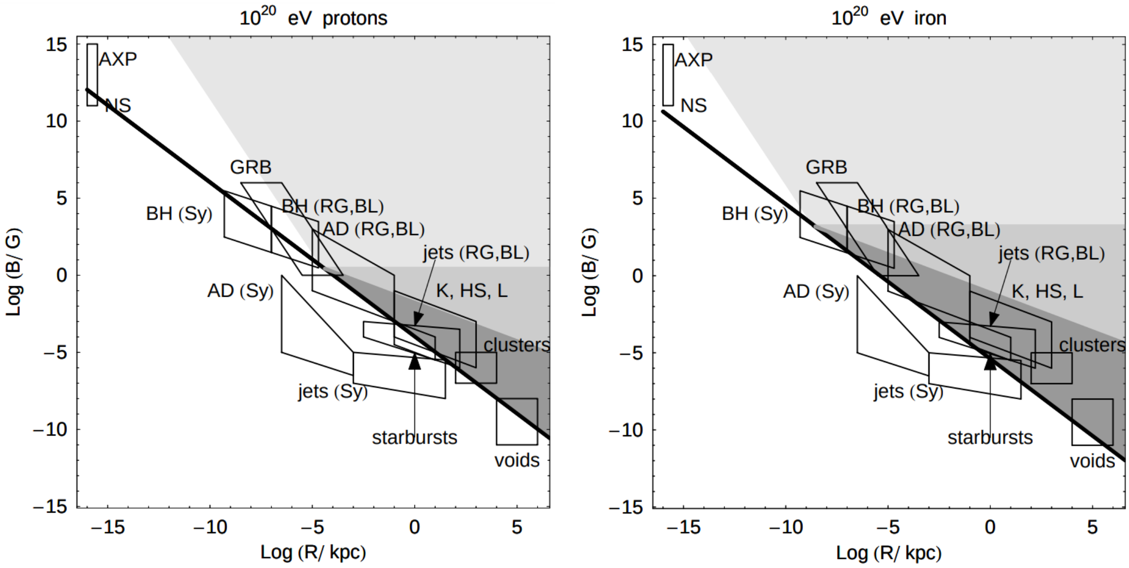

Figure 1.4: The Hillas plot with constraints due to geometry and radiation losses for a) 10 TeV protons and b) 10 TeV iron nuclei, with the following abbreviations: central parsecs (AD) of active galaxies: Seyfert galaxies (Sy), radio galaxies (RG) and blazars (BL); knots (K); hot spots (HS) and lobes (L); gamma-ray bursts (GRB); neutron stars (NS); anomalous X-ray pulsars and magnetars (AXP); supermassive central black holes (BH). (Ptitsyna and Troitsky, 2008)

The particle experiences an increase in energy proportional to $\frac{v}{c}$:

$$\left\langle \frac{\Delta E}{E} \right\rangle \propto \frac{v}{c}. \tag{1.4}$$

In astrophysical environments, first-order Fermi acceleration is thought to play a crucial role in the acceleration of cosmic rays. These are high-energy particles that travel through space and interact with the magnetic fields of stars and galaxies. The most probable sites of acceleration are non-relativistic shocks produced by supernova explosions and their remnants (Ptuskin, Zirakashvili and Seo, 2010). This mechanism is also thought to play a role in the acceleration of particles in solar flares and in the production of relativistic jets from active galactic nuclei. According to Ptitsyna and Troitsky (2008), a particle accelerator should satisfy several general conditions:

- the particle is accelerated only if it is in the acceleration region of the source,
- the source should have the required amount of energy to accelerate the particle,
- the radiation and interaction energy losses should not exceed the energy gain,
- the ensemble of sources should reproduce the observed CR spectrum.

The maximum energy that can be achieved during acceleration can be estimated using simple principles. The particles will escape when their gyroradius r exceeds the physical size R of the accelerator. This maximum energy E that can be reached during acceleration is calculated using the Hillas criterion (Hillas, 1984) $E \leq q \cdot B \cdot R$, where q is the particle charge and B is the magnetic field of the accelerating region. The Hillas plot (Figure 1.4) shows the size of potential CRs sources as a function of the strength of the magnetic field.

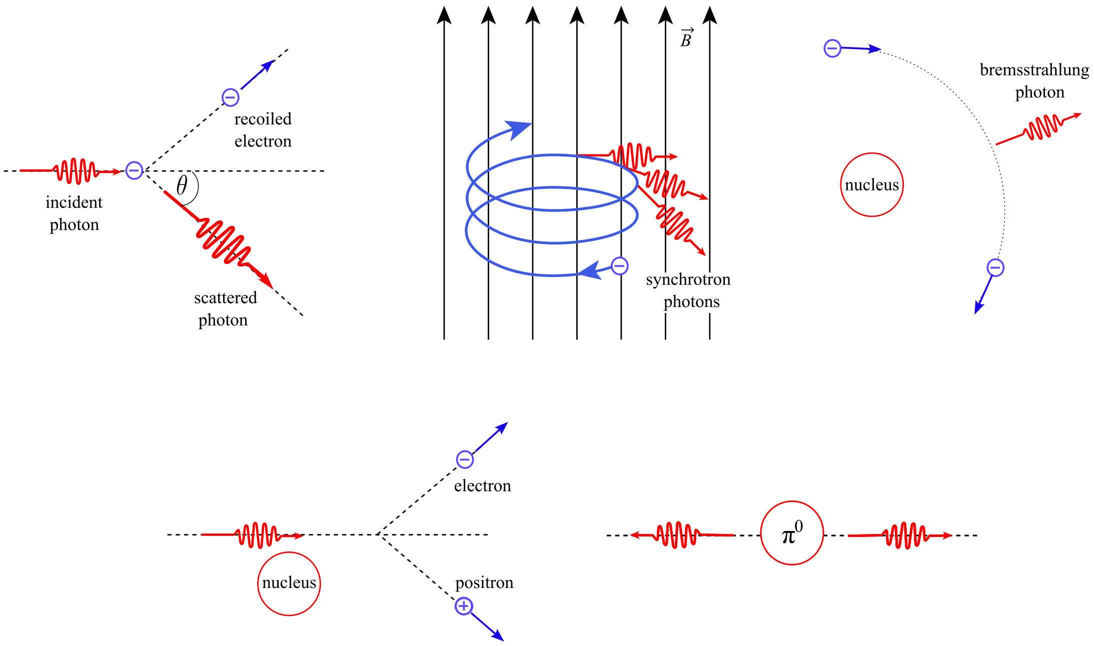

Figure 1.5: Most significant processes for the production of gamma rays and extensive air showers. *Top panels, from left to right*: Compton scattering, synchrotron radiation, bremsstrahlung. *Bottom panels, from left to right*: pair production, pion decay.

Photons have proven crucial for probing the most extreme cosmic phenomena, as charged particles are deflected by galactic and intergalactic magnetic fields, losing directional information. Other possible astronomical messengers include neutrinos and gravitational waves. Neutrinos are uncharged but weekly interacting particles that require an enormous amount of dense material to be detected, while gravitational waves require extremely sensitive detectors and are difficult to detect, making gamma rays the most suitable information carrier to date. Gamma rays span 16 orders of magnitude in the energy spectrum (from 10^5 eV to 10^{20} eV), more than the rest of the electromagnetic spectrum. Different techniques and instruments are therefore required to study gamma rays in detail. In the very-high-energy (VHE, $\gtrsim 100$ GeV) range both the low flux of gamma rays and the high atmospheric opacity makes direct observations difficult. Therefore, researchers rely on indirect detection methods such as the Imaging Atmospheric Cherenkov Technique (IACT), air shower arrays or Water Cherenkov detectors (see e.g. Bose et al. (2021) or Sitarek (2022) for a review).

1.2 Gamma rays production mechanisms

The basic concepts of gamma rays production mechanisms (Figure 1.5) can be divided into two main groups: *Bottom-up models*, in which the generation of gamma rays is due to the acceleration of charged particles from astrophysical sources (Weekes, 2003; Grieder, 2010), and *top-down models*, in which gamma rays are attributed to the decay of exotic particles (Bertone et al., 2007; De Angelis and Mallamaci, 2018).

1.2.1 Bottom-up scenarios

Inverse Compton scattering

Inverse Compton scattering (IC) is the process by which a low-energy photon is scattered by a high-energy electron. The process is called inverse because, unlike the standard Compton effect, the electrons lose energy, not the photons. The process is important when low-energy photons interact with high-energy electrons. Two regimes can typically be distinguished:

1. the Thomson regime when the energy of the photon is less than the energy of the rest mass of the electron m_e, i.e. $\gamma E_\gamma(1-\frac{v}{c}\cos\theta) < m_e c^2$:

$$\sigma_T = \frac{e^4}{6\pi\epsilon_0 m_e^2 c^4}, \tag{1.5}$$

2. the Klein-Nishina regime when the energy of the photon exceeds the energy of the rest mass of the electron in the rest frame of the electron, i.e. $E_\gamma > m_e c^2$:

$$\sigma_{KN} = \frac{3}{4}\sigma_T\left(\frac{1+x}{x^3}\left[\frac{2x(1+x)}{1+2x} - \log(1+2x)\right] + \frac{1}{2x}\log(1+2x) - \frac{1+3x}{(1+2x)^3}\right), \tag{1.6}$$

where $\epsilon_0 = 8.854\cdot 10^{-12}$ F m^{-1} is the vacuum permittivity, $c = 3\cdot 10^8$ m s^{-1} is the speed of light, $x = \frac{h\nu}{m_e c^2}$, γ is the relativistic Lorentz factor of the electron, and E_γ is the initial energy of a photon. At low energies ($x \gg 1$), the effective cross-section for the inverse Compton process asymptotically approaches the Thomson regime. The energy of the scattered photon is given by:

$$E \simeq 6.5\left(\frac{E_e}{1\ \text{TeV}}\right)^2 \frac{E_\gamma}{\text{MeV}}\ \text{GeV}. \tag{1.7}$$

The Thomson regime applies in general to the interactions of electrons with the photons of the cosmic microwave background radiation (Grieder, 2010).

Synchrotron radiation

Charged particles moving at relativistic speeds and driven by magnetic fields emit electromagnetic radiation known as synchrotron radiation (SR) as they orbit around magnetic field lines. A continuous spectrum of radiation is emitted in a conical pattern with an angle of $\theta = \frac{1}{\gamma}$, where γ is the Lorentz factor. The rate of energy loss due to SR is given by:

$$-\frac{\mathrm{d}E}{\mathrm{d}x} = \frac{2e^4}{3m_e^2 c^4}\gamma^2 B^2\ \text{ergs cm}^{-1}, \tag{1.8}$$

where $e = 1.602\cdot 10^{-19}$ C is the elementary charge, $m_e = 9.109\cdot 10^{-31}$ kg is the mass of an electron, B is the strength of the magnetic field, and c is the speed of light. The SR emission spectrum falls off steeply beyond a critical frequency, ω_c:

$$\omega_c = \frac{3}{2}\frac{eB}{m_e c}\gamma^2 \sin\theta. \tag{1.9}$$

The critical frequency of SR depends on the rest mass of the particle as $1/m^3$. Therefore, the observed SR is generally considered to be leptonic. However, the classical SR is not capable of producing high-energy gamma rays unless it is from sources with extremely strong magnetic fields, such as pulsars, and it serves as a target for other processes. The energy emitted by an electron from SR is (De Angelis and Mallamaci, 2018):

$$E = 0.2 \frac{B}{10\ \mu\text{G}} \left(\frac{E_e}{1\ \text{TeV}} \right)^2\ \text{eV}, \tag{1.10}$$

where E_e is the rest energy of an electron. There is another similar process called curvature radiation. Here the radiation is emitted by electrons following the curved magnetic field lines. Both SR and IC can occur in the same astrophysical source. Specifically, in such a source, ultra-relativistic electrons are accelerated in a magnetic field, resulting in the emission of photons in a broad spectrum ranging from the infrared to the X-ray band. These emitted photons subsequently interact by Compton scattering with the electrons responsible for their production, leading to an increase in their energy. This process is called Synchrotron Self Compton (SSC).

Pion decay

Hadronic processes, such as pp collisions or $p\gamma$ interactions, can also lead to the emission of photons through the production of neutral pions. Neutral pions π^0 are unstable particles with a lifetime of $8.4 \cdot 10^{-17}$ s that can decay into gamma rays. The primary decay mode of a neutral pion (with a branching ratio of 0.98823) is:

$$\pi^0 \longrightarrow \gamma + \gamma, \tag{1.11}$$

and the second most common decay mode (with a branching ratio of 0.01174):

$$\pi^0 \longrightarrow \gamma + e^+ + e^-. \tag{1.12}$$

1.2.2 Top-down scenarios

Another mechanism responsible for the production of gamma rays would be the annihilation of dark matter particles (DM), such as weakly interacting massive particles[2] (WIMPs). Such gamma rays could have sharp spectral features, such as $\gamma\gamma$ or $Z\gamma$ annihilation lines. However, since WIMPs are electrically neutral, these processes are loop-suppressed and therefore likely rare. Another process implies the annihilation of two WIMPs to form quark or lepton pairs, which could give rise to secondary neutral pions. The expected flux of gamma rays from annihilation processes is given by (De Angelis and Mallamaci, 2018):

$$\Phi = \frac{1}{4\pi} \frac{\langle \sigma_{\text{ann}} v \rangle}{2 m_{\text{DM}}^2} \frac{\mathrm{d}N}{\mathrm{d}E} \int_{\Delta\Omega} \rho_{\text{DM}}^2 \mathrm{d}l(\Omega), \tag{1.13}$$

---

[2] A WIMP is a hypothetical particle with a large mass (10 or 100 times the mass of a proton) that interacts by gravitational force but interacts only weakly with ordinary matter and moves through it without being decelerated.

Figure 1.6: Images of quasar Mrk 231 (*left*), GRB 190114C (*center*, artist's impression) and SBG NGC 253 (*right*). Credits: European Space Agency, National Aeronautics and Space Administration.

where $\langle\sigma_{\text{ann}}v\rangle$ is the annihilation rate (i.e. the velocity-weighted annihilation cross section) of DM particles of mass m_{DM}, $\frac{\mathrm{d}N}{\mathrm{d}E}$ is the differential gamma-ray flux per annihilation event, ρ^2_{DM} is the boost factor (i.e., the line-of-sight integral of squared DM density).

1.3 Astrophysical gamma-ray sources

The processes described in section 1.2 can occur in different astrophysical sources. The following sections give a brief overview of the identified gamma-ray sources, sorted according to their extragalactic (Figure 1.6) or galactic (Figure 1.7) nature.

1.3.1 Extragalactic sources

Active Galactic Nuclei Active galactic nuclei (AGNs) consist of a central supermassive black hole and an accretion disk composed of gas and dust. The disk is enveloped by a dust torus, a donut-shaped region known as the obscuring torus. Above and below the accretion disk are two absorption regions: the *Broad Line Region* and the *Narrow Line Region*, which are extended regions of broad and narrow emission lines from different parts of the AGN core. The conversion of gravitational energy into the kinetic energy of accreting material leads to the ejection of matter in the form of two, highly collimated relativistic jets of plasma. A typical non-thermal broadband spectrum of an AGN shows two bumps (Maraschi, Ghisellini and Celotti, 1992; Dermer and Schlickeiser, 1993; Maraschi and Tavecchio, 2003; Ghisellini, Tavecchio and Ghirlanda, 2009): the low-energy bump (from the optical band to the X-ray band), modeled by synchrotron emission from relativistic electrons in the jets, and the high-energy bump (from X-rays to VHE gamma rays), which is explained by IC of low-energy photons, either by SSC or, alternatively, the photons originate from an external radiation field, a model known as external Compton (EC). Hadronic models have also been proposed to explain the VHE radiation from AGNs (Cerruti et al., 2015). The brightest AGNs exceed the combined light of the billions of stars in the galaxies.

Starburst galaxies Starburst galaxies (SBGs) are a type of galaxy characterized by a very high star formation rate ($\approx 10^3$ times higher than in normal galaxies like the Milky Way). They are formed by collisions of galaxies or by the disturbance of the dynamical equilibrium of interstellar gas. Radiation from such objects is dominant in the optical and infrared regions, indicating high concentrations of gas and radiation in localized regions. Observations show hadronic-dominated

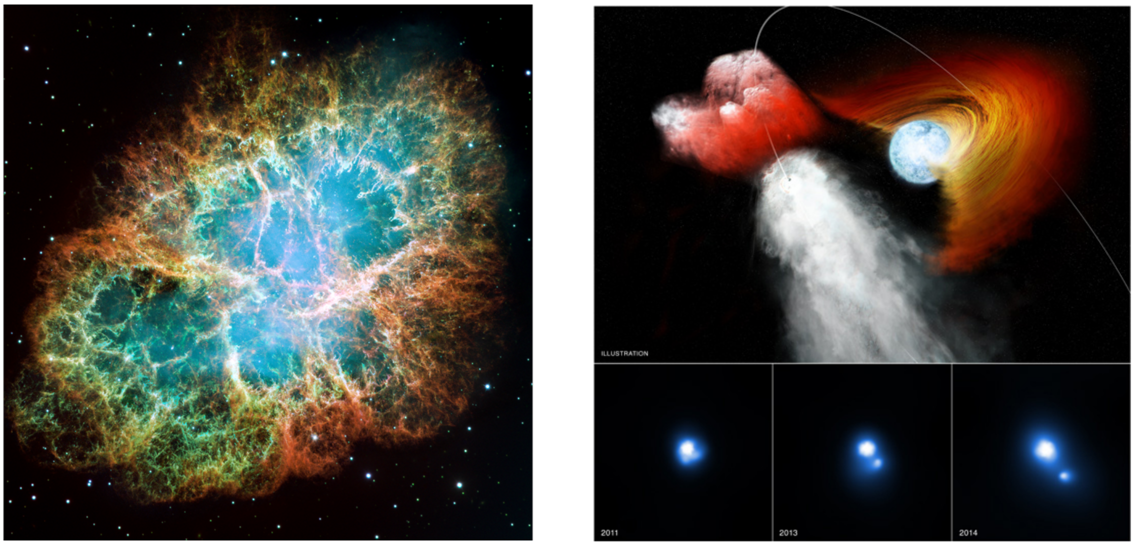

Figure 1.7: *Left*: Image of Crab Nebula SNR taken by the Hubble telescope. Credits: European Space Agency, National Aeronautics and Space Administration. *Right*: Image of a binary system PSR B1259-63 taken by the Chandra X-Ray observatory (upper panel is an artistic impression of a binary system). Image taken from: `https://chandra.harvard.edu/photo/2015/psrb1259/`.

gamma-ray emission up to several TeV, with gamma-ray emission originating mainly from pp interactions between CRs and the particles of the surrounding gas and the subsequent decay of neutral pions. Although hadronic processes dominate gamma-ray emission, there is also some contribution from bremsstrahlung and IC emission of primary and secondary electrons. To date, two SBG VHE gamma-ray sources have been discovered: NGC 253 (Abramowski et al., 2012; Abdalla et al., 2018) and M 82 (Acciari et al., 2009).

Gamma-ray bursts Gamma-ray bursts (GRBs) are the brightest known sources of electromagnetic radiation in the universe. They are sudden bursts of radiation lasting from milliseconds to thousands of seconds. The emission from GRBs occurs in two phases, a short, prompt emission phase that typically lasts tens of seconds, and a second, longer afterglow phase. During the afterglow, the shock-like outflow produced by the interaction between the ejected material and the circumburst medium slows down, resulting in a gradual decrease in brightness. GRBs typically emit most of their energy in the form of gamma rays with energies in the keV to MeV range, but a few photons with energies of tens of GeV have also been detected by space-based instruments. The first TeV emission from GRB was announced in 2019 by the HESS collaboration (Abdalla et al., 2019), and followed by the MAGIC collaboration (Acciari et al., 2019).

1.3.2 Galactic sources

Supernova remnants A supernova is the explosion of a massive star in which a collapsed stellar core forms a neutron star or black hole, while the outer layers of stellar material are ejected into interstellar space, forming a supernova remnant (SNR). The ejected material, which expands as a result of the explosion, penetrates the interstellar material and creates a shock wave. Under typical interstellar conditions, where the density is about 1 proton cm^{-3}, it takes about a millennium for 10 solar masses of material moving at a speed of 5000 km s^{-1} to accumulate an equivalent mass of interstellar material. This period corresponds to the characteristic duration of supernova expansion, during which most of the particle acceleration takes place. In the context of first-order Fermi acceleration and these conditions, the highest achievable particle energy is limited to less than $z \cdot 30$ TeV at a magnetic field strength of 3 μG in the interstellar medium (Weekes, 2003; Dermer and Powale, 2013). This process yields a power-law energy spectrum with a spectral index of −2.0, consistent with the intrinsic spectrum, given the effects of cosmic-ray propagation within the galaxy, which can lead to a slight steepening of the spectral index, around −0.6, resulting in a final observed index of −2.7 for the local cosmic-ray spectrum. Cosmic ray ions and electrons can interact with target particles (the ejected mass, the suspended mass, or the gas of the interstellar medium) to produce gamma rays by secondary nuclear production or bremsstrahlung (Weekes, 2003). In addition, relativistic electrons can shift photons of the surrounding radiation fields into the gamma-ray region by Compton scattering.

Pulsars and pulsar wind nebulae Pulsars are very compact, highly magnetized (10^8-10^{11} T), and rapidly spinning neutron stars formed from the collapse of the core of exploding massive stars. As the neutron star spins, charged particles are ripped away from its surface and accelerated along the magnetic field lines. This creates intense electromagnetic radiation, ranging from radio to gamma rays. Due to the misalignment of the magnetic and rotational axes, the radiation beam emanating from a particular region in the magnetosphere sweeps across the line of sight in a regular pattern, causing the observed pulsations. These pulses can occur at incredibly large frequencies, sometimes up to hundreds of times per second, making pulsars some of the most accurate natural clocks known to science. The primary radiation mechanism is synchrotron and curvature radiation produced by relativistic electrons and positrons trapped in the magnetosphere of the pulsar, near the magnetic poles (Ruderman and Sutherland, 1975; Daugherty et al., 1982), or in the outer gaps (Arons et al., 1979; Harding et al., 2008; Hirotani, 2008; Cheng et al., 1986). The first pulsar emitting in the VHE gamma-ray region was confirmed by the observations of the MAGIC collaboration in 2008 (Aliu et al., 2008). Driven by the rotational energy of the rapidly spinning pulsar, a strong, ultra-relativistic stream of particles is ejected from the young pulsar. When these particles collide with the surrounding medium, a Pulsar Wind Nebula (PWN) is formed. The point of interaction serves as the birthplace of violent shock waves that lead to the acceleration of particles to energies of several hundred TeV, mainly through the process of IC scattering involving electrons with energies from 1 to 100 TeV. The first detection of photons of highest energy beyond 100 TeV from the Crab Nebula in 2019 by the ASγ observatory in Tibet (Amenomori et al., 2019) opened the possibility that sub-PeV electrons may scatter from the low-energy cosmic microwave background (CMB) photons in the Crab Nebula.

Binary systems Binary systems detected in the VHE range can be divided into four classes (Dubus, 2015; Chernyakova and Malyshev, 2020): Gamma-ray binaries driven by the rotation of a pulsar, microquasars driven by the accretion of matter onto a black hole or neutron star, novae where the energy results from the thermonuclear runaway of a white dwarf, and colliding wind

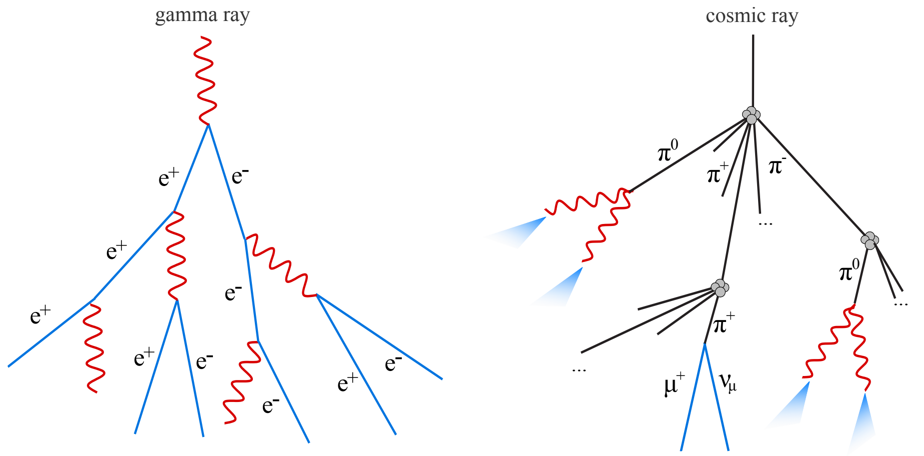

Figure 1.8: Schematic of the development of electromagnetic (*left*) and hadronic (*right*) air showers. Note that a hadronic shower consists of hadronic, muonic and electromagnetic components.

binaries, where the energy is produced by the stellar winds of massive stars. By October 2023, a total of 11 binary systems have been discovered. Unlike microquasars, where the non-thermal emissions are caused by relativistic jets, the radiative output of pulsar binaries is triggered by the interaction between the pulsar wind and the stellar wind emanating from a main sequence companion star. The best-known example of a pulsar binary system is PSR B1259-63 (Aharonian et al., 2005; Chernyakova and Malyshev, 2020), a pulsar in a 3.4-year orbit around a massive Be star LS 2883. The system emits gamma rays only during the periastron passage when the pulsar crosses the disk of the star.

1.4 Extensive air showers

Extensive Air Showers (EASs) are cascades of secondary particles produced by high-energy CRs interacting with the atmosphere. When a CR enters the atmosphere, it collides with molecules and produces a shower of secondary particles, including electrons, positrons, photons, and various types of mesons (Figure 1.8) (Stanev, 2010). These secondary particles continue to interact with molecules in the atmosphere, producing more secondary particles that can spread over large areas and reach the ground. EAS events can be detected and studied by their effects on the atmosphere and by ground-based detectors. Depending on the type of particles that triggered an EAS, a distinction is made between *hadronic* and *electromagnetic* showers. Before we get into the details of their development, let us describe the relevant interaction processes and some frequently used terms.

Screening energy The screening is the dumping of the Coulomb field of the nuclei by the atomic electrons. At very low energies, screening can be safely neglected, while at higher energies it becomes more effective. At energies $\gg E_{\mathrm{scr}}$, the screening is considered complete and defined as:

$$E_{\mathrm{scr}} = \frac{m_e c^2}{\alpha Z^{1/3}}, \tag{1.14}$$

where $m_e c^2 = 0.51$ MeV is the rest mass energy of the electron, $\alpha = \frac{1}{137}$ is the fine structure constant, and Z is the atomic number of the medium. In the air, for which $Z \simeq 7.4$ holds on average, the screening energy is 36.5 MeV.

Critical energy At low energies, electrons in the medium lose their energy mainly by ionization. The critical energy E_{crit} is at which an electron loses equal amounts of energy per unit of radiation length through ionization and radiation. For $E < E_{\text{crit}}$ the most important mechanisms of the multiplication processes are Compton scattering and collisions, which produce electron-ion pairs of very low energy. In gaseous media, the critical energy is given by:

$$E_{\text{crit}} \approx \frac{710}{Z+0.92}, \tag{1.15}$$

expressed in units of MeV, where Z is the atomic number. In air, $E_{\text{crit}} = 84$ MeV.

Bremsstrahlung Bremsstrahlung or braking radiation is electromagnetic radiation emitted by free electrons that are accelerated in the Coulomb field of the atomic nucleus. The electron traveling through matter is deflected by the nucleus. This deflection causes a deceleration of the electron which, at the expense of its kinetic energy, emits a photon. In air $E_{\text{crit}} > E_{\text{scr}}$, complete screening applies. In the case of complete screening and for very high energies, the bremsstrahlung cross-section as a function of the energy k of the emitted photon is (Tsai, 1974; Grieder, 2010):

$$\frac{\mathrm{d}\sigma_{\text{br}}}{\mathrm{d}k} = \frac{4\alpha r_e^2}{k}\left\{\left(\frac{4}{3}-\frac{4}{3}y+y^2\right)\left[Z^2(L_{rad}-f(Z))+ZL'_{rad}\right]+\frac{1}{9}(1-y)(Z^2+Z)\right\}, \tag{1.16}$$

where $y = \frac{k}{E_e}$ is the fraction of electron's energy E_e transferred to the photon, α is the fine structure constant, Z is the atomic number, r_e is the classical radius of the electron, $f(Z)$ is the Coulomb correction:

$$f(Z) = \alpha^2 Z^2\left[\frac{1}{1+\alpha^2 Z^2}+0.20206-0.0369\alpha^2 Z^2+0.0083\alpha^4 Z^4-0.002\alpha^6 Z^6\right], \tag{1.17}$$

and:

$$L_{rad} = \ln\left(\frac{184.15}{Z^{1/3}}\right), \quad L'_{rad} = \ln\left(\frac{1194}{Z^{2/3}}\right). \tag{1.18}$$

A simplified expression can be found by calculating the average energy loss of an electron due to bremsstrahlung and neglecting the second term in curly brackets for $y \ll 1$:

$$-\left\langle\frac{\mathrm{d}E}{\mathrm{d}x}\right\rangle\bigg|_{\text{br}} = \frac{4\alpha r_e^2 N_A}{A}\left[Z^2(L_{rad}-f(Z))+ZL'_{rad}\right]E = \frac{E}{X_0}, \tag{1.19}$$

where N_A is Avogadro's number, A is the mass number of the medium, and X_0 is the radiation length. Substituting equation (1.19) in equation (1.16), the cross section becomes:

$$\frac{\mathrm{d}\sigma_{\text{br}}}{\mathrm{d}k} = \frac{A}{X_0 N_A k}\left(\frac{4}{3}-\frac{4}{3}y+y^2\right), \tag{1.20}$$

The differential probability, $\varphi_{\mathrm{br}}(y)$, for an electron to undergo bremsstrahlung per unit radiation length, X_0, is given by (Grieder, 2010):

$$\varphi_{\mathrm{br}}(y)\mathrm{d}y = \left[1 + (1-y)^2 - (1-y)\left(\frac{2}{3} - 2b\right)\right]\frac{\mathrm{d}y}{y}, \tag{1.21}$$

where

$$b = \frac{1}{18\ \ln 184.15\ Z^{-1/3}} = 0.0122 \quad \text{in air.} \tag{1.22}$$

The differential probability, $\varphi_{\mathrm{br}}(y)$, depends only on the fractional energy, y, carried away by the photon, while the amount of energy loss is proportional to the energy of an electron. The minimum energy required by an electron to emit gamma ray by bremsstrahlung is twice the energy of the resulting gamma ray.

Pair production The basic mechanism of the creation of EAS above tens of MeV is pair production. Pair production occurs when a photon (of energy at least twice the energy corresponding to the electron rest-mass, i.e. $\gtrsim 1.052$ MeV) radiated by an electron interacts with a virtual photon in the Coulomb field of a nucleus to form an electron-positron pair. In the ultrarelativistic regime and in the case of complete screening, the differential cross-section is defined as:

$$\frac{\mathrm{d}\sigma_{\mathrm{pp}}}{\mathrm{d}x} = \frac{A}{X_0 N_A}\left[1 - \frac{4}{3}x(1-x)\right], \tag{1.23}$$

where $x = \frac{E}{k}$ the fractional energy transferred to electron (positron) and X_0 is the radiation length. The differential probability for an incident photon of energy E_i to produce an electron-positron pair per unit radiation length, X_0, in air with energy fractions xE_i and $(1-x)E_i$, respectively, for complete screening is given by (Grieder, 2010):

$$\varphi_{\mathrm{pp}}(x)\mathrm{d}x = \left[x^2 + (1-x)^2 + \left(\frac{2}{3} + 2b\right)x(1-x)\right]\mathrm{d}x, \tag{1.24}$$

where b is given by equation (1.22).

Compton scattering Compton scattering is an interaction between a photon and an electron in which the incident photon of wavelength λ_i is scattered by the electron of mass m_e at scattering angle θ, resulting in a wavelength shift given by:

$$\Delta\lambda = \lambda_f - \lambda_i = \frac{h}{m_e c}(1 - \cos\theta), \tag{1.25}$$

where λ_f is the final wavelength of the photon and $h = 6.626 \cdot 10^{-34}$ m^2 kg s^{-1} is Planck's constant. The differential cross-section is described by the Klein-Nishina formula (Klein and Nishina, 1929):

$$\frac{\mathrm{d}\sigma_{\mathrm{KN}}}{\mathrm{d}\Omega} = \frac{r_e^2}{2}\frac{1}{(1+\epsilon(1-\cos\theta))^2}\left(1 + \cos^2\theta + \frac{\epsilon^2(1-\cos\theta)^2}{1+\epsilon(1-\cos\theta)}\right), \tag{1.26}$$

where $\epsilon = \frac{E_\gamma}{m_e c^2}$ and r_e is the classical electron radius. At very low energies the Compton cross section reduces to the Thomson cross section:

$$\frac{d\sigma_T}{d\Omega} = \frac{r_e^2}{2}(1+\cos^2\theta). \tag{1.27}$$

1.4.1 Electromagnetic showers

The word *electromagnetic* itself indicates that the cascades are initiated by high-energy electrons (positrons) or gamma rays (Figure 1.8). The primary mechanisms driving the evolution of electromagnetic cascades are $e^\pm$ pair production and bremsstrahlung. Compton scattering plays some role in the later stages of cascade development when the energy of secondary particles falls below ≈ 10 MeV (Grieder, 2010) and contributes to the flux of low-energy electrons.

Heitler's toy model for electromagnetic showers

A simple approach, the toy model introduced by Walter Heitler in 1936 (Heitler, 2010), can be used to describe the longitudinal development of electromagnetic showers. An electromagnetic shower begins when a cosmic gamma ray of energy E_0 enters the atmosphere and interacts with the nuclei of molecules in the atmosphere. The primary gamma ray can trigger a cascade by producing $e^\pm$ pairs at the atmospheric nuclei if the photon energy is at least 20 MeV. The Heitler model assumes that after the distance $d = X_0 \cdot \ln 2$, where X_0 is the radiation length, $e^\pm$ pair is produced, each particle carrying half of the primary gamma-ray energy, $E_0/2$. Note that in air, $X_{br} = 37$ g cm^{-2} and $X_{pp} = 47$ g cm^{-2}, i.e., $X_{pp} = \frac{9}{7}X_{br}$. Thus, the approximation $X_{pp} \approx X_{br} = X_0$ is valid. Produced $e^\pm$ pair undergoes bremsstrahlung process, after traversing the same distance d, emitting photons each with an energy of $\frac{E_0}{4}$. After n splittings, the cascade consists of 2^n secondary particles, each with mean energy $\frac{E_0}{2^n}$, assuming that energy is equally divided between $e^\pm$ pair production and the consequent bremsstrahlung. The production of secondary particles continues until the average energy of the particles reaches the critical value of ≈ 84 MeV (Matthews, 2005). Below critical energy E^{e}_{crit}, the ionization losses (losses due to collisions with atmospheric molecules) overcome radiative energy losses. For gamma rays, the critical energy is where Compton scattering overcomes pair production. In the atmosphere, for instance, a photon of 24 MeV has an equal probability for Compton scattering and $e^\pm$ pair production (Grieder, 2010). The cascade reaches its maximum when all particles have energy equal to critical energy $E_0 = N_{max} \cdot E_c$, after n_c splittings:

$$n_c = \frac{\ln \frac{E_0}{E^{e}_{crit}}}{\ln 2}, \tag{1.28}$$

at the atmospheric depth X_{max}:

$$X_{max} = X_0 \cdot \ln \frac{E_0}{E^{e}_{crit}}. \tag{1.29}$$

The Heitler model of electromagnetic showers does not give correct quantitative predictions for several reasons. First, the model does not take into account atmospheric extinction, thus overestimating the total number of secondary particles. Furthermore, according to the model,

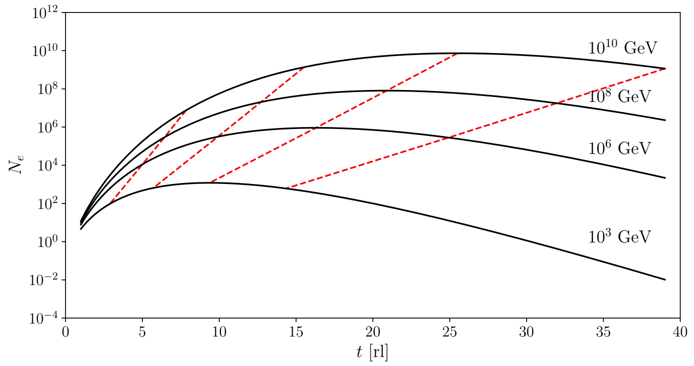

Figure 1.9: The longitudinal profiles of gamma-ray air showers of different energies calculated with the Greisen equation (1.31). The plotted red lines show the respective shower age parameters, from left to right: $s \in [0.4,\ 0.7,\ 1,\ 1.3]$.

the fraction of the number of electrons in the cascades is $\approx 2/3\ N_{max}$. In reality, through the bremsstrahlung process, several photons may be emitted, thus the ratio of the number of electrons to the number of gamma rays is overestimated. Even though, the model predicts two important properties of EAS: (1) the number of secondary particles in the shower is proportional to the primary energy: $N_{\mathrm{max}} \propto E_0$, (2) the altitude of the shower maximum is inversely proportional to the logarithm of primary energy: $X_{\mathrm{max}} \propto \ln E_0$.

Longitudinal development of electromagnetic air showers

Rossi and Greisen (1941) gave an analytical expression for the differential energy spectra of electrons and photons at atmospheric depth t in the units of radiation length (rl):

$$t = \frac{X}{X_0} \approx \frac{X_{\mathrm{air}}}{X_0 \cdot \cos\varphi} \cdot \exp - \frac{H}{H_0}, \tag{1.30}$$

using two sets of simplifying assumptions called *Approximation A* and *Approximation B*, where E_0 is the primary energy of a photon, $X_{\mathrm{air}} = 1013$ g cm^{-1} is the air column height at ground, $H_0 = 8$ km is the scale height and φ is the incident angle of shower. In approximation A, only pair production and bremsstrahlung are considered, while electron energy losses due to collisions are neglected. However, these approximations are not practical for everyday use. In his review paper, Greisen (1960) introduced a more practical expression for calculating the shower size as a function of the primary energy E_0 and t when N_e is large, i.e. at distances several radiation lengths away from the point of the first interaction (Figure 1.9):

$$N_{\mathrm{e}}(E_0, E^{\mathrm{e}}_{\mathrm{crit}}, t) \simeq \frac{0.31}{\sqrt{\ln\left(E_0/E^{\mathrm{e}}_{\mathrm{crit}}\right)}} \exp\left[t\left(1 - \frac{3}{2}\ln(s)\right)\right], \tag{1.31}$$

where s is the shower age:

$$s \approx 3t\left(t + 2\ln\frac{E_0}{E^{\mathrm{e}}_{\mathrm{crit}}}\right)^{-1}. \tag{1.32}$$

The *young showers* ($s < 1$) are those that haven't yet reached their maximum at a specific observation level, whereas *old showers* ($s > 1$) are those that have progressed beyond their peak (Grieder, 2010). The rate at which the position of the shower maximum in the atmosphere changes with primary energy is called the elongation rate:

$$ER^{\mathrm{em}} = \frac{\mathrm{d}X_{max}}{\mathrm{d}(\ln E_0)}, \tag{1.33}$$

or expressed per decade of primary energy:

$$ER^{\mathrm{em}}_{10} = \frac{\mathrm{d}X_{max}}{\mathrm{d}(\log_{10} E_0)}. \tag{1.34}$$

The shower fluctuations (without the fluctuation of the first interaction height), which are intrinsically large, are described by the following term:

$$\Delta N_{\mathrm{e}}(s) \simeq \frac{9}{14}(s - 1 - 3\ln s) \cdot N_{\mathrm{e}}(s). \tag{1.35}$$

Lateral structure of electromagnetic air showers

Another difficult problem in the description of electromagnetic air showers is the lateral spread of the shower particles. Air showers develop along the direction of the primary particles. However, the secondary particles are not emitted exactly in the direction of the primary particle because the average transverse momentum is on the order of the electron mass and many low-energy electrons are deflected from their primary direction due to Coulomb scattering. The opening angles of electron-positron pairs and the emission angle of photons in bremsstrahlung contribute insignificantly compared to the angles of multiple scattering. The density of electrons and positrons $\rho_e(r)$ as a function of the perpendicular radial distance r from the shower axis is given by the Nishimura-Kamata-Greisen (NKG) function (Kamata and Nishimura, 1958; Greisen, 1960) (Figure 1.10):

$$\rho(r) = \frac{N_{\mathrm{e}}}{2\pi r_M^2}\left(\frac{r}{r_M}\right)^{s-2}\left(1 + \frac{r}{r_M}\right)^{s-4.5}\frac{\Gamma(4.5 - s)}{\Gamma(s)\Gamma(4.5 - 2s)}, \tag{1.36}$$

where $\Gamma(s)$ is a gamma function and s it the shower age. The Moliére radius is given as:

$$r_{\mathrm{M}} = X_0 \frac{E_{\mathrm{scatt}}}{E^{\mathrm{e}}_{\mathrm{crit}}}, \tag{1.37}$$

where $E_{\mathrm{scatt}} = m_e c^2 \sqrt{\frac{4\pi}{\alpha}} \simeq 21.1$ MeV. In the air $r_{\mathrm{M}} \simeq 9.5$ g cm^{-2} (or $\simeq 79$ m) at the sea level. About 99% of the shower energy is contained within $3.5 \cdot r_{\mathrm{M}}$ (Wagner, 2006).

1.4.2 Hadronic showers

Hadronic showers result from the reaction of charged cosmic rays with the atmospheric nuclei, produced by the strong interaction (Figure 1.8). In these interactions, pions make up most of the secondary particles produced (90%), but there are also kaons (10%), protons, antiprotons, neutrinos,

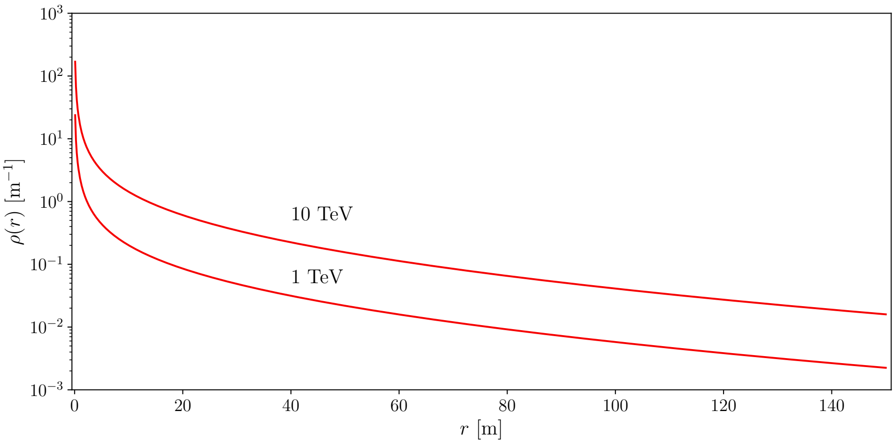

Figure 1.10: The lateral profiles of gamma-ray air showers of different energies calculated with the NKG equation (1.36) at the shower maximum ($s = 1$, $r_M = 200$ m).

and antineutrinos. The fragments and nuclei produced form new interactions until the energy per nucleus is less than the threshold for pion production ($\approx$ 1 GeV). Charged pions can decay into muons and neutrinos, while neutral pions decay into gamma rays that induce electromagnetic subshowers. Muons interact primarily by ionization and rarely decay before reaching the Earth's surface. Muons with large transverse momentum can significantly diverge from the shower axis.

Heitler's toy model for hadronic showers

This model of hadronic showers was developed by Matthews (2005) based on Heitler's description of electromagnetic showers. Imagine the atmosphere as a set of layers of fixed thickness $\lambda_{\text{int}} \ln 2$, where λ_{int} is the interaction length of the particles and in the air is $\approx 120\ \ \text{g cm}^{-2}$. After passing through such a layer, pions are produced. Since the probability of production of positively charged, negatively charged and neutral pions is about equal, there are $N_\pi = N_{\text{ch}}$ charged pions carrying two-thirds of the initial energy E_0 and $\frac{N_{\text{ch}}}{2}$ neutral pions carrying one-third of the energy. The process of particle production continues until the critical energy E^π_{crit} is reached, assuming that all charged pions decay into muons. The value of the critical energy varies slowly with the primary energy, from $\approx$ 30 GeV at 10^{14} eV to $\approx$ 10 GeV at 10^{17} eV. After n interactions, there are $N_\pi = (N_{\text{ch}})^n$ charged pions, each with an energy of $E_0 \cdot (3/2N_{\text{ch}})^{-n}$. The number of interactions required to reach the critical energy is given by:

$$n_c = \frac{\ln\left(E_0/E^\pi_{\text{crit}}\right)}{\ln\left(\frac{3}{2}N_{\text{ch}}\right)} \simeq 0.8\log_{10}\left(\frac{E_0}{E^\pi_{\text{crit}}}\right). \tag{1.38}$$

From (1.38) one can read the number of muons in the shower (with $N_\mu = N_\pi$):

$$\ln N_\mu = n_c \ln N_{\text{ch}} = \frac{\ln N_{\text{ch}}}{\ln \frac{3}{2} N_{\text{ch}}} \cdot \ln \frac{E_0}{E^\pi_{\text{crit}}} = 0.85 \cdot \ln \frac{E_0}{E^\pi_{\text{crit}}}. \tag{1.39}$$

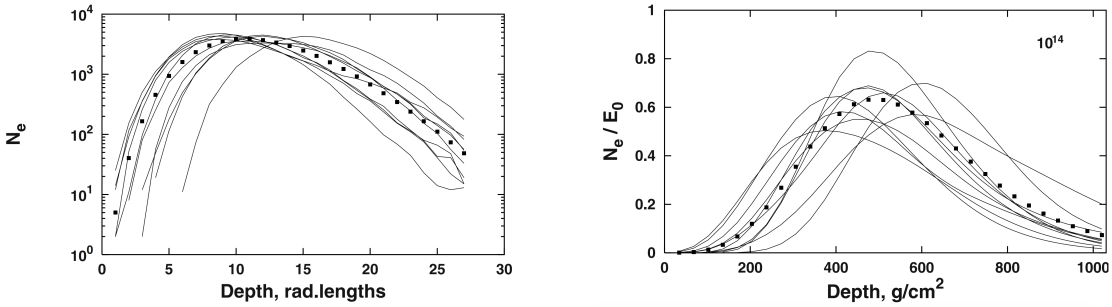

(a) **(b)**

Figure 1.11: Fluctuations in the longitudinal profile of 10 individual air showers from a vertical a) gamma ray b) proton of energy 10^5 GeV. The squares show the averages of 100 air showers (Stanev, 2010).

Calculating the depth of the shower maximum for hadronic showers $X^{\mathrm{p}}_{\mathrm{max}}$ with a simple model is more complicated than for electromagnetic showers. Accurate determination of the depth of the shower maximum requires careful summation of the individual subshowers generations from their individual origins, taking into account their attenuation both near and after they reach their maxima. For simplicity, only the first generation of electromagnetic subshowers is used to determine shower maximum depth. Although using only the first interaction $X^{\mathrm{p}}_{\mathrm{max}}$ underestimates the depth of the shower maximum, because subsequent subshowers are neglected, it provides a reliable measure of the elongation rate. The first interaction begins at an atmospheric depth of $\lambda_{\mathrm{int}} \ln 2$. During this first interaction, $\frac{N_{\mathrm{ch}}}{2}$ neutral pions are produced, leading to N_{ch} photons. Each photon triggers an electromagnetic shower with energy $\frac{E_0}{3N_{\mathrm{ch}}}$, which evolves simultaneously. The depth of the shower maximum is then given by:

$$X^{\mathrm{p}}_{\mathrm{max}} = \lambda_{\mathrm{int}} \ln 2 + X_0 \ln \frac{E_0}{3N_{\mathrm{ch}} E^{\mathrm{e}}_{\mathrm{crit}}}. \tag{1.40}$$

Rewriting the equation (1.29) as:

$$X^{\mathrm{p}}_{\mathrm{max}} = \lambda_{\mathrm{int}} \ln 2 + X_0 \ln \frac{E_0}{E^{\mathrm{e}}_{\mathrm{crit}}} - X_0 \ln\left(3N_{\mathrm{ch}}\right), \tag{1.41}$$

and differentiating it by $\log_{10} E_0$ yields:

$$\frac{\mathrm{d}X^{\mathrm{p}}_{max}}{\mathrm{d}(\log_{10} E_0)} = \frac{\mathrm{d}\left(X_0 \ln \frac{E_0}{E^{\mathrm{e}}_{\mathrm{crit}}}\right)}{\mathrm{d}(\log_{10} E_0)} + \frac{\mathrm{d}(\lambda_{\mathrm{int}} \ln 2 - X_0 \ln\left(3N_{\mathrm{ch}}\right))}{\mathrm{d}(\log_{10} E_0)}. \tag{1.42}$$

The first term on the right-hand side is the elongation rate of the electromagnetic shower $ER_{10} = ER^{\mathrm{em}}_{10}$, therefore the final equation is given as:

$$ER^{\mathrm{p}}_{10} = ER^{\mathrm{em}}_{10} + \frac{\mathrm{d}(\lambda_{\mathrm{int}} \ln 2 - X_0 \ln\left(3N_{\mathrm{ch}}\right))}{\mathrm{d}(\log_{10} E_0)}. \tag{1.43}$$

Figure 1.11 shows fluctuations in the longitudinal profile of electromagnetic and hadronic air showers and the average profile of 100 such showers.

Superposition model

The superposition model (Matthews, 2005) provides a simplified perspective on the interaction between a cosmic ray nucleus and the Earth's atmosphere. In this model, a nucleus characterized by atomic number A and total energy E is conceptually decomposed into A individual nucleons, each with energy E/A and acting independently. The resulting air shower is then considered to be the sum of A individual proton air showers, all emanating from the same point. To analyze and quantify the observable properties of the showers, the reduced primary energy is substituted into the previously derived expressions for proton showers. Then A of such proton showers are combined. The resulting properties of the nuclear-initiated showers are easily expressed in terms of the equivalent quantities of a proton shower with the same total energy E:

$$N_\mu^A = N_\mu A^{0.15}, \tag{1.44a}$$

$$X_{\mathrm{max}}^A = X_{\mathrm{max}}^{\mathrm{p}} - X_0 \ln A, \tag{1.44b}$$

$$E_0 = 0.85\ \mathrm{GeV}\ (N_{\mathrm{e}} + 25 N_\mu). \tag{1.44c}$$

1.5 Atmospheric Cherenkov radiation

Cherenkov light is a form of electromagnetic radiation emitted by medium when charged particles in the air shower (mainly electrons and protons) travel at a speed greater than the velocity of light in the air. When a charged particle travels through a dielectric medium, a polarization of nearby electric dipoles occurs. The excited molecules of the dielectric medium quickly return to their ground state and emit excess energy in the form of electromagnetic radiation. According to the Huygens principle, the radiated electromagnetic waves are emitted in a spherical shape with a velocity that corresponds to the phase velocity of the medium. If the velocity of the particle is less than the speed of light in the medium, the symmetry in the alignment of the dipoles around the position of the charged particle is such that there is no net effect at long distances, i.e. there is no radiation. The wavefronts are slightly bundled in the direction of motion, but there is no interference. If the charged particle moves at a speed greater than the speed of light in the medium, the induced dipoles are no longer radially aligned with the position of the particle. Instead, a net induced dipole emerges in the direction of the particle. The emitted waves interfere constructively and result in coherent radiation at a certain angle θ relative to the trajectory of the particle (Figure 1.12):

$$\cos\theta = \frac{1}{n\beta}, \tag{1.45}$$

where n is the index of refraction and $\beta = \frac{v}{c}$ is the ratio of the speed of the particle and the speed of light in the vacuum. The Cherenkov condition, i.e. the minimum speed of a particle to produce Cherenkov radiation is $\beta_{\mathrm{min}} = n^{-1}$. Obviously, the maximum of the emission angle occurs when the particle travels at ultrarelativistic speed: $\beta = 1$. The energy threshold for a charged particle with

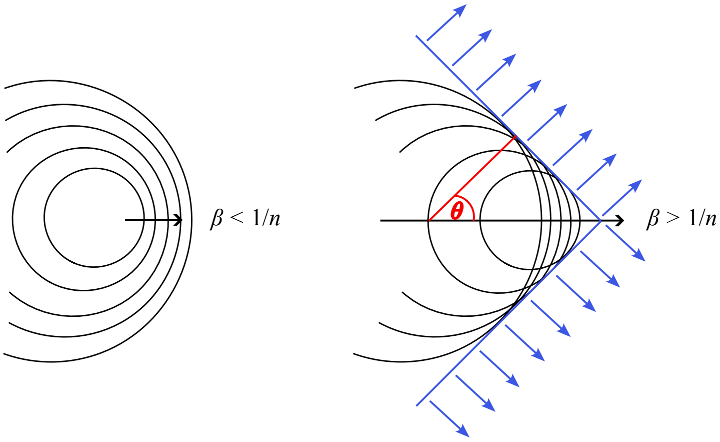

Figure 1.12: Schematic representation of the process leading to the emission of Cherenkov radiation. *Left:* The charged particle travels with a velocity less than the phase velocity of the medium, therefore no Cherenkov radiation occurs. *Right:* When a charged particle is traveling faster than the phase velocity of the medium, a net induced dipole is formed in the direction of the particle and Cherenkov light is emitted.

rest mass m_0 to emit Cherenkov light is set by the Cherenkov condition:

$$E = \frac{m_0 c^2}{\sqrt{1 - \beta_{\text{min}}^2}}. \tag{1.46}$$

1.5.1 Spectrum and lateral spread of Cherenkov light

The number of Cherenkov photons emitted per unit length traveled by the particle per wavelength is given by Frank and Tamm (1937):

$$\frac{\mathrm{d}^2 N}{\mathrm{d}x \mathrm{d}\lambda} = \frac{2\pi\alpha z}{\lambda^2} \cdot \left(1 - \frac{1}{\beta^2 n^2(\lambda)}\right), \tag{1.47}$$

where α is the fine structure constant, and z is the charge in units of e. In the wavelength range between 300 nm and 600 nm for $\beta = 1$, about 500 Cherenkov photons are emitted per GeV of primary gamma-ray energy in the electromagnetic shower (Wagner, 2006). Cherenkov light, of course, like any other form of electromagnetic radiation, is subject to atmospheric attenuation, i.e., it is absorbed by molecules and scattered by aerosols and clouds. The difference between the spectrum of Cherenkov light at 10 km above sea level (a.s.l.) and that at ground level is shown in Figure 1.13. More information on this topic will be given in Chapter 2.

Due to the change of atmospheric density with altitude, the Cherenkov angle increases from $\approx 0.2°$ at an altitude of 30 km to $\approx 1.2°$ at 2200 m a.s.l. Therefore, each charged particle emits a Cherenkov light cone, which produces a ring-shaped pattern on the ground, while the contribution of all particles involved results in the Cherenkov light pool, which typically has a size of 0.05 km^2 (Figure 1.14). Figure 1.15a illustrates the lateral distribution of Cherenkov photons on the ground. The light intensity appears to be uniformly distributed in the central region of the light pool (where the radius is approximately less than 150 meters). The density of the Cherenkov light

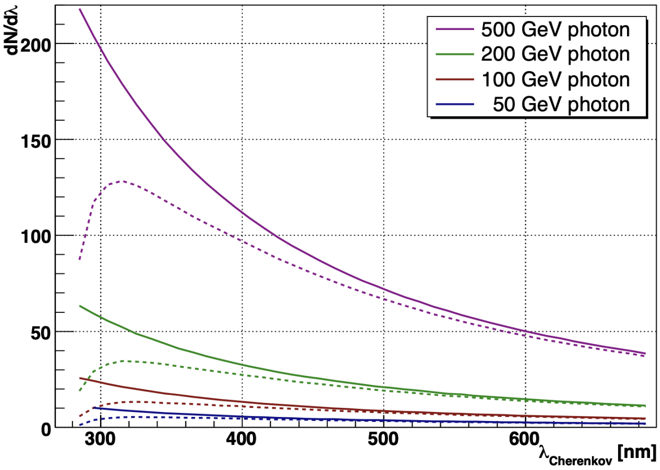

Figure 1.13: Cherenkov spectrum from a vertical gamma-ray-induced air shower at 10 km a.s.l. (solid lines) and at ground level (2200 m a.s.l., dashed lines) (Wagner, 2006).

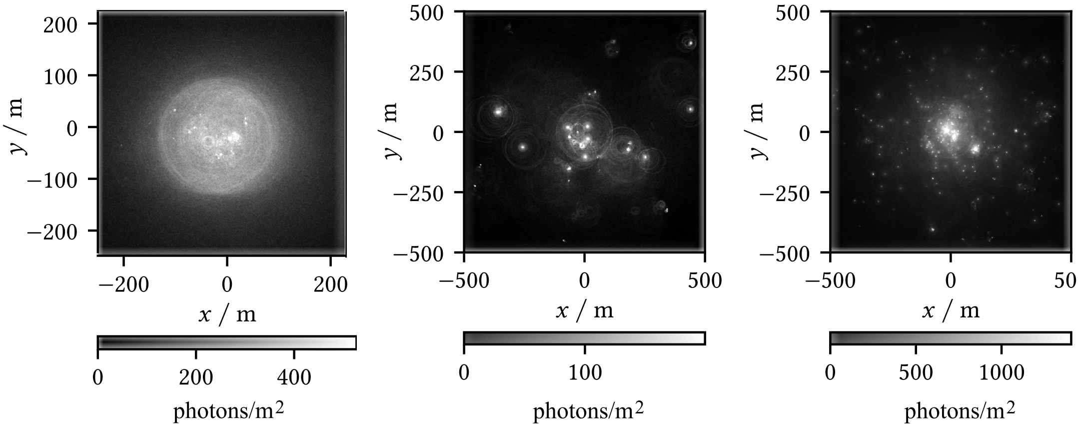

Figure 1.14: Cherenkov light pool for 1 TeV gamma rays, 1 TeV protons, and 10 TeV iron-induced air showers. Gamma rays produce a homogeneous single pool consisting mainly of electrons and positrons. The Cherenkov light produced by hadronic showers originates from the electromagnetic subshowers and muons, and therefore hadronic showers yield multiple Cherenkov pools (Nöthe, 2020).

pool is closely related to the energy of the primary gamma rays. As the energy of the primary gamma rays increases, the number of particles produced in the cascade also increases, leading to a proportional increase in the Cherenkov photon density. In hadronic showers which produce more subshowers, many Cherenkov pools are formed. After 150 m from the core of the shower, there is a visible hump. The hump is a result of a change in the refractive index and a change in the Cherenkov angle (the so-called focusing effect).

1.5.2 Time spread of Cherenkov light

The variations in the arrival time of photons at the ground can be attributed to two main factors. First, it is because charged particles within the shower travel at a speed exceeding that of light. Consequently, near the axis of the shower, photons emitted at lower altitudes reach the detector earlier than those emitted at higher altitudes. Second, at greater distances from the shower axis,

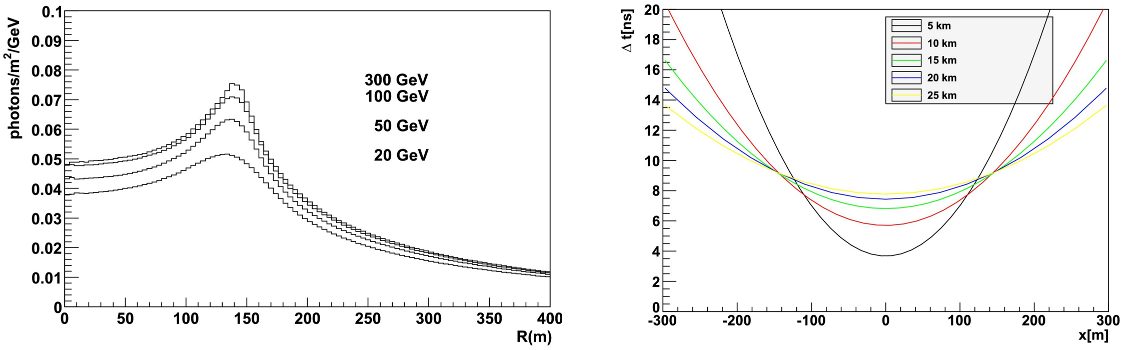

(a) **(b)**

Figure 1.15: a) The lateral profile of the Cherenkov light at sea level for gamma rays of different primary energies, where *R* is the radial distance from the shower axis. b) Time delay as a function of radial distance from the shower axis for different emission altitudes (de Naurois and Mazin, 2015).

photons originating at lower altitudes follow a longer geometric path, traversing the first, smaller path of the trajectory as (faster) secondary particles and the larger, remaining path as (slower) Cherenkov photons. The resulting temporal discrepancy in the arrival of Cherenkov photons from different emission points is shown in Figure 1.15b.

1.6 Imaging Atmospheric Cherenkov Technique

Over the past three decades, the Imaging Atmospheric Cherenkov Technique (IACT) has become a powerful tool in VHE gamma-ray astronomy. (Weekes et al., 1989; Hinton, 2004; Krennrich et al., 2004; Cortina, 2005; Holder, 2006; Lopez-Coto et al., 2022). As the name implies, Cherenkov telescopes observe gamma rays indirectly by capturing short flashes of Cherenkov light produced in the cascade of secondary particles. Cherenkov telescopes are usually operated in stereoscopic mode, providing multiple images of the same air shower. Compared to monoscopic observations, better angular and energy resolution and better background suppression are achieved.

Cherenkov telescopes are essentially optical alt-azimuthal telescopes with excellent angular and energy resolution (compared to other types of gamma-ray detectors), a field of view (FoV) typically between 3° and 10°, good background suppression, and very large effective area. On the other hand, they are characterized by a low duty cycle, operating only during the night and dry atmospheric conditions (10%, including clear, dark nights). The structure consists of a segmented mirror that focuses the light onto a camera with a matrix of photomultiplier tubes (PMTs). The mirror tiles are typically round, square, or hexagonal. Typically, these mirrors are either parabolic or Davies-Cotton design to mitigate the temporal dispersion of Cherenkov light or the optical aberrations that occur at large field angles. The mirrors must be large enough to collect as much Cherenkov light as possible. The Davies-Cotton design is preferable because it keeps the optical aberration at a low level and has an acceptable temporal dispersion of only ≈ 4 ns. However, for very large telescopes, the Davies-Cotton anisochronism exceeds a tolerable level, so parabolic mirrors are required. To achieve good spatial resolution and structure of the shower image, a sufficiently small ($\leq 0.1°$) pixel FoV is also required.

To overcome the challenges posed by extremely low signal intensity, short signal duration, and the presence of a significant background (including the night sky background and the hadronic background), the implementation of a fast and highly sensitive data acquisition system is required. In most of modern IACTs, the triggering system usually follows a three-level concept (de Naurois and Mazin, 2015). The first level is the threshold discriminator, i.e., a minimum charge in the pixel is required. At the second level, either groups of adjacent pixels or a certain number of pixels within a predefined range must satisfy the trigger condition of the first level. The third level requires a coincidence between at least two IACTs within a certain time window. Detected events triggered by gamma rays yield elliptical patterns on the camera plane. This is a valuable resource for extracting crucial physical parameters, such as determining the primary particle type or estimating its energy. The Cherenkov imaging approach can effectively distinguish events emanating from a gamma-ray source from the prevailing cosmic-ray background. The shower triggered by a gamma ray gives a narrow, compact, elliptical Cherenkov image, where the major axis of the ellipse corresponds to the projection of the shower axis onto the camera plane, i.e., describes the longitudinal structure of the shower, while the minor axis describes the lateral structure of the air shower. Hillas (1985) has shown that it is possible to distinguish between the hadronic background and the signal by evaluating the width, length, and orientation of the Cherenkov image.

The main sources of systematic uncertainties lie in two closely related aspects: the precision of the absolute energy scale and the accuracy of knowledge of atmospheric conditions. The first challenge arises from the lack of a calibration beam for cosmic gamma rays, which makes it difficult to establish a precise energy reference. The second factor is due to variations in atmospheric conditions, including changes in temperature, pressure, humidity, and the presence of aerosols or thin clouds. These atmospheric conditions significantly change the density of Cherenkov light pool, thus affecting the trigger yield, effective area and energy reconstruction. According to recent assessments, the accuracy of the energy scale and the absolute flux level are within 10% – 15% (Aleksić et al., 2016a).

1.6.1 Cherenkov Telescope Array

The Cherenkov Telescope Array[3] (CTA) is the future ground-based observatory for VHE gamma-ray astronomy (Actis et al., 2011; Acharya et al., 2013), capable of detecting $\approx 0.1\%$ of the Crab Nebula flux in only 50 observing hours. CTA will consist of two arrays located in the northern (La Palma, Spain, $28.8°43.7904'$ N, $17°53'31.218''$ W) and southern (Paranal, Chile) hemispheres, covering a broad energy range between 20 GeV and 300 TeV by combining three types of telescopes: 23-meter Large-Sized Telescopes (LSTs) (Pierro, 2023), 12-meter Medium-Sized Telescopes (MSTs) (Bergström, Goobar and Jaffe, 2001; Wood et al., 2016) with Davies-Cotton optics, and 4.3-meter Small-Sized Telescopes (SSTs) (Amans et al., 2021) with a Schwarzchild-Couder optical system.

Large telescopes with larger mirror areas are capable of detecting faint gamma-ray signals with higher sensitivity, while smaller telescopes are less expensive and can be used in larger numbers to increase the overall sensitivity of the observatory and increase the upper energy limit. Because of the unique advantage of observing the Galactic plane from the Southern Hemisphere at a considerable

---

[3] `https://www.cta-observatory.org/`

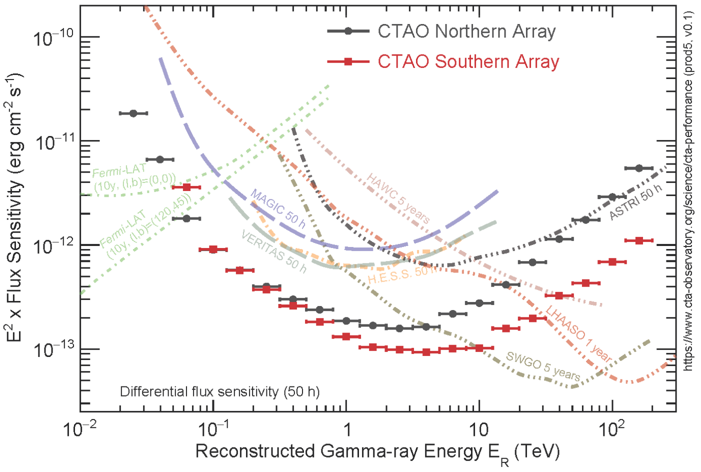

Figure 1.16: Differential sensitivity for both CTA sites and other operational IACT arrays for 50 hours of observations for the showers arriving from 20° at zenith. More information on CTA performance is available at `https://www.cta-observatory.org/`.

altitude, southern CTA primarily targets Galactic sources whose emissions typically extend to energies above a few TeV. In contrast, northern CTA will focus on the study of extragalactic sources, exploring the lowest energies within the VHE gamma-ray band. This split will allow CTA to optimize its observations and science investigations based on the different characteristics of the sources and their energy profiles in different regions of the sky.

The design and construction of the CTA are part of a more than decade-long effort to find a compromise between cost, scientific goals, and geographic and orographic constraints. The design of the CTA has been the subject of many studies (Bernlöhr et al., 2013; Szanecki et al., 2015; Hassan et al., 2017; Acharyya et al., 2019) to meet the stated requirements for angular resolution, energy resolution, effective area, and differential sensitivity. After the initial construction phase, the northern CTA Observatory (CTAO-N) will cover an area of ≈ 0.25 km^2 and put 4 LSTs and 9 MSTs into operation. This is the *Alpha Configuration*, which is currently the official configuration of the CTA Observatory. However, the *Omega Configuration*, which refers to the full-scope design that could be implemented depending on available funding, is expected to consist of 6 more MSTs. The southern CTA Observatory (CTAO-S) will span over 3 km^2 and include 14 MSTs and 37 SSTs telescopes. A unique operational concept and a wide energy range will allow CTA to achieve exceptional sensitivity. Figure 1.16 shows the differential sensitivity for both CTA sites and other operational IACT arrays for 50 hours of observations. Differential sensitivity is defined as the minimum flux required to detect a point-like source with 5 standard deviations. It is calculated in five per decade, non-overlapping logarithmic energy bins. The dynamic analysis cuts have been applied in each bin to maximize the flux sensitivity.

The prototype of Large-Sized Telescope

The prototype of Large-Sized Telescope (LST-1, Figure 1.17) is the first CTA telescope ever built (Pierro, 2023; Abe et al., 2023b). The telescope was built between 2016 and 2018 and began

Figure 1.17: *Left:* The LST-1 telescope at La Palma. Credit: Iván Jiménez. *Right:* The camera of LST-1 telescope. Credit: Tomohiro Inada.

operations in October 2018, initially for the commissioning phase and later for science observations. LST-1 will cover the low-energy sensitivity range down to 20 GeV. Three more LSTs are planned to be built on La Palma, with construction to be completed by mid-2024.

According to a recent study by Abe et al. (2023b), based on the Crab Nebula observations with LST-1 during the period from November 2020 to March 2022, when the telescope was still in its commissioning phase, the energy threshold of the LST-1 telescope at the trigger level is ≈20 GeV, increasing to ≈ 30 GeV after quality cuts are applied. The performance parameters depend strongly on the energy and the gamma-ray selection cuts applied: The angular resolution varies from 0.12° to 0.40° and the energy resolution varies from 15% to 50%. The integrated flux sensitivity above 250 GeV for a 50-hour observation is ≈ 1.1% of the Crab Nebula flux (12% for 30 minutes). The following paragraphs provide a brief description of the major parts of the LST-1 hardware. For a more detailed description, see papers by Ambrosi et al. (2013), Deleglise, Geffroy and Lamanna (2013), Delgado et al. (2013), and Kubo et al. (2013).

Camera and trigger system LST-1 camera (Saito et al., 2021; Kobayashi et al., 2022; Kobayashi, 2022) consists of 1855 PMTs grouped in 7-PMT modules, with a quantum efficiency of ≈ 40% at 350 nm and a pulse repetition rate of 3 ns. Each pixel has a size of 0.1°, so a camera has a total FoV of 4.5°. The signal from the PMTs is sampled at a rate of 1 GHz using Domino Ring Sampler 4$^{\text{th}}$ Generation (DRS4) chips (Nozaki et al., 2020). Each DRS4 chip has 8 usable channels, each consisting of an array of 1024 capacitors. The output signal is amplified with 2 different gains covering a wide dynamic range from 1 to 3000 photoelectrons. The LST-1 trigger system consists of two trigger levels (L0 and L1), the Trigger Interface Board (TIB) and the backplanes (Saito et al., 2021). The L0 acts at the level of the individual pixels and its circuitry allows both the times and amplitudes of the signals coming from the PMTs to be adjusted. These signals are then summed for a range of 21 adjacent pixels at the L1 level. A local camera trigger is released when one of the summed signals is above an adjustable discriminator threshold. The TIB manages all possible trigger inputs like the pedestal trigger, the calibration trigger and the camera trigger. To calibrate the PMT signals, the telescope is equipped with a calibration box positioned in the center of the reflector dish that provides consistent and uniform calibration over a wide dynamic range, extending up to 10^4 photoelectrons (Palatiello et al., 2021).

Figure 1.18: The MAGIC telescopes. Credit: Daniel López.

Optical system The LST-1 reflector (Hayashida et al., 2016; Mazin, Cortina and Teshima, 2017) consists of 198 hexagonal mirror tiles, each with an area of 2 m^2. The focal length of the parabolic dish is 28 m and its diameter is 23 m. The total effective reflective area, taking into account the shadows of the mechanical structures (e.g., the photo-sensors camera, mast, etc.), is about 368 m^2. The mirrors on the LST structure are fixed using two actuators and a stationary point. These actuators use precision step motors with a step size of 5 μm and are controlled by Active Mirror Control software, which ensures that the required optical performance is maintained at all times. Each mirror tile is equipped with a miniature complementary metal-oxide semiconductor (CMOS) camera that monitors a fixed point generated by a laser on the camera plane. The position of the fixed point serves as a reference for correcting any mirror misalignment.

Pointing system The pointing system is designed to accurately map the gamma-ray image in the Cherenkov camera to celestial coordinates, achieving a precision of better than 14 arcseconds. The LST-1 pointing system is composed of several key components located at the center of the dish, including the Starguider Camera, Camera Displacement Monitor, inclinometers, distance meters, and the Optical Axis Reference Laser (Zarić et al., 2021; Zarić, 2022).

1.6.2 MAGIC telescopes

Major Atmospheric Gamma Imaging Cherenkov Telescopes (MAGIC, Figure 1.18) is a system of two IACTs on La Palma ($28°45'43''$ N, $17°53'24''$W) at 2200 m a.s.l., with an integral sensitivity of $(0.66 \pm 0.03)\%$ of the Crab Nebula flux in 50 hours of observation above 220 GeV (Aleksić et al., 2016a,b). The angular resolution of MAGIC telescopes above 220 GeV amounts to 0.07°, while the energy resolution is 16%. For more details on the MAGIC telescopes, the reader is referred to numerous doctoral theses associated with the MAGIC telescopes[4]. The spatial distance between the MAGIC telescopes and LST-1 is only $\approx$ 100 m, allowing joint, stereoscopic observations (Di Pierro et al., 2021; Abe et al., 2023a). Thanks to the resulting increase in collection area and better

---

[4] https://magic.mpp.mpg.de/backend/publications/thesis

background suppression, the joint observations lead to a significant improvement in sensitivity. Compared to the MAGIC-only observations, 30% weaker fluxes can be detected in the energy range between 200 GeV and 3 TeV (Abe et al., 2023a).

Camera and trigger system The MAGIC system has a circular camera with a diameter of 1.2 m and a FoV of 3.5°. The cameras consist of 1039 evenly distributed PMTs, each with a field of view of 0.1°. The PMTs are grouped in 169 clusters of 7 PMTs each, with a quantum efficiency of ≈ 33% at 350 nm. The signal from the PMTs is sampled using DRS4 (Sitarek et al., 2013), which operates at a sampling rate of 2 GSamples s^{-1} and consists of 1024 capacitors (Sitarek et al., 2013). The DRS4 digitizes and records only the selected regions of interest, 60 in total, reducing the dead time to only 26 μs. Similar to LST-1, the MAGIC trigger system has three levels. However, there is also an additional level, the *sum trigger* level (García et al., 2013; Dazzi et al., 2016), which aims to lower the energy threshold down to 30 GeV and increase the sensitivity for lower energies below 200 GeV. The operating principle is to group signals from adjacent pixels (called a macrocell) and then apply a threshold to the combined signal. To accomplish this, the trigger region is overlaid with three layers of overlapping macrocells. A notable advantage of this method is the improvement in signal-to-noise ratio. This improvement results from the fact that all pixels within a given macrocell contribute to the determination of the trigger, which allows the inclusion of small photon signals that fall below the threshold of the single channel, i.e., the threshold at which the standard trigger becomes sensitive.

Optical system The MAGIC optical system consists of two 17 m parabolic mirrors with the same focal length of 17 m and a total reflecting area of 236 m^2. The reflector consists of 964 square 1 m × 1 m all-aluminum (glass-aluminum in MAGIC-II) mirror tiles. The point spread function (PSF) for the optical system is ≈ 10 mm for the on-axis observations. To keep PSF constant, the individual mirrors of the MAGIC-II telescope and the 2×2 tiles of the MAGIC-I telescope are individually adjustable. The AMC (Biland et al., 2008) consists of two actuators with a precision of < 20 μm.

Pointing system Three 14-bit encoders, two in azimuth and one in zenith, precisely determine the telescopes' pointing direction. At the same time, the Starguider camera (Wagner, 2006) continuously checks the telescope alignment during observations. To correct any deviations, a bending model is created by comparing the recorded positions of bright stars at the end of each night with the T-Points camera, a type of charge-coupled device (CCD) camera.

CHAPTER 2

The sky above the Roque de los Muchachos Observatory

In the field of ground-based high-energy gamma-ray astrophysics, the atmosphere is an important factor affecting the observation and interpretation of gamma-ray signals. The atmosphere is both a gateway and a challenge for IACTs. This chapter addresses the specifics of the interaction of radiation with the atmosphere and the methods used to model and mitigate its effects on IACTs.

2.1 Structure and composition of the atmosphere

The atmosphere is a gaseous layer that surrounds the Earth and is responsible for the transfer of energy between the universe and the Earth and the various parts of the planet. It is held in place by gravity and accounts for only $\approx 1\%$ of the Earth's total radius. It consists of a mixture of gasses, the most important of which are nitrogen (78%) and oxygen (21%), while the remaining 1% consists of CO_2, ozone, water vapor, and other minor constituents (Salby, 2012). According to its thermal nature, the atmosphere is divided into several layers, each of which has different dynamic properties. From the Earth's surface to an altitude of 10 km, in the troposphere, the temperature decreases with increasing altitude at an almost constant rate of 6.5 K km^{-1}. The troposphere contains 90% of the mass of the atmosphere. In the uppermost layer of the troposphere, the tropopause, which lies at an altitude of 10 km, a strong change in lapse rate is observed. The second layer above the ground is the stratosphere, which extends from 10 km (about 8 km at the poles) to an altitude of about 55 km and whose temperature, unlike the troposphere, increases constantly with altitude, from −55°C (at mid-latitudes and at the poles) or from −85°C (at the equator) to 0°C. The layer is stable due to temperature inversion, which results from the decomposition of molecular oxygen (O_2) into ozone (O_3) under the influence of ultraviolet (UV) radiation. The stratosphere contains 90% of atmospheric ozone.

The third, middle layer is the mesosphere. The temperature in the mesosphere decreases with altitude, so the upper boundary, the mesopause, is the coldest part of the Earth, where temperatures fall below −100°C. The height and thickness of the layer are not well defined because of frequent and extensive changes in a relatively short time, but the lower boundary is usually thought to be 50 km and the upper boundary nearly 100 km, except at mid-latitudes and the poles, where the upper boundary is 85 km. The next layer, the thermosphere, extends up to 500 km. The temperature in the thermosphere rises up to 1500°C due to ionization of the air. In the thermosphere, the air is extremely thin and most of it is above the Kármán line at an altitude of 100 km, where the outer space begins. The exosphere is a final layer above the thermosphere, from which it is separated by the thermopause at an altitude of 800 to 3000 kilometers, and which represents the contact between the Earth and space. The temperature in the exosphere reaches up to 1500°C.

2.2 Radiative transfer through the atmosphere

Radiative transfer in the Earth's atmosphere is a process that controls the propagation of electromagnetic radiation through the air and includes the process of extinction of terrestrial and extraterrestrial radiation by atmospheric gasses and particles. The thermal structure and stratification of the atmosphere, as described in the previous section, are determined in large part by radiative transfer.

2.2.1 Atmospheric absorption

Without scattering, the absorption of electromagnetic radiation of frequency ν in a layer of thickness $\mathrm{d}s$ is described by the Beer-Lambert law (Liou, 2002; Salby, 2012):

$$\frac{\mathrm{d}I_\nu}{I_\nu} = -\rho\sigma_{\mathrm{abs},\nu}\mathrm{d}s, \tag{2.1}$$

where $\sigma_{\mathrm{abs},\nu}$ is the absorption cross section (or mass absorption coefficient) describing the effective absorption area of the mass $\rho\mathrm{d}A\mathrm{d}s$ of the layer, ρ is the density of the layer, and I_ν is the intensity of the incident radiation. The absorption coefficient $\beta_{\mathrm{abs},\nu} = \rho\sigma_{\mathrm{abs},\nu}$ measures the characteristic distance over which the energy is attenuated. In a mixture of different constituents, the total absorption coefficient is given by:

$$\beta_{\mathrm{abs},\nu} = \sum_i r_i\rho_i\sigma_{\mathrm{abs},\nu,i}, \tag{2.2}$$

where r_i is the mass mixing ratio of the i-th absorbing species. Integrating the equation (2.1) along the radiation path gives:

$$I_\nu(s) = I_\nu(0)\cdot\exp\left(-\int_0^s \rho\sigma_{\mathrm{abs},\nu}\mathrm{d}s'\right). \tag{2.3}$$

where $I_\nu(0)$ is the intensity of the incident radiation. Introducing the optical depth as:

$$\tau(s) = \int_0^s \rho\sigma_{\mathrm{abs},\nu}\mathrm{d}s' \tag{2.4}$$

gives a definition of monochromatic transmittance, i.e., the fraction of incident radiation remaining after the passage through the absorbing material:

$$T_\nu(s) = \frac{I_\nu(s)}{I_\nu(0)} = e^{-\tau(s)}. \tag{2.5}$$

Accordingly, the monochromatic absorbance A_ν can be introduced as the fraction of incident radiation that has been absorbed. Provided that:

$$T_\nu(s) + A_\nu(s) = 1, \tag{2.6}$$

the absorbance follows as:

$$A_\nu(s) = 1 - e^{-\tau(s)}. \tag{2.7}$$

The absorption cross section $\sigma_{\mathrm{abs},\nu}$ at frequency ν is defined by the position, strength and shape of the spectral line (Salby, 2012):

$$\sigma_{\mathrm{abs},\nu} = S f(\nu - \nu_0), \tag{2.8}$$

where

$$S = \int \sigma_\nu \mathrm{d}\nu \tag{2.9}$$

is the line strength, ν_0 is the line center, and f is the shape factor accounts for line broadening. A fundamental source of line width is the natural broadening that results from the finite lifetime of excited states and can be described by the Lorentz line shape (Figure 2.1) (Salby, 2012):

$$f_L(\nu - \nu_0) = \frac{\alpha_L}{\pi[(\nu - \nu_0)^2 + \alpha_L^2} \tag{2.10}$$

where $\alpha_L = \frac{1}{2\pi \bar{t}}$ is the half-width at the half-maximum of the line and $\bar{t}$ is the mean lifetime of the excited state. The shape of the Lorentz line can also include the broadening due to collision (pressure) at temperature T and pressure p with collisional half-width (Salby, 2012):

$$\alpha_c = \alpha_0 \left(\frac{p}{p_0}\right)\left(\frac{T}{T_0}\right)^{1/2}, \tag{2.11}$$

where $\alpha_0 = 0.1\ \mathrm{cm}^{-1}$ is the half-width at standard temperature T_0 and standard pressure p_0. The molecular motion v along the line of sight introduces another source of line width, called Doppler broadening (Figure 2.1), which together with the Boltzmann probability distribution gives the shape factor (Salby, 2012):

$$f_D(\nu - \nu_0) = \frac{1}{\alpha_D \sqrt{\pi}} \exp\left[-\left(\frac{\nu - \nu_0}{\alpha_D}\right)^2\right], \tag{2.12}$$

where $\alpha_D = \frac{\nu_0}{c}\sqrt{\frac{2kT}{m}}$ is the Doppler half width divided by a factor of $\sqrt{\ln 2}$, k is Boltzmann's constant, m is the particle mass, and c is the speed of light.

For vibrational and rotational transitions in the infrared (IR) band, natural broadening is insignificant compared to other sources of line width. Below 30 km, the pressure dependence of α_c makes collisional broadening dominant for IR bands of CO_2 and H_2O. With increasing altitude,

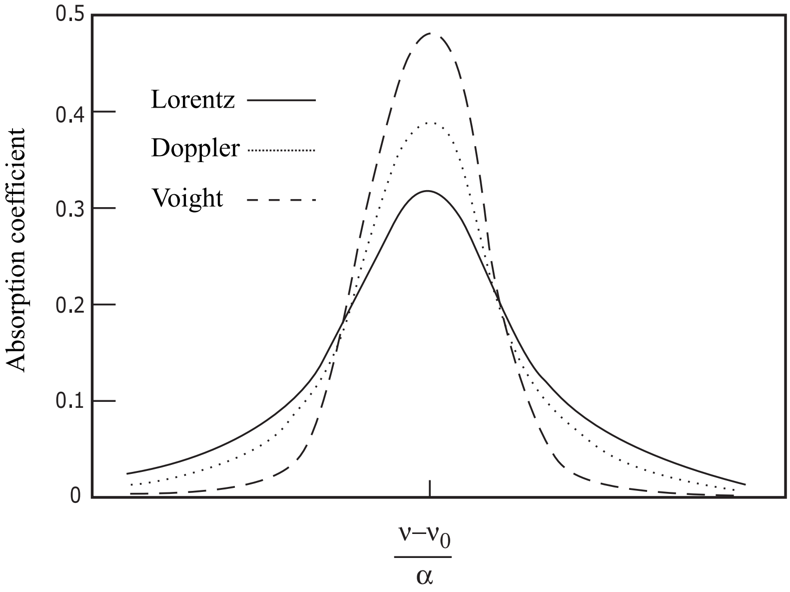

Figure 2.1: Lorentz, Doppler, and Voight line shape factors as functions of $\frac{\nu-\nu_0}{\alpha}$. The meaning of each quantity is defined in the text. The curves are normalized to give the same area under them (Salby, 2012).

both Doppler broadening and natural broadening become important in the visible and UV bands. In the upper stratosphere and mesosphere, natural broadening of O_2 bands becomes as important as collisional broadening. These two sources are treated with the Voigt line profile (Salby, 2012). The Voigt profile (Figure 2.1) is a convolution of a Gaussian profile (used to treat the Doppler broadening) and a Lorentzian profile (used to treat the natural broadening) (Liou, 2002):

$$f_V(\nu-\nu_0)=\int_{-\infty}^{+\infty} f_L(\nu'-\nu_0)f_D(\nu-\nu')\mathrm{d}\nu'. \tag{2.13}$$

2.2.2 Atmospheric scattering

In addition to absorption and emission, the transfer of electromagnetic radiation is affected by a process known as scattering. Scattering is the absorption and subsequent re-emission of energy by matter. In a population of molecules, there are various forms of internal energy, including translational energy related to temperature, electronic energy, vibrational energy, and rotational energy (Salby, 2012). These internal forms of energy can be excited by the absorption of a photon and subsequently released in various ways. The excited state can lead to the re-emission of energy at wavelengths and in directions that differ from those of the incident radiation. Analogous interactions also occur between radiation and atmospheric aerosols or clouds.

The process is described by the scattering cross section $\sigma_{\mathrm{scat},\nu}$. Given that the processes of absorption and scattering are additive, the extinction cross section is defined as (Salby, 2012):

$$\sigma_{\mathrm{ext},\nu}=\sigma_{\mathrm{abs},\nu}+\sigma_{\mathrm{scat},\nu}, \tag{2.14}$$

and extinction coefficient:

$$\beta_{\mathrm{ext},\nu} = \rho\sigma_{\mathrm{ext},\nu}. \tag{2.15}$$

While scattering can remove radiation from one direction of space, it can also direct it in other directions. Alternatively, photons from all directions may be scattered into a particular solid angle $\mathrm{d}\Omega$. The directionality of the scattering is described by the phase function $P_\nu(\hat{\Omega},\hat{\Omega}')$, which corresponds to the fraction of radiation scattered by a single particle from the direction $\hat{\Omega}'$ into the direction $\hat{\Omega}$. For the normalized phase function (Salby, 2012):

$$\frac{1}{4\pi}\int_{4\pi} P_\nu(\hat{\Omega},\hat{\Omega}')\mathrm{d}\Omega' = 1, \tag{2.16}$$

$\omega_\nu \frac{P_\nu(\hat{\Omega},\hat{\Omega}')}{4\pi}\mathrm{d}\Omega'$ represent the fraction of radiation lost by extinction from the layer in the direction $\hat{\Omega}'$ and scattered into the layer in the direction $\hat{\Omega}$, where $\omega_\nu = \frac{\sigma_{\mathrm{scat},\nu}}{\sigma_{\mathrm{ext},\nu}}$ is the single scattering albedo, i.e. the ratio of scattering efficiency to total extinction efficiency. The scattered contribution to the source function is then given as:

$$J_{\mathrm{scat},\nu} = \frac{\omega_\nu}{4\pi}\int_{4\pi} I_\nu(\hat{\Omega}')P_\nu(\hat{\Omega},\hat{\Omega}')\mathrm{d}\Omega'. \tag{2.17}$$

The source function is a measure of the effect of a material on the electromagnetic radiation that passes through it, i.e. the ratio of the rate per distance at which radiation is introduced in material to the rate at which the radiation is removed from material.

Rayleigh scattering

Rayleigh scattering describes the interaction between electromagnetic radiation and atmospheric molecules, i.e., it applies to particles much smaller than the wavelength of the radiation. Such a molecule is considered as an oscillating dipole. The strength of this oscillation is measured by the dipole moment $\vec{p}$:

$$\vec{p} = \alpha\vec{E}_0, \tag{2.18}$$

where α is the polarizability of the scattering particle and $\vec{E}_0$ the electric field. The applied field $\vec{E}_0$ produces the oscillation of an electric dipole in a fixed direction. The oscillating dipole, in turn, emits a scattered wave with electric field $\vec{E}$, which is a plane wave at a large distance r:

$$\vec{E} = \frac{1}{c^2}\frac{\sin\gamma}{r}\frac{\partial^2\vec{p}}{\partial t^2}, \tag{2.19}$$

where γ is the angle between the dipole moment $\vec{p}$ and the direction of observation, and c is the speed of light. In an oscillating periodic field, the scattered dipole moment can be written in terms of the induced dipole moment as (Liou, 2002):

$$\vec{p} = \vec{p}_0 \cdot \exp\left(-ik(r-ct)\right), \tag{2.20}$$

where k is the wavenumber. Combining the equations (2.19) and (2.20) gives:

$$\vec{E} = -\vec{E}_0 \frac{\exp\left(-ik(r-ct)\right)}{r} k^2 \alpha \sin\gamma. \tag{2.21}$$

If the plane of scattering is determined by the direction of incident radiation and the direction of scattered radiation, $\vec{E}$ can be decomposed into orthogonal components, one perpendicular ($E_\perp$) to the plane of scattering and one parallel ($E_\parallel$) to the plane of scattering (Figure 2.2a):

$$E_\perp = -E_{0,\perp} \frac{\exp\left(-ik(r-ct)\right)}{r} k^2 \alpha \sin\gamma_\perp, \tag{2.22a}$$

$$E_\parallel = -E_{0,\parallel} \frac{\exp\left(-ik(r-ct)\right)}{r} k^2 \alpha \sin\gamma_\parallel, \tag{2.22b}$$

or written in matrix form:

$$\begin{bmatrix} E_\perp \\ E_\parallel \end{bmatrix} = -\frac{\exp\left(-ik(r-ct)\right)}{r} k^2 \alpha \begin{bmatrix} 1 & 0 \\ 0 & \cos\theta \end{bmatrix} \begin{bmatrix} E_{0,\perp} \\ E_{0,\parallel} \end{bmatrix}. \tag{2.23}$$

Note that $\gamma_\perp = \frac{\pi}{2}$ and $\gamma_\parallel = \frac{\pi}{2} - \theta$, where θ is the scattering angle between the incident and scattered waves. The intensity (per solid angle) of the scattered radiation is proportional to the square of the electric field, i.e., $I = C|E|^2$, where C is a constant of proportionality such that $\frac{C}{r^2}$ implies a solid angle. For vertically polarized incident radiation, the scattering intensity is then independent of the direction of the scattering plane and the scattered radiation is isotropic:

$$I_\perp = I_{0,\perp} \frac{k^4 \alpha^2}{r^2}, \tag{2.24}$$

For horizontally polarized incident radiation, the scattered intensity depends on $\cos^2\theta$:

$$I_\parallel = I_{0,\parallel} \frac{k^4 \alpha^2 \cos^2\theta}{r^2}. \tag{2.25}$$

The total scattered intensity of the unpolarized incident radiation is given by:

$$I = I_\perp + I_\parallel = (I_{0,\perp} + I_{0,\parallel} \cos^2\theta) \frac{k^4 \alpha^2 \cos^2\theta}{r^2}. \tag{2.26}$$

Assuming that for unpolarized radiation:

$$I_{0,\perp} = I_{0,\parallel} = \frac{I_0}{2} \tag{2.27}$$

and $k = \frac{2\pi}{\lambda}$, the intensity of Rayleigh scattering is given by:

$$I = I_0 \frac{\alpha^2}{r^2} \left(\frac{2\pi}{\lambda}\right)^4 \frac{1+\cos^2\theta}{2}. \tag{2.28}$$

It is obvious that the maximum of Rayleigh scattering is in the forward (0°) and minimum in the

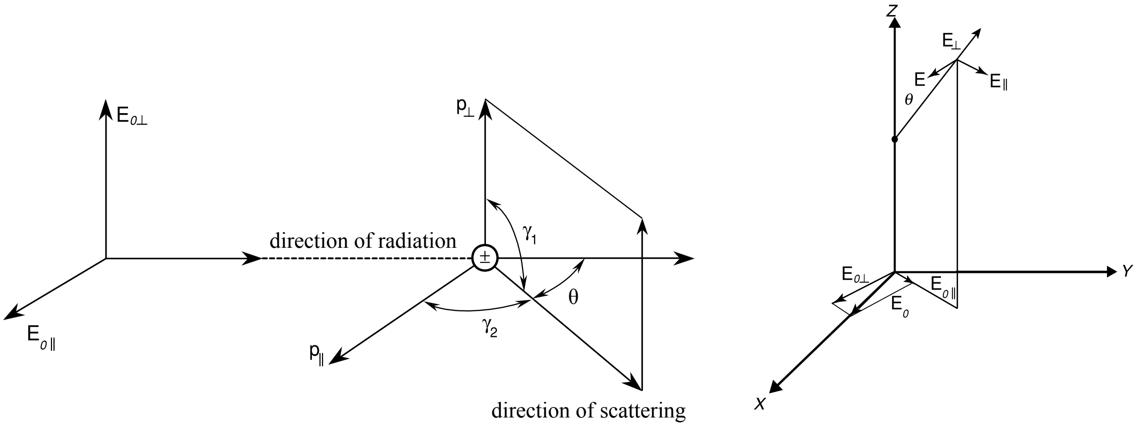

(a) **(b)**

Figure 2.2: Decomposition of the incident (E_0) and scattered (E) electric field vectors into perpendicular ($\perp$) and parallel ($||$) components for a) Rayleigh and b) Mie scattering (Liou, 2002).

backward (180°) direction. According to equation (2.2.2) and given that $d\Omega = \sin\theta d\theta d\phi$, the phase function of Rayleigh radiation describing the angular distribution of the energy of the scattered radiation is given by:

$$P(\cos\theta) = \frac{3}{4}(1+\cos^2\theta). \tag{2.29}$$

Finally, the equation (2.28) can be written as:

$$I(\theta) = \frac{I_0}{r^2}\frac{128\pi^5}{3\lambda^4}\frac{P(\theta)}{4\pi} \tag{2.30}$$

The degree of linear polarization for Rayleigh scattering is given by:

$$LP(\theta) = -\frac{I_{||}-I_{\perp}}{I_{||}+I_{\perp}} = \frac{\sin^2\theta}{\cos^2\theta+1}. \tag{2.31}$$

In the forward and backward directions, the scattered light remains completely unpolarized, while at a scattering angle of 90°, it becomes completely polarized. In the other directions, the scattered light is partially polarized, with the percentage of polarization ranging from 0 to 100%. The total scattering cross section and absorption cross section can be obtained by the following expressions:

$$\sigma_{\text{scat}} = \frac{2\lambda^2}{3\pi}\alpha^6\left|\frac{\overline{m}^2-1}{\overline{m}^2+2}\right|^2, \tag{2.32a}$$

$$\sigma_{\text{abs}} = \frac{-\lambda^2}{\pi}\alpha^3\text{Im}\left\{\frac{\overline{m}^2-1}{\overline{m}^2+2}\right\}, \tag{2.32b}$$

where $m = m_r - m_i$ is the refraction index. The real and imaginary parts of m refer to the scattering and absorption properties of the medium.

Mie scattering

The Mie solution of Maxwell's equations (also known as the Lorenz–Mie solution or Mie scattering) describes the scattering of electromagnetic radiation by a homogeneous sphere whose radius is comparable to the wavelength of the radiation. The theory imposes no specific constraints on particle size and converges to geometric optics for larger particles. Consequently, Mie theory is a valuable tool for describing a wide variety of systems involving spherical particles, even encompassing phenomena such as Rayleigh scattering. Nevertheless, it is worth noting that Rayleigh scattering theory is often the preferred choice when it can be effectively applied, mainly due to the complicated formulation of Mie scattering.

Similar to Rayleigh scattering, imagine that an incident electromagnetic plane wave, propagation in $+z$ direction, strikes a homogeneous spherical particle at the origin of a coordinate system (Figure 2.2b). For a homogeneous spherical particle, the scattered wave is described as follows (Liou, 2002):

$$\begin{bmatrix} E_\perp \\ E_\parallel \end{bmatrix} = -\frac{\exp\left(-ik(r-ct)\right)}{r} k^2 \alpha \begin{bmatrix} S_2 & 0 \\ 0 & S_1 \end{bmatrix} \begin{bmatrix} E_{0,\perp} \\ E_{0,\parallel} \end{bmatrix}, \tag{2.33}$$

where S_j, $j = 1,2$ are the non-zero elements of the amplitude scattering matrix. The difficult part of Mie's solution is to calculate these elements for a given particle radius a, the complex refractive index of the spherical particle $m_s = n_s + ik_s$, and the real refractive index of a medium n_m. Maxwell's equations are solved in spherical coordinates by separating the variables. The incident plane wave is expanded by Legendre polynomials so that the solutions inside and outside the sphere can be approximated at the boundary. The far-field solution is expressed by two scattering functions:

$$S_1(\theta) = \sum_{n=1}^{\infty} \frac{2n+1}{n(n+1)} \left[a_n \pi_n(\cos\theta) + b_n \tau_n(\cos\theta) \right], \tag{2.34a}$$

$$S_2(\theta) = \sum_{n=1}^{\infty} \frac{2n+1}{n(n+1)} \left[b_n \pi_n(\cos\theta) + a_n \tau_n(\cos\theta) \right]. \tag{2.34b}$$

The angle-dependent functions π_n and τ_n are expressed in terms of the Legendre polynomials (Arfken, Weber and Harris, 2011) expressed in terms of:

$$\pi_n(\cos\theta) = \frac{P_n^{(1)} \cos\theta}{\sin\theta}, \tag{2.35a}$$

$$\tau_n(\cos\theta) = \frac{\mathrm{d}P_n^{(1)} \cos\theta}{\mathrm{d}\theta}. \tag{2.35b}$$

a_n and b_n are the Mie coefficients describing the multipole expansion of the electric and magnetic fields waves, respectively, where $n = 1$ is the dipole term, $n = 2$ is the quadrupole term, etc.:

$$a_n = \frac{\psi_n(x)\psi_n'(mx) - m\psi_n(mx)\psi_n'(x)}{\xi(x)\psi_n'(mx) - m\psi_n(mx)\xi_n'(x)}, \tag{2.36a}$$

$$b_n = \frac{m\psi_n(x)\psi'_n(mx) - \psi_n(mx)\psi'_n(x)}{m\xi(x)\psi'_n(mx) - \psi_n(mx)\xi'_n(x)}, \tag{2.36b}$$

where ψ and ξ are the Ricatti-Bessel functions (Abramowitz, Stegun and Romer, 1988), $x = \frac{2\pi a}{\lambda}$ is the size parameter, and $m = \frac{n_s}{n_m} + i\frac{k_s}{n_m}$ is the refractive index of the sphere relative to that of the surrounding medium. The intensity functions for the perpendicular and parallel components is given by:

$$I_\perp(\theta) = |S_1(\theta)|^2, \tag{2.37a}$$

$$I_\parallel(\theta) = |S_2(\theta)|^2, \tag{2.37b}$$

while the average intensity function is given by:

$$\bar{I} = \frac{1}{2}\left(|S_1(\theta)|^2 + |S_2(\theta)|^2\right) \tag{2.38}$$

Equation (2.33) can be expressed in terms of an incident and scattered Stokes vector (Collett, 2005), yielding the scattering phase matrix (Liou, 2002):

$$\vec{P}(\theta) = \begin{bmatrix} P_{11}(\theta) & P_{12}(\theta) & 0 & 0 \\ P_{12}(\theta) & P_{11}(\theta) & 0 & 0 \\ 0 & 0 & P_{33}(\theta) & -P_{34}(\theta) \\ 0 & 0 & P_{34}(\theta) & P_{33}(\theta) \end{bmatrix}, \tag{2.39}$$

where

$$P_{11}(\theta) = \frac{2\pi}{k^2\sigma_{\text{scat}}}\left(|S_1(\theta)|^2 + |S_2(\theta)|^2\right), \tag{2.40a}$$

$$P_{12}(\theta) = \frac{2\pi}{k^2\sigma_{\text{scat}}}\left(|S_2(\theta)|^2 - |S_1(\theta)|^2\right), \tag{2.40b}$$

$$P_{33}(\theta) = \frac{2\pi}{k^2\sigma_{\text{scat}}}\left(S_2(\theta)S_1^*(\theta) + S_1(\theta)S_2^*(\theta)\right), \tag{2.40c}$$

$$P_{34}(\theta) = \frac{2\pi}{k^2\sigma_{\text{scat}}}\left(S_1(\theta)S_2^*(\theta) - S_2(\theta)S_1^*(\theta)\right), \tag{2.40d}$$

where $S_j^*(\theta)$ is the complex conjugate of $S_j(\theta)$. Here, the element $P_{11}(\theta)$ corresponds to the phase function of Mie scattering. Finally, one can obtain the total extinction and the scattering cross section from the following expressions:

$$\sigma_{\text{ext}} = \frac{\lambda^2}{2\pi}\sum_{n=0}^{\infty}(2n+1)\text{Re}\{a_n + b_n\}, \tag{2.41a}$$

$$\sigma_{\mathrm{scat}} = \frac{\lambda^2}{2\pi}\sum_{n=0}^{\infty}(2n+1)(|a_n|^2+|b_n|^2). \tag{2.41b}$$

The degree of linear polarization as a function of scattering angle for Mie scattering is given by:

$$LP(\theta) = -\frac{P_{21}(\theta)}{P_{11}(\theta)} = -\frac{|S_2(\theta)|^2-|S_1(\theta)|^2}{|S_2(\theta)|^2+|S_1(\theta)|^2} \tag{2.42}$$

Note that scattering by real particles in the atmosphere is never even close to isotropic and the calculations become very difficult, although they can be simplified by using the Henyey-Greenstein phase function (Henyey and Greenstein, 1941):

$$P_{\mathrm{HG}}(\theta) = \frac{1-g^2}{(1+g^2-2g\cos\theta)^{\frac{3}{2}}}, \tag{2.43}$$

where g is the asymmetry parameter:

$$g \equiv \langle\cos\theta\rangle = \frac{1}{4\pi}\int_{4\pi} P_{11}(\theta)\cos\theta \mathrm{d}\Omega. \tag{2.44}$$

The asymmetry parameter $g \in [-1,1]$ indicates the degree of scattering in the forward direction. If the light is isotropically scattered (e.g., for small grains in the Rayleigh regime), then $g = 0$.

2.2.3 Radiative transfer equation

The net rate at which the intensity of radiation in a material changes within a distance s is given by the radiative transfer equation:

$$\frac{\mathrm{d}I_\nu}{\rho\sigma_{\mathrm{ext},\nu}\mathrm{d}s} = -I_\nu + J_\nu. \tag{2.45}$$

In the absence of scattering, emission is the only process contributing to the source function, and the source function reduces to $J_\nu = B_\nu(T)$, where $B_\nu(T)$ is Planck's law:

$$B_\nu(T) = \frac{2h\nu^3}{c^2}\frac{1}{\exp\left(\frac{h\nu}{kT}\right)-1}, \tag{2.46}$$

where h is Planck's constant, c is the speed of light, k is Boltzmann's constant, and T is the temperature. In such cases, by introducing the optical thickness, which increases in the opposite direction to $\hat{\Omega}$:

$$\mathrm{d}\chi_\nu = -\mathrm{d}\tau(s) = -\rho\sigma_{\mathrm{ext},\nu}\mathrm{d}s, \tag{2.47}$$

equation (2.45) becomes:

$$\frac{\mathrm{d}I_\nu}{\mathrm{d}\chi_\nu} = I_\nu - B_\nu(T), \tag{2.48}$$

which is known as the Schwartzschild equation. Multiplying the equation (2.48) by $\exp(-\chi_\nu)$ and integrating it from 0 to $\chi_\nu(s)$ yields (Salby, 2012):

$$I_\nu(s) = I_\nu(0)\exp(\chi_\nu(s)) - \int_0^{\chi_\nu(s)} B_\nu[T(\chi'_\nu)]\exp(\chi_\nu(s) - \chi'_\nu)\mathrm{d}\chi'_\nu. \tag{2.49}$$

The first term in the above equation describes an exponential decrease with optical depth, while the second term describes cumulative emission and absorption. If T, ρ and $\sigma_{\mathrm{ext},\nu}$ are known functions of s, the radiative transfer equation determines the intensity along the radiation path.

2.3 Previous studies of the atmosphere on La Palma and its impact on IACT

The observatories of the Canary Islands, the Roque de los Muchachos Observatory (ORM) and the Teide Observatory (OT), are among the best, if not the best, characterized astronomical sites on Earth. The atmosphere over the Canary Islands, especially the islands of Tenerife and La Palma, has been extensively characterized in recent decades (Lombardi et al., 2008; García-Gil, Muñoz-Tuñón and Varela, 2010; Sicard et al., 2010; Varela et al., 2014; Laken et al., 2016; Hidalgo et al., 2021; Fruck et al., 2022).

Due to their latitude and eastern location in the North Atlantic, the Canary Islands have a vertical tropospheric structure with a thermal trade wind (easterlies) inversion layer called the Alisio inversion. The combination of the large-scale atmospheric circulation on the descending branch of the Hadley cell (responsible for the trade winds in the tropics that control low-latitude weather patterns), the trade winds from the Bermuda-Azores high area and the southward cold Canary ocean current produce a stable and strong thermal inversion layer, typically peaking at altitudes around 800 m a.s.l. in summer and 1600 m a.s.l. in winter (Castro-Almazán and Muñoz-Tuñón, 2018; Hidalgo et al., 2021). In the summer months, the easterly winds exert a stronger influence on the north, while in the winter months the influence of the westerly winds is most pronounced. Each season brings with it different weather phenomena that can influence observations. In winter, the westerly winds transport moist sea air from the Atlantic, which leads to cloud formation even at medium and high altitudes, while in summer the easterly winds frequently transport large amounts of Saharan dust over the Canary Islands. The Alisio inversion is a quasi-permanent layer, being present 78% of the time throughout the year. At the altitudes of ORM and OT (> 2300 m a.s.l., i.e. in the free troposphere) even more stable atmospheric conditions prevail.

Castro-Almazán and Muñoz-Tuñón (2018) analyzed atmospheric data over a 10-year period (2003-2012) from the Izaña Atmospheric Observatory, located 140 km from ORM. The study found a mean temperature of 9.6°. The temperature shows the usual seasonal behavior of the Northern Hemisphere with a maximum in July (18.9°C) and a minimum in February (3.8°C). Daily precipitation shows a clear absence of precipitation in Izaña, with $\approx 90\%$ of days without any type of precipitation. Precipitation is less frequent and intense during the night hours. Relative humidity has a low median value of 29% and remains below 56% for 75% of the night time, and below 15% for 25% of the time. This is a result of the typical elevation of the inversion layer, which is usually below the Izaña summit. No differences between day and night were observed for relative humidity.

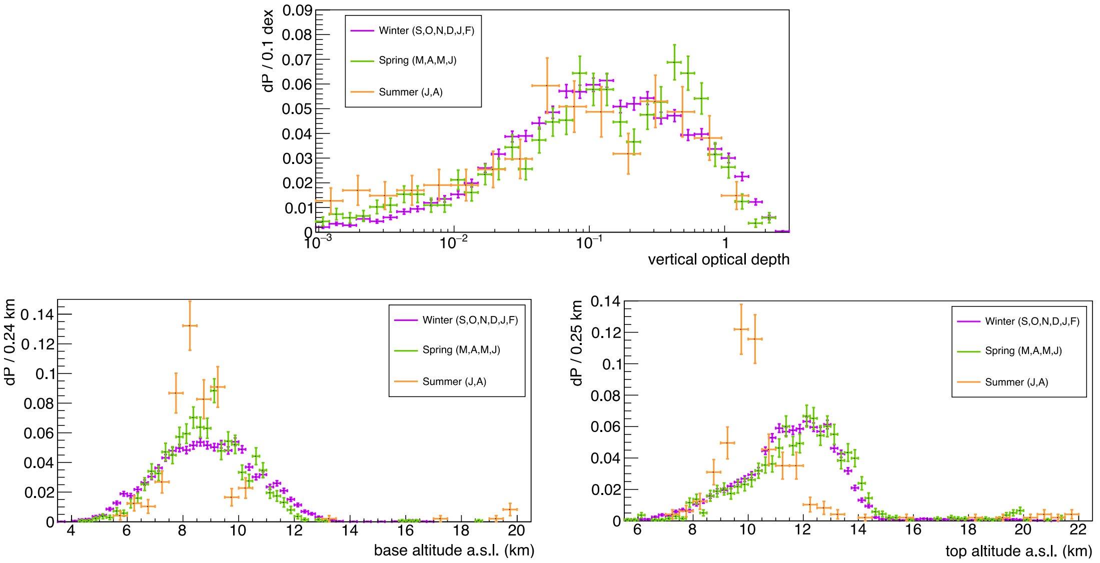

Figure 2.3: Distributions of various cloud parameters for the CTAO-N site (La Palma) according to Fruck et al. (2022). *Top*: vertical optical depth. *Bottom* (from left to right): cloud base height, and cloud top height. Data were divided into winter (October, November, December, January, February), spring (March, April, May, June), and summer (July, August, September) period.

2.3.1 Clouds coverage

In general, clouds over ORM are infrequent. According to García-Gil, Muñoz-Tuñón and Varela (2010), 29% of summer nights and 13% of other nights at ORM are affected by cirrus clouds or dust. However, this study does not distinguish between clouds and dust because the photometric method was used to measure atmospheric extinction. Given other studies of dust at the ORM site, the high percentage of summer nights with reduced atmospheric transmission is likely due to the presence of dust rather than clouds. The probability of cloud occurrence is higher in winter and lowest in summer months when the influence of trade winds is strong. In addition, trade winds push clouds against the peaks, making the humidity condense at mid-elevations in the north and northeast between 600 and 1800 m a.s.l. According to a recent study by Fruck et al. (2022), which analyzed seven years of quasi-continuous data from the Light Detection and Ranging (LIDAR) system measurements, the majority of the cloud cover over La Palma consists of single-layer clouds (Figure 2.3). In spring and winter, the cloud bases were typically between 8 and 10 km a.s.l., while in summer the cloud bases were found at an average height of 8 km a.s.l. The overall distribution of clouds over La Palma ranges from 4 to 14 km a.s.l., although in some cases clouds can occur even in the stratosphere, reaching heights of up to 22 km a.s.l. The study also reported a minimum total vertical transmission of $\approx 40\%$. For most clouds, the thickness is between 1 km and 3 km, with clouds being thicker in the winter months (Figure 2.4). It is important to note that the observations were not conducted in the presence of lower clouds. Therefore, caution should be used when interpreting the data for lower clouds, as they may have been underestimated. Clouds at altitudes above 6 km a.s.l. are mostly optically thin cirrus clouds. Lower, optically thick clouds above the ORM are usually cumulonimbus and altostratus clouds. More than two-layer clouds were detected

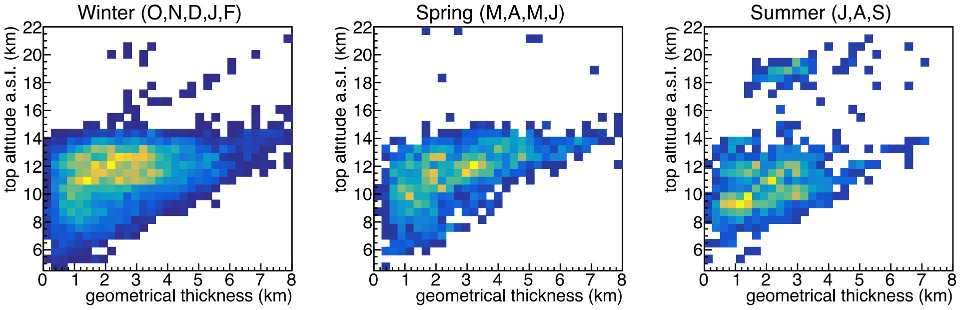

Figure 2.4: Distribution of reconstructed cloud top altitudes versus geometric thickness for the CTAO-N site (La Palma) according to Fruck et al. (2022). Data were divided into winter (October, November, December, January, February), spring (March, April, May, June), and summer (July, August, September) period.

during December, but they are very rare ($\lesssim 0.4\%$). However, the sample is heavily biased towards nights without cumulonimbus, as the MAGIC telescopes and LIDAR used in the study normally stop operating under these conditions.

2.3.2 Dust intrusions

Due to its proximity to the Sahara Desert, winds from the center of the Sahara carry large amounts of dust (Goudie and Middleton, 2001; Barreto et al., 2022) removing 10^8 tons of dust from the Sahara Desert annually. This seasonal event can cause extensive dust clouds in the sky, reaching heights of up to 6 km a.s.l. and leading to a phenomenon known locally as *Calima*. The distribution of dust particles increases from February to April and from July to September, while May and June are the months with the least amount of dust. Dust intrusions usually last three to four days, but sometimes short intrusions of two days long or, less frequently, long-lasting intrusions (up to a week) are possible (Lombardi et al., 2008). As mentioned above, García-Gil, Muñoz-Tuñón and Varela (2010) have shown that $\approx 30\%$ of summer nights are affected by Saharan dust, with only marine-oceanic (water droplets and salt) and anthropogenic aerosols (carbon and sulfates) present during the remaining nights. In the presence of Saharan dust, the optical thickness of aerosols varies between 0.233 and 0.157 at 532 and 1064 nm, respectively (Sicard et al., 2010). A more detailed description can be found in the article by Fruck et al. (2022).

2.3.3 Night sky brightness

The main factors contributing to the brightness of the night sky are airglow (emitted by molecules in the upper layers of the atmosphere excited by UV radiation), zodiacal light (the faint glow of diffuse sunlight scattered by interplanetary dust), starlight, extragalactic light, light pollution, and moonlight. The night sky brightness at the ORM is 21.9 mag arcsec^{-2} in the V band, 22.7 mag arcsec^{-2} in the B band, and 22.0 mag arcsec^{-2} in the U band at low solar activity and out of the Galactic plane (Benn and Ellison, 1998). The ORM has the reputation of being one of the darkest places on Earth. This is mainly because the night sky is protected by the law (Díaz-Castro, 1998), and because of the excellent atmospheric conditions. The two largest contributors to light pollution on La Palma are the two largest cities on the island: Los Llanos (with about 20,000 inhabitants),

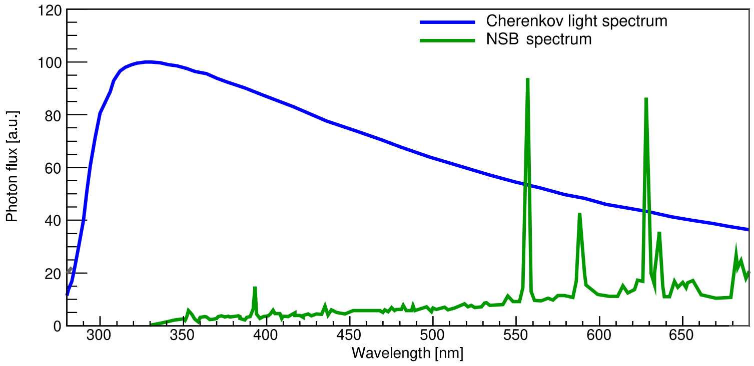

Figure 2.5: Difference between the Cherenkov light spectrum and the NSB spectrum at 2200 m a.s.l. on La Palma (Guberman et al., 2015).

located south-southwest of ORM, and Santa Cruz de La Palma (with about 16,000 inhabitants), located southeast of ORM (Pavletić et al., 2022; Fruck et al., 2022). For ORM the Night Sky Background (NSB) amounts to $(1.5 \pm 0.4) \cdot 10^{12}$ photons m^{-2} sr^{-1} s^{-1} (Mirzoyan, 1998). Figure 2.5 shows the NSB spectrum compared to the Cherenkov light spectrum.

2.3.4 Clouds and aerosols impact on IACT

Even though it is an integral part of the detector, the atmosphere itself is a source of systematic uncertainties if not fully taken into account in the simulations. The amount of Cherenkov light emitted depends on the quantitative properties of the atmosphere, e.g. the density profile and the refractive index. At small core distances, the lateral density of Cherenkov light is strongly dependent on the atmospheric density profile and shows variations from 15% to 20% between different profiles (absorption included) for mid-latitudes (Bernlöhr, 2000), although more recent studies (Munar-Adrover and Gaug, 2019) suggest that the effect is an order of magnitude smaller at CTA sites.

In addition, the Cherenkov light may be absorbed or scattered by molecules and particles in the atmosphere. The scattering and absorption of Cherenkov light by aerosols and clouds result in the loss of Cherenkov photons that would otherwise reach the telescopes, reducing the Cherenkov light yield and effective area. As a result, the reconstructed gamma-ray energy and flux may be underestimated if no corrections are made or inappropriate Monte Carlo simulations are used (Nolan, Pühlhofer and Rulten, 2010; Gaug et al., 2013; de Los Reyes et al., 2013; Hahn et al., 2014; Devin et al., 2019; Schmuckermaier et al., 2023). While molecular (Rayleigh) scattering is well-known and almost independent of geographical location, ozone absorption and scattering by clouds and aerosols (Mie scattering) are time-variable and depend on location and pointing position (Bernlöhr, 2000; Dubovik et al., 2006; Liou, 2002).

The spectrum of Cherenkov light ranges from the UV (≈ 240 nm) to the near IR (≈ 900 nm), with most of the light emitted in the visible range. UV absorption by molecular oxygen is relevant only up to 260 nm, in the *Herzberg band* (Figure 2.6). Absorption by this band system is weak and of little importance for the Cherenkov light because it overlaps with the much stronger ozone bands in this spectral region. Moreover, molecular oxygen absorption is insignificant for most

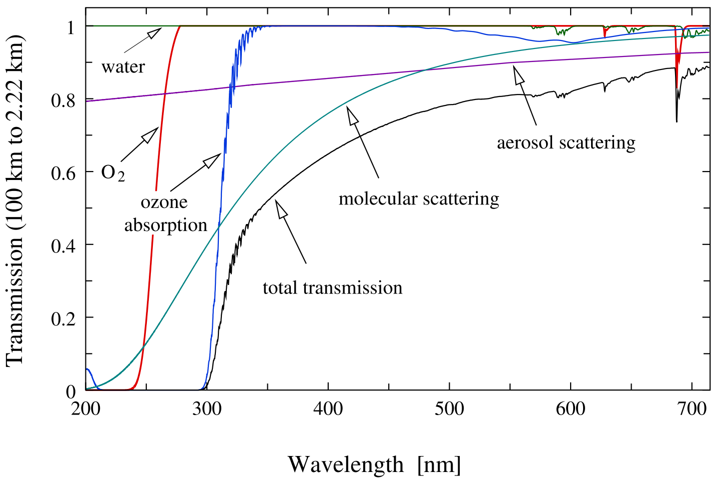

Figure 2.6: Vertical transmission of the main contributors to the total extinction from 100 km to 2.2 km for the tropical model of the atmosphere (Bernlöhr, 2000).

Cherenkov experiments because typically PMTs use windows made of borosilicate glass insensitive below 290 nm. The absorption by ozone is due to electronic transitions. The strongest ozone bands are the *Hartley bands*, which cover the range up to 300 nm (with the center at 255.3 nm). This absorption occurs mainly in the upper stratosphere and mesosphere (at altitudes above 10 km a.s.l.), which means that for the Cherenkov light is of little importance since the average height of the shower maximum is below this altitude. There is also a weak band between 300 nm and 360 nm called the *Huggins band*. Ozone also shows weak absorption bands in the visible and near IR region (from about 440 nm to 850 nm). These bands are referred to as *Chappuis bands*. The absorption coefficients in these bands are slightly temperature-dependent. Other molecules are of minor importance in the wavelength range of Cherenkov light (Liou, 2002).

Nolan, Pühlhofer and Rulten (2010) have shown that increased aerosol concentrations reduce the trigger yield (and hence the effective area) over the entire energy range. Furthermore, the reconstructed energies of all events (regardless of energy) are biased toward lower energies if the effects are not properly accounted for. The influence of atmospheric aerosols and clouds on IACT performance, particularly on energy estimation and energy threshold, was also studied by Garrido et al. (2013). Although the study does not use accurate atmospheric modeling (the standard aerosol density profile is multiplied by a fixed factor to mimic conditions of increased aerosol concentration, or in the case of a cloud, the aerosol density profile is simply increased to a fixed value within the boundaries of the cloud which corresponds to a particular optical depth), it draws two important conclusions for further research: the energy threshold increases with the overall aerosol density profile and decreases with increasing cloud height, while the intermediate height layers produce energy-dependent effects (Figure 2.7). The study did not examine the effects of clouds on other performance parameters such as energy and angular resolution or differential sensitivity.

Sobczynska and Bednarek (2014) studied the influence of clouds on IACT images (Figure 2.8). The main effect is a decrease in the trigger rate, since the number of Cherenkov photons reaching the telescope may be too small to trigger the telescope. The effect is also seen in a decrease in the

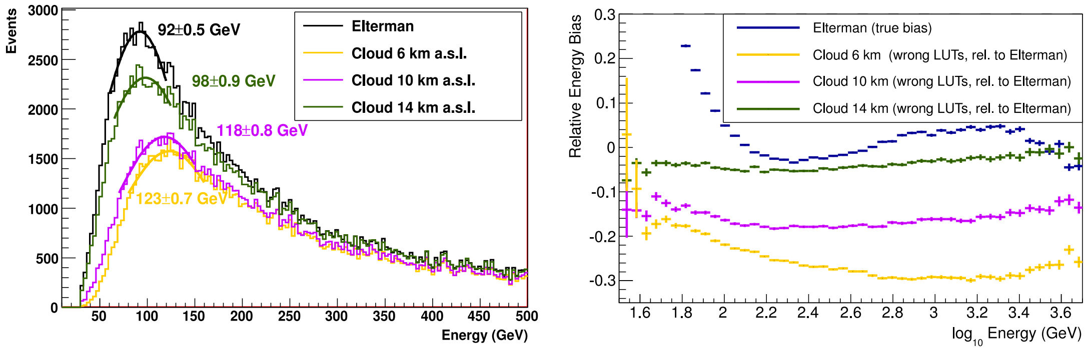

Figure 2.7: *Left*: Energy distribution of detected events in the cloudless atmosphere (Elterman profile) and in the presence of clouds. The peak of the distribution indicates the energy threshold. *Right*: Energy bias in the cloudless atmosphere ("true bias") and energy bias in the presence of clouds relative to the energy bias in the cloudless atmosphere (Garrido et al., 2013).

size parameter, i.e., the charge in the pixels. The second effect is a deformation of the observed images, which become wider and longer. The images are also shifted away from the camera center. High-altitude aerosols and clouds near the shower maximum affect only part of the shower. In higher layers of the atmosphere, the Cherenkov angle is smaller and the angular distribution of charged particles is narrower. Consequently, Cherenkov photons with very small Cherenkov angles are not recorded by the camera when the clouds are completely opaque. Therefore, part of the image near the center of the camera is missing. In contrast to semi-transparent clouds, the length of the image is reduced when the cloud is completely opaque because the Cherenkov photons emitted above the cloud are not recorded at all. Adamczyk and Sobczyńska (2017) have shown that the influence of the water and ice clouds on the Cherenkov light densities are very similar as the relative differences obtained from the simulations of water and ice clouds with the similar transmissions at 200 nm are $\lesssim 8\%$. Multiple scattering is not important for IACTs due to the limited and small FoV (Bernlöhr, 2000).

Some preliminary studies and conclusions on the effects of different molecular profiles on CTAO-N performance are also presented in the conference proceedings of Vrastil (2017) and Valore et al. (2018). The authors have shown that different molecular profiles do not significantly affect the performance of CTAO-N. The energy bias is $\lesssim 5\%$, while the changes in angular and energy resolution are less than 2%, depending on the molecular profile and Monte Carlo simulations used in the training sample. The study is based on the atmospheric density profiles modeled with MODTRAN software (section 2.4). The effects of clouds were not studied.

Sobczyńska et al. (2020) have studied the effects of clouds on the performance of the CTAO-S array of 5 SST telescopes. The additional extinction due to the presence of clouds was approximated by calculating the extinction coefficient using equation (3.11) of Kokhanovsky (2004). The authors proposed an approximate equation for determining the energy bias based on the fractions of photons produced above the cloud to total number of photons with the assumption is that Cherenkov photons above the cloud participate in the energy reconstruction with a weight equal to the cloud transmission, while light produced below the cloud has a weight of 1. They have also shown that

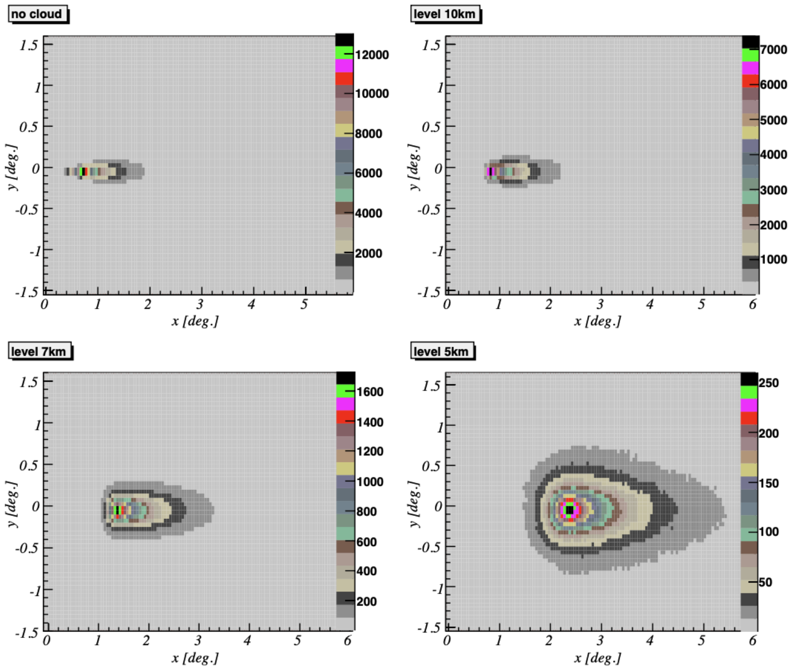

Figure 2.8: The expected mean images of 10 TeV gamma rays with the impact parameter 112.5 m in the presence of a non-transparent cloud at different altitudes. The color scale indicates the number of detected Cherenkov photons (Sobczynska et al., 2013).

the energy resolution, angular resolution, and flux are degraded in the presence of clouds. However, due to the high energies measured by the SSTs, the effects are small.

In recent years, a significant body of research has been conducted to investigate the effects and role of the atmosphere in IACT. A number of studies have examined the effects of clouds and aerosols on the performance of Cherenkov telescopes. The previous studies, while commendable in their own right, were conducted primarily with relatively crude and simple cloud models. While these models served as valuable tools for initial investigations, they lacked the comprehensive depth and precision required for a detailed understanding of the effects of clouds on IACT. What sets this work apart is the careful integration of clouds into the simulations of extensive air showers by including the clouds within the simulations of atmospheric transmission profiles needed for Monte Carlo simulation, a valuable and unavoidable tool in the analysis of IACT data. This approach not only refines the precision of the study, but also expands the scope of our understanding and paves the way for a method that allows reliable reconstruction of IACT data even in the presence of clouds. Section 2.4 provides a description of a software used to model atmospheric profiles (including clouds), which then serve as input to Monte Carlo simulations (Chapter 3).

2.4 Modeling of atmospheric transmission profiles with MODTRAN

The extinction of Cherenkov light in the atmosphere is treated during simulations of the detector response with `sim_telarray` (section 3.2). For this purpose, appropriate atmospheric transmission models are required as input. The modeling of atmospheric transmission profiles was done with MODerate spectral resolution atmospheric TRANsmittance algorithm and computer model

(MODTRAN) software. This section is heavily based on MODTRAN reports and articles (Berk, Bernstein and Robertson, 1987; Berk et al., 2005; Abreu and Anderson, 1996; Stotts and Schroeder, 2019). The spectral resolution of MODTRAN version 5.2.2 used in this thesis extends to 0.1 cm^{-1} full-width half maximum in averaged steps of 1 cm^{-1}.

Calculations of atmospheric transmission using this detailed technique fall into two categories. The first group of models are those that sum the contributions of individual molecular absorption lines to the total absorption, called line-by-line (LBL) models (Clough, Iacono and Moncet, 1992; Kratz et al., 2005). LBL radiative transfer models are based on the calculation of the transmittance of different atmospheric layers for gasses that exhibit spectroscopic activity within the region of interest in the wavenumber space. For this purpose, the atmosphere is divided into several homogeneous sublayers, each of which is represented by appropriate Curtis-Godson absorber-weighted average parameters (section 2.4.5). For each gas within a layer, a monochromatic optical depth is calculated by summing the contribution of all absorption lines. The optical depths are then vertically summed and finally integrated over the spectrum. To ensure accuracy, the wavenumber grid should ideally be fine enough to adequately capture the narrowest line and evaluate the absorption coefficient for each line at each wavenumber grid point. A review of some LBL radiative transfer models can be found in Matricardi (2007). At higher resolutions, the absorption spectrum indeed consists of a complex set of lines that may be randomly distributed. Theoretically, all these lines should be taken into account in radiative calculations. However, due to their numerous and complex nature, the use of LBL calculations is impractical for most applications. Therefore, radiative transport calculations often depend on band models.

Semi-empirical band models (BMs) (Plass, 1958; Udo and Akpan, 2002; Maghrabi, 2007) were developed with the goal of simplifying transmission calculations related to radiative transfer modeling. These models provide a simple mathematical representation for calculating the average transmittance over a spectral band that includes multiple absorption lines. The spectral band is defined by a width $\Delta\nu$ chosen to be wide enough to smooth out spectral features, yet narrow enough to allow the use of the constant value of the Planck function $B(T)$ (Maghrabi, 2007). The parameters required to characterize a particular spectral interval can be extracted from experimental measurements or by matching it to the spectroscopic theory. Notable examples of well-known BMs include the work of Elsasser (1938) and Goody (1952). In Elsasser's model, the transmission function is averaged over uniformly distributed intervals, while in Goody's model, the transmission is calculated assuming that the position and strength of the lines can be described by a random function with randomly distributed lines (Liou, 2002). Because the half-width of the lines varies with changing factors such as pressure, temperature, and the amount of absorber along vertical paths through the atmosphere, it is essential that these BMs are adjusted to account for the inhomogeneities that occur. The basic approach to solving this problem and accounting for the effects of inhomogeneity is to transform the radiative transfer problem into one associated with a homogeneous path. This is achieved by introducing averaged values for the temperature, pressure, and amount of absorber within the spectral band, which allows accurate calculation of the properties of the spectral lines and optical depth. Two main techniques commonly used to accomplish this task are the one-parameter and two-parameter scaling methods described by Goody and Yung (1989).

One such BM is MODTRAN. The basic approach in MODTRAN is to approximate the atmosphere as a set of N spherical and symmetric shells with boundaries at altitudes z_j, $j = 1,2,...,N$. The temperature, pressure and absorber density (gasses and aerosols) are defined at the boundary layers. Between layers, the temperature profile is linear, while the pressure and density follow an exponential profile. The spectroscopic information for each spectral line needed to calculate the absorbtion coefficents are derived from the HIgh-resolution TRANsmission molecular absorption (HITRAN)[1] database. The MODTRAN BM uses three temperature-dependent parameters: an absorption coefficient, a line density, and a line width. The absorption coefficient measures the total strength of the lines in an interval. The line density is a line strength weighted average of the number of lines in the frequency bin, and the line width parameter is a line strength weighted average line width. The bin is divided into 1 cm^{-1} bins for each absorption species. Within each frequency bin, the contributions of transitions whose line centers lie within the bin are modeled separately from the line tails. Absorption due to lines within the bin is calculated by integration over a Voigt line shape. The Curtis-Godson approximation (section 2.4.5), which is appropriate for the moderate temperature variations in the Earth's atmosphere, is used to replace multilayer paths with an equivalent homogeneous path.

2.4.1 Molecular absorption

Line-center parameters

Each frequency bin corresponds to a 1 cm^{-1} interval and contains parameters for molecules with lines in that interval. The molecular absorption coefficients (S/d) (cm^{-1} amagat^{-1})[2] are calculated for five reference temperatures $T \in [200, 225, 250, 275, 300]$ K from the line strength S_j (Berk, Bernstein and Robertson, 1987):

$$(S/d) = \frac{1}{\Delta\nu}\sum_j S_j(T), \tag{2.50}$$

where $S_j(T)$ is the integrated line strength at temperature T of the j-th line in the i-th bin. For the temperature inside the interval, the absorption coefficients are calculated by linear interpolation, while for the values outside the interval, the extreme values are used. The line strength at an arbitrary temperature is scaled from the line width of the HITRAN data at the standard temperature of $T_s = 296$ K:

$$S_j(T) = \frac{Q_r(T_s)Q_\nu(T_s)}{Q_r(T)Q_\nu(T)} \cdot \frac{1 - \exp\left(-\frac{hc\nu_j}{kT}\right)}{1 - \exp\left(-\frac{hc\nu_j}{kT_s}\right)} \cdot \exp\left(\frac{E_j}{k}\frac{T - T_s}{TT_s}\right) \cdot S_j(T_s), \tag{2.51}$$

where Q_r and Q_ν are the rotational and vibrational partition functions, E_j is the energy of the lower transition state, ν_j is the transition frequency, c is the speed of light, k is Boltzmann's constant, and h is Planck's constant.

---

[1] `https://hitran.org`

[2] An amagat is a unit of number density, defined as the number of ideal gas particles per unit volume at standard pressure and temperature: 1 amagat $\simeq$ 44.615 mol m^{-3}.

The Lorentz line-width at temperature T and pressure T is modeled by:

$$\gamma_c(T,P) = \gamma_c^0 \frac{P}{P_0}\left(\frac{T_0}{T}\right)^x \begin{cases} x = 0.75, & \mathrm{CO_2}, \\ x = 0.5, & \text{other molecules.} \end{cases} \tag{2.52}$$

where γ_c^0 is the Lorentz line-width at standard temperature and pressure (273.15 K, 101325 Pa). Then the final Lorentz line-width of BM is calculated as the line-strength averaged $\gamma_c(T_s)$:

$$\gamma_{c,\mathrm{BM}}^0 = \left(\frac{T_s}{T_0}\right)^x \frac{\sum_j \gamma_{c,j}(T_s) S_j(T_s)}{\sum_j S_j(T_s)}. \tag{2.53}$$

The line-density band-model parameters $1/d$ (cm) are also calculated at the five reference temperatures and interpolated in between:

$$1/d = \frac{1}{\Delta\nu} \frac{\left(\sum_j S_j(T)\right)^2}{\sum_j S_j^2(T)}. \tag{2.54}$$

The expression for calculating molecular transmittance T is based on a statistical model for a finite number of lines within a spectral interval:

$$T = \left(1 - \frac{\langle W_{\mathrm{sl}}\rangle}{\Delta\nu}\right)^{\langle n\rangle} \tag{2.55}$$

where $\langle W_{\mathrm{sl}}\rangle$ is the Voigt single-line equivalent width for the line-strength distribution in a frequency bin and $\langle n\rangle = \Delta\nu\langle 1/d\rangle$ is the effective number of lines in the frequency bin averaged over the path line spacing. For large $\langle n\rangle$ and fixed $\Delta\nu$ and (S/d), the transmittance simplifies to the form of Beer-Lambert law $T = \exp(-\langle W_{\mathrm{sl}}\rangle\langle 1/d\rangle$.

Numerous approximations have been devised to compute the equivalent width of a Voigt line shape. Each of these approximations is well-suited for distinct scenarios, depending on factors such as the presence of Doppler or collision broadening, the line's strength, and other variables. Nevertheless, no singular approximation can comprehensively address the diverse range of pressures and optical path lengths relevant to atmospheric transmission calculations. In response to this challenge, in MODTRAN the exact expression for the equivalent width of a single spectral line within a finite spectral interval is obtained directly by the following expressions:

$$\langle W_{\mathrm{sl}}\rangle = \frac{\Delta\nu}{X_m}\int_0^{X_M} 1 - \exp\left(-\frac{[Su/d]\sqrt{\ln 2/\pi}F(X,Y)}{\langle\gamma_d/d\rangle}\right)\mathrm{d}x, \tag{2.56}$$

$$F(X,Y) = \frac{Y}{\pi}\int_{-\infty}^{+\infty} \frac{\exp(-T^2)}{Y^2 + (X-T)^2}\mathrm{d}T, \tag{2.57}$$

$$X_M = \frac{0.5\sqrt{\ln 2}\langle n\rangle}{\langle\gamma_d/d\rangle}, \quad Y = \frac{\sqrt{\ln 2}\langle\gamma_c/d\rangle}{\langle\gamma_d/d\rangle}, \tag{2.58}$$

where $F(X,Y)$ is the Voigt line shape function, $[Su/d]$ is the total optical depth, and $\langle\gamma_c/d\rangle$

and $\langle \gamma_d / d \rangle$ are the path averaged Doppler and collision broadened line shape BM parameters, respectively. To accurately calculate transmittance, line-center contribution to total transmittance $\langle W^0_{\mathrm{sl}} \rangle$ is calculated separately from the line-tail contribution $\langle W^1_{\mathrm{sl}} \rangle$:

$$\langle W_{\mathrm{sl}} \rangle = \langle W^0_{\mathrm{sl}} \rangle - \langle W^1_{\mathrm{sl}} \rangle. \tag{2.59}$$

Lorentz (L) and Doppler (D) equivalent widths are given by:

$$L \equiv \frac{4}{4 + [Su/d] / \langle \gamma_c / d \rangle}, \tag{2.60}$$

and

$$D \equiv \frac{2}{\ln 2} \frac{\langle \gamma_d / d \rangle^2}{[Su/d]^2} \ln \left(1 + \frac{\ln 2}{2} \frac{[Su/d]^2}{\langle \gamma_d / d \rangle^2} \right). \tag{2.61}$$

Finally, $\langle W^0_{\mathrm{sl}} \rangle$ is calculated as:

$$\langle W^0_{\mathrm{sl}} \rangle = \left[\frac{[Su/d]^2}{\langle 1/d \rangle^2} \cdot \left(\frac{1 - (1-L)(1-D)}{\sqrt{1 - LD(2-L)(2-D)}} \right) \right]^{\frac{1}{2}}. \tag{2.62}$$

The total optical depth is the sum of the contributions of the individual layers:

$$[Su/d] = \sum_l (S/d)_l \cdot \Delta u_l, \tag{2.63}$$

where Δu_l is the incremental absorber amount of layer l.

Line-tail parameters

All absorption lines lying outside a certain frequency bin but within the range of ±25 cm^{-1} are included in the calculation of the line-tail parameters. The line-tail absorption coefficient is determined by integrating the Lorentz line shape over this interval.

The tail-line contribution to transmittance is evaluated in terms of error function $\mathrm{erf}(z)$ since in calculations with MODTRAN $X_M \gg Y$:

$$\langle W^1_{\mathrm{sl}} \rangle \approx \exp \left(\frac{1}{z^2} \right) + \sqrt{\pi} \cdot z \cdot \mathrm{erf}(z) - 1, \tag{2.64}$$

where:

$$z \equiv \frac{2}{\langle n \rangle} \sqrt{\frac{[Su/d] \langle \gamma_c / d \rangle}{\pi}}. \tag{2.65}$$

The effect of line-tail absorption is included in the transmittance by adjoining an exponential term:

$$T = \left(1 - \frac{\langle W_{\mathrm{sl}} \rangle}{\Delta \nu} \right)^{\langle n \rangle} \exp - \left(\sum_l C_l \cdot \Delta u_l \right). \tag{2.66}$$

2.4.2 Aerosol transmission

In MODTRAN, aerosol particles are treated as homogeneous spheres. Mie scattering theory is used to calculate the extinction and scattering cross sections. The transmittance T due to aerosol extinction along path length z is calculated as follows (Abreu and Anderson, 1996):

$$T_{\mathrm{aerosol}} = e^{-EXTV(\nu)\cdot HAZE\cdot z}, \tag{2.67}$$

where $EXTV(\nu)$ is the normalized extinction coefficient for the wavenumber ν of the corresponding aerosol model and altitude z (normalized to the extinction coefficient at a wavelength of 550 nm), and is determined by interpolating the values stored in the code for the required wavenumber and relative humidity. $HAZE$ is the altitude-dependent aerosol concentration (scaling factor) and is determined by interpolating the corresponding aerosol scaling factor according to the meteorological range (visibility) and season of the aerosol model (Carr, 2005). The size distribution of the aerosol models in MODTRAN, in the range of radius from 10^2 nm 10^4 nm to is the sum of two log-normal distributions (Shettle and Fenn, 1976):

$$\frac{\mathrm{d}N(r)}{\mathrm{d}r} = \sum_{i=1}^{2}\left(\frac{N_i}{\ln 10\cdot r\cdot \sigma_i\sqrt{2\pi}}\cdot \exp\left[-\frac{(\log r-\log r_i)^2}{2\sigma_i^2}\right]\right), \tag{2.68}$$

where $N(r)$ is the cumulative number density of particles of radius r, σ_i is the standard deviation of the distribution, r_i is the mode radius, and N_i is the number density within r_i.

2.4.3 Molecular scattering

The molecular scattering coefficient (km^{-1}) is calculated in MODTRAN as follows:

$$ABS = \frac{\nu^4}{9.26799\cdot 10^8 - 1.07123\cdot 10^9\ \nu^2}, \tag{2.69}$$

where ν is the wavenumber (Abreu and Anderson, 1996). Equation 2.69 was obtained by performing the least squares fit to the molecular scattering coefficients reported by Penndorf (1957).

2.4.4 Cloud model

The simplest approach to characterizing a cloud in MODTRAN is to specify the base height h_{base} and thickness L in km, along with the extinction coefficient β_{ext} derived from the models in MODTRAN (Mazuk and Lynch, 2002). The thickness must be chosen such to give the correct optical depth at a wavelength of 550 nm. The relationship between the optical depth τ, and β_{ext}, is as follows:

$$\tau = \beta_{\mathrm{ext}}\cdot L. \tag{2.70}$$

In addition, the user must specify the number of layer boundaries used to describe the cloud structure and specify the extinction, absorption, and asymmetry of water and ice for each wavelength. Also, the user must specify the asymmetry values of the model instead of relying on the default Henyey-Greenstein values.

2.4.5 Curtis-Godson approximation

Consider the atmospheric optical depth τ_ν for a layer of thickness ds for a single line. Assuming the homogeneous layer so that $\sigma_{\nu,\mathrm{abs}}$ is independent of the distance s, τ_ν depends on the path length du as:

$$\tau_\nu = \int_s \sigma_{\nu,\mathrm{abs}}(p,T)\rho \mathrm{d}s = \int_u \sigma_{\nu,\mathrm{abs}}(p,T)\mathrm{d}u \tag{2.71}$$

The main goal of the approximate solutions for inhomogeneous path lengths is to transform the problem into that of a homogeneous path defined by a reference pressure p_0 and a reference temperature T_0, so that analytical exponential functions can be used to calculate the spectral transmittance (Liou, 2002). By analogy with the equation (2.11) for the Lorentz half-width $\alpha(p,T)$, one can write the absorption cross section for an arbitrary temperature T and pressure p for the n-th absorption line as follows:

$$\sigma_{\nu,\mathrm{abs}}(p,T) \cong \sigma_{\nu,\mathrm{abs}}(p_0,T_0)\left(\frac{p}{p_0}\right)\left(\frac{T_0}{T}\right)^n, \tag{2.72}$$

such that the ratio of absorption coefficients for the temperatures T and T_0 is:

$$\frac{\sum_j \frac{S_j(T)\alpha_j(p_0,T_0)}{(\nu-\nu_{0,j})^2}}{\sum_j \frac{S_j(T_0)\alpha_j(p_0,T_0)}{(\nu-\nu_{0,j})^2}} \approx 1. \tag{2.73}$$

where $j = 1,\ 2,\ \ldots,\ N$ is the index of the absorption coefficient for the j-th line. The is the one-parameter Curtis-Godson approximation (Curtis, 1952; Godson, 1953; Liou, 2002). From equation (2.71), a scaled optical depth is defined as $\tau_\nu = \sigma_{\nu,\mathrm{abs}}(p_0,T_0)\tilde{u}$, where:

$$\tilde{u} = \int_u \left(\frac{p}{p_0}\right)\left(\frac{T_0}{T}\right)^n \mathrm{d}u. \tag{2.74}$$

By replacing u with $\tilde{u}$, one can calculate the spectral transmittance using the absorption coefficient at a reference temperature and pressure. One can also search for an adjusted absorption coefficient, for example:

$$\tau_\nu = \int_u \sigma_{\nu,\mathrm{abs}}(p,T)\mathrm{d}u = \sigma_{\nu,\mathrm{abs}}(\tilde{p},\tilde{T})u. \tag{2.75}$$

Combining equations (2.8) and (2.10) gives:

$$\sigma_{\nu,\mathrm{abs}}(\tilde{p},\tilde{T}) = \sum_j \tilde{S}_j \tilde{f}_{\nu,j} = \sum_j \frac{\tilde{S}_j}{\pi}\frac{\tilde{\alpha}_j}{(\nu-\nu_{0,j})^2+\tilde{\alpha}_j^2}. \tag{2.76}$$

Two adjusted parameters $\tilde{S}$ and $\tilde{\alpha}$ are required to satisfy equation 2.75. This is called a two-parameter approximation. This is a standard procedure for extending the results of BM for homogeneous paths to heterogeneous paths. In the MODTRAN BM, the main idea is to replace the line strength and line width parameters with appropriate path-averaged values of the parameters. Note that the

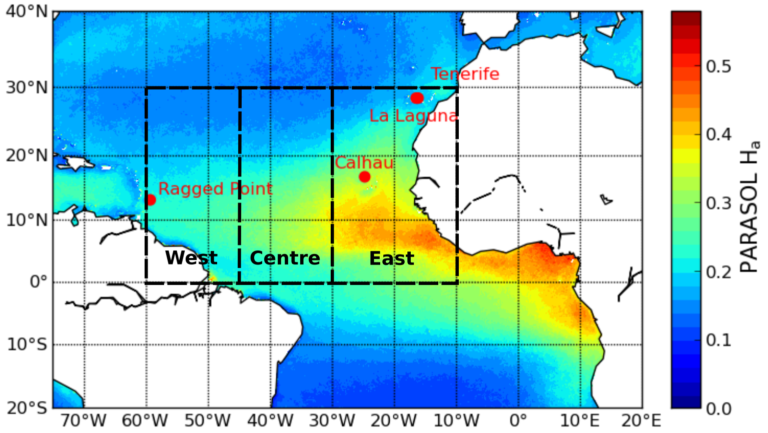

Figure 2.9: Aerosol distribution over the North Atlantic. The color scale indicates the average value of atmospheric optical depth at 550 nm as derived from the POLAC/PARASOL measurement during the period from 2005 to 2013 (Fréville, Chami and Mallet, 2020).

Curtis-Godson approximation varies from model to model.

2.4.6 Details of the simulations

MODTRAN is executed by means of input cards. These are text files containing all necessary and adjustable simulation parameters (e.g., base atmosphere, aerosol model, cloud type, cloud water/ice content, etc.). The file labeled `tape5` is the main input card that drives MODTRAN simulations and invokes other mandatory or optional input cards. Each of these cards handles a different aspect of the atmosphere (for example, `card2` is used for aerosol profiles and cloud characteristics). The MODTRAN output consists of several files, the most important of which is `tape7` file containing all spectral data. The final product of MODTRAN for the purposes of this thesis is a large table of transmittance values as a function of wavelength and height. Atmospheric transmission calculations in MODTRAN are based on predefined atmospheric models (e.g., tropical atmosphere, mid-latitude atmosphere, U.S. Standard Atmosphere) or on user-defined atmospheric models. Each atmospheric profile is defined by temperature, pressure, density, and mixing ratios for water vapor, ozone, methane, nitric oxide, and carbon monoxide.

In this study, the U.S. Standard Atmosphere 1976 predefined atmospheric model (US1976) (National Geophysical Data Center, 1992) was used as a baseline. US1976 is a widely accepted reference model for the Earth's atmosphere. It provides a well-defined and standardized atmospheric profile and is therefore commonly used for modeling and simulation purposes. The use of the standard atmosphere provides consistency and comparability between different studies. The atmosphere over La Palma (and the atmosphere in general) is too large and too complex to be fully described, so only models that roughly describe the atmosphere are used. Although the US1976 model does not perfectly describe the atmosphere above ORM, it meets the objectives of the study because of its reliability and the fact that this work is a comparative study focusing on the relative degradation of the performance parameters of IACTs in the presence of clouds compared to cloudless conditions. Furthermore, as Vrastil (2017) and Valore et al. (2018) have shown, the differences in the performance of CTAO-N are small for different density profiles for the CTAO-N site.

MODTRAN categorizes aerosol models based on the typical sources of aerosols in various regions (Carr, 2005). These sources represent rural, urban, desert, and maritime environments. At higher altitudes, the assumption is that aerosols remain consistent, whether above land or sea. To assign these aerosol models, the atmosphere is divided into distinct vertical regions. These regions include the boundary layer (0 - 2 km) and non-boundary layers, which are further divided into the free troposphere (background troposphere aerosols) (2 - 10 km), the lower stratosphere (10 - 30 km), and the upper atmosphere (30 - 100 km). In this study, the desert aerosol extinction model of default visibility of 75.748 km for the boundary layer was used. The default spring-summer seasonal dependence of the U.S. Standard Atmosphere is chosen for tropospheric aerosols, and the background stratospheric aerosol profile for layers above 10 km. The model gives a total atmospheric optical depth of ≈ 0.16 at 550 nm, which is in agreement with previous studies of aerosol profiles over the North Atlantic (Kinne et al., 2006; Barreto et al., 2022; Fréville, Chami and Mallet, 2020; Gallo et al., 2023, e.g.) (Figure 2.9) and a relative difference of only 1.43% compared to the official atmospheric model for CTAO-N used in `sim_telarray`.

Figure 2.11 shows the differences between the base atmospheric profile used in this study (U.S. Standard Atmosphere) and the standard atmospheric profile for CTAO-N used in `sim_telarray` (tropical atmosphere). Differences in transmission profiles for altitudes < 7 km above ground level (a.g.l.) are of the order of a few percent ($\lesssim 5\%$) over the entire wavelength range. At higher altitudes, where there is naturally more absorption, the relative differences in the transmission profiles around the peak of the Cherenkov light (300 - 350 nm) are $\lesssim 30\%$, while at longer wavelengths they drop well below 10%. At altitudes of $\gtrsim 7$ km a.s.l. and below 300 nm, the transmission of the atmosphere is intrinsically very low, hence, the relative differences tend to be much higher. On the other hand, to test the method on the real IACT data, the atmospheric profile is tuned to the atmospheric profile used in the standard Monte Carlo simulations for the joint LST-1 and MAGIC observations (see Chapter 5 for more details).

As described in section 2.3.1, the recent study by Fruck et al. (2022) has shown that the majority of the cloud cover over La Palma consists of single-layer clouds with bases ranging from 4 to 14 km a.s.l., with the lowest reported total vertical transmission of $\approx 40\%$. Accordingly, the transmission profiles for the atmosphere including clouds were simulated with cloud bases at six different heights above the ground (a.g.l., from 3 km to 13 km in increments of 2 km) and six different transmissions T (0.5, 0.6, 0.75, 0.8, 0.9, 0.95). The ground level for the studies of CTAO-N corresponds to 2147 m a.s.l. The cloudless atmosphere ($T = 1$), which serves as a benchmark for evaluating the influence of clouds on the CTAO-N performance, was also modeled. Considering the altitude of the CTAO-N observatory (free troposphere), low clouds are not simulated because they usually remain below the mountain tops. Furthermore, Fruck et al. (2022) have reported that most clouds over La Palma during the observations are of the cirrus and altostratus type. Cirrus clouds are high-altitude, thin clouds composed of ice crystals. In temperate regions, their average altitude rises to ≈ 9 km a.s.l., while in tropical regions cirrus clouds form at an average altitude of 13 km a.s.l. (Dowling and Radke, 1990). Altostratus are mid-altitude clouds in the form of an extended gray or bluish

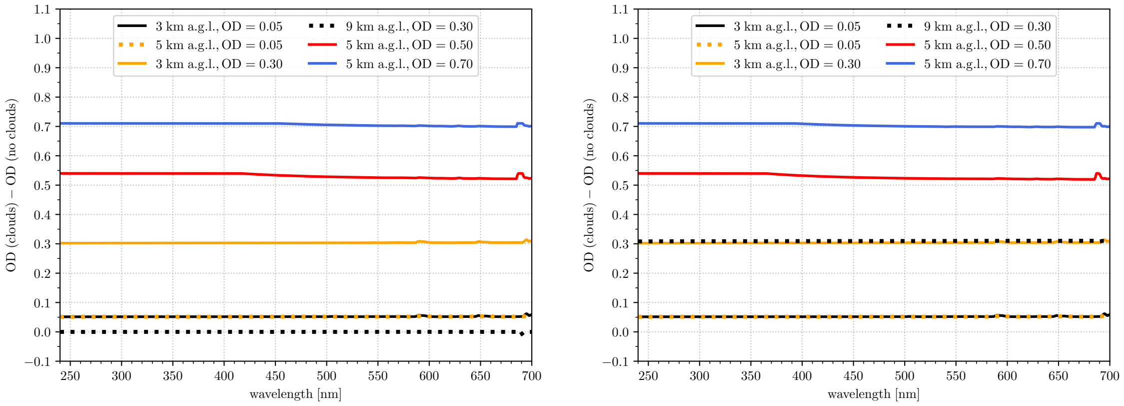

(a) **(b)**

Figure 2.10: Difference between total OD in the presence of clouds and total atmospheric optical depth in cloudless conditions: a) from 9 km a.g.l. to the ground level, b) from 13 km a.g.l. to the ground level. Note the wavelength-independent OD difference.

homogeneous layer at heights between 2 and 5 km, extending up to 8 km a.s.l. in temperate and tropical regions[3]. Considering that the maximum of air showers typically occurs at an altitude of 8 km a.s.l. (which corresponds to ≈ 6 km a.g.l. for the CTAO-N site, although the height of the shower maximum varies from 4 to 17 km a.s.l.), we believe that homogeneous altostratus clouds (rather than fibrous, optically thin cirrus clouds) would be more suitable for studying the effects of clouds on the reconstruction of air showers with IACTs. Therefore, atmospheric transmission was calculated in the presence of 1 km thick altostratus clouds in the wavelength range from 200 nm to 1000 nm (in the steps of 1 nm).

The optical properties of clouds have been extensively studied in the past, focusing on the wavelength-dependence of optical depth (Fu, 1996; Hu et al., 1993; Min, Joseph and Duan, 2004; Serrano et al., 2015). According to calculations based on Mie scattering theory, the variations in optical depth typically remain in the range of $\lesssim 2\%$ over the wavelength range from 300 to 1000 nm, indicating a negligible dependence of optical depth on wavelength. Consequently, the simulated clouds are considered as gray, assuming uniform extinction throughout the cloud while neglecting their internal structure. Figure 2.10 illustrates the difference between the total atmospheric optical depth (OD) in the presence of clouds and the total OD under cloudless conditions from altitudes of 9 km and 13 km a.g.l. to the ground for selected scenarios. The OD difference is shown as a function of wavelength within the range of Cherenkov light simulated in CORSIKA (see Chapter 3). For example, the mean OD difference for a cloud at an altitude of 3 km a.g.l. with OD = 0.05 (corresponding to $T = 0.95$) is 0.0519 ± 0.0012. Conversely, the mean OD difference for a cloud at an altitude of 5 km a.g.l. with OD = 0.70 ($T = 0.50$) is 0.7359 ± 0.0044. The results show that the simulated optical depths are indeed independent of the wavelength.

---

[3] `https://cloudatlas.wmo.int`

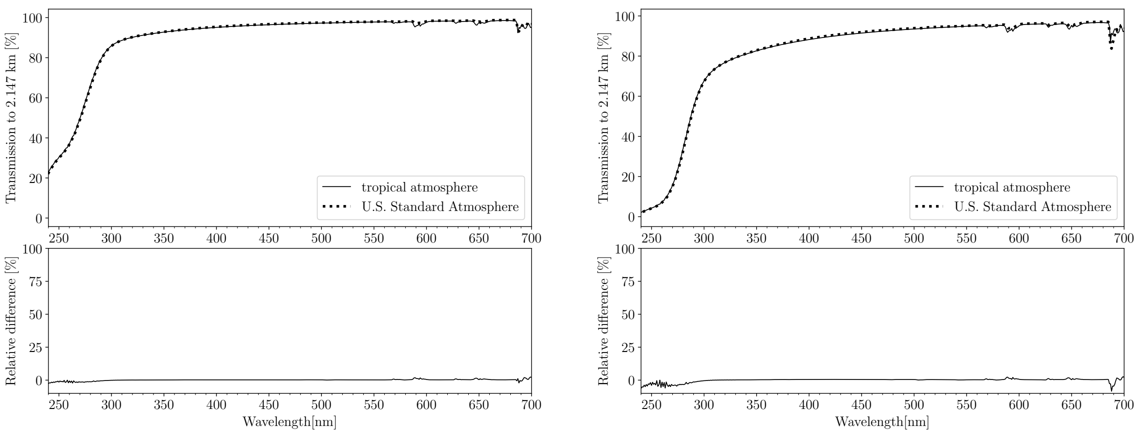

(a) 3 km a.g.l. **(b)** 5 km a.g.l.

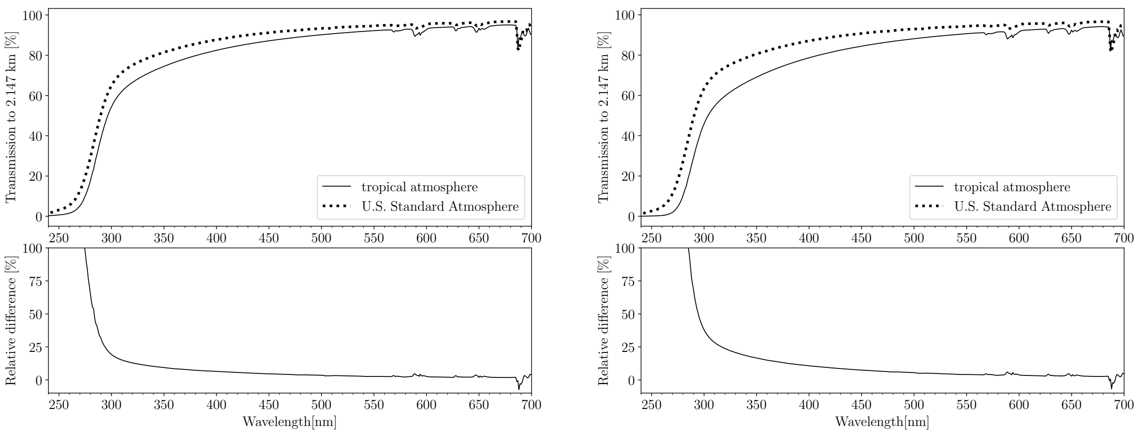

(c) 7 km a.g.l. **(d)** 9 km a.g.l.

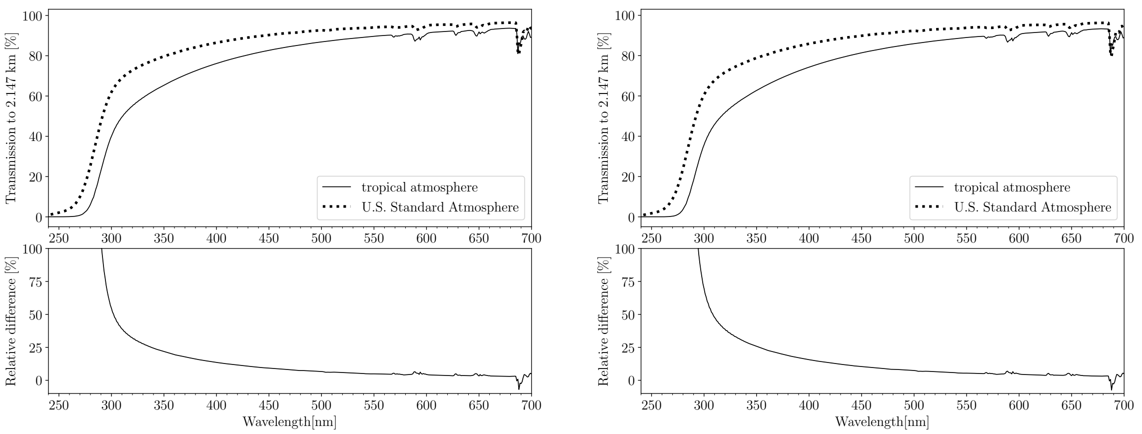

(e) 11 km a.g.l. **(f)** 13 km a.g.l.

Figure 2.11: Transmission from height h to ground level (2.147 km a.s.l.) for the base atmospheric profile used in this study (U.S. Standard Atmosphere) and the standard atmospheric profile for CTAO-N used in `sim_telarray` (tropical atmosphere) and the relative differences between them.

CHAPTER 3

Monte Carlo simulations

Monte Carlo (MC) simulations are computational algorithms based on a large number of repeated random virtual experiments to obtain a representative sample of possible outcomes, driven by the means of random number generators. MC simulations have many applications in various fields, including economics, physics and engineering. In the field of astrophysics, they hold a pivotal role, particularly in evaluating the performance of different telescope arrays, in considering the effects of geographic location and climate on telescope efficiency, and in analyzing observational data. In the IACT experiments, the calibration and optimization of the detector rely on the MC simulations, which are usually performed in two steps. The first step is common to all IACT experiments and consists of simulations of the development of extensive air showers and the emission of Cherenkov light. The second step involves simulations of the detector, including detailed telescope properties, the extinction of Cherenkov light in the atmosphere, optical ray tracing and signal digitization. Due to the inherent stochasticity of the processes involved, MC simulations are particularly well suited for IACT simulations. As there is no specific test beam for IACTs, these simulations are also an indispensable resource.

3.1 Simulations of extensive air showers

The simulations of extensive air showers are based on the computer code named COsmic Ray SImulations for KAscade[1] (CORSIKA) (Heck et al., 1998; Bernlöhr, 2008), a standard MC tool of the IACT community originally developed for the KASCADE experiment. Before starting the simulations, it is necessary to define a set of input parameters that determine the nature of the simulations, such as the type of primary particle, the primary energy, the incoming zenith and azimuth angles, etc. In CORSIKA, which is governed by the means of input cards, several dozen types of elementary particles are available. All particles are tracked through the atmosphere, undergoing interactions, annihilation or decay processes. The height and target nucleus of the first interaction are chosen at random. For this purpose, CORSIKA uses RANMAR (James, 1990), a pseudo-random number generator that provides uniformly distributed numbers. The primary particle energy (direction) can be predefined or randomly selected in a defined energy (angular) range. CORSIKA uses a Cartesian coordinate system with the positive x-axis pointing to magnetic

---

[1] `https://www.iap.kit.edu/corsika/`

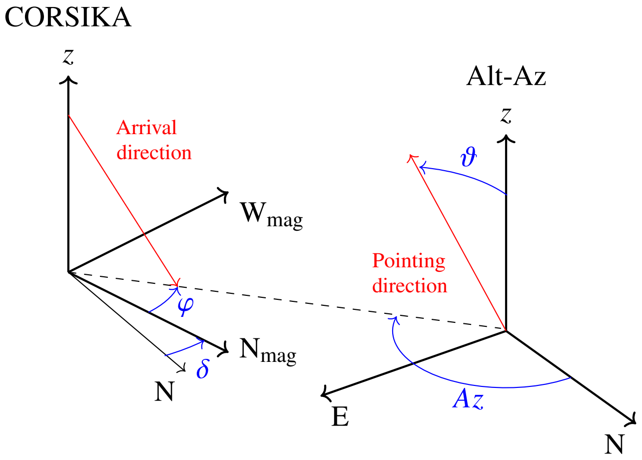

Figure 3.1: Relationship between the CORSIKA coordinate system and the horizontal coordinate system (i.e. the local IACT pointing direction coordinates). The horizontal coordinate system is defined by two angles, altitude Alt and azimuth Az. Therefore, the horizontal coordinate system is sometimes called the alt-az system. The altitude is the angle between the object in the sky and the horizon, although usually the zenith distance ϑ is used instead of an altitude: $\vartheta = 90° - Alt$. The relationship between the pointing azimuth Az and the azimuth φ in the CORSIKA coordinates is given by $\varphi = 180° - Az + \delta$, where δ is the magnetic declination, i.e. the angle between magnetic north and geographic north.

north, the positive y-axis pointing to the west and the z-axis pointing upwards (Figure 3.1). The z-axis corresponds to the position of the shower core on the ground. The origin of the coordinate system is at sea level. The zenith angle of a particle trajectory is measured between the particle momentum vector and the negative z-axis, while the azimuth angle is defined counterclockwise with respect to the north. The simulation environment of the selected site is defined by the density profile of the atmosphere and the strength and orientation of the geomagnetic field. The deflection of charged particles in the geomagnetic field is also calculated.

The distance a particle travels before two subsequent interactions or decays is determined by the cross-section for a hadronic interaction, the distribution of atmospheric constituents along the path, and the probability of decay. The probability P_{int} to traverse a layer with thickness χ without interaction is:

$$P_{\text{int}}(\chi) = \lambda_{\text{int}}^{-1} \cdot e^{-\chi/\lambda_{\text{int}}}, \tag{3.1}$$

where

$$\chi = -\ln(\texttt{RNDM} \cdot \lambda_{\text{int}}) \tag{3.2}$$

is a thickness of traversed matter, with random number $0 < \texttt{RNDM} < 1$, and λ_{int} the mean free path defined as:

$$\lambda_{\text{int}} = \frac{\sum_{i=1}^{3} n_i \cdot A_i}{\sum_{i=1}^{3} n_i \cdot \sigma_{\text{int}}}, \tag{3.3}$$

where A_i is the atomic weight of component i, σ_{int} energy dependent inelastic cross-section of component i, and n_i the atomic fractions of component i of air (i.e., fractions of N_2, O_2, Ar). The probability P_d to traverse a path l without decay is:

$$P_\mathrm{d}(l) = l_\mathrm{d}^{-1} \cdot e^{-l/l_\mathrm{d}}, \tag{3.4}$$

where $l = -\ln(\mathtt{RNDM} \cdot l_\mathrm{d})$ is a traversed path and $l_\mathrm{d} = c \cdot \tau \cdot \beta \cdot \gamma$ is the mean free path, where c is the speed of light in vacuum, τ is the particle lifetime in the rest, β is particle velocity in units of c, and γ is the Lorentz factor. For unstable particles, the two processes compete. Whether an unstable particle will decay or interact depends on the decay length and an interaction length, where the smaller one is considered. Electromagnetic and hadronic interactions are treated in CORSIKA with several interaction models, which were developed independently of CORSIKA. The entire process of simulation can be summarized in four steps:

1. particle tracking, energy losses by ionization, particles scattering, deflection, and decay,
2. simulation of high-energy hadronic interactions,
3. simulation of low-energy hadronic interaction,
4. propagation and interaction of the electromagnetic components of the shower.

The CPU and memory requirements of CORSIKA depend strongly on the type of primary particle and the number of simulated showers. For low-energy gamma-ray simulations (≈ 100 GeV), the computation of several hundred thousand showers can be completed within a few days using a single CPU. However, for high-energy events (several hundred TeV), the simulations take much longer, mainly because of the larger number of secondary particles and the resulting interactions. Hadron-induced showers require even more time due to their more complicated nature. The chart flow of processes in CORSIKA is shown in Figure 3.2 on page 65.

3.1.1 Electromagnetic interaction models

The electromagnetic interactions are treated with two different models. The **Electron Gamma Shower system version 4 (EGS4)** (Nelson, Hirayama and Rogers, 1985; Bielajew et al., 1994) is the MC simulation package for the treatment of electromagnetic interactions in an arbitrary geometry for electrons and photons with energies above a few keV up to several TeV. The EGS4 code takes into account many physical processes such as bremsstrahlung, electron-positron annihilation, Moliere multiple scattering, pair production, photoelectric effect, Compton scattering, etc. Photoproduction of muon pairs and the photo-nuclear reaction with protons and neutrons from atmospheric nuclei are also included. Alternatively, one can use the analytical **Nishimura-Kamata-Greisen model**, a faster but less accurate method that provides only a total number of secondary particles at different atmospheric depths. The former model was used in this thesis.

3.1.2 Hadronic interaction models

The hadronic interactions depend on the energy of the particle variable along the trajectory. The low-energy hadronic interaction models are considered at energies $\lesssim$ 80 GeV:

- Gamma-Hadron-Electron-Interaction SHower code (GHEISHA) (Fesefeldt, 1985) - hadronic collisions up to 100 GeV comprising elastic and inelastic interactions and include slow neutron capture processes,

- FLUctuating KAscade (FLUKA) (Ferrari et al., 2005) - interaction and propagation in the matter for different particles, including photons and electrons from 1 keV to thousands of TeV, neutrinos, muon, hadrons of energies up to 20 TeV, corresponding antiparticles, etc.,
- Ultra-relativistic Quantum Molecular Dynamics (UrQMD) (Bass, 1998) - microscopic many body approach for low-energy hadron-nucleus and nucleus-nucleus interaction.

According to Drescher et al. (2004), the combination of GHEISHA with CORSIKA yields discrepancies in reproducing measured data, while FLUKA is exclusively available as a compiled binary with a restrictive licensing policy. High-energy hadronic interaction models are more numerous (Heck et al., 1998), most of which are used: Quark Gluon String model with JETs (QGSJET) (Ostapchenko, 2006), Very Energetic NUclear Scattering (VENUS) (Werner, 1993), and Dual Parton Model with JETs (DPMJET) (Ranft, 1995). All models provide hadronic and nuclear collisions based on the Gribov-Regge theory, as multiple scattering processes, where individual scattering contributions are described phenomenologically as Pomeron exchanges. The main difference between models is in the details of realization of MC simulations. For a detailed explanation of the mentioned models, the reader is referred to appropriate references. In this thesis, QGSJET-II-04 and UrQMD models were used as standard procedures for the CTA simulations.

3.1.3 IACT/ATMO package

The CORSIKA subroutine named CERENKOV is responsible for simulating the production of Cherenkov light by electrons, positrons, muons, and charged hadrons. Together with the IACT/ATMO package[2], it enables the realistic simulation of non-horizontal IACT arrays, offers the capability to utilize tabulated atmospheric profiles and provides a flexible interface for configuring IACTs in various arrangements. To optimize computational efficiency, Cherenkov photons are simulated in bunches rather than individually. Therefore, the package also incorporates a customized, machine-independent output format for storing photon bunches - `eventio` (Bernlöhr, 2014a).

The array is defined by the (x_i, y_i, z_i) position of the telescope centers and the radii r_i of the spheres surrounding the telescopes, while the observation plane is divided into grid cells. A shower can be reused multiple times by randomly changing the impact point with respect to the nominal shower core. Each sphere is associated with one or more grid cells, as shown in Figure 3.3. In this way, only the spheres connected to the grid cell hit by the photon bunch are checked for possible overlap, reducing computation time. To reduce the memory requirements for a large number of photon bunches, the number of photon bunches is reduced while increasing the number of photons in the remaining bunches. For each event, the following parameters are stored upon completion of this phase: Type and energy of the primary particle, a list of Cherenkov photons with their respective positions, wavelengths, incidence angles, emission heights, arrival times (measured from the entry of the primary particle into the atmosphere), and bunch sizes.

---

[2] `https://www.mpi-hd.mpg.de/hfm/~bernlohr/iact-atmo/`

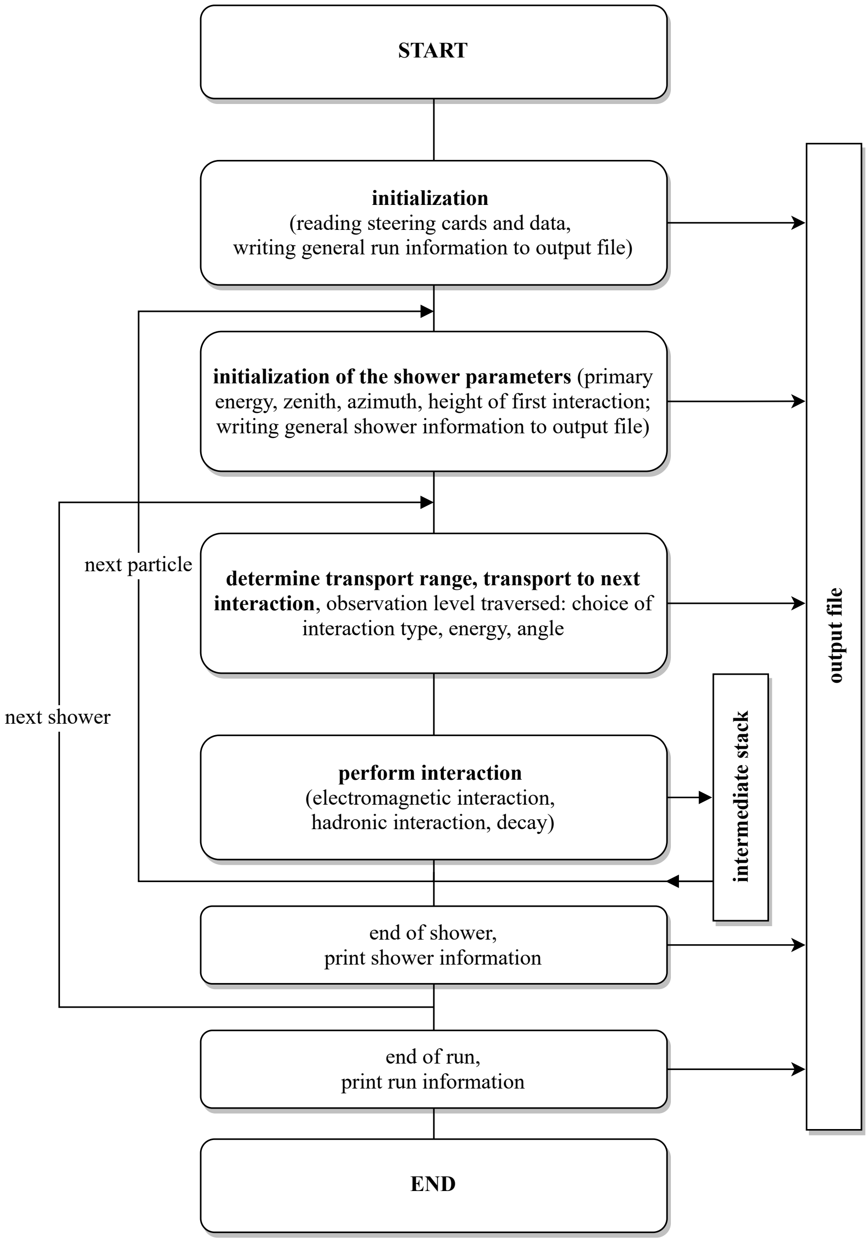

Figure 3.2: Simplified flow of processes in CORSIKA code for simulations of extensive air showers according to Heck and Pierog (2012).

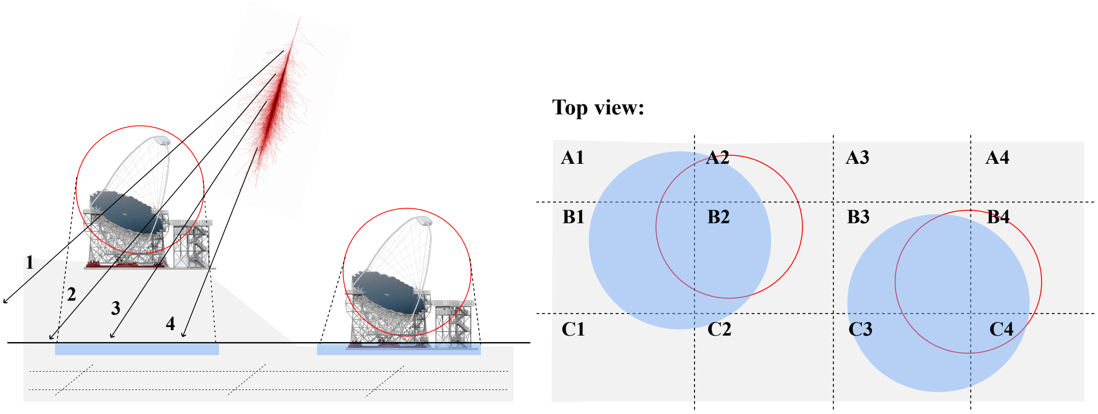

Figure 3.3: Definition of the grid cells as used in the IACT/ATMO package. Photon bunch (1) is not detected because it does not intersect a shadow grid cell, while photon bunch (4) is not detected because it does not intersect the sphere. Photon bunch (2) is not in the shadow (blue color), but it is detected because it hits the shadow grid cell and intersects the sphere. Photon bunch (3) is both in the shadow and intersects the sphere, so it is also detected. The horizontal solid black line denotes the CORSIKA observation plane.

3.2 Simulations of the detector

The `sim_telarray` (Bernlöhr, 2008) is a telescope simulation package originally developed for the High-Energy Gamma-Ray Astronomy (HEGRA) experiment. Although it was hard-wired at the beginning, the package is now fully configurable, allowing the configuration of the properties of each telescope, such as the arrangement of the mirrors, the characteristics of the cameras, the triggering scheme, the method of signal recording and digitization, etc. Therefore, different telescope systems can be simulated if appropriate configuration files are provided. With the `multipipe_corsika` option, the same CORSIKA output can be directed to multiple `sim_telarray` configurations (e.g. different arrangements of telescopes or different atmospheric conditions).

The optical system of the telescope is defined by a table of mirror positions (x_i, y_i) perpendicular to the optical axis, optional z_i positions, size and shape of the tiles, the total focal length, and the focal length of each mirror tile. Since checking the intersection of the incoming photon with each mirror tile would be very time-consuming, a grid scheme along the dish is used. Each mirror is associated with one or more grid cells. The detailed intersection is evaluated only for the mirrors associated with a particular grid cell. The camera and the trigger are defined by the properties of the pixels, the camera rotation, the pixel positions before rotation, and the trigger topology. The definition of a pixel includes its geometric shape, size, position in the camera body, depth of light-collecting elements, and their reflectivity or angular acceptance. Optionally, shading by the supporting structure of the camera can be simulated, while shading by the camera is explicitly included. The angular acceptance of the pixels is evaluated directly by checking which pixels are hit at the base of the Winston cone (assuming an efficiency of 100% when the photon hits the cathode directly), or given in tabular form. In the latter case, the efficiencies are given as a function of the angle of incidence without distinguishing between direct and reflected hits on the cathode.

The photon detection probability ε depends on the atmospheric transmission $T(\lambda)$, shadowing factor S by the camera and its support structure, the mirror reflectivity $R(\lambda)$, the efficiency $E(\lambda)$

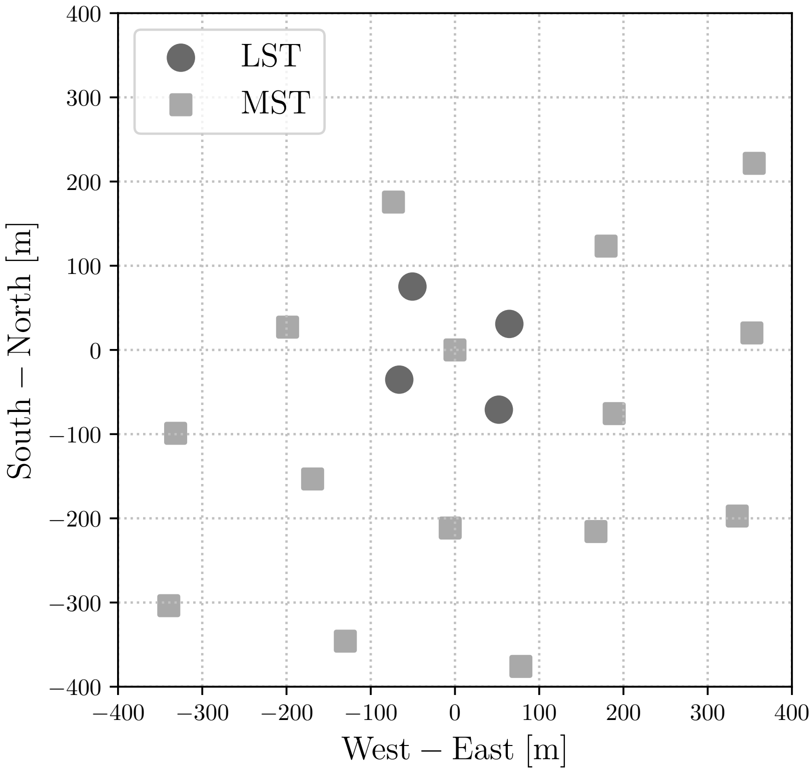

Figure 3.4: The simulated telescope array consists of 4 LSTs and 15 MSTs, the so-called *Omega configuration*. The positions of the telescopes are as specified in the Prod3 settings.

of the light concentrator, the quantum efficiency $Q(\lambda)$ of the photo-cathode and the collection efficiency $C(\lambda)$ of the photo-multiplication tube:

$$\varepsilon = T(\lambda) \cdot S \cdot R(\lambda) \cdot E(\lambda) \cdot Q(\lambda) \cdot C(\lambda). \tag{3.5}$$

The final step in the simulation is the multi-level triggering scheme. Each telescope produces a trigger signal based on the pixel signals in the telescope camera. The `sim_telarray` software supports different triggering schemes such as analog sum trigger, digital sum trigger, and majority trigger. Then the system trigger combines the triggers from individual telescopes, and if at least two telescopes are triggered within a short time window, the event is processed further. The output files of `sim_telarray` contain the waveform for each event and each pixel, along with all the information needed for signal extraction and calibration, resembling the raw telescope data. Note that the detector response simulations require only a small fraction of the total CPU and memory requirements compared to the air shower simulations.

3.3 Details of the simulations

For the purposes of this work, the development of air showers and detector response were simulated for the array of 4 LSTs and 15 MSTs (CTAO-N, 2147 m a.s.l., Figure 3.4). Extensive air showers

	gamma (on-axis)	**proton**	**electron**
ERANGE (TeV)	0.003 - 330	0.003 - 600	0.004 - 600
spectral index	−2	−2	−2
NSHOW	$2{\cdot}10^8$	$4{\cdot}10^9$	$2{\cdot}10^8$
VIEWCONE (°)	0	0 - 10	0 - 10
NSCAT	10	20	20
CSCAT ($R_{\max}$, m)	1400	1900	1900

Table 3.1: Basic CORSIKA parameters: energy range; spectral index, number of simulated air showers, the direction of a primary particle from a cone around a pointing zenith and azimuth angle, the number of reuses of the same air shower, the maximum simulated impact from the center of the array.

induced by gamma rays, protons, and electrons arriving from a fixed angle of 20° in zenith and 180° in azimuth (measured in the CORSIKA coordinate system) were simulated. Proton-induced and electron-induced air showers were simulated arriving from a cone with a half-opening angle of 10° around the zenith and azimuth angles mentioned above, while gamma-ray showers were simulated at the center of the camera. The energies of the simulated events are derived from a power-law distribution characterized by a spectral index Γ in the energy range $[E_{\min}, E_{\max}]$. The impact parameter is chosen so that the events are uniformly contained within a circle of radius $R_{\max}$, while Cherenkov light was simulated in the wavelength range from 240 nm to 700 nm. Prod3[3] `sim_telarray` technical description was used. More than 700 TB raw data were produced using the Bura supercomputer, a SLURM[4] cluster at the Center for Advance Computing and Modeling[5] at the University of Rijeka. More details on the simulations are given in Table 3.1.

---

[3] `https://www.mpi-hd.mpg.de/hfm/CTA/MC/Prod3/`

[4] `https://slurm.schedmd.com/overview.html`

[5] `https://cnrm.uniri.hr`

CHAPTER 4

Effects of clouds on the reconstruction of gamma-ray-induced air showers with CTA

This chapter provides a comprehensive overview of the results of the analysis aimed at investigating the influence of clouds on the arrival direction and energy reconstruction of gamma-ray events detected by CTAO-N and its corresponding subarrays. The effects of various cloud parameters, such as height and optical depth (transmission), are used to quantify their influence on the bias and uncertainty of the reconstructed gamma-ray energy and direction. The results provide valuable insight into the potential optimization of CTA observations under different atmospheric conditions and demonstrate the importance of considering the effects of clouds in the development and operation of CTA.

4.1 Overview of data analysis chain

Simulated data (see Chapter 3 for details) were analyzed using MAGIC Analysis and Reconstruction Software (MARS) (Moralejo et al., 2009; Zanin, 2013), a ROOT-based code written in C++ adapted for CTA use and dedicated MARS-based software Convert Hessio Into Mars inPut (CHIMP), forming the CHIMP/MARS analysis chain (Sitarek et al., 2018). The MARS data analysis chain is designed as a series of sequential steps, each executed by a different program. Data is passed from one step to the next, with each program receiving input from the output of the previous step(s). The data are structured in ROOT trees (e.g. `RunHeaders` tree containing the information about observational (sub)runs or MC simulation runs, or `Events` tree containing information for each event), where each entry consists of the parameter containers (e.g. `MStereoShowerPar`). The core functionality of any MARS program is a loop that processes a list of ordered tasks for each event in the input file. The loop is paired with a parameter list that contains pointers to the parameter containers with the input data required by the tasks. The results of the calculations are also stored in the corresponding containers. The software includes tools for data visualization, quality control and statistical analysis.

4.1.1 Signal extraction and calibration

The output of `sim_telarray` contains the waveform of the signal for each event and each pixel in the camera, just like the real data observed during the night. The signal extraction is done with

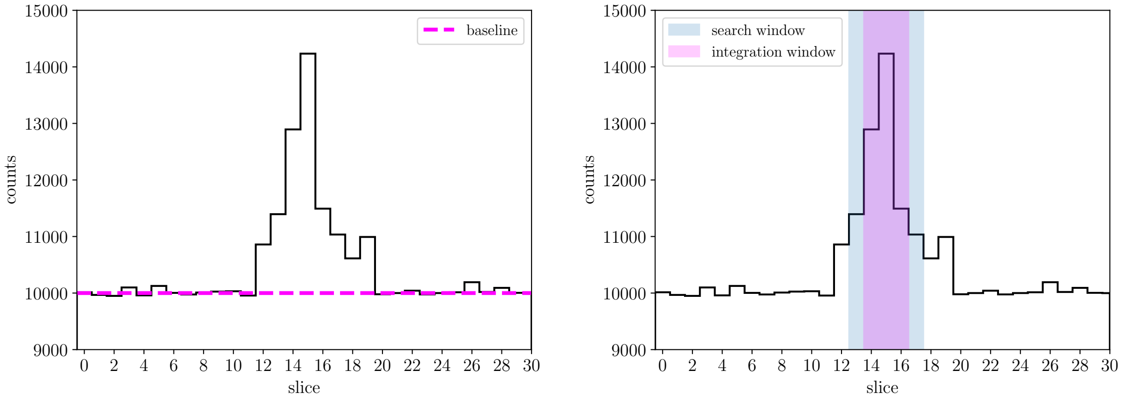

(a) **(b)**

Figure 4.1: a) The baseline of a signal (pedestal value) refers to the level of noise or background signal recorded by the detector when the sensor is not receiving a Cherenkov photon. b) The integration window is moved over the waveform and the signal charge (in readout counts) is calculated as the largest sum of three consecutive slices in the fixed readout window of 3 ns.

CHIMP which integrates the waveforms using a pixel-wise peak-search algorithm. The waveform is a signal binned in time slices (sampled at a frequency of 1 Gsamples s^{-1}). To obtain an accurate value of the signal charge, the pedestal value, i.e. the baseline of the waveform, is evaluated (Figure 4.1a). Pedestal events are events with random triggers without a pulse that are recorded at the beginning and during data acquisition. The pedestal value is calculated as the mean value of a Gaussian fit to the histogram (which includes all time slices) and is already subtracted from the waveform by `sim_telarray`. This procedure reduces the signal in each pixel to two numbers: the charge (in photoelectrons) and the arrival time (in nanoseconds).

CHIMP performs a two-pass signal extraction for each triggered telescope, using a sliding window algorithm for the first pass and a fixed window extractor for the second pass (Albert et al., 2008a). In the first pass, the algorithm searches for the maximum sum of three consecutive time slices in a fixed readout window (3 ns) over the entire range of readout slices for each pixel. After the maximum sum of three consecutive time slices has been determined, two additional samples, one on each side of the readout window, are summed to obtain the total pixel charge (Figure 4.1b). In the second pass, a time gradient along the major axis is calculated on the preliminary cleaned image (section 4.1.2). In this step, the signal is searched in non-significant pixels (all pixels except the core pixels of the main island of the preliminary image) in a reduced time window (again 5 samples) resulting from the time fit. If the predicted time for a pixel is outside the readout window, the first or last five samples are integrated, recovering some weaker signals around the main island. The image obtained after integrating the waveform in the second pass is cleaned again, using final cleaning cuts (Table 4.1) and finally parameterized to the Hillas parameters (Hillas, 1985).

The factor for the conversion of the integrated readout counts into photoelectrons is calculated directly by `sim_telarray`. The mean arrival time in the readout samples is determined as the average of the slice time weighted by the readout counts. Note that the integration of five samples in CHIMP does not include the pulse tails, while the `sim_telarray` conversion factor is determined for the total waveform integration. Therefore, the number of photoelectrons calculated with CHIMP

	preliminary cleaning		**final cleaning**	
	Q_c (phe)	Q_b (phe)	Q_c (phe)	Q_b (phe)
LST	6	3	4	2
MST	8	4	4	2

Table 4.1: Boundary pixels (Q_b) and core pixels (Q_c) cleaning thresholds expressed in photoelectrons (phe). In the second pass of signal extraction, a preliminary cleaning is performed to recover some weak signals. After the final cleaning, the surviving pixels are used to parameterize the image.

is underestimated. However, this does not lead to systematic errors because the entire sample is processed in the same way.

4.1.2 Image cleaning and parametrization

The image cleaning is performed to suppress background data, i.e., the signal from pixels dominated by NSB, stars in FoV, or electronic noise. The standard cleaning algorithm is the two-level absolute image cleaning (Shayduk et al., 2005; Aliu et al., 2008). In this method, pixels are distinguished based on their charges and divided into two groups: *core pixels* and *boundary pixels*. A core pixel is a pixel with a charge above a certain threshold Q_c and at least one neighboring pixel that also meets this threshold. The boundary pixels are the pixels with a charge above the threshold Q_b and at least one neighboring core pixel. All pixels that are not marked as core or boundary pixels are excluded, i.e., their charge is set to zero. The thresholds for core and boundary pixels used in the final cleaning are 4 and 2 for LSTs and MSTs, respectively, but the thresholds can be changed depending on the conditions during the observations, e.g., the degree of NSB.

After image cleaning, the distribution of surviving pixels in the Cherenkov camera is parameterized with the Hillas parameters (Hillas, 1985) (with a minimum of three surviving pixels). The basic idea of this method is to fit a two-dimensional Gaussian distribution to the remaining pixels and derive the parameters from the moments (up to third order) of the charge distribution in the pixels (Figure 4.2). The image parameters are an important key for the analysis. They play an important role in distinguishing between hadronic and gamma-ray events, but also in reconstructing the energy and direction of arrival of the primary particle. Air showers triggered by gamma rays typically produce elliptical images in the camera, while hadronic showers typically result in more chaotic patterns, with sub-showers forming distinct islands in the camera image.

Main parameters:

- *size*: the total charge (in photoelectrons) contained in the shower image. If the event is contained in the Cherenkov light pool with a radius of ≈ 140 m, the number of photoelectrons is roughly proportional to the energy of the primary particle.
- *length*: the length (in millimeters)[1] of the major semi-axis of the ellipse. The longitudinal development is encoded along the major axis of the image and can therefore be used to

---

[1] Other units of length may be used in different analysis chains.

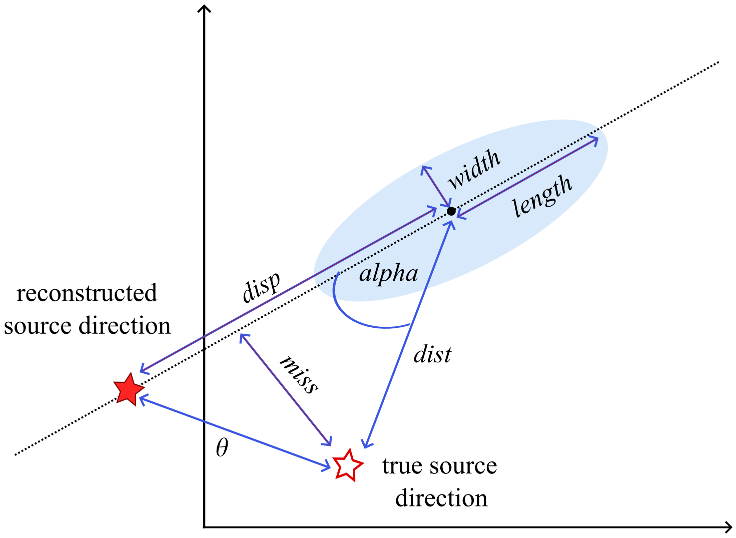

Figure 4.2: Basic Hillas parameters. The origin of the coordinate system is the center of the camera.

distinguish the type of the primary. It can be defined as the standard deviation of the distribution of photoelectrons along the major axis of the image.

- *width*: the length (in millimeters) of the minor semi-axis of the ellipse. The *width* is a measure of the lateral development of the shower and can therefore be used to distinguish the type of primary particle (hadronic showers have greater lateral development). It can be defined as the standard deviation of the distribution of photoelectrons along the minor axis of the image.
- *conc-N*: the proportion of the number of photoelectrons contained in the N brightest pixels, i.e. the ratio of the number of photoelectrons in the N brightest pixels to *size*. This parameter gives information about the core of the shower, i.e. the compactness of the image, which is more compact for electromagnetic showers than for hadronic showers. Normally, $N = 2$.
- $\langle X\rangle$, $\langle Y\rangle$: the position (in millimeters) of the X and Y coordinates of the image center of gravity (CoG) (i.e. the center of the ellipse) measured with respect to the origin of the coordinate system. The cut on the image CoG position aims to remove the showers with high leakage from further analysis.

Source-dependent parameters:

- *dist*: the angular distance (in degrees) between the true position of the source and CoG of the image. It describes the angle between the direction of the source and the maximum of the shower. *dist* depends on the energy, the impact parameter, and the zenith angle.
- *disp*: the angular distance (in degrees) between the reconstructed position of the source and COG of the image.
- *alpha*: the angle (in degrees) between the major axis of the ellipse and the line connecting the CoG of the image and the position of the source. In monoscopic observations, the *alpha*

plays an important role in gamma-hadron separation, since gamma-triggered showers should point to the camera center and therefore have a smaller *alpha* value.

- *miss*: the angular distance (in degrees) between the image axis and the point in the camera corresponding to the true gamma-ray direction.

Time-dependent parameters:

- *Time Gradient*: describes the rate of change of the arrival time along the major axis of the ellipse. The pixel coordinates are projected along the major axis to reduce the problem to one dimension. The linear function is fitted to the arrival time t as a function of the spatial coordinate x, $t = m \cdot x + q$. The slope of the line m is the measure of the *time gradient*.
- *Time RMS*: the standard deviation of the arrival time of the surviving pixels. This parameter is smaller for gamma-initiated showers compared to hadron-initiated showers (it takes less than 3 ns for the electromagnetic shower to develop and about 10 ns for the hadronic shower).

Directional parameters:

- *M3Long*: the third moment of charge distribution along the major axis of the ellipse. This parameter is useful to determine the head-tail distinction of the shower - the head of the image should have a higher charge concentration than the tail, i.e. the value should be positive when the head of the shower is closer to the center of the camera.
- *asymmetry*: the direction of the line between the CoG of the image and the pixel with the highest charge.

Image quality estimation parameters:

- *leakageN*: the proportion of the number of photoelectrons contained in the N (usually one or two) outermost camera rings. This parameter is used to estimate the loss of signal, since in very energetic and high impact parameter showers not the whole event may be contained in the camera.
- *number of islands*: the number of surviving isolated pixel groups after image cleaning has been performed. In general, hadronic showers have a large number of different islands in the camera, and an electromagnetic shower has only one island.

Stereoscopic parameters:

- *impact* parameter - distance (in centimeters) between the shower axis and the telescope position,
- *Cherenkov radius* - Radius of the Cherenkov light pool on the ground produced by an electron with the critical bremsstrahlung energy of 86 MeV at the maximum height of the shower,

- *Cherenkov photon density* - density (in grams per square centimeter) of the Cherenkov light pool on the ground produced by an electron with the critical bremsstrahlung energy of 86 MeV at the height of the shower maximum,
- *multiplicity* - the number of telescopes used in the directional reconstruction,
- θ - the angular separation (in degrees) between the reconstructed source position and the actual source position.

The stereoscopic technique for observing air showers involves the simultaneous observation of the same source with several telescopes all pointing in the same direction. Each point in the camera corresponds to a direction in the sky. In the small angle approximation, which applies to IACTs with a relatively small FoV, a line on a camera corresponds to a plane. Thus, the shower image major axis corresponds to a plane containing the shower axis and the telescope. The use of two or more telescopes enables a three-dimensional representation of the shower. All stereoscopic parameters are calculated for each event, except for the *impact* parameter, which is calculated for each telescope. The stereoscopic reconstruction (section 4.1.3) is an important part of the analysis as it provides a three-dimensional description of the event, i.e. parameters necessary for the reconstruction of energy and direction.

4.1.3 Reconstruction of the arrival direction

Rather than using all the triggered telescopes to characterize an event, a number of quality cuts are made to avoid the use of poorly reconstructed showers, which greatly improves the analysis. To be used for the stereoscopic reconstruction of events (the event-by-event characterization of the shower, i.e. from the images collected by all the telescopes triggered), the image taken by the telescope must meet the following requirements:

- *size* of at least 50 photoelectrons,
- images with poorly defined axes or with poor axis alignment within the true direction are kept based on the ratio between *width* and *length* of the image: $0.1 < width/length < 0.6$; the upper cut aims to exclude roundish images with poorly defined axes. The lower cut aims to exclude hadron-induced images with extremely high impact parameters or, for example, events where there are two distinctive, but small and close islands fitted as a single island, i.e. with one set of Hillas parameters,
- the distance between the image CoG and the camera center is less than 80% of the camera radius (2.31° for the LST camera and 4.05° for the MST NectarCam),
- at least 10 events in the corresponding bin of the lookup table (see next paragraph for details),
- the *impact* must be smaller than 200 meters to avoid charge losses due to photons arriving after the end of the readout window.

Direction Lookup Tables The primary gamma-ray direction is calculated using the lookup tables (LUTs). The directional LUTs (DirLUTs) are two-dimensional histograms filled with the square of the mean *miss* in bins of *size* and *width*/*length*. In this way, for certain values of *size*, *length* and *width*, it is possible to estimate how well the image axis matches the true gamma-ray direction in

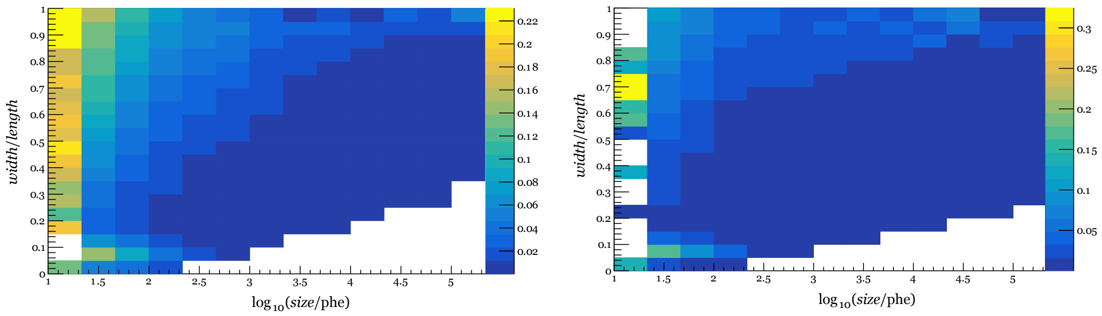

(a) LSTs **(b)** MSTs

Figure 4.3: Directional Lookup Tables. The color bars represent the values of the squares of the mean *miss*, i.e. the quantities used as weights in the reconstruction of the direction.

the camera. In the stereoscopic reconstruction of the events with at least three valid images, the values stored in the DirLUTs are used to set relative weights for different telescopes.

Reconstruction of the shower core The shower core is the (x, y) position where the shower axis intersects the horizontal plane $z = 0$ (i.e. the ground plane). It is sometimes called the impact point and is defined as the point in the ground intersected by the shower axis (corresponding to the center of the Cherenkov light pool). First, for each telescope, the intersection of the plane $z = 0$ with the plane formed by the image axis and the optical axis of the telescope is defined. In the case of two telescopes, the core position is simply the intersection of the two such lines (Figure 4.4a). In the case of three or more telescopes, a minimization is performed, similar to the direction reconstruction (see lower paragraphs), but without weights.

Reconstruction of the height of the shower maximum The maximum height of the shower, H_{max}, is the altitude (a.g.l.) at which the number of secondary particles in the shower is maximum. For each telescope (i.e. image), the line between the mirror center and the CoG of the camera image is defined. Each of these lines intersects the horizontal plane at height z (Figure 4.4a). Finding the (x, y) coordinates of these intersections, and taking z as a free parameter, one can perform minimization to obtain the value $z = H_{\text{max}}$. The value $z = H_{\text{max}}$ is the one that minimizes the dispersion of N points in the plane, and it is measured relative to the plane of the observatory $(z = 0)$:

$$H_{\text{max}} = \sum_{i=1}^{N} \left((x_i - \overline{x})^2 + (y_i - \overline{y})^2 \right). \tag{4.1}$$

The maximum height of the shower depends on the energy of the primary particle - the higher the energy, the smaller H_{max}. At lower energies, this parameter can be very helpful in determining the primary particle type, as the distribution of H_{max} for hadronic showers has two peaks, the second of which is due to single muon events (Aleksić et al., 2012).

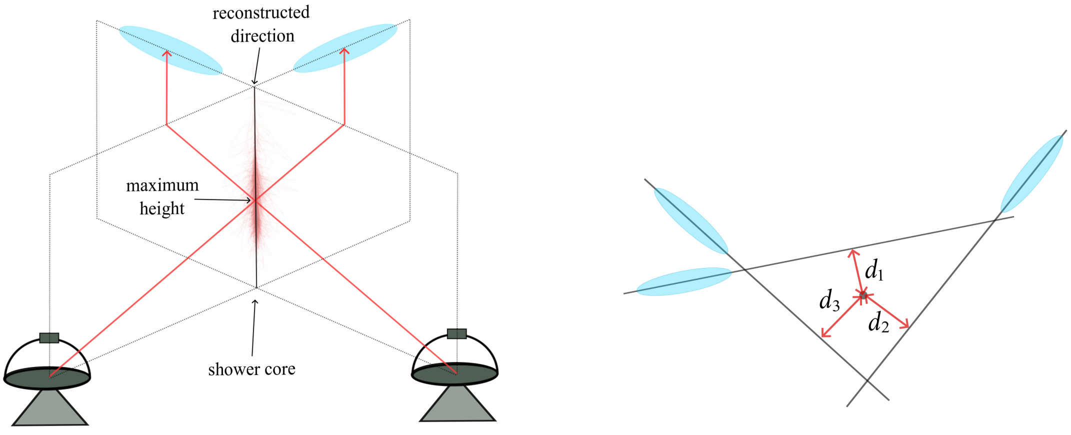

(a) **(b)**

Figure 4.4: The principle of reconstruction of: a) the shower core and the maximum height of the shower, b) the arrival direction.

Direction reconstruction In the case where only two images survive the selection cuts, the crossing point method is used. The orientation of the shower axis (source direction) is simply determined as the intersection of the major axis of the two images. This results from the fact that the shower axis points in the direction of the source. Since the image in the camera is a projection of the shower, the major axis of the image also represents the direction of the incidence of the shower in the camera plane. Each telescope observes the shower at a different position in the sky. However, the major axes of all telescope images must point in the direction of incidence, so that the intersection of the axes represents the direction of incidence of the primary signal that initiated the shower. This method cannot be used for monoscopic observations.

If there are $N > 2$ valid images, the direction is calculated as the point in the camera that minimizes the sum $\sum_{i=1}^{N} w_i \cdot d_i^2$, where d_i is the distance between the point and the major axis of the i-th image and w_i is the weight for the i-th image obtained from the DirLUTs (Figure 4.4b). The weight is the square of the mean *miss* parameter in the respective $(\frac{width}{length}, \log_{10} size)$ bin (Figure 4.3). The minimization is performed with Minuit (James and Roos, 1975).

4.1.4 Energy reconstruction

Random Forest In CTA data analysis using MARS, energy reconstruction is usually performed using the Random Forest (RF) algorithm (Albert et al., 2008b). However, energy reconstruction can also be performed with energy LUTs. Therefore, the latter is also described, although it was not used for the analysis of the data presented in this paper, as RF provides better energy resolution and lower energy bias (Ishio, 2020; Ishio and Paneque, 2022). RF is trained on the gamma-train subsample and created per telescope type. For each event and each valid image, the energy is calculated assuming that the image in the camera is from the gamma-initiated shower. The RF is trained in a similar way as the gamma-hadron separation (for details the reader is referred to section 4.1.5), with the difference in how the optimal cut is chosen in each node. The target value is the simulated energy: $\log_{10} E_{\mathrm{MC}}$.

The RF consists of 50 trees. In the training process, a single data sample is usually assigned. To create independent trees, a straightforward method is to divide the training sample into non-overlapping subsamples corresponding to the number of trees to be constructed. However, due to limited statistics in the training sample, an alternative approach is used. For each tree, a bootstrap sample is generated by iteratively sampling n samples from the original training sample, which consists of n events. The selection probability for an event in the sample is $1/n$, resulting in diverse bootstrap samples without the same events. This procedure ensures that the distributions of the image parameters for events in all bootstrap samples are statistically identical, reflecting those of the original training sample (Albert et al., 2008b). To construct a node, three randomly selected parameters are considered and the one with the smallest dispersion (i.e. the smallest variance) of the true energy is selected. The splitting is done when the final node content is 5 events. The output of RF is the estimated or reconstructed energy, E_{est}, and the standard deviation of the results of 50 trees. The final reconstructed energy is calculated as a weighted average of the E_{est} from all telescopes, using $1/\sigma^2$ as the weight, where σ is the standard deviation. The tree is fed with the following parameters:

- the shower maximum height, *impact*, *size*, *width*, *length*,
- *conc*-2, *leakage*1, $\frac{width \cdot length}{size}$, *dist*^{2},
- the angle between the positive x-axis and the line projected by the source position and the CoG: $\arctan^2(\langle Y\rangle - \mathrm{dir}_y, \langle X\rangle - \mathrm{dir}_x)$.

Energy Lookup Tables Energy reconstruction can also be performed using energy LUTs derived from MC simulations. Assuming that the energy of the primary particle is proportional to the number of Cherenkov photons in the shower and that most of the light produced by the primary gamma ray is contained in the Cherenkov pool of radius R_C, there must be proportionality between the energy and the *size* of the images. A two-dimensional histogram is produced, filled with the *size* per telescope in bins of *impact* and H_{max}. The LUTs also contain the corresponding standard deviations. The estimated energy, E_{est}, is the average of the corresponding E_{MC} for each image from all telescopes, weighted by $1/\sigma^2$, where σ is the standard deviation. Before applying LUT to the test sample, the *size* is corrected using empirical equations to establish a linear relationship between *size* and *energy*, including zenith correction, *leakage* correction and correction due to the influence of the geomagnetic field. The energy RF method improves the resolution by up to 50% over the entire energy range compared to LUTs (Hassan Collado, 2015), without significant impact on sensitivity or angular resolution.

4.1.5 Gamma-hadron separation

During observations, Cherenkov telescopes are triggered not only by Cherenkov photons produced in the electromagnetic cascades, but also by those produced in the showers triggered by hadrons or electrons, which are the main contributors to the background. Telescopes can also be triggered, for example, by fluctuations in the background light or by mouns (Gaug et al., 2013; Compagnino et al., 2022; Aab et al., 2015; Olivera-Nieto et al., 2021; Gámez et al., 2020). However, the signal fluctuations caused by the background light are well managed in the low-level analysis (image cleaning) and in the case of a muon event, the event is not processed because only one telescope is triggered. For this reason, a method was developed to distinguish between gamma-ray events and background events, whether they are hadrons or electrons.

Statistical learning methods, such as the Convolutional Neural Network or RF, are a powerful tools for suppressing hadronic background. In this work, the method to separate the background from the signal is based on RF (Albert et al., 2008b). The separation between the signal and the background is based on the distribution of a set of parameters with high discriminatory power between the gamma-ray events and the background events, without parameterizing the cuts. However, the technique of dynamic and scaled cuts has been developed. The result of the gamma-hadron separation procedure is a single number called *hadronness* with values between 0 and 1. The closer the value for *hadronness* is to 0, the more the event is gamma-like, and the closer the value for *hadronness* is to 1, the more the event is hadron-like. RF is trained with events of known nature, namely the gamma ray and proton train subsamples of the MC production (or, if the real data are available, with MC gamma-ray events and real hadronic background data). Each event is characterized by a vector whose components are strongly discriminating parameters used to construct 100 decision trees:

- the maximum height of the shower,
- $\log_{10} E_{\mathrm{est}}$, both the average of all telescopes and per telescope,
- $\log_{10}$ *size*, *width*, *length*, *conc*-2, *impact*.

The growth of the tree begins with the bootstrap sample contained in a single node, called the root node. In this node, three parameters are randomly selected and considered for a cut. Of the parameters considered, the one that best splits the sample is used. In this way, the starting sample is divided into two parts, called branches. The procedure is repeated iteratively until a node contains only one type of event. To estimate the classification power and optimize the cut values, the Gini index is used. The Gini index can be expressed in terms of the populations of the classes of nodes:

$$Q_{\mathrm{Gini}} = 4\frac{N_\gamma \cdot N_h}{N^2} = 4\frac{N_\gamma \cdot (N - N_\gamma)}{N^2}, \tag{4.2}$$

where N_γ is the number of gamma-like events in the node, N_h is the number of hadron-like events, and N is the total population in the node. The parameters that minimize the Gini index are used for the selection cut. The Gini index of the split is obtained by adding the Gini indices of the left (L) and right (R) successor nodes and scaling the result to $[0,1]$:

$$Q_{\mathrm{Gini}} = 2\left(\frac{N_{\gamma,L} \cdot N_{h,L}}{N_L^2} + \frac{N_{\gamma,R} \cdot N_{h,R}}{N_R^2}\right). \tag{4.3}$$

The RF is applied to the test sample, assigning *hadronness* value to each individual event. For each event, its parameter vector is processed through each tree until it reaches a final branch with a given *hadronness*. The final *hadronness* value, $h \in [0,1]$, is calculated as a weighted average of the

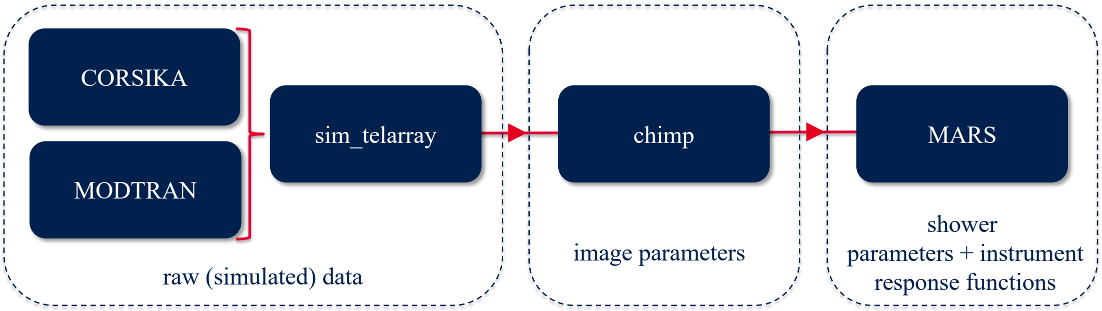

Figure 4.5: Simulation and analysis chain used in the study.

hadronness calculated by different telescopes:

$$h = \frac{\sum_{i=1}^{n} H_i \cdot size_i^{0.54}}{\sum_{i=1}^{n} size_i^{0.54}}, \tag{4.4}$$

where $H_i \in [0,1]$ is the mean *hadronness* per telescope averaged over all trees. The gamma-hadron separation method performs better at higher energies because the images are better defined. The gamma-ray efficiency is defined as the ratio of gamma-ray events that survived the selection cuts to the total number of simulated gamma-ray events:

$$\varepsilon = \frac{N_{\gamma}^{\mathrm{MC}}\ \text{(after cuts)}}{N_{\gamma}^{\mathrm{MC}}\ \text{(simulated)}}. \tag{4.5}$$

Once the information relevant to event characterization (direction, energy, *hadronness*, etc.) is available, selection cuts can be applied to select a particular subset of the data for subsequent higher-level analysis, e.g. the *hadronness* cut or the θ^2 cut, where θ is the angular distance between the true position of the source and the reconstructed arrival direction. The θ^2 cut results from the fact that gamma-ray events should be distributed near the source position, i.e. the signal should peak at zero and the background should be uniformly distributed.

The following two independent analyses were performed for each simulated data set:

1. in the first analysis, the RF algorithm used to estimate the energy and *hadronness* of the events and DirLUTs were trained on MC simulations assuming the same atmospheric conditions (the so-called *adaptive MC simulations*) as the observations (here the *observations* refer to the rest of the simulations that were not used for training, i.e. the test sample),
2. in the second analysis, the RFs and DirLUTs were trained on *standard MC simulations* (for cloudless atmospheric conditions).

The complete simulation and analysis chain is summarized in Figure 4.5.

4.2 Data sample

As described in the previous chapter, the data sample consists of simulations for 36 different transmission profiles, which differ in cloud height and transmission, and a clean atmosphere that serves as a reference model. For each case, the total number of simulated gamma-ray showers in CORSIKA is equal to $2 \cdot 10^9$. However, a small fraction of the simulations ($\lesssim 5\%$) is subject to various errors. Such simulations are neither completed nor saved in the output files.

A loose θ^2 cut of 0.2 deg^2 and a *hadronness* efficiency cut of 90% are applied to the data to exclude the events with poorly reconstructed arrival direction and consequently impact parameter and energy. These loose cuts provide sufficiently large statistics for the low transmission cases, even in the low energy bins. Since the focus at this stage is only on the performance of the energy and direction estimator and not on the significant detection of a signal, more strict cuts are not necessary. Therefore, for each energy bin, the optimal *hadronness* cut is the one where the fraction of surviving events is higher than the chosen efficiency, and only events with $\theta^2 < 0.2$ deg^2 are considered for further analysis. A *multiplicity* cut of 2 was also applied, which means that only events detected by at least two telescopes are stored and processed.

4.2.1 Detection efficiency

When considering the effects of clouds on the performance of IACTs, the most obvious effect is a reduction in the Cherenkov light yield and consequently an increase in the energy threshold. This reduction is caused by the loss of photons in the processes of scattering and absorption in clouds, resulting in a lower photon density in the light pool, which decreases the total charge in the camera or, even worse, is insufficient to trigger the telescope. In this way, the low-energy events that could potentially trigger the telescope under clear atmospheric conditions are no longer detectable. It is also possible that the detected events, although they triggered the telescopes, are subsequently rejected by the application of the *size* cut. Figure 4.6 shows, for example, the correlation between the *size* parameter of images taken by 4 LST telescopes in cloudless conditions and *size** of images taken in the presence of clouds for the same CORSIKA events. From here on, all altitudes are given in km a.g.l. unless otherwise stated. In the presence of low cloud cover, Cherenkov light emitted at different heights has an equal probability to be absorbed, and a systematic shift of *size** to lower values is visible across the entire range. For comparison, a *size* density plots for mid-level and high clouds are also given. In the case of clouds at intermediate heights, only the light emitted above the cloud is affected. On the other hand, high clouds affect only a small fraction of the emitted Cherenkov light and the change in the *size* parameter is minimal.

The total number of detected events (Figure 4.7) that survived all cuts and the gamma-ray detection efficiency as a function of cloud transmission and height are listed in Table 4.2. The data show that as the height and transmission of the cloud decrease, the number of detected events also decreases, resulting in a worse gamma-ray detection efficiency. Whether the event is detected or not depends on the relationship between the height of the shower maximum and the height of the cloud, or more precisely on the fraction of photons produced above the cloud that can be affected by the cloud (Figure 4.11). On the other hand, the height of the shower maximum is proportional to the gamma-ray energy, which means that the high-energy gamma-ray air showers reach their maximum

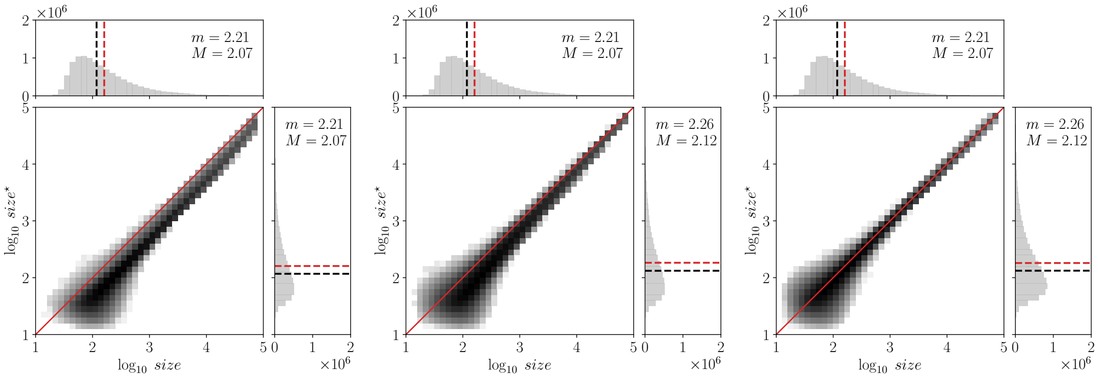

(a) $T = 0.5$, 3 km **(b)** $T = 0.5$, 7 km **(c)** $T = 0.5$, 13 km

Figure 4.6: Correlation of the parameter *size* of images taken in cloudless conditions and *size** of images taken in the presence of clouds with LSTs. The dashed red and black lines show the position of the mean and median of the distribution, respectively. Only events with the *impact* parameters ≤ 150 m detected by at least 2 LSTs are shown. No other cuts were applied. The horizontal and vertical one-dimensional histograms show $size$ distribution in the clear atmosphere and in the presence of clouds, respectively. Mean (m) and median (M) values are indicated.

deeper in the atmosphere. Thus, if the cloud is very high in the atmosphere, it affects only a very small fraction of the Cherenkov light produced by the secondary particles in the air shower, even in the case of low-energy gamma rays. The energy of the event is naturally underestimated if it is not corrected, but the event is detected.

The data show that gamma-ray detection efficiency decreases sharply with low and less transparent clouds, although there is no significant difference in the influence of clouds on the gamma-ray detection efficiency of the individual subarrays compared to CTAO-N Note, however, that the performance of MSTs is slightly better than that of LSTs for clouds at ≥ 7 km height. This is not unexpected given the relationship between the height of the shower maximum and gamma-ray energy: LSTs observe less energetic gamma rays for which the height of the shower maximum is in the upper layers of the atmosphere (compared to showers triggered by more energetic gamma rays observed by MSTs), and Cherenkov photons are more likely to be absorbed even by high clouds. In addition, MSTs have a wider FoV and may be able to detect the lowest part of the air shower that forms even below the lowest clouds simulated. Low clouds (≤ 5 km) reduce the efficiency of gamma-ray detection by up to a factor of 2 compared to the efficiency in the absence of clouds ($T = 1.00$). Mid-level clouds between 7 and 9 km, for which $T \geq 0.90$, reduce the efficiency by less than 5%, while at lower transmission values the degradation increases up to 40% for a cloud at 7 km and up to 30% for a cloud at 9 km. High clouds (≥ 11 km) have a significant impact only for $T \leq 0.75$. For example, a cloud at an altitude of 11 km for which $T = 0.50$ reduces the gamma-ray detection efficiency by $\approx 19\%$, while the cloud with the same transmission but at 13 km reduces the efficiency by $\approx 10\%$.

Regarding the influence of transmission, clouds with $T = 0.95$ have a very small effect on the gamma-ray detection efficiency, while clouds with $T = 0.90$ play an important role only at altitudes below 5 km and reduce the detection efficiency by only 10%. At lower transmission values, the altitude of the cloud plays a more important role, as described earlier. For example, clouds

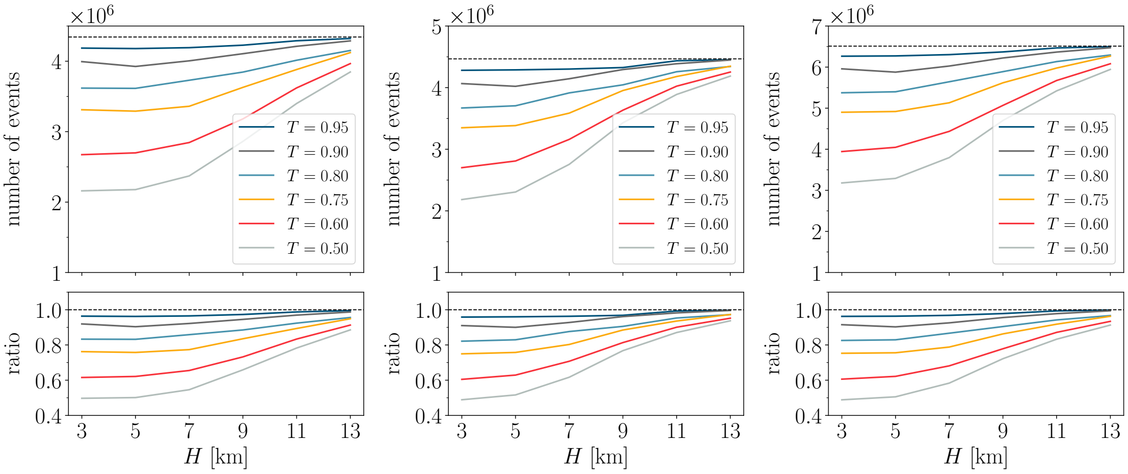

(a) 4 LSTs **(b)** 15 MSTs **(c)** CTAO-N

Figure 4.7: The total number of detected events that survived all cuts as a function of cloud transmission and height. The horizontal dashed lines show the number of events detected in cloudless conditions. Note the different scales. The lower panels show the fraction of the total number of events in the presence of clouds compared to the clean atmosphere.

for which $T = 0.80$ and $T = 0.75$ have detection efficiencies comparable to cloudless conditions when found high in the atmosphere (≥ 11 km), while lower clouds reduce efficiency by 20% and 25%, respectively. Clouds for which $T \leq 0.60$ decrease the detection efficiency by 20% to 50%, depending on altitude.

4.2.2 Energy distribution

The ratio of the energy distribution of the gamma-ray events (surviving standard analysis cuts) detected in the presence of clouds compared to the cloudless condition as a function of cloud transmission and height is shown in Figures 4.8-4.10. Each event is renormalized to obtain Crab-like spectra, i.e., spectra with a spectral index of −2.6, as measured by the HEGRA collaboration (Aharonian et al., 2004), since CORSIKA events are generated following a power law with index −2 to produce enough events above 10 TeV.

From the data presented, it appears that there is a certain energy beyond which the decrease in the number of detected events reaches a plateau (within statistical differences). The value of the breaking energy increases with decreasing cloud transparency and height and is always above the threshold energy (section 4.3). Note that the value of this energy is smaller for higher clouds than for low clouds. This can be explained by the fact that, on average, only air showers with the lowest energies are affected by high clouds. Most of the detected events in the simulated energy range have a maximum at altitudes between 7 and 9 km. However, due to variations in the data, it is difficult to determine the exact values of the breaking energy.

Subarray of 4 LSTs

The energy distribution as a function of cloud height for a subarray of 4 LSTs is shown in Figure 4.8a. The figures show the ratios of the number of detected events (surviving all cuts) in the energy bin in the presence of clouds compared to cloudless conditions. The low clouds (≤ 5 km) have a

T	events	ε [%]	events	ε [%]	events	ε [%]	events	ε [%]	events	ε [%]	events	ε [%]
	3 km		5 km		7 km		9 km		11 km		13 km	
	4 LSTs (4344348 events, $\varepsilon = 0.22\%$)											
0.95	4186547	0.21	4179772	0.21	4192602	0.21	4227747	0.22	4290676	0.22	4322857	0.22
0.90	3994472	0.20	3925770	0.20	4005620	0.21	4106738	0.21	4211890	0.22	4288948	0.22
0.80	3618362	0.19	3614820	0.19	3729957	0.19	3845874	0.20	4014183	0.21	4152639	0.22
0.75	3311165	0.17	3290983	0.17	3360364	0.17	3628801	0.19	3882238	0.20	4122569	0.21
0.60	2673264	0.14	2698691	0.14	2845538	0.15	3181101	0.17	3621233	0.19	3966482	0.20
0.50	2159546	0.11	2177195	0.12	2371367	0.13	2861708	0.15	3399859	0.18	3847477	0.20
	15 MSTs (4467204 events, $\varepsilon = 0.23\%$)											
0.95	4281314	0.22	4288368	0.22	4301409	0.22	4326194	0.23	4436205	0.23	4452898	0.23
0.90	4065975	0.21	4021400	0.21	4144201	0.21	4293738	0.22	4387860	0.23	4448294	0.23
0.80	3669683	0.19	3705580	0.19	3914648	0.20	4045328	0.21	4258248	0.22	4343147	0.22
0.75	3348732	0.17	3384217	0.17	3586411	0.19	3953272	0.20	4180611	0.22	4347643	0.22
0.60	2701130	0.14	2809598	0.15	3160264	0.16	3634455	0.19	4023937	0.21	4252974	0.22
0.50	2183678	0.12	2306067	0.12	2755075	0.15	3429668	0.18	3889480	0.20	4187278	0.22
	CTAO-N (6510189 events, $\varepsilon = 0.34\%$)											
0.95	6265301	0.32	6272164	0.32	6303361	0.32	6369424	0.33	6467084	0.33	6497925	0.33
0.90	5957735	0.31	5877146	0.31	6025818	0.31	6222151	0.32	6365832	0.33	6470937	0.33
0.80	5375095	0.28	5399246	0.28	5643025	0.29	5889028	0.30	6134294	0.32	6294197	0.33
0.75	4900883	0.25	4919289	0.25	5131201	0.27	5617582	0.29	5977101	0.31	6268918	0.32
0.60	3944426	0.21	4047069	0.21	4435816	0.23	5067873	0.26	5674107	0.29	6081609	0.31
0.50	3179868	0.17	3290859	0.17	3797481	0.20	4699998	0.24	5421551	0.28	5943606	0.31

Table 4.2: The number of surviving events and the gamma-ray detection efficiency as a function of cloud transmission and height (a.g.l.).
For comparison, the number of surviving events and the gamma-ray detection efficiencies in cloudless conditions ($T = 1$) are given in the brackets.

similar effect on the energy distribution for a given transmission value. This is not unexpected, considering that these heights are below the average height of the shower maximum and therefore the total shower is attenuated by the same amount in both cases. The number of detected events at 100 GeV is lower than in the clear atmosphere between 5% and 45%, while the ratio increases as the transmission increases. At higher energies, the influence of clouds is much smaller, less than 15% at 1 TeV, reaching a plateau of 10% or less. Clouds at intermediate altitudes, ranging from 7 to 9 km, reduce the number of detected events at 100 GeV by up to 35% compared to cloudless conditions and $\lesssim$ 20% at energies above 1 TeV. Further on, high clouds at an altitude of 11 km reduce the number of detected events by less than 20% at 100 GeV and less than 10% at higher energies. Clouds at 13 km show very similar behavior above 100 GeV regardless of transmission: from $\approx$ 5% to comparable to cloudless conditions, while at 100 GeV the reduction is less than 10% compared to the number of detected events of the same energy without clouds. Below 100 GeV, the number of events detected in the presence of clouds is smaller by 20%.

Figure 4.8b displays the energy distribution for various cloud transmission. Clouds with low transmission ($T \leq 0.60$) cause a reduction of 10% to 45% compared to cloudless conditions, and $\lesssim$ 20% at energies above 1 TeV, depending on the cloud height. For clouds of intermediate transmission (between $T = 0.75$ and $T = 0.80$), the number of detected events decreases by $\lesssim$ 20% and $\lesssim$ 10% at 100 GeV, respectively, and by $\lesssim$ 15% at energies $\gtrsim$ 1 TeV. High transmission clouds ($T \geq 0.90$) behave similarly at a given height, reducing the detected events by up to 10% at 100 GeV and to less than 5% at energies above 1 TeV. At energies above 300 GeV, the effect of high transmission clouds at 13 km is negligible, resulting in telescope performance comparable to that without clouds. Note that at energies below the threshold, the number of detected events decreases sharply for all cloud heights and transmissions, although the loss for $T \geq 0.90$ is $\lesssim$ 20%.

Subarray of 15 MSTs

The effects of cloud height on the number of detected events for a subarray of 15 MSTs (Figure 4.9a) are similar to those for a subarray of 4 LSTs, although the factor of decrease in the common energy range (80 GeV to 3 TeV) is higher, as MSTs are naturally less sensitive to these energies compared to LSTs. The behavior of MSTs below the energy threshold is similar to the behavior of LSTs below their energy threshold - there is a sharp drop in detection efficiency, up to 90% in the worst case (cloud at 3 km, for which $T = 0.50$). Low clouds ($\leq$ 5 km) reduce the number of detected events by up to 80% at 100 GeV, 50% at 1 TeV and less than 10% at the highest energies, compared to conditions without clouds. Clouds at 7 km altitude show a substantial reduction in the number of detected events, reaching up to 65% at 100 GeV and $\lesssim$ 20% at 1 TeV and beyond. Conversely, clouds at 9 km show a smaller reduction in the number of detected events, with the reduction above 1 TeV being less than 10%. The effect of high altitude clouds ($\geq$ 11 km) is consistent across the energy range, leading to a reduction of less than 5% above 1 TeV, while at lower energies the differences between the individual transmission values become more pronounced, leading to a reduction of up to 30% at 100 GeV.

The effects of cloud transmission on the number of events detected by a subarray of 15 MSTs are shown in Figure 4.9b. The results show that clouds with low transmission ($T \leq 0.60$) can significantly degrade the performance of the subarray, leading to a reduction of up to 90% at 100 GeV and up to 30% at energies above 1 TeV. Clouds with intermediate transmission (i.e. between $T = 0.75$ and $T = 0.80$) have a reduced detection efficiency of about 45% at 100 GeV and 15% at 1 TeV, with telescope performance under such conditions being comparable to cloudless conditions at the highest energies. On the other hand, clouds with high transmission ($T \geq 0.90$) have a similar effect on the energy distribution over the entire energy range. In particular, the number of detected events decreases by less than 20% at 100 GeV and by less than 10% at 1 TeV, while the distribution at energies above 1 TeV is comparable to that observed under cloudless conditions.

CTAO-N array

The performance of CTAO-N has been analyzed over a wide energy range and the results indicate that, as expected, the number of detected events at lower energies is mainly dominated by 4 LSTs, i.e., at energies $\lesssim$ 80 GeV the performance of CTAO-N is comparable to that of a subarray consisting of 4 LSTs. For energies $\geq$ 3 TeV, the performance of CTAO-N is equivalent to that of MSTs. In the energy range where both LSTs and MSTs contribute, the performance of CTAO-N is better than that of MSTs. For instance, the presence of clouds at 3 km altitude with $T = 0.50$ reduces the number of detected events at 80 GeV by 60% compared to cloudless conditions (Figures 4.10a, 4.10b), which is better than the performance of MSTs alone (80%).

At energies $\gtrsim$ 500 GeV for the subarray of 4 LSTs and CTAO-N and $\approx$ 5 TeV for the subarray of 15 MSTs, an intriguing trend is seen when the energy distribution is plotted as a function of cloud altitude. In particular, the detection efficiency improves for lower clouds ($\leq$ 5 km) compared to higher clouds between 7 and 11 km. This is unexpected, as it is a natural assumption that the lowest clouds should have the greatest impact on detection efficiency. However, the apparent improvement in detection efficiency is actually due to the application of quality cuts (section 4.1.3).

If a cloud is at a height of 5 km or less, the height of the shower maximum is above the height of the cloud. In this case, the whole shower is attenuated by the same amount. The result is an image of lower intensity. Consequently, the *size* parameter decreases, but other image parameters do not change significantly. In the case of higher clouds, however, only a fraction of the Cherenkov photons emitted above the cloud is attenuated. Consequently, the part of the image closer to the edge of the camera (the tail of the shower) remains unaffected, while the region closer to the center of the camera (the head of the shower) is scaled down by a factor of $\frac{1}{T}$, resulting in a change of the image parameters and a shift of the image CoG towards the edge of the camera (Figure 4.11). These effects are well described in the article by Sobczynska et al. (2013), although the effects in semi-transparent clouds are not as strong as in the presence of opaque clouds. The result is not only an attenuated image, but also a cropped image. Since cropped images are not considered in the standard analysis, a cut is applied to the position of the image CoG, assuming that the distance between the image CoG and the camera center is less than 80% of the camera radius. The number of such images increases in the presence of intermediate clouds, resulting in a larger number of rejected events. The effect of this cut is more pronounced at high energies, where the differences between the various clouds are small. However, it should be kept in mind that the number of detected events at the image level is always smaller in lower clouds with lower transmission.

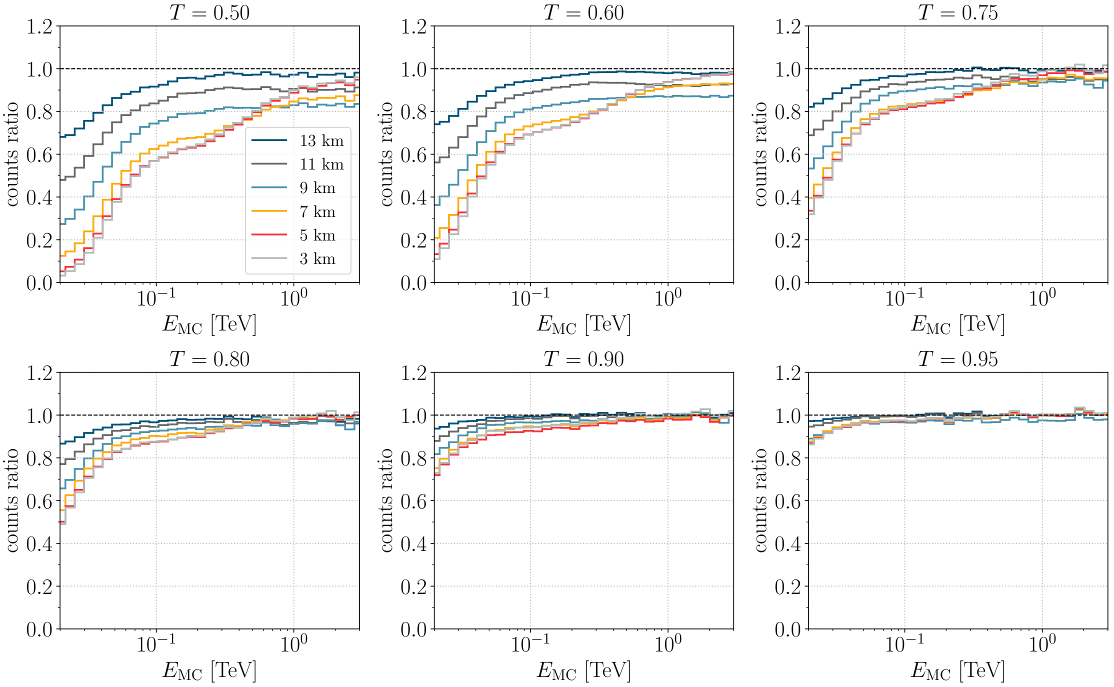

(a) 4 LSTs, height dependence of energy distribution for fixed transmission

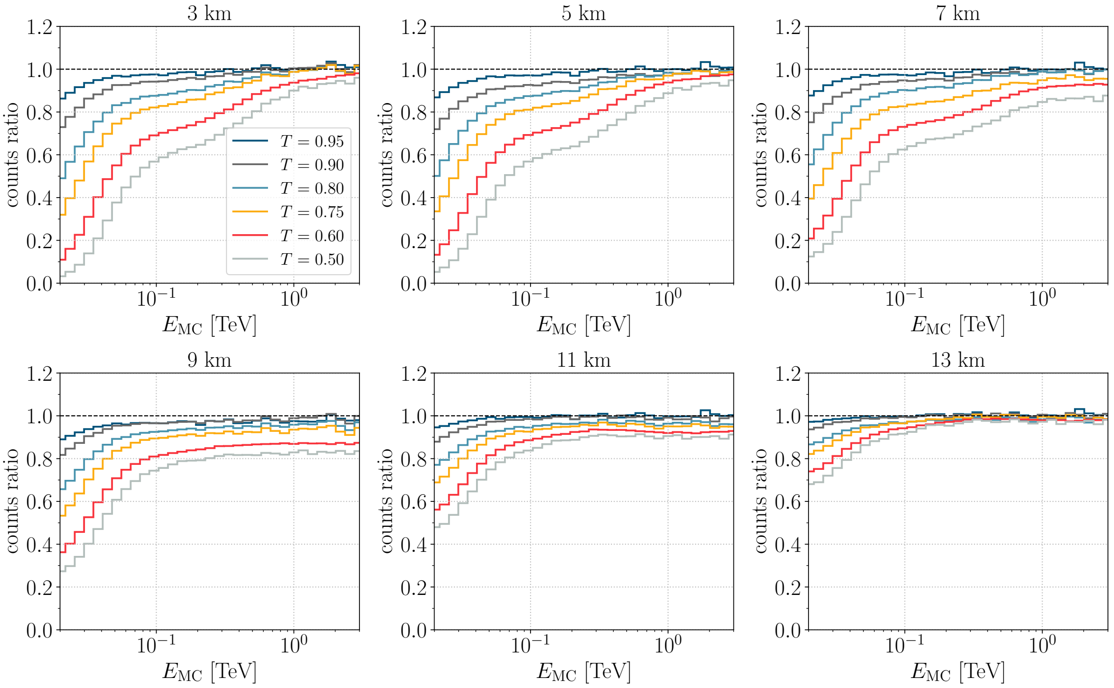

(b) 4 LSTs, transmission dependence of energy distribution for fixed height

Figure 4.8: The distributions of E_{MC} in the presence of clouds compared to the clean atmosphere for the subarray of 4 LSTs.

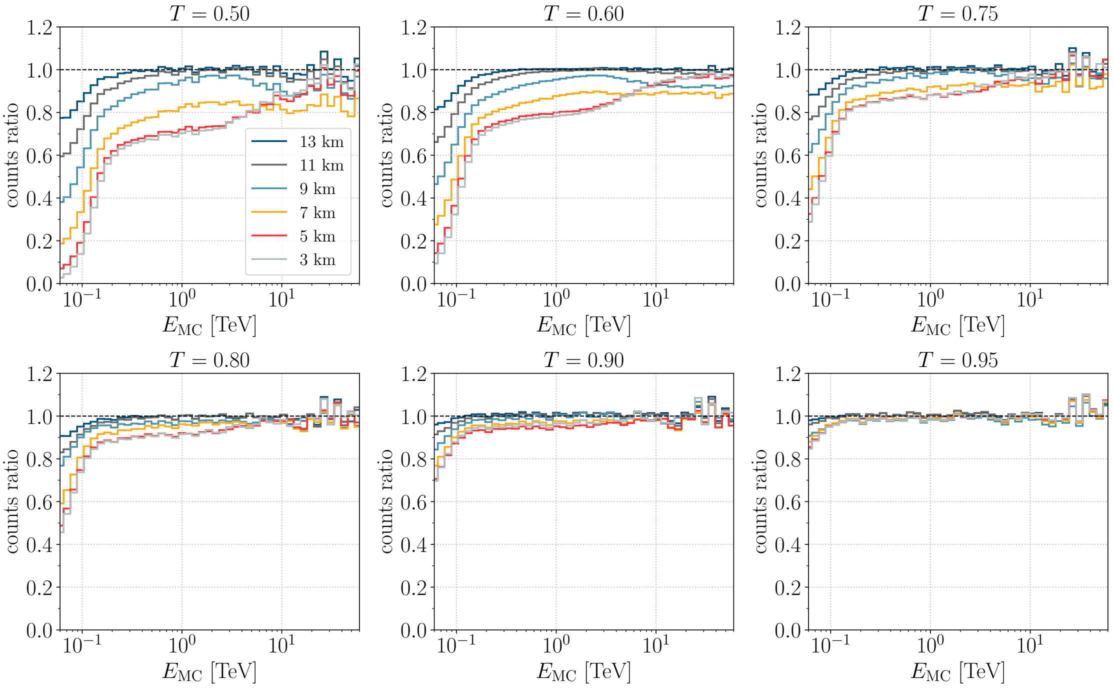

(a) 15 MSTs, height dependence of energy distribution for fixed transmission

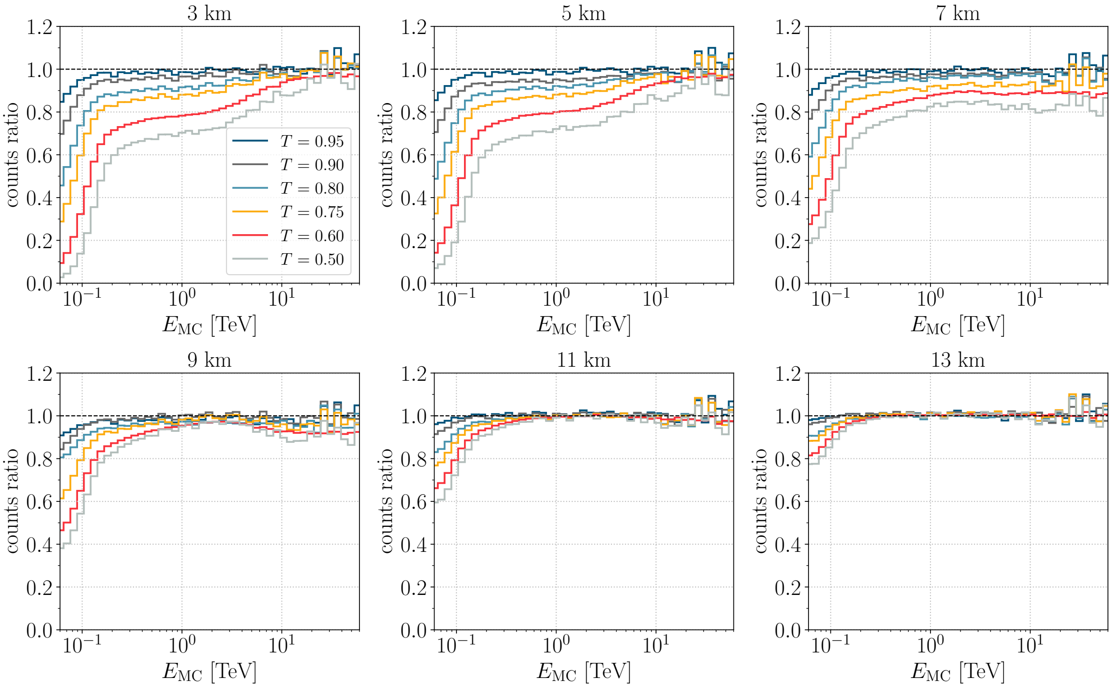

(b) 15 MSTs, transmission dependence of energy distribution for fixed height

Figure 4.9: The distributions of E_{MC} in the presence of clouds compared to the clean atmosphere for the subarray of 15 MSTs.

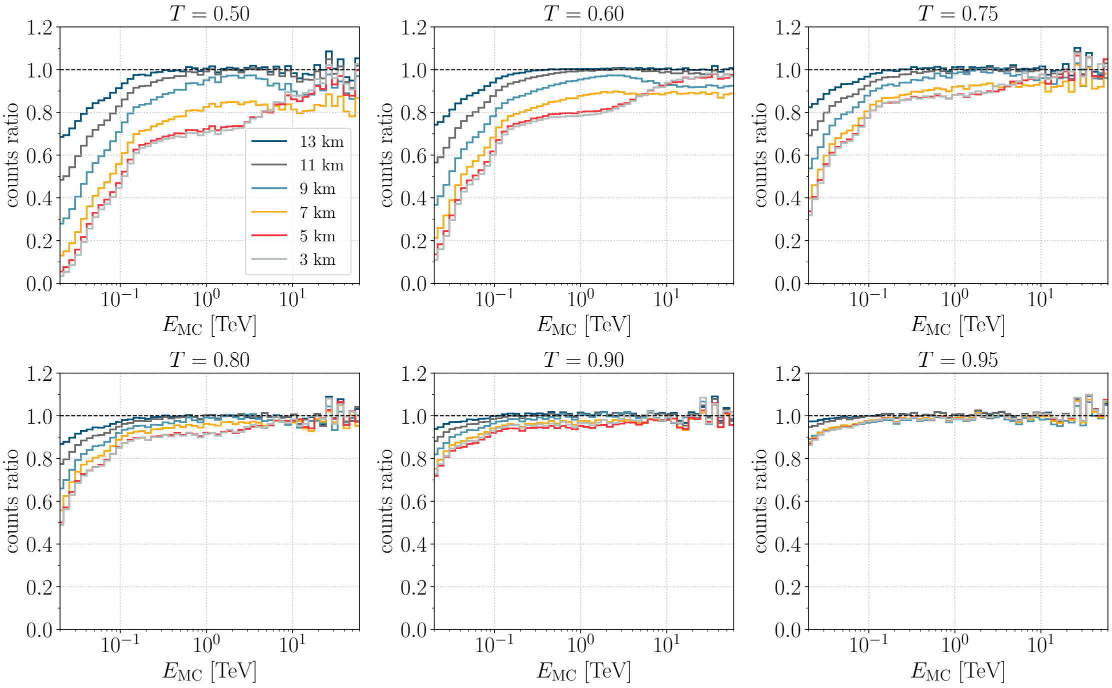

(a) CTAO-N, height dependence of energy distribution for fixed transmission

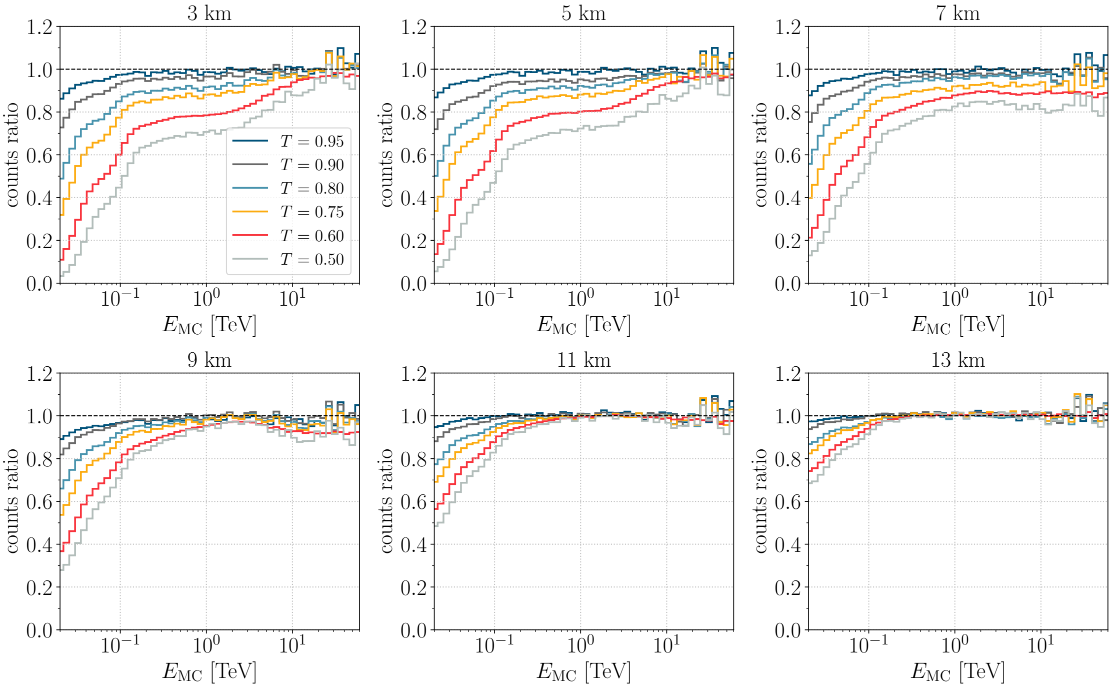

(b) CTAO-N, transmission dependence of energy distribution for fixed height

Figure 4.10: The distributions of E_{MC} in the presence of clouds compared to the clean atmosphere for CTAO-N

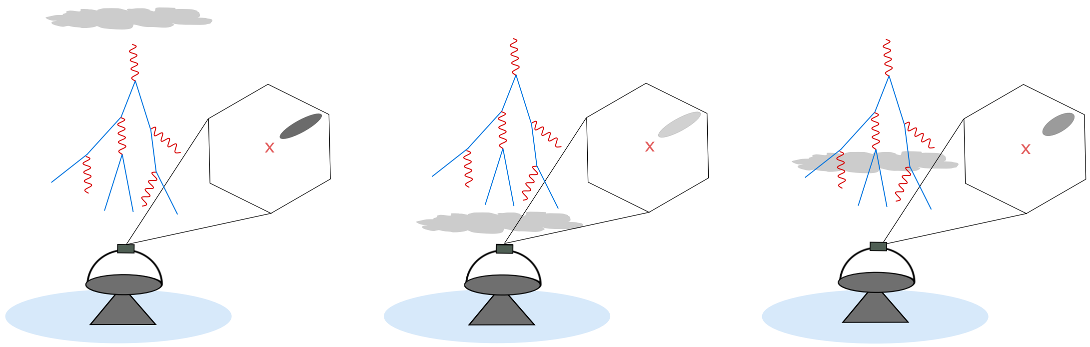

Figure 4.11: Schematic representation of the effects of high (*left*), low (*center*), and middle (*right*) clouds. The center of the camera is highlighted.

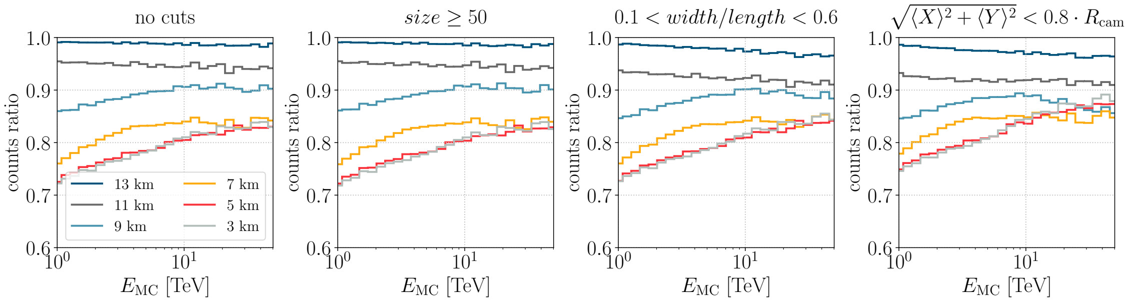

(a) 4 LSTs

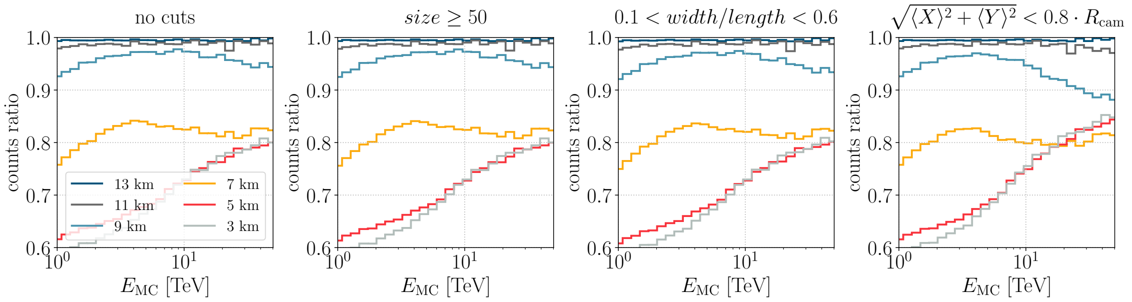

(b) 15 MSTs

Figure 4.12: The distributions of E_{MC} in the presence of clouds compared to cloudless conditions. The energy distributions are given for images triggered by gamma-ray air showers with energies above 1 TeV detected by LSTs and MSTs. The left figure in a row shows the data after image cleaning before any cuts were applied. The remaining figures show the energy distribution for various applied cuts. As expected, the cuts in terms of *size* and *width*-to-*length* ratio have a very small effect on the energy distribution of the data. The cut to CoG image position results in increased detection efficiency for lower clouds compared to higher clouds, leading to an apparent increased detection efficiency in lower clouds.

The effect of different cuts on the distribution of E_{MC} in the presence of clouds compared to the clean atmosphere is shown in Figure 4.12. As expected, a *size* cut has no important effect at high energies. The cut *width*/*length* plays a minor role, but only for lower clouds (≤ 7 km) for which the change of the *width* and *length* parameter is larger, resulting in more oval figures that usually affect the direction reconstruction due to poorly defined axes. The cut to the CoG position leads to less

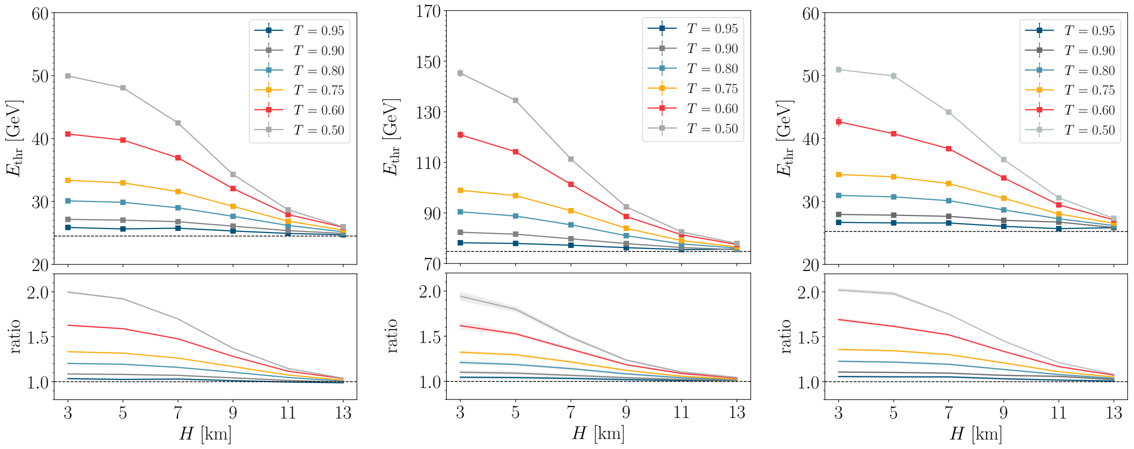

(a) 4 LSTs **(b)** 15 MSTs **(c)** CTAO-N

Figure 4.13: *Top panels*: Energy threshold as a function of cloud transmission and altitude. *Bottom panels*: Energy threshold cloud-to-clear atmosphere ratio.

affected detection efficiency for lower clouds compared to higher clouds for the reasons explained.

4.3 Energy threshold

The energy threshold is determined as the energy peak in the differential rate of reconstructed gamma rays from a Crab-like source. In the first step, the simulated data are renormalized to obtain Crab-like spectra. The threshold is then determined by fitting a Gaussian in a narrow energy range around the peak of the distribution. The resulting energy thresholds in the presence of clouds are shown in Figure 4.13 and Table 4.3.

Subarray of 4 LSTs

The energy threshold for the subarray of 4 LSTs in the clean atmosphere is (25.0 ± 0.2) GeV. In the presence of clouds, however, the energy threshold rises considerably. In the case of low clouds ($\lesssim$ 5 km), the energy threshold for the subarray of 4 LSTs increases by a factor approximately equal to $\frac{1}{T}$ (± 5%). Since most air showers are almost fully developed at these altitudes, even those with the highest energies, the Cherenkov light emitted at different altitudes is attenuated by the same factor. The number of detected events decreases over the entire energy range, especially in the low energy bins, shifting a maximum of the distribution to higher energies. Consequently, the energy threshold increases. For example, a cloud at an altitude of 3 km, for which $T = 0.50$, almost doubles the threshold, increasing it by 100% (Figure 4.13a). In the presence of a cloud with the same transmission but at an altitude of 5 km, the values are slightly lower, but the increase is still above 90%. In the presence of low clouds with high transmission ($T \geq 0.90$), the change in the energy threshold is minimal ($\lesssim$ 8%), and the threshold is comparable to that for $T = 1$.

In higher clouds, the relationship between the threshold and the cloud properties is more complicated because the showers are unevenly attenuated, and the clouds have a greater influence on low-energy air showers than on high-energy showers. Therefore, the increase in the energy threshold strongly depends on both the transmission and the height of the cloud. Mid-clouds at

T	E_{thr} [GeV]					
	3 km	5 km	7 km	9 km	11 km	13 km
			4 LSTs			
0.95	25.9 ± 0.2	25.6 ± 0.2	25.8 ± 0.2	25.3 ± 0.2	24.9 ± 0.2	24.7 ± 0.2
0.90	27.2 ± 0.2	27.0 ± 0.2	26.8 ± 0.2	26.1 ± 0.2	25.4 ± 0.1	24.9 ± 0.1
0.80	30.1 ± 0.2	29.9 ± 0.2	29.0 ± 0.2	27.6 ± 0.1	26.2 ± 0.1	25.2 ± 0.1
0.75	33.4 ± 0.2	32.9 ± 0.2	31.6 ± 0.1	29.2 ± 0.2	26.9 ± 0.1	25.5 ± 0.1
0.60	40.7 ± 0.2	39.8 ± 0.2	37.0 ± 0.2	32.1 ± 0.1	27.9 ± 0.1	25.9 ± 0.2
0.50	49.9 ± 0.3	48.1 ± 0.2	42.5 ± 0.1	34.3 ± 0.2	28.7 ± 0.1	26.0 ± 0.1
			15 MSTs			
0.95	78.2 ± 0.4	77.9 ± 0.4	77.2 ± 0.4	76.3 ± 0.5	75.5 ± 0.4	75.7 ± 0.6
0.90	82.4 ± 0.7	81.6 ± 0.6	79.8 ± 0.4	77.9 ± 0.4	76.3 ± 0.4	75.5 ± 0.5
0.80	90.4 ± 0.8	88.8 ± 0.4	85.3 ± 0.4	81.0 ± 0.5	77.7 ± 0.4	76.1 ± 0.4
0.75	98.4 ± 0.6	96.8 ± 0.5	90.9 ± 0.4	83.9 ± 0.3	79.0 ± 0.3	76.5 ± 0.4
0.60	120.9 ± 1.2	114.2 ± 0.5	101.3 ± 0.4	88.6 ± 0.3	81.4 ± 0.4	77.5 ± 0.3
0.50	145.3 ± 1.3	134.5 ± 0.8	111.3 ± 0.5	92.4 ± 0.3	82.5 ± 0.3	77.9 ± 0.4
			CTAO-N			
0.95	26.7 ± 0.3	26.6 ± 0.3	26.6 ± 0.3	26.1 ± 0.3	25.7 ± 0.3	25.4 ± 0.3
0.90	27.9 ± 0.3	27.8 ± 0.6	27.6 ± 0.3	27.0 ± 0.3	26.7 ± 0.3	25.9 ± 0.3
0.80	30.9 ± 0.3	30.7 ± 0.3	30.1 ± 0.3	28.7 ± 0.2	27.3 ± 0.2	26.2 ± 0.2
0.75	34.3 ± 0.3	33.9 ± 0.3	32.9 ± 0.3	30.5 ± 0.2	28.0 ± 0.2	26.5 ± 0.2
0.60	42.7 ± 0.7	40.8 ± 0.3	38.4 ± 0.3	33.7 ± 0.1	29.5 ± 0.2	27.1 ± 0.2
0.50	50.9 ± 0.5	49.9 ± 0.5	44.2 ± 0.2	36.7 ± 0.1	30.6 ± 0.1	27.3 ± 0.2

Table 4.3: Energy threshold for CTAO-N and the corresponding subarrays as a function of transmission and height of a cloud. Energy thresholds in the clean atmosphere are as follows: (25.0 ± 0.2) GeV for the subarray of 4 LSTs, (74.8 ± 0.5) GeV for the subarray of 15 MSTs, (25.2 ± 0.3) GeV for CTAO-N

an altitude of 7 km increase the energy threshold by up to 70%, while those at 9 km increase it by 40%, depending on the transmission of the cloud. For example, in the presence of clouds for which $T = 0.80$, the energy threshold increases by 19.9% and 10.5% for the cloud at 7 and 9 km, respectively. At higher transmissions, the threshold is increased up to 15% compared to the threshold for cloudless conditions. For high clouds at 11 km altitude, an increase of 15% can be expected, while for clouds at 13 km the change in energy threshold compared to the threshold in the absence of clouds is very small, on the order of a few percent.

Subarray of 15 MSTs

Similarly to LSTs, low clouds ($\lesssim 5$ km) increase the energy threshold of the subarray with 15 MSTs by a factor of $\approx \frac{1}{T}$ (Figure 4.13b). For example, in the presence of a cloud at 3 km for which $T = 0.50$, the energy threshold is (145.3 ± 1.3) GeV, which is twice the value of the energy threshold under cloud conditions: (74.8 ± 0.5) GeV. In the presence of a very transparent cloud ($T \geq 0.90$), the energy threshold is increased by $\lesssim 10\%$. Clouds at mid-height of 7 km increase the energy threshold between 20% and 50% for $T \leq 0.75$ and $\lesssim 10\%$ for $T \geq 0.80$. Clouds at 9 km have even smaller effects, where the energy threshold increases by less than 25% in the presence of clouds for which $T = 0.50$, while the contribution of clouds decreases with increasing transmission and eventually reaches a value comparable to that obtained in the absence of clouds. High clouds (≥ 11 km) tend to have a very small effect on the energy threshold of the subarray, which amounts to 10% for $T \leq 0.60$ and $\lesssim 5\%$ for higher transmissions.

CTAO-N array

Low clouds ($\lesssim 5$ km) increase the energy threshold of CTAO-N by a factor of $\approx \frac{1}{T}$, giving a 102% higher energy threshold in the presence of clouds with $T = 0.50$, and a 5.7% higher energy threshold for $T = 0.95$ (Figure 4.13c). In the presence of mid-level clouds, the CTAO-N energy threshold is increased by up to 75% depending on the transmission, where highly transparent clouds at medium altitudes ($T \geq 0.90$) increase the energy threshold by $\lesssim 10\%$. On the other hand, the energy threshold of CTAO-N in the presence of high clouds increases by 20% for the lowest transmission, while for $T \geq 0.90$ being $\lesssim 5\%$.

It is worth noting that the relative shift of the energy threshold in the presence of low and high clouds is similar regardless of the number and type of telescopes, but strongly depends on the properties of the clouds. On the other hand, middle clouds lead to larger differences between subarrays in terms of the relative shift of the threshold. For example, a cloud at an altitude of 7 km for which $T = 0.50$ increases the energy threshold by 69.8%, 48.8%, and 75.2% for the subarray of 4 LSTs, 15 MSTs, and CTAO-N, respectively. In contrast, the cloud with the same transmission but at an altitude of 13 km increases the energy threshold of the subarray with 4 LSTs by 3.9%, that of 15 MSTs by 4.2%, and the energy threshold of CTAO-N by 8.3%. This poorer performance of LSTs can be explained by the fact that LSTs (compared to MSTs) detect events with lower energy, whose maximum is higher in the atmosphere, and which are more likely to be affected by mid-level clouds.

Model of the influence of clouds on the energy threshold

To find a useful relation for determining the energy threshold in the presence of clouds, a fit to the data was performed. The natural assumption, following the considerations described in the preceding paragraphs, is that the Cherenkov light yield in the presence of clouds is simply reduced by a factor of $\sim T$, increasing the energy threshold by the same amount:

$$E_{\mathrm{thr}}(T) = \frac{E_{\mathrm{thr}}(T=1)}{T}, \tag{4.6}$$

where $E_{\mathrm{thr}}(T = 1)$ is the energy threshold in the cloudless conditions. To assess the validity of this assumption, a fit to $E_{\mathrm{thr}}(T)$ is performed for each height H. The results of such a model are shown in Figures 4.14a, 4.14b, and 4.14c for the subarrays or 4 LSTs, 15 MSTs and CTAO-N, respectively. As can be seen from the figures, this assumption applies only to low clouds below the shower maximum, when the total shower is attenuated by the same factor. For higher clouds (≥ 7 km a.s.l.), model performance is poor. For example, the coefficient of determination $r^2 = -99.38$ and the

	$E_{\text{thr}}(T=1)$ [GeV]	$\overline{H}_{\max}$ [km]	ε [km]
4 LSTs	24.5 ± 0.1	9.6 ± 0.1	3.3 ± 0.1
15 MSTs	75.3 ± 0.2	8.1 ± 0.1	3.7 ± 0.1
CTAO-N	25.4 ± 0.1	9.9 ± 0.1	3.6 ± 0.1

Table 4.4: Parameters of the semi-analytical model describing the increase of energy threshold in the presence of clouds. Each row shows results for different layouts. The clear-sky energy threshold resulting from the fit to the model is consistent with the same energy threshold calculated from the data: $E_{\text{thr}}(4\text{ LSTs}) = 25.1 \pm 0.2$ GeV, $E_{\text{thr}}(15\text{ MSTs}) = 74.8 \pm 0.5$ GeV, $E_{\text{thr}}(\text{CTAO}-\text{N}) = 25.2 \pm 0.3$ GeV.

reduced chi-square $\chi^2/\text{NDF} = 3475.50/5$ of the fit for a cloud at an altitude of 13 km indicates poor agreement between the data and the model for CTAO-N, although the agreement for other arrays is no better. In contrast, the agreement between the data and the model is worse for LSTs because the clouds have a stronger influence on the gamma-ray differential rate of LSTs. Obviously, E_{thr} also strongly depends on the relationship between the cloud height and the height of the shower maximum, i.e. on the fraction of Cherenkov light that is affected by the cloud. Therefore, we also introduce a dependence on the height of the cloud in the form of a sigmoid function as follows:

$$E_{\text{thr}}(T,H) = \frac{E_{\text{thr}}(T=1)}{T^{1/\cos\xi} + (1 - T^{1/\cos\xi}) \cdot S(H)}, \tag{4.7}$$

where

$$S(H) = \frac{1}{2} \cdot \left[\arctan\left(\frac{H - \overline{H}_{\max}}{\varepsilon}\right) + 1\right] \tag{4.8}$$

is a sigmoid function that describes the relationship between the height of the cloud and the height of the shower maximum and its influence on E_{thr}, $\overline{H}_{\max}$ is the average height of the shower maximum, and ε is a parameter describing the fluctuations in the height of the shower maximum and its width. The term $1/\cos\xi$ was introduced to take into account the observations at the zenith angle $\xi > 0°$. With increasing zenith angle, the amount of Cherenkov light additionally decreases, as the photons travel a longer distance from the emission point to the detector. The sigmoid function also depends on the zenith angle, but in a somewhat more complicated way than the dependence of transmission on the zenith. However, this study concentrates on rather low zenith angels (20°), where such a factor would not have much effect anyway. However, the introduced parameter is expected to play a crucial role in observations at higher zenith angles. The performance of the model described by equation (4.7) is shown in in Figures 4.15a, 4.15b, and 4.15c for the subarrays or 4 LSTs, 15 MSTs and CTAO-N, respectively. The results show good agreement between the data and the model, with slightly increased uncertainties for lower transmission values (≤ 0.6). The values of the fit parameters are given in Table 4.4.

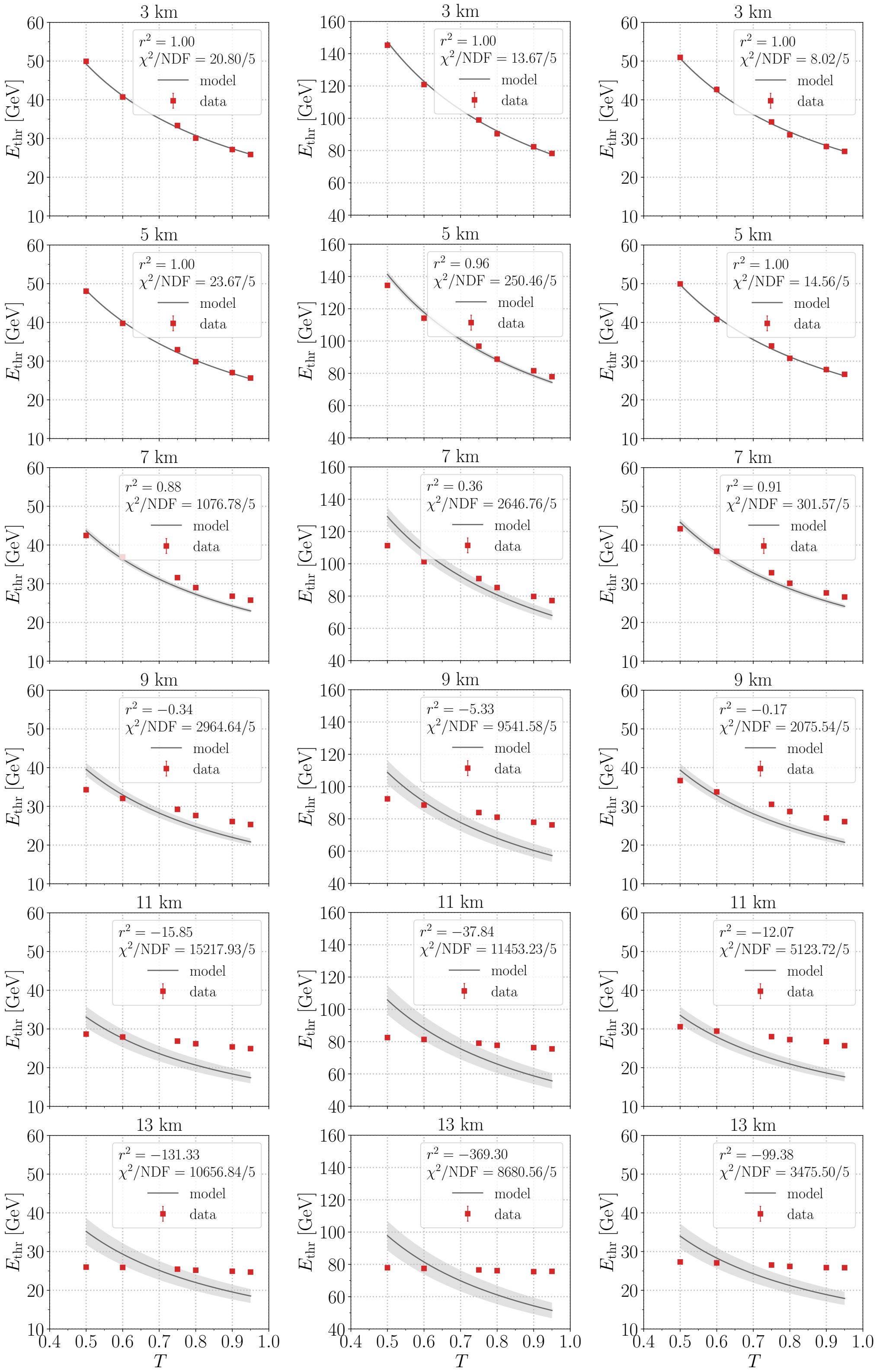

(a) 4 LSTs **(b)** 15 MSTs **(c)** CTAO-N

Figure 4.14: The performance of the simple model described by equation (4.6) for the CTAO-N and its corresponding subarrays. The dots represent the data obtained from MC simulations, while the lines represent the model.

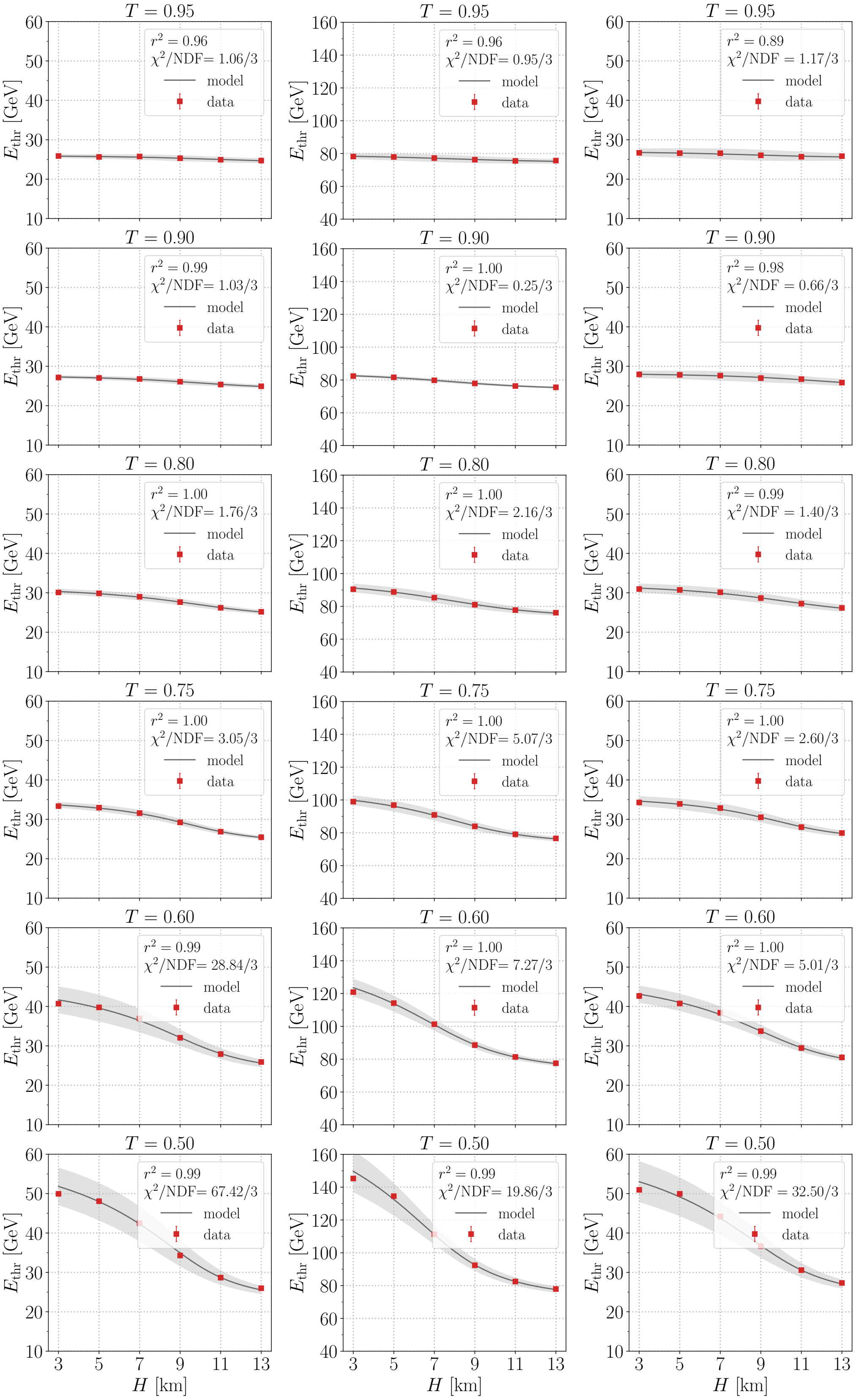

(a) 4 LSTs **(b)** 15 MSTs **(c)** CTAO-N

Figure 4.15: The performance of the simple model described by equation (4.7) for the CTAO-N and its corresponding subarrays. The dots represent the data obtained from MC simulations, while the lines represent the model.

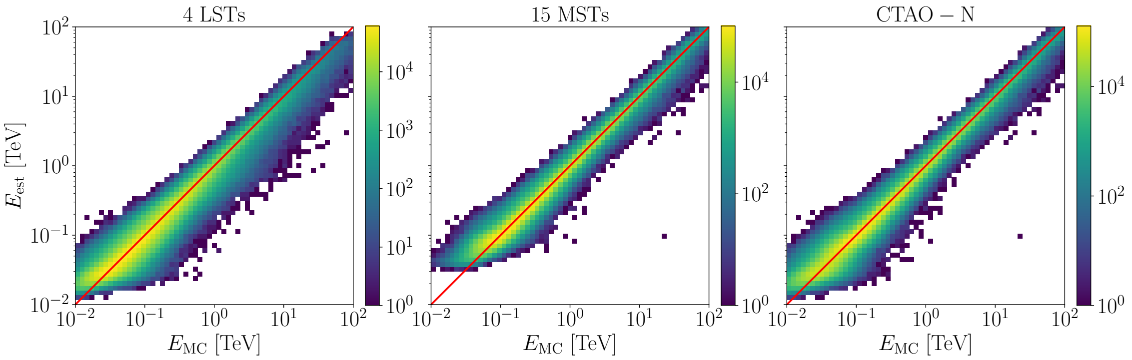

Figure 4.16: Migration matrices for the subarray of 4 LSTs, 15 MSTs, and CTAO-N when there are no clouds in the atmosphere. Red line indicates $E_{\mathrm{est}} = E_{\mathrm{MC}}$.

4.4 Energy bias

The performance of the energy estimator depends strongly on the height of the shower maximum and the *impact* parameter, as well as on many other parameters such as *size*, *width*, *length*, etc., which are related to the development of the shower in the atmosphere (see section 4.1.4). The *size* itself is closely related to the primary energy and the impact parameter. However, as the previous studies show, most of these parameters change in the presence of clouds, especially *size*. Since the energy reconstruction is based entirely on MC simulations, the choice of atmospheric profiles used in the simulations has a significant impact on the reconstructed energy. Two showers triggered by gamma rays of the same energy are perceived differently by the same telescope in different atmospheric conditions. Thus, it is reasonable to assume that performance degrades even further when cloudy data are analyzed using the standard MC simulations, with high-energy events shifted to lower energies.

Figure 4.16 displays two-dimensional density histograms, known as migration matrices, illustrating the relationship between the reconstructed energy E_{est} and the simulated energy E_{MC} for a subarray of 4 LSTs, 15 MSTs, and CTAO-N when there are no clouds present. The migration matrix describes how much the reconstructed energies of the detected events are scattered by the process of energy estimation compared to the simulated energies. In a perfect reconstruction scenario, all events would align along the line $E_{\mathrm{est}} = E_{\mathrm{MC}}$. In reality, the limited detector resolution introduces some scattering of events around the diagonal. Moreover, due to the imperfect nature of MC simulations, the observed data will not match simulations perfectly, further contributing to the uncertainty in the energy estimate.

The migration matrices for the subarray of 4 LSTs, 15 MSTs, and CTAO-N in the presence of clouds are shown in Figures 4.17, 4.18 and 4.19. The migration matrices are given for the case when the data is analyzed using adaptive MC simulations in the RF training sample. As can be seen from the figures, there is no significant change in the distribution of events around the diagonal except in the density of the histogram, i.e. a smaller number of detected events is visible as the transmission and height of a cloud decrease, especially in the low energy bins. Note, however, that at low energies, the trigger threshold effects lead to an overestimation of the energy near the threshold. And since the energy threshold shifts to higher energies in the presence of less transparent and lower clouds, this effect shifts accordingly. The width of the distribution does not change significantly, if at all, indicating that the influence of clouds on the energy resolution is small, i.e., the differences in the energy resolution of individual cases are likely to be small (see section 4.5). However, when using RFs trained on MC simulations for cloudless conditions, the situation is quite different (Figures 4.20, 4.21 and 4.22). In the presence of low clouds (≤ 5 km), the events are systematically shifted downwards, i.e. their reconstructed energies are underestimated over the whole energy range. The higher the cloud, the less dominant its effects become. Thus, in the case of the highest clouds, only the air showers triggered by low-energy gamma rays whose maximum is still above the cloud base are affected. For clouds of medium height, there are strong energy-dependent effects, because showers of different energy are not affected equally and their height of maximum differs. From the migration matrices, it can be concluded that clouds with high transmission ($T \geq 0.90$) do not cause significant changes in the performance of the energy estimator when the standard MC simulations are used for RF training, regardless of altitude.

To estimate the effects of clouds on the performance of the energy estimator more accurately, a thorough study of the energy bias was carried out for CTAO-N and its corresponding subarrays. The bias of an estimator $\hat{\delta}$ of a parameter δ is the difference between the expected value of $\hat{\delta}$, $\mathbb{E}(\hat{\delta})$ and δ, that is:

$$\mathrm{bias}(\hat{\delta}) = \mathbb{E}(\hat{\delta}) - \delta. \tag{4.9}$$

Considering that the energy range of IACTs exceeds several orders of magnitude, it is much more convenient to calculate the relative bias. Therefore, energy bias is defined as a relative difference between the estimated or reconstructed energy E_{est} and the simulated energy E_{MC}, and is the basic measure of energy estimator performance (along with the energy resolution, see section 4.5). The procedure is as follows. First, for each bin in E_{MC} (as in the migration matrix), the distribution of the relative difference between E_{est} and E_{MC} is calculated (for events that survived all the cleaning and quality cuts imposed during the analysis):

$$\frac{\Delta E}{E} = \frac{E_{\mathrm{est}} - E_{\mathrm{MC}}}{E_{\mathrm{MC}}} \tag{4.10}$$

The energy bias is calculated as the mean of a Gaussian fit to the distribution. It has been tested and it can be confirmed that the use of the arithmetic mean or the median does not give significantly different results. An overall distribution of $\Delta E/E$ for CTAO-N and the corresponding subarray is shown in Figure 4.23. In all three cases, the distribution is unimodal, centered around zero, with no visible outliers, and slightly skewed to the right, indicating that there are a smaller number of events for which the energy is overestimated, but for most of them, the reconstructed energy is underestimated. The width of the distribution is slightly higher in the case of LSTs ($\sigma = 0.32$), indicating poorer energy resolution compared to MSTs ($\sigma = 0.21$) or CTAO-N ($\sigma = 0.26$). This is to be expected as LSTs observe lower energies that are more susceptible to shower-to-shower fluctuations that limit the achievable energy resolution.

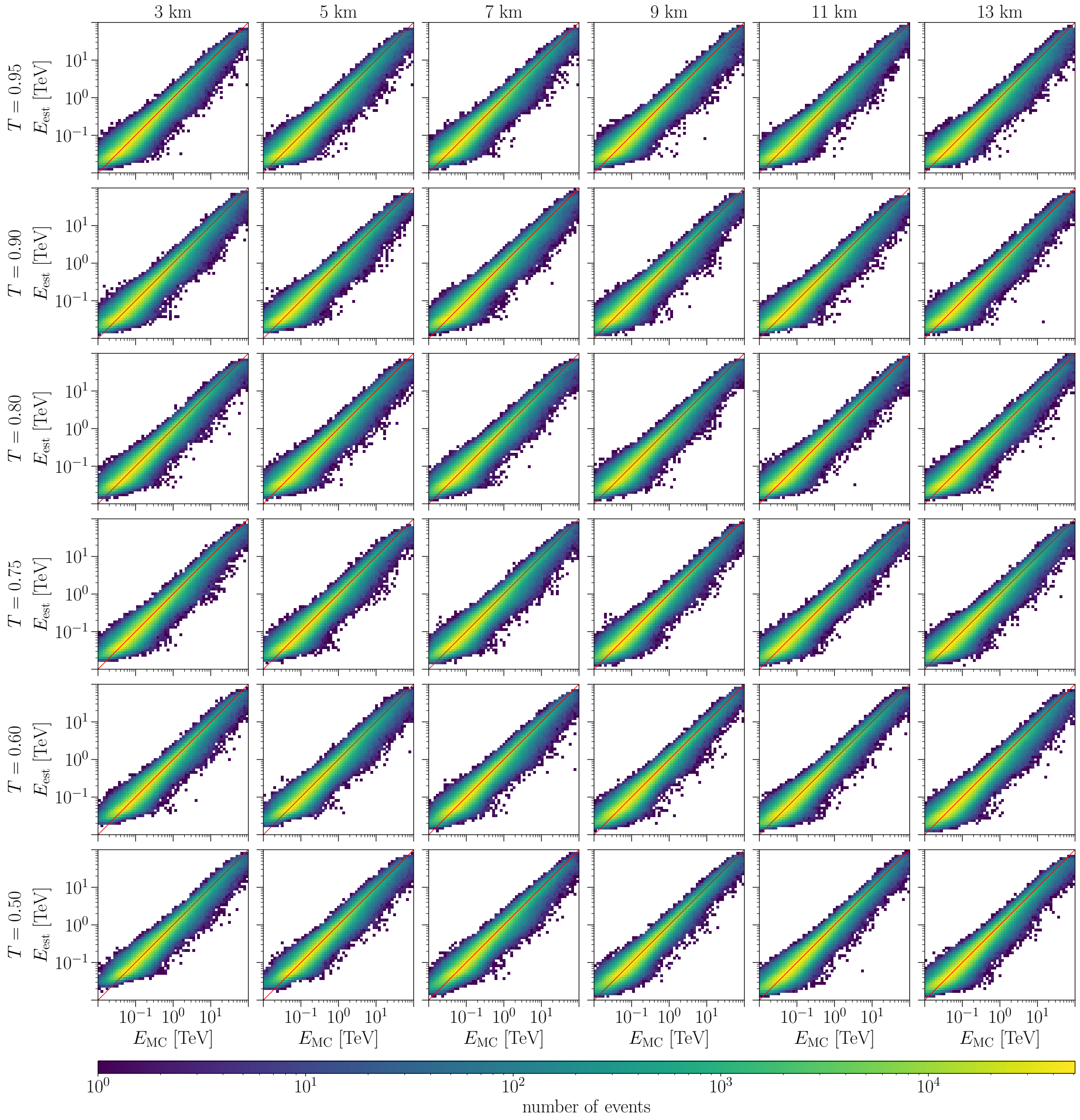

Figure 4.17: Migration matrices for the subarray of 4 LSTs for different transmission profiles. The data indicate the results of the energy reconstruction performed with RFs trained on adaptive MC simulations (clouds included). Each row represents a different cloud transmission and each column represents a different cloud height. Red line indicates $E_{\mathrm{est}} = E_{\mathrm{MC}}$.

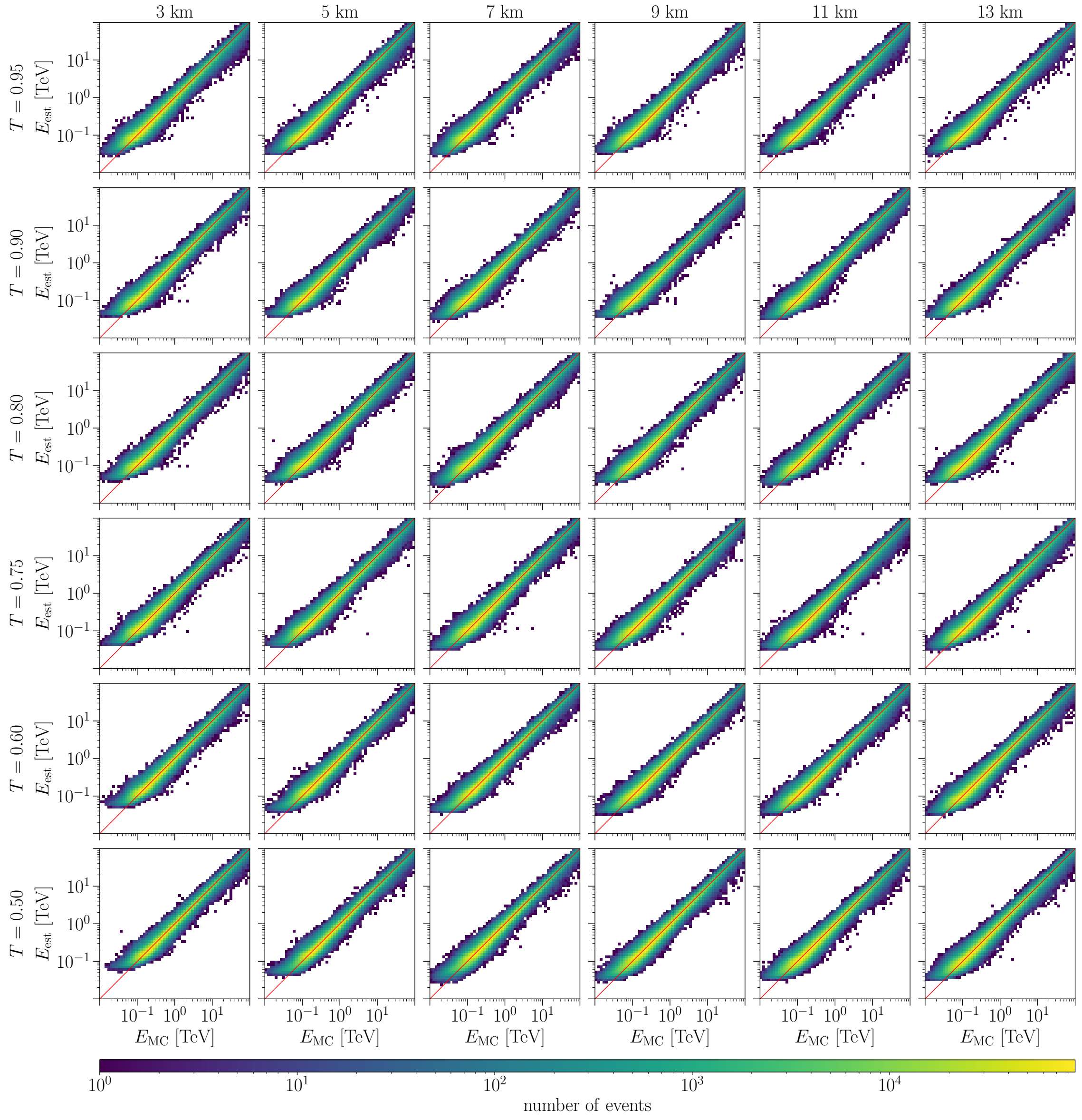

Figure 4.18: Migration matrices for the subarray of 15 MSTs for different transmission profiles. The data indicate the results of the energy reconstruction performed with RFs trained on adaptive MC simulations (clouds included). Each row represents a different cloud transmission and each column represents a different cloud height. Red line indicates $E_{\mathrm{est}} = E_{\mathrm{MC}}$.

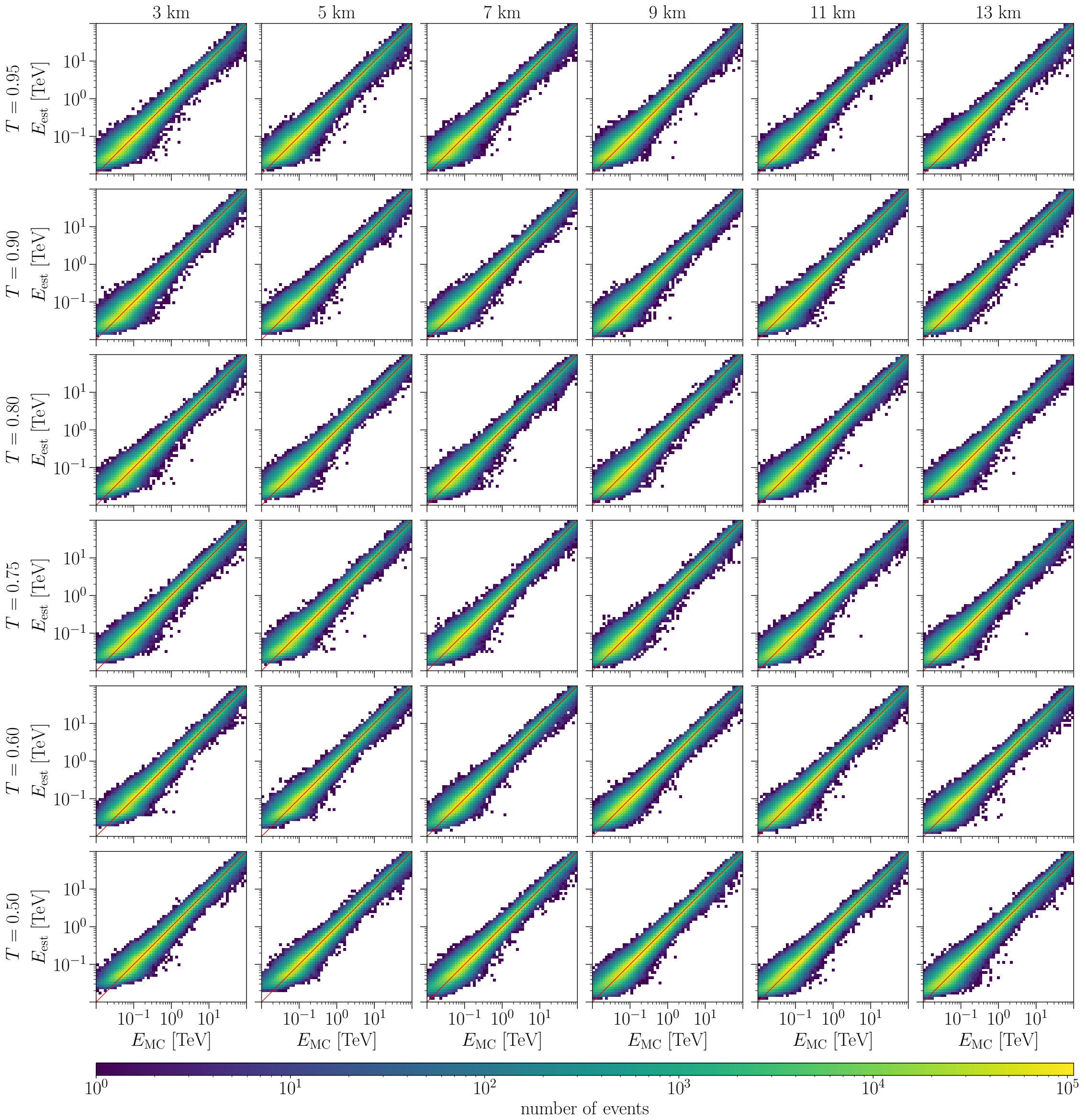

Figure 4.19: Migration matrices for CTAO-N array for different transmission profiles. The data indicate the results of the energy reconstruction performed with RFs trained on adaptive MC simulations (clouds included). Each row represents a different cloud transmission and each column represents a different cloud height. Red line indicates $E_{\mathrm{est}} = E_{\mathrm{MC}}$.

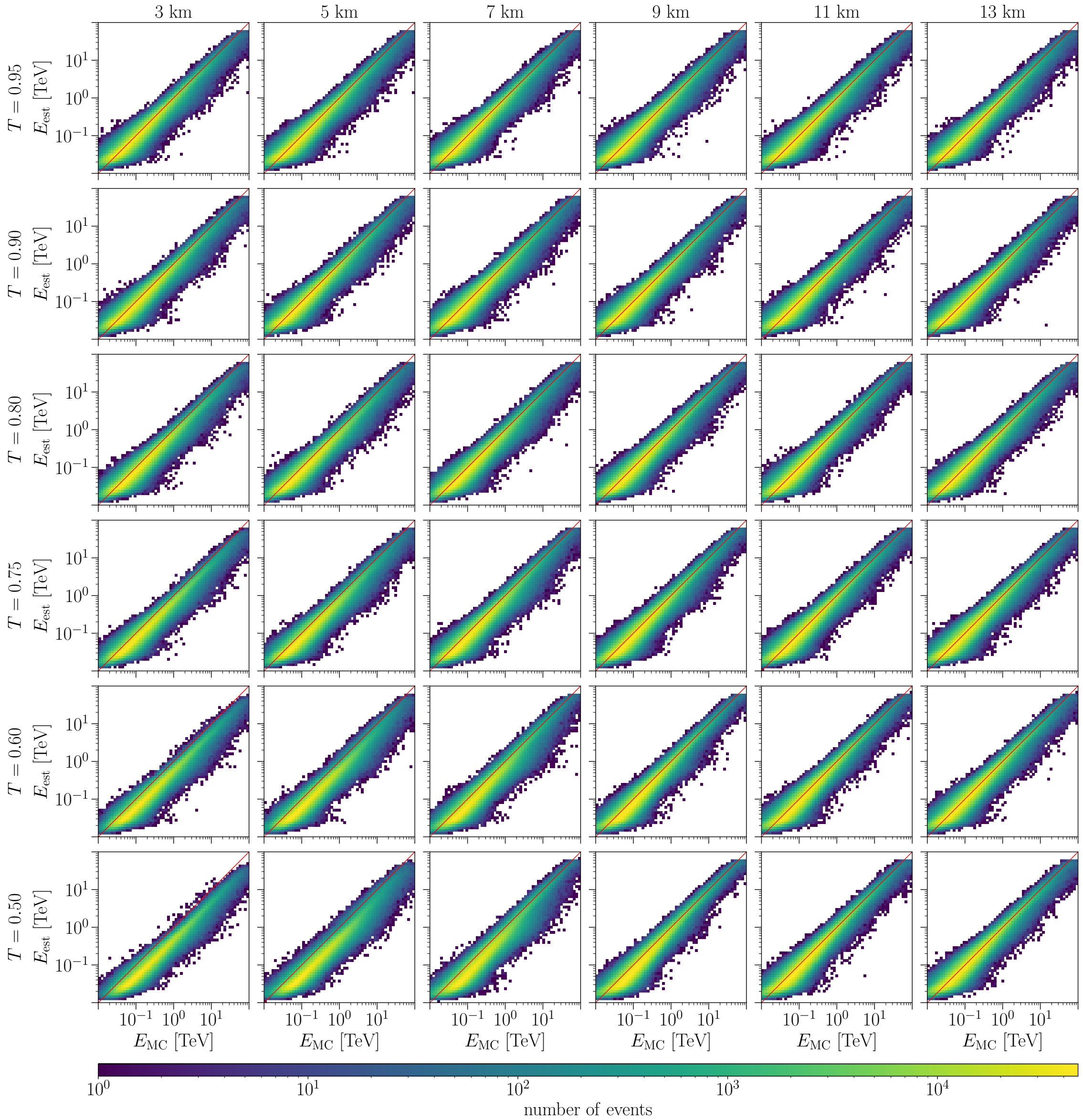

Figure 4.20: Migration matrices for the subarray of 4 LSTs for different transmission profiles. The data indicate the results of the energy reconstruction performed with RFs trained on standard (without clouds) MC simulations. Each row represents a different cloud transmission and each column represents a different cloud height.

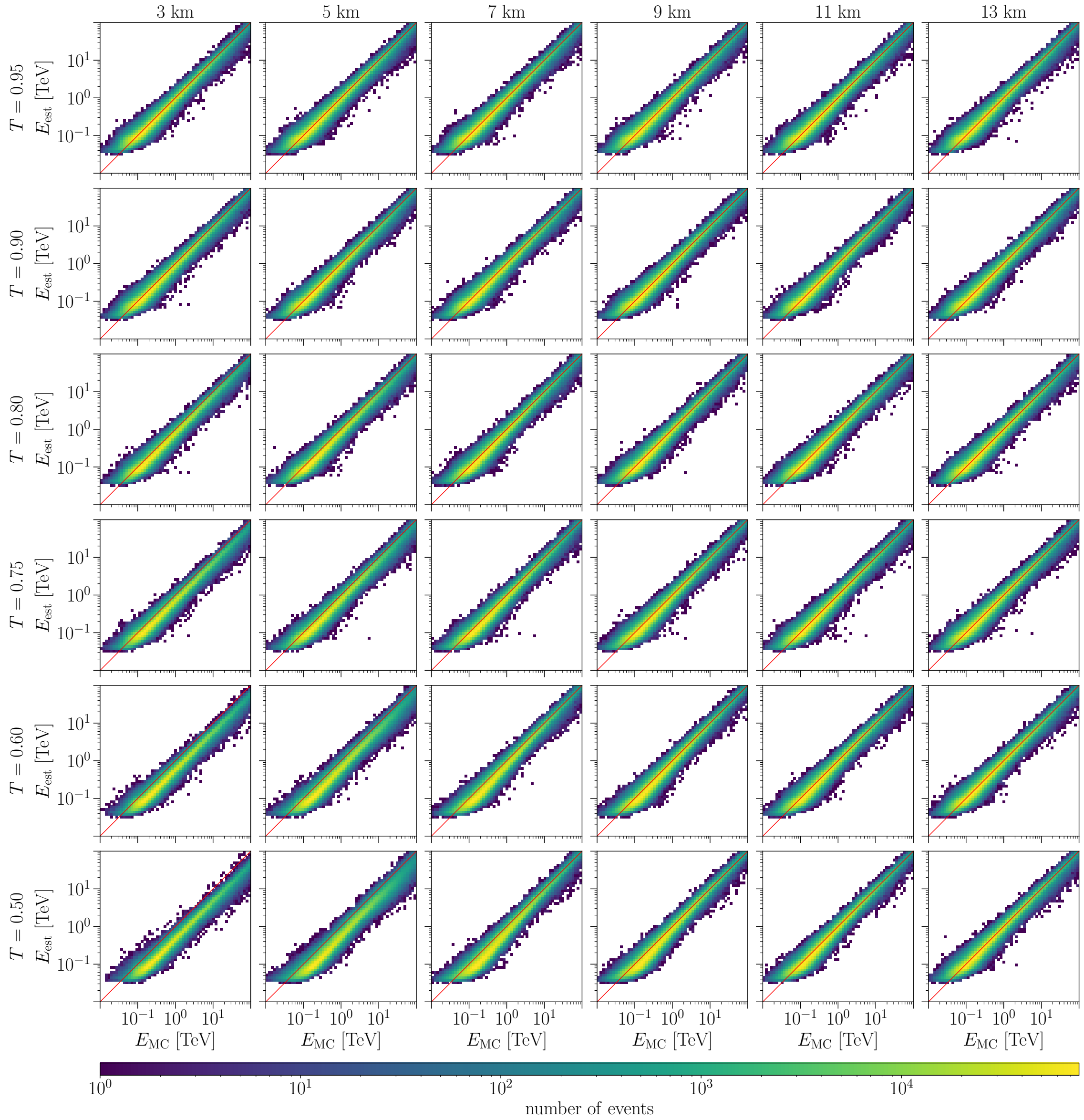

Figure 4.21: Migration matrices for the subarray of 15 MSTs for different transmission profiles. The data indicate the results of the energy reconstruction performed with RFs trained on standard (without clouds) MC simulations. Each row represents a different cloud transmission and each column represents a different cloud height. Red line indicates $E_{\mathrm{est}} = E_{\mathrm{MC}}$.

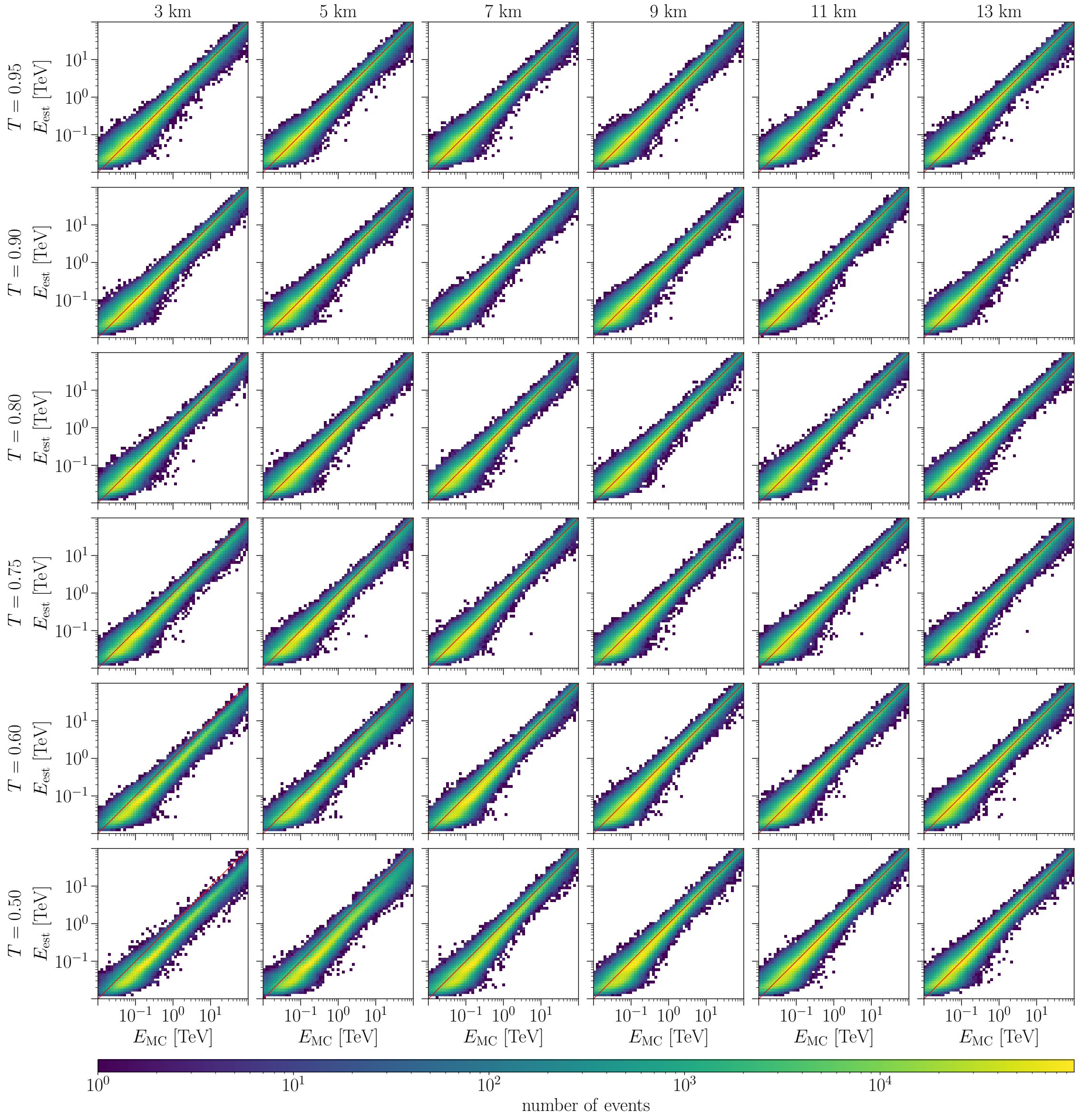

Figure 4.22: Migration matrices for CTAO-N array for different transmission profiles. The data indicate the results of the energy reconstruction performed with RFs trained on standard (without clouds) MC simulations. Each row represents a different cloud transmission and each column represents a different cloud height. Red line indicates $E_{\mathrm{est}} = E_{\mathrm{MC}}$.

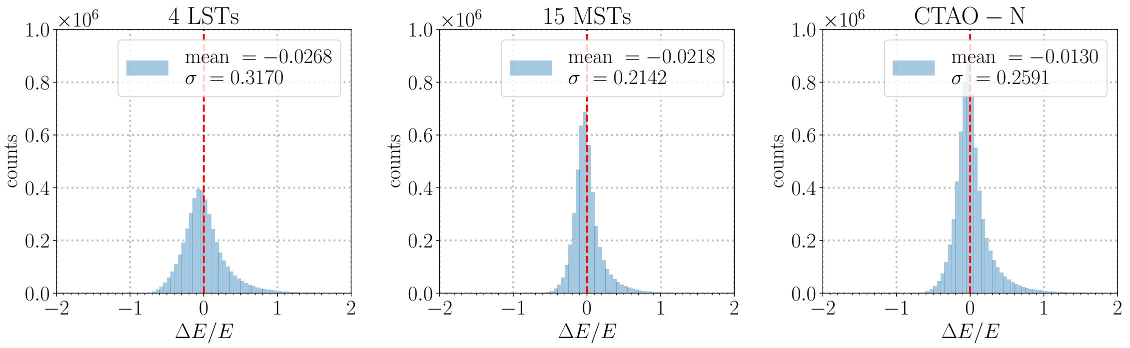

Figure 4.23: Distribution of $\Delta E/E$ for clean atmosphere. The vertical red line $\Delta E/E = 0$ represents the case of perfect energy reconstruction, i.e., no bias.

Figure 4.24 illustrates the energy bias observed in cloudless conditions for the subarray of 4 LSTs, 15 MSTs, and CTAO-N At energies above a few hundred GeV, the energy bias typically remains below a few percent ($\lesssim 5\%$ for MSTs and CTAO-N; $\lesssim 10\%$ for LSTs), indicating good performance of an energy estimator. However, the layout of the 4 LSTs shows a significant underestimation of the energies above ≈ 3 TeV, which is due to several factors, such as the low sensitivity of the LSTs to the high-energy gamma rays and thus poor statistics in the training sample, pixel saturation, a larger number of truncated images, etc. At the lowest energies ($\lesssim 100$ GeV), the energy bias increases rapidly due to the threshold effect, leading to the overestimation of energies of up to $\approx 75\%$ in the case of LSTs and CTAO-N and 90% in the case MSTs.

In contrast, Figure 4.25 illustrates the energy bias in the presence of clouds. When RF is trained on MC simulations assuming the same atmospheric conditions as the observations (the adaptive MC simulations; solid lines in the figure), there is no significant difference in the performance of an energy estimator compared to the case in which $T = 1$, regardless of the height and transmission of the cloud. Above ≈ 100 GeV, the (negative) energy bias is less than 5% in the case of MSTs and CTAO-N, and less than 10% in the case of LSTs. Again, in the case of LSTs reconstructed energies are significantly underestimated above 3 TeV for the reasons already mentioned, but the overall performance is equivalent to that in the clean atmosphere.

Next, the effects of clouds on the performance of the energy estimator when RF is trained on MC simulations for standard atmospheric conditions (Figure 4.25, dashed lines) are evaluated. In the presence of low clouds (≤ 5 km), the reconstructed energy above 100 GeV is underestimated over the entire energy range by the same amount, between 10% ($T = 0.95$) and 50% ($T = 0.50$), compared to E_{MC}. The degradation of the estimated energy in the presence of higher clouds shows strong energy-dependent effects. While the values at 100 GeV vary between 10% and 45% depending on transmission and cloud height, the bias at energies $\gtrsim 1$ TeV does not exceed 35% for a cloud at 7 km and 20% for 9 km. The large variations in the energies are a consequence of the properties of the longitudinal development of the air showers. In particular, the height of the shower maximum is proportional to the gamma-ray energy. This means that air showers initiated by higher energy gamma rays generally have their maximum lower in the atmosphere, closer to the ground. Only low clouds are significant for such gamma rays, while high clouds are usually above the maximum of the shower and have a small or even negligible influence. High clouds at 11 km

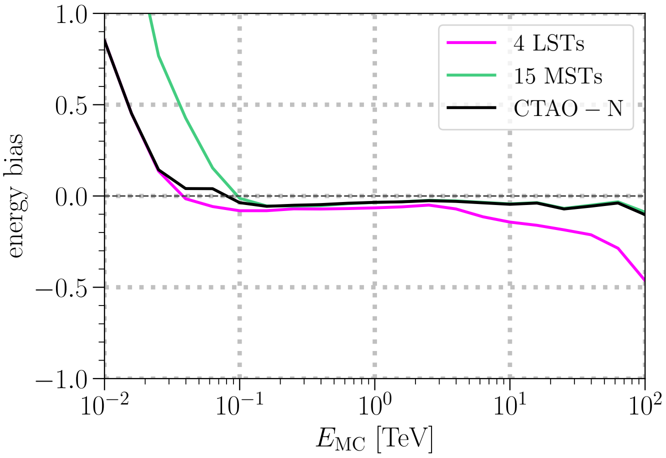

Figure 4.24: Energy bias as a function of simulated energy for CTAO-N and the corresponding subarrays when clouds are not present in the atmosphere.

and 13 km affect the estimated energy only in the energy range up to 1 TeV ($\lesssim$ 15% at 100 GeV and $\lesssim$ 5% at 1 TeV, while the values at 1 TeV are slightly higher in the case of 4 LSTs), which is to be expected since the shower maximum at higher energies is lower in the atmosphere, below the base of the mentioned clouds. At higher energies, clouds have small effect ($\lesssim$ 5%).

The results above show a comparison of the mean bias with respect to the type of MC simulations used for RF training for each bin of E_{MC}. However, the two energy estimates E_{est} for the same event with the true energy E_{MC} can also be compared directly by linking them through MC simulation parameters: E_{MC}, (x,y) coordinates of the simulated shower core position, the height of the 1st interaction, the depth of the shower maximum. Therefore, the change in E_{est} can be estimated. To determine the deviation between the reconstructed energies, the relative difference between the two estimated energies is calculated as $\Delta E_{\mathrm{est}} = E^{\star}_{\mathrm{est}}/E_{\mathrm{est}} - 1$, where $E^{\star}_{\mathrm{est}}$ is the estimated energy when the standard MC simulations are used to train the RF algorithm, and E_{est} is the estimated energy when the atmospheric conditions of the MC simulations used for RF training match the atmospheric conditions during observations. All events detected both with and without clouds that survive the quality cuts are used. Further details on the distribution of ΔE_{est} for the Crab-like source can be seen in Figure 4.26. The distribution of ΔE_{est} is unimodal and appears to be relatively symmetric, with no significant skewness or obvious outliers in most cases. For clouds between 5 and 11 km, for which $T \leq 0.60$, there is a slight skewing of the data to the left or right, as not all data are affected by clouds in the same way. For example, in the case of the cloud at 7 km altitude, for which $T = 0.50$, the distribution is skewed to the left, which is not unexpected given the bias (Figure 4.25), since the majority of events are affected by the cloud and only the events with the highest energies are not affected. In contrast, the situation is exactly the opposite for the cloud at 11 km altitude, where only the low energy events are affected.

The most obvious effect is a decrease in the number of detected events, as described in the previous sections. Furthermore, the distributions tend to shift to the left of $\Delta E_{\mathrm{est}} = 0$ (to lower values) by the amount dependent on the cloud transmission and height. Lower clouds with low transmission have a greater influence on the ΔE_{est} distribution than higher and more transparent clouds. For example, if a cloud is present in the atmosphere at an altitude of 3 km with the transmission of $T = 0.50$, the mean value of $\Delta E_{\mathrm{est}} \approx -0.50$, while for that 13 km for $T = 0.95$, the mean value is ≈ -0.001. There are no substantial differences in the distribution of the individual subarrays compared to CTAO-N

The width of the distribution seems to be relatively consistent across the range for most of the cases. However, there is a visible change in the distribution width for clouds with lower transmission ($T < 0.90$) at altitudes between 5 and 11 km, where the standard deviation varies from 0.02 to 0.08. For high clouds at 13 km, the width of the distribution is very similar regardless of transmission. In this particular case, most of the air showers reach their maximum below the cloud, so the reconstructed energies of both low-energy and high-energy events are underestimated by a similar and very small amount compared to the case where there are no clouds in the atmosphere or the training sample used for the analysis corresponds to the test sample in terms of atmospheric conditions. The width of the distribution is similar even with low cloud cover at 3 km altitude. Since the clouds are very low, most air showers reach their maximum above the cloud. Thus, energies are uniformly underestimated over the whole energy range and the variations in the ΔE_{est} are small.

However, in the presence of mid-level clouds, the picture is somewhat more complicated, as the air showers are no longer attenuated to the same degree. The height of the shower maximum can vary greatly even for events with the same energy. Therefore, the amount by which the reconstructed energy is underestimated depends on the fraction of Cherenkov photons that are affected by the cloud. In general, higher energy showers reach their maximum deeper in the atmosphere and they are, on average, less influenced by the cloud than lower energy showers. Therefore, larger fluctuations are observed and the distributions become broader. This is particularly noticeable for clouds at 7 km and 9 km altitude, considering that the average maximum height of the air showers is at these altitudes. Note that the transmission itself does not affect the width of the distribution, only the number of events in the corresponding energy bins and the peak position.

The mean of the relative difference between two estimated energies as a function of the simulated energy E_{MC} is shown in Figure 4.27. In the presence of low clouds (≤ 5 km), the reconstructed energy is underestimated by an additional factor of $\approx \frac{1}{T}$ when the standard MC simulations are used in the training sample, compared to the case when the adaptive MC simulations are used. In the presence of clouds at intermediate altitudes (between 7 and 9 km), the reconstructed energy is underestimated by an additional $\lesssim 45\%$ at 100 GeV and $\lesssim 30\%$ at 1 TeV, depending on the transmission, compared to the case when adaptive MC simulations are used. On the other hand, high transmission clouds ($T \geq 0.80$) have a small effect, less than 10%, over the whole energy range. The effects of high clouds (≥ 11 km) are very small ($\lesssim 5\%$) at energies above 1 TeV (for $T \geq 0.80$ over the whole energy range) and less than 20% at 100 GeV. Regarding the effects of cloud transmission, clouds with a high transmission $T \geq 0.90$ have a significant effect only at altitudes of ≤ 5 km, where the relative differences are proportional to $\frac{1}{T}$. At lower transmission values, the influence of clouds becomes stronger with decreasing transmission and altitude. Significant differences between the performance of the individual arrays are only visible below 100 GeV for $T \leq 0.75$, where the threshold effects are dominant. Note again the visible spread of distribution for clouds with lower transmissivity ($T < 0.90$) at altitudes between 5 and 11 km.

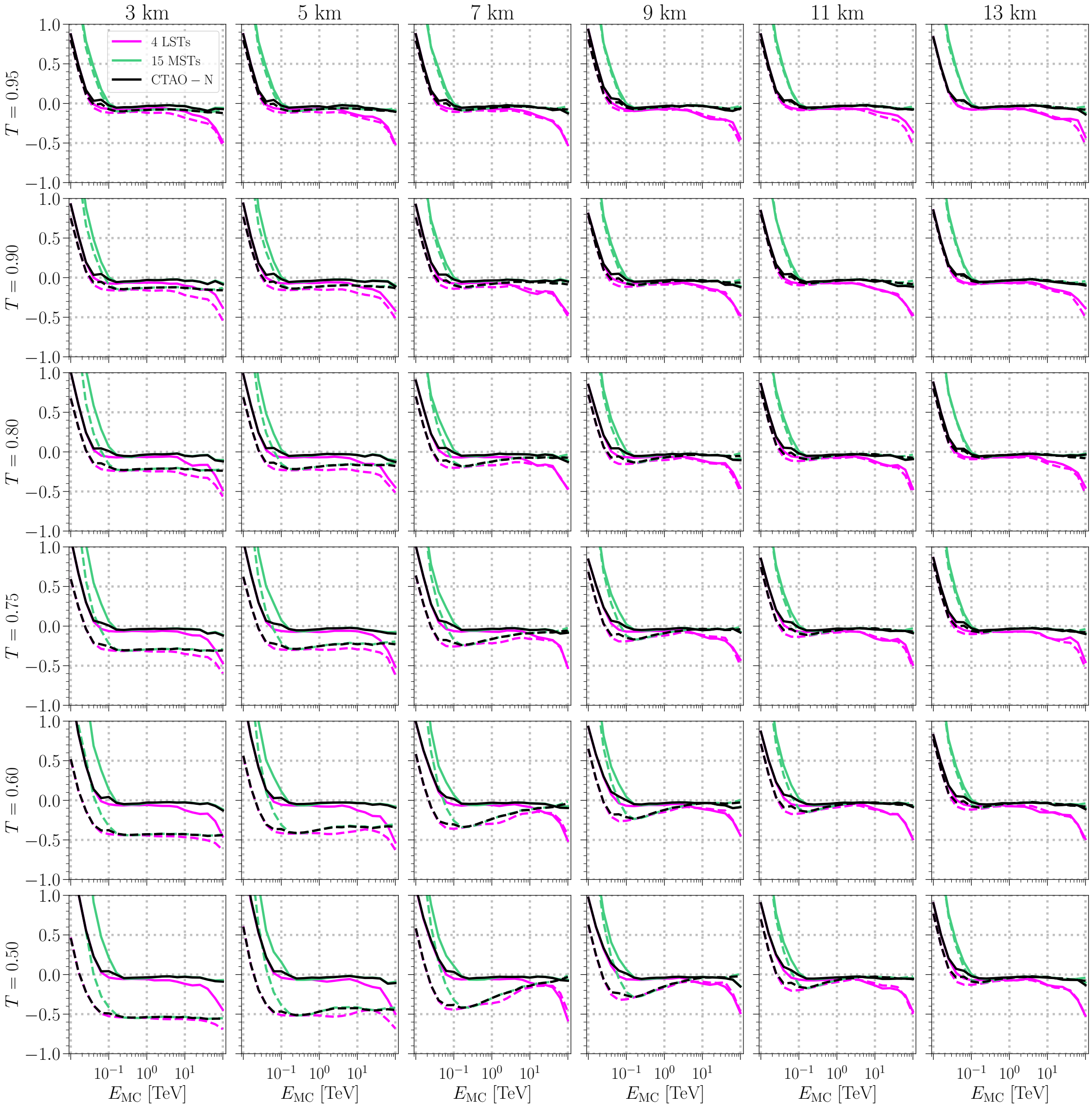

Figure 4.25: Energy bias as a function of simulated energy E_{MC} for CTAO-N and the corresponding subarrays. The solid lines show the results of the analysis based on the RF algorithm trained on MC simulations assuming the same atmospheric conditions as the observations, while the dashed lines show the results of the analysis based on the RF algorithm trained on the standard MC simulations. The columns represent the height of the cloud, while the rows represent the transmission of the cloud.

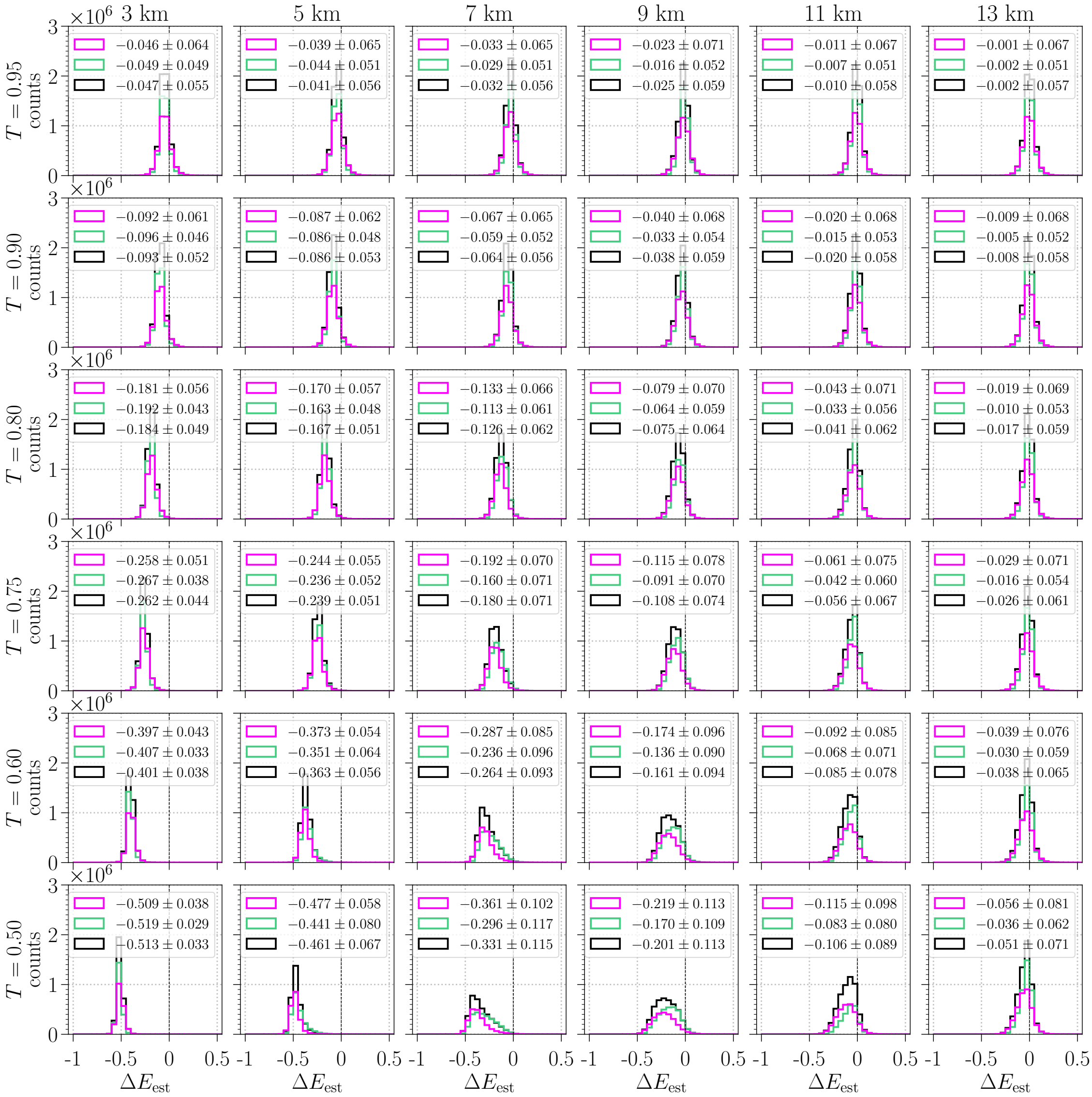

Figure 4.26: A distribution of ΔE_{est} for CTAO-N and the corresponding subarrays. The colors black, green, and pink represent CTAO-N, 15 MSTs, and 4 LSTs, respectively. The column represents the height of the cloud, while the row represents the transmission of the cloud. For each case and array, the mean and width of the distribution are reported.

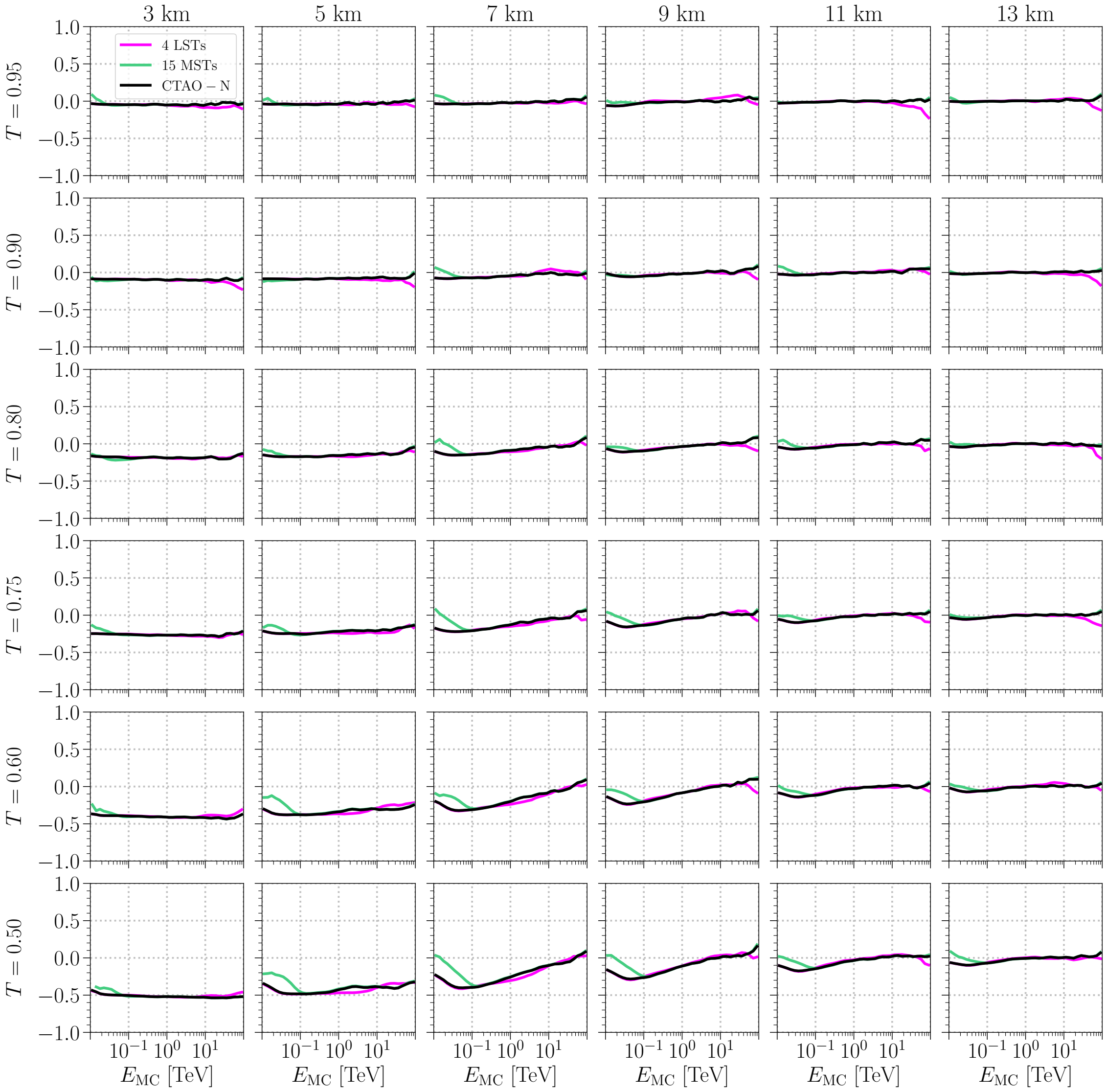

Figure 4.27: Relative difference of two estimated energies as a function of simulated energy for CTAO-N and the corresponding subarrays. The column represents the height of the cloud, while the row represents the transmission of the cloud.

4.5 Energy resolution

A standard way to measure accuracy in energy reconstruction is to calculate the energy resolution. There are many definitions of energy resolution, but most commonly energy resolution is calculated as the standard deviation of a Gaussian fit to the $\Delta E/E$ distribution or as 68% containment. Even within the latter method, there are variations. For example, some authors prefer to compute it as a central 68% containment, while others compute it as the smallest interval containing 68% of the distribution. For consistency with section 4.4, the energy resolution is calculated as the standard deviation of the Gaussian fit. The energy resolution of an IACT refers to the ability of the telescope to accurately measure the energy of the detected gamma ray. In other words, it is a measure of how well the telescope can distinguish between gamma rays of different energies. Energy resolution can be expressed as a percentage of the true energy of the gamma rays, although is typically expressed as a dimensionless number. For example, an energy resolution of 10% means that if the telescope detected a gamma ray with an energy of 1 TeV, the energy will be reconstructed in the range from 0.9 TeV to 1.1 TeV with a 68% confidence interval. The lower the energy resolution, the better. More strict cuts improve energy resolution but at the cost of a smaller effective area.

The energy resolution in a clean atmosphere is shown in Figure 4.28a. In the case of 4 LSTs, the energy resolution varies between 16% and 30%. The subarray of 15 MSTs shows slightly worse energy resolution at energies below 100 GeV (up to 40%), while at higher energies it is improved compared to the LSTs, averaging 10%. At lower energies ($\lesssim$ 100 GeV), CTAO-N has an energy resolution comparable to that of LSTs, while at higher energies the energy resolution of CTAO-N is comparable to that of MSTs.

Energy resolution in the presence of clouds is shown in Figure 4.29. As expected, the effects of clouds on the energy resolution are rather small when adaptive MC simulations are used in the training sample (solid lines), since the overall distribution of $\Delta E/E$ (compared to the clear atmosphere case) does not change very much. Above 100 GeV, the relative differences between the energy resolution in the presence of clouds and the energy resolution in the clean atmosphere are on average less than 10% and show no energy-dependent or layout-dependent effects. Below 100 GeV, the differences are larger (up to 40%) in the case of 15 MSTs, which is not unusual given the poor flux sensitivity of MSTs at these energies. The same effect is also observed for LSTs and CTAO-N, but only for dominant clouds where a decrease in detection efficiency becomes significant ($T \leq 0.75$, height $\leq$ 9 km).

The energy resolution in the presence of clouds when the standard MC simulations are used in the training sample is shown in Figure 4.29 (dashed lines). However, energy resolution is not the most useful measure when assessing the effect of clouds on energy reconstruction, especially when the standard MC simulations are used in the training sample. As shown in section 4.4, the reconstructed energies are more or less underestimated when the analysis of data taken in the presence of clouds is based on RFs for the standard atmosphere. In such cases, there is a strong negative bias over the entire energy range or only part of it. Since the standard definition of energy resolution does not account for the bias, this results in apparently better energy resolution in cases where standard MC simulations are used in the training sample. This would also be the case if the energy resolution were calculated as a 68% containment.

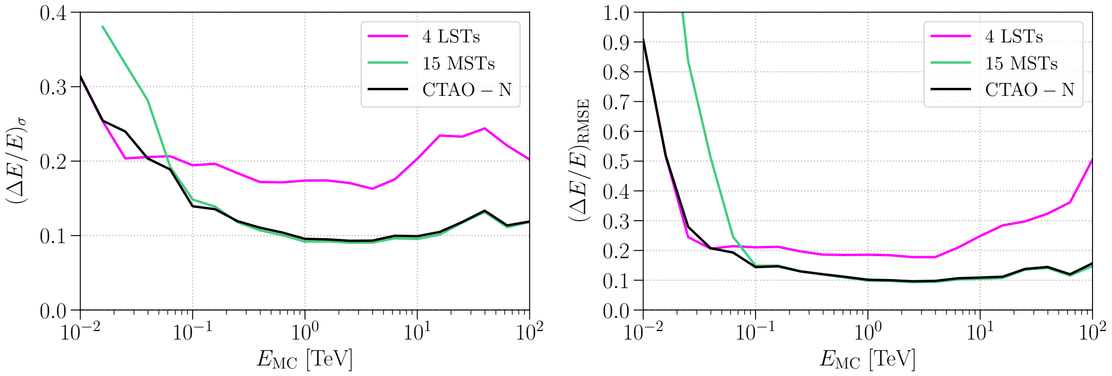

(a) energy resolution **(b)** root mean square error

Figure 4.28: a) Energy resolution and b) root mean square error of the CTAO-N array and its corresponding subarrays.

Therefore, the root mean square error (RMSE) is used instead of the standard deviation. The mean square error (MSE) of an estimator $\hat{\delta}$ of a parameter δ is the function of δ defined by $\mathrm{MSE}(\hat{\delta}) = \mathbb{E}(\hat{\delta}-\delta)^2$. Given that:

$$\mathbb{E}(\hat{\delta}-\delta)^2 = \underbrace{\mathbb{E}(\hat{\delta})^2}_{\sigma^2(\hat{\delta})} + \underbrace{\mathbb{E}(\delta^2)}_{[\mathbb{E}(\hat{\delta})]^2+\delta^2} - 2\delta\mathbb{E}(\hat{\delta}), \tag{4.11}$$

which can be expressed as:

$$\mathbb{E}(\hat{\delta}-\delta)^2 = \sigma^2(\hat{\delta}) + \underbrace{[\mathbb{E}(\hat{\delta})-\delta]^2}_{\mathrm{bias}(\hat{\delta})^2}, \tag{4.12}$$

yielding the root mean square error as:

$$\mathrm{RMSE}(\hat{\delta}) = \sqrt{\sigma^2(\hat{\delta}) + \mathrm{bias}(\hat{\delta})^2}. \tag{4.13}$$

Note that in the cases of the unbiased estimator, $\mathrm{bias}(\hat{\delta}) = 0$, the RMSE is equal to the standard deviation. The RMSE in the clear atmosphere is shown in Figure 4.28b. In the energy range between 100 GeV and 1 TeV, where the energy bias approaches zero (Figure 4.24), the RMSE is similar to the energy resolution (Figure 4.28a). On the other hand, if the bias is strong (whether positive or negative), the RMSE increases by the square of the bias. In the case of LSTs, the RMSE is 0.21 at 100 GeV and 0.19 at 1 TeV. In the case of MSTs and CTAO-N, the RMSE is 0.14 at 100 GeV and 0.10 at 1 TeV. Below 100 GeV, the RMSE increases up to 0.90 for all telescope arrays due to the high positive energy bias.

The RMSE in the presence of clouds is shown in Figure 4.30. As expected, the observed effects of clouds are rather small when adaptive MC simulations are used in the training sample (solid lines), since the overall bias and energy resolution do not change significantly compared to the clear atmosphere case. Apart from the features resulting from the behavior of the energy resolution (as described above), there are no significant differences between the effects of the different clouds. It can be concluded that the error in energy reconstruction in the presence of clouds when the adaptive MC simulations are used in the training sample is not significantly increased compared to the error in energy reconstruction in the clean atmosphere.

However, when the standard MC simulations are used in the training sample (Figure 4.30, dashed lines), the effects of clouds become even more severe, as even a factor of 3 in the error in the energy reconstruction can be expected. In the presence of low clouds (≤ 5 km), the RMSE of LSTs in the energy range from 100 GeV to 10 TeV is between 0.19 and 0.57, depending on the transmission. For example, for a cloud at 3 km altitude for which $T = 0.50$, the RMSE at 1 TeV is 0.55, while the RMSE in the clean atmosphere at the same energy is 0.18, which corresponds to a $\approx 200\%$ increase of the error in the energy constructions compared to the RMSE for the clean atmosphere. In middle clouds, the observed energy-dependent effects are more pronounced. The error in the energy reconstruction at 100 GeV increases to 0.47 for 7 km and 0.37 for 9 km, corresponding to an increase of 110% and 75%, respectively, compared to $T = 1$. At 1 TeV the RMSE is smaller, 0.40 for 7 km and 0.25 for 9 km, corresponding to an increase of 116% and 32%, respectively. At higher energies up to 10 TeV, the RMSE drops to the level of the RMSE in a clean atmosphere. Note that above 10 TeV the RMSE is very large in all cases, due to the naturally large energy bias of the LSTs at these energies. High clouds at 11 km increase the error in the energy reconstruction only for $T \leq 0.75$, by 30% at 100 GeV and less than 10% at 1 TeV in the worst-case scenario. Clouds at 13 km increase the error in the energy reconstruction by only a few percent over the entire energy range compared to that in a clean atmosphere.

The increase in the error in energy reconstruction is also visible in the case of MSTs. When low clouds (≤ 5 km) are present in the atmosphere, the RMSE at 100 GeV ranges from 0.15 to 0.65, depending on cloud transmission and height. This corresponds to an increase of up to 320% compared to $T = 1$. It should be noted that for energies above 100 GeV, the RMSE of MSTs remains constant over the entire energy range when the cloud is at 3 km altitude. However, for a cloud at 5 km altitude, the RMSE above 1 TeV is slightly lower, with a maximum value of 0.43, corresponding to an increase of $\approx 300\%$. In the intermediate clouds, the energy-dependent effects are more pronounced, similar to those observed in LSTs. The error in the energy reconstruction at 100 GeV increases to 0.40 for 7 km and 0.30 for 9 km, corresponding to increases of 227% and 149%, respectively, compared to $T = 1$. At 1 TeV, the RMSE increases by up to 200% and 80% for clouds at 7 and 9 km, respectively. At higher energies, the RMSE decreases to the level of the RMSE in a clean atmosphere. In the case of high clouds at 11 and 13 km, their impact on energy reconstruction is minimal above 1 TeV, and the RMSE reaches a peak of 0.17 and 0.20, respectively, at 100 GeV (representing a 50% and 80% increase compared to a clear atmosphere).

Above 100 GeV, the performance of CTAO-N is dominated by MSTs, while at lower energies it is comparable to that of LSTs. Note that in all cases the RMSE increases very sharply at energies below 100 GeV, which is due to a large positive bias explained in section 4.4. Regarding the effects of cloud transmission, clouds with a high transmission $T \geq 0.90$ have a significant effect only at altitudes of ≤ 5 km. At lower transmission values, the influence of clouds becomes stronger with decreasing transmission and altitude.

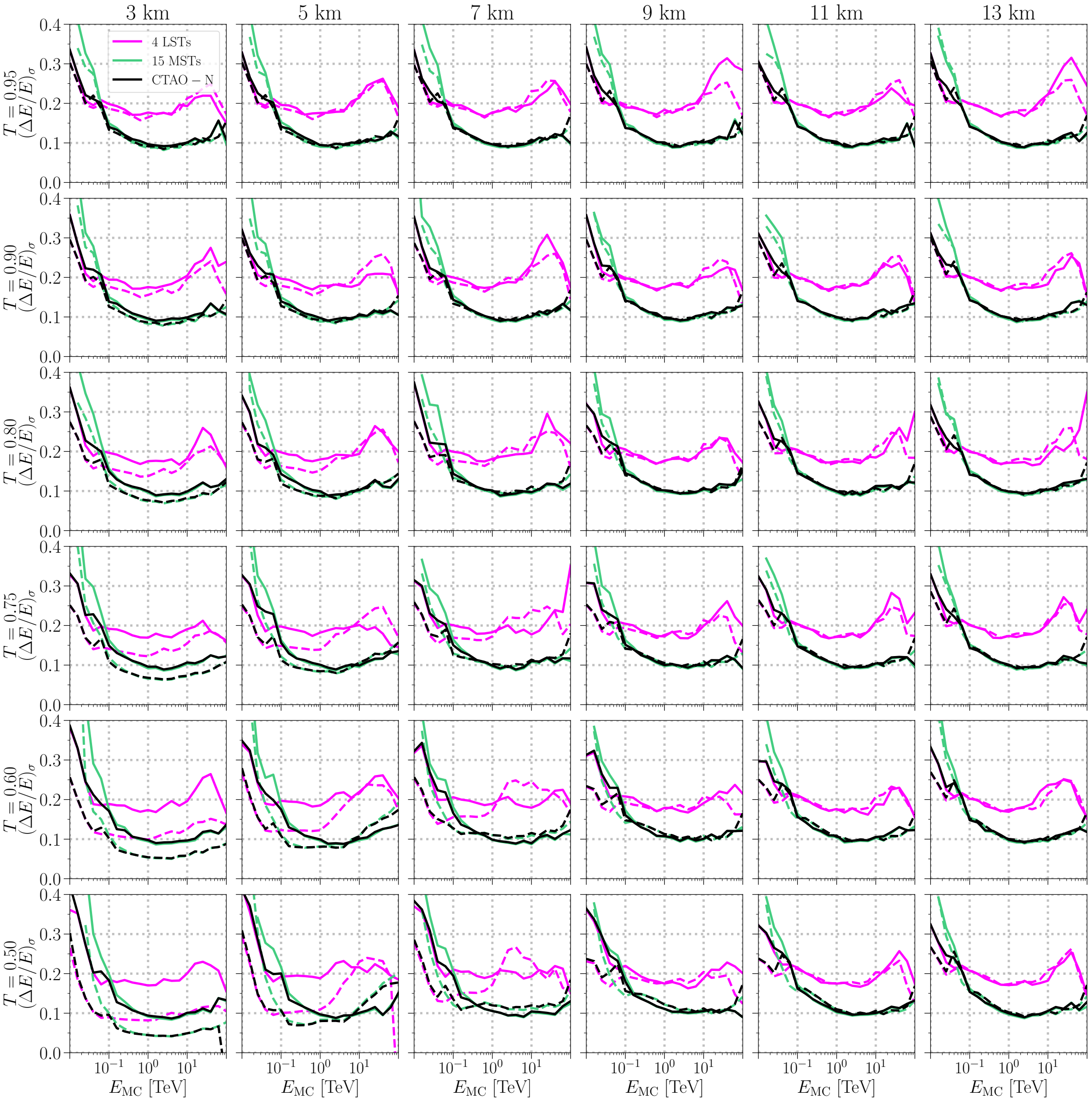

Figure 4.29: Energy resolution as a function of simulated energy for CTAO-N and the corresponding subarrays. The solid lines show the results of the analysis based on the RF algorithm trained on MC simulations assuming the same atmospheric conditions as the observations. The dashed lines show the results of the analysis based on the RF algorithm trained on the standard MC simulations. The column represents the height of the cloud, while the row represents the transmission of the cloud.

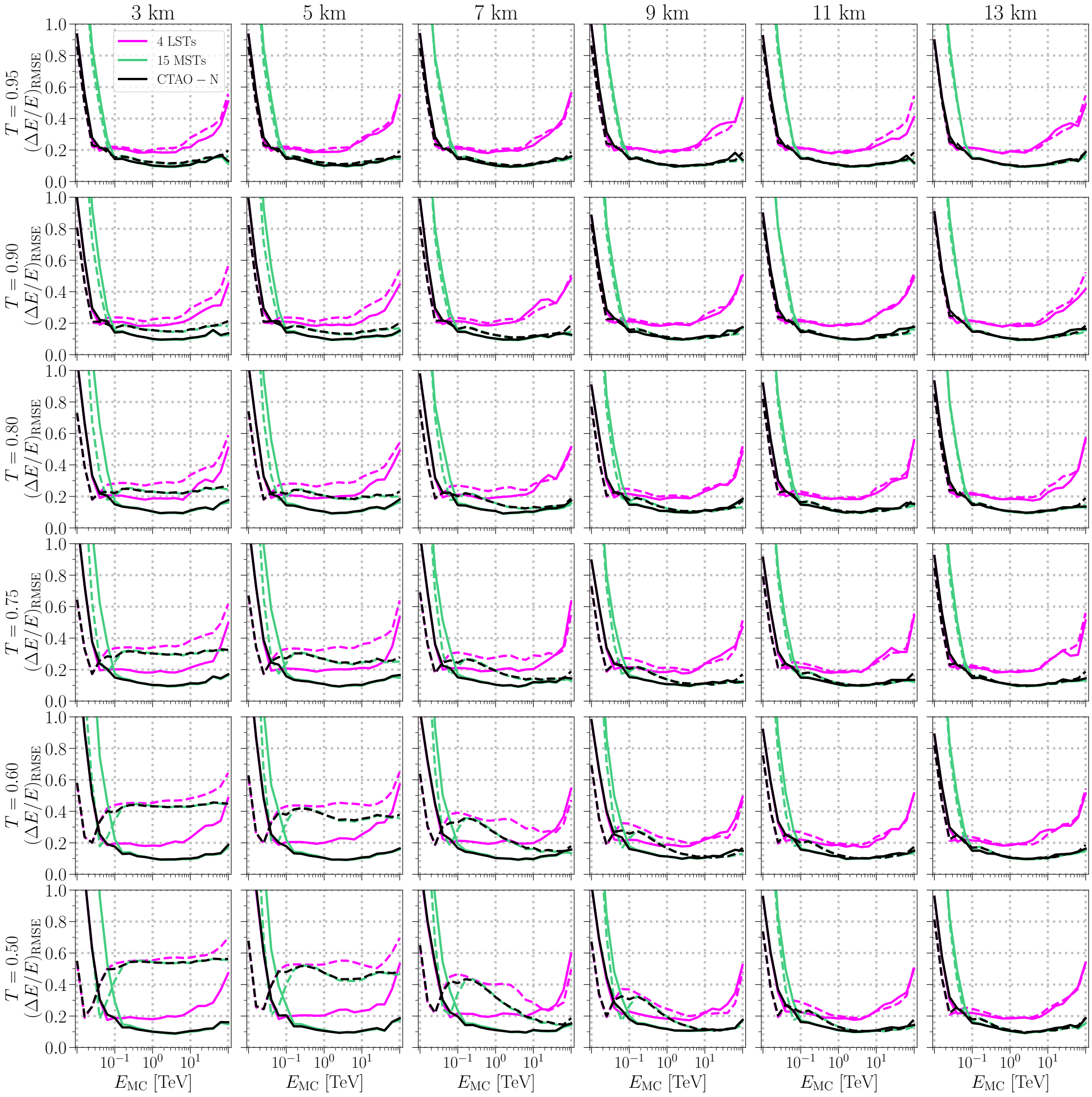

Figure 4.30: Root mean square error as a function of simulated energy for CTAO-N and the corresponding subarrays. The solid lines show the results of the analysis based on the RF algorithm trained on MC simulations assuming the same atmospheric conditions as the observations. The dashed lines show the results of the analysis based on the RF algorithm trained on the standard MC simulations. The column represents the height of the cloud, while the row represents the transmission of the cloud.

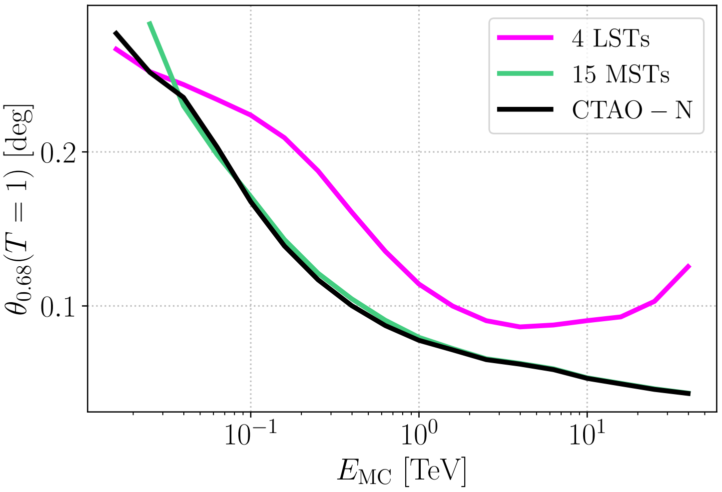

Figure 4.31: Angular resolution as a function of simulated energy for CTAO-N and the corresponding subarrays when clouds are not present in the atmosphere.

4.6 Angular resolution

The angular resolution is a measure of the accuracy with which the origin of the gamma-ray source can be reconstructed with the system of IACTs. It results from the distribution of the angular distance between the true and the reconstructed gamma-ray direction, i.e. the distribution of the parameter θ. The angular resolution θ_{68} is defined as the containment radius of 68% of the gamma rays that fall within a certain bin of the true (simulated) energy. The angular resolution in the cloudless atmosphere is shown in Figure 4.31. In the case of 4 LSTs, the angular resolution varies between 0.27° at an energy of 15 GeV and approaches the best performance between 150 and 250 GeV with an angular resolution of 0.08°. In the case of 15 MSTs and CTAO-N, the angular resolution varies from 0.28° at 25 GeV to an excellent angular resolution of 0.04° above 15 TeV.

As shown in section 4.1.3, the reconstruction of the position of the source is based on the orientation of the major axis of the Cherenkov images. The deviations from the nominal shower axis due to the presence of clouds are small. In contrast to the energy reconstruction, where lower clouds increase the energy resolution and the negative bias over the entire energy range by a higher factor than higher clouds (with the same transmission), clouds at different heights (and with the same transmission) can cause an improvement (e.g. by rejecting poorly defined images) or degradation of direction reconstruction (e.g. in the case of air shower of lower energies and intermediate clouds, where only the head of the shower is significantly affected, increasing the width of θ distribution). This leads to a complicated relationship between angular resolution and cloud base height. However, for the layout of 4 LSTs (Figure 4.32), the effects remain below ±20% for clouds at or below 5 km (or $T \leq 0.6$) and below ±10% for higher clouds bases and transmission values. In the case of MSTs (Figure 4.34) or the whole CTAO-N (Figure 4.36), the angular resolution changes by ±5% for clouds above 7 km (or $T \geq 0.6$) and by ±10% for the rest of the cases. The use of standard Monte Carlo simulations does not lead to significant changes in the angular resolution compared to the case of the adaptive MC simulations (Figures 4.33, 4.35, 4.37).

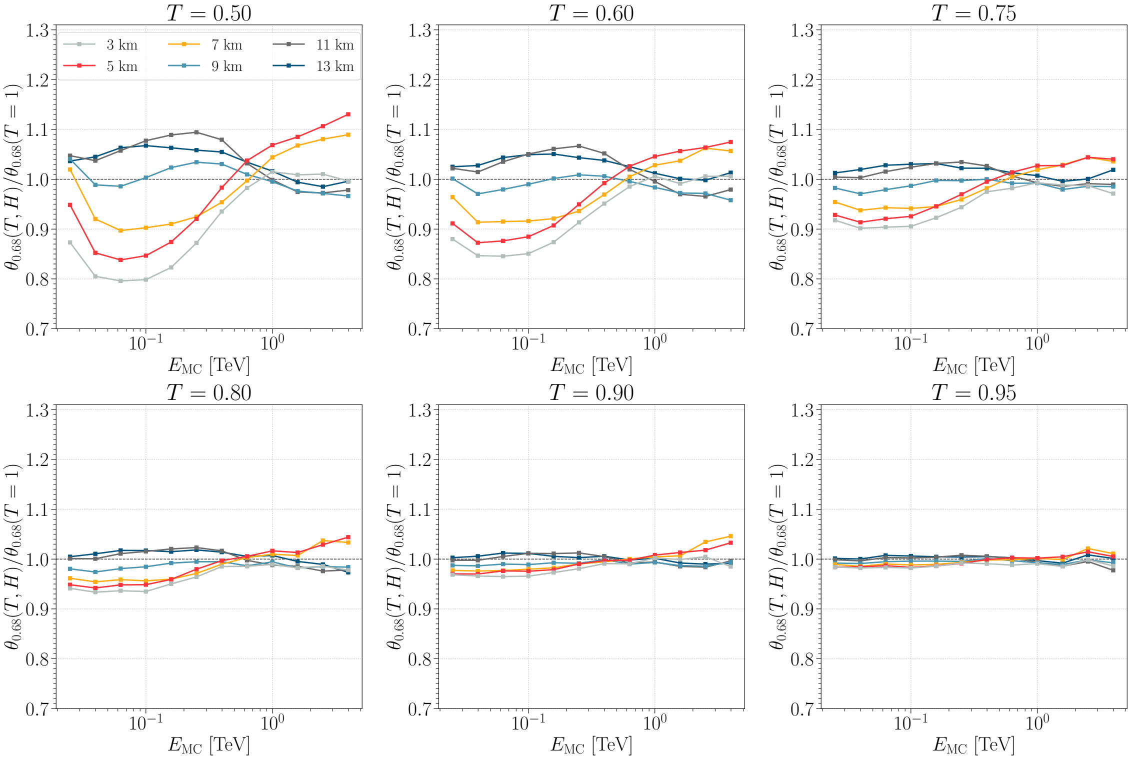

(a) 4 LSTs, height dependence of angular resolution ratio for fixed transmission

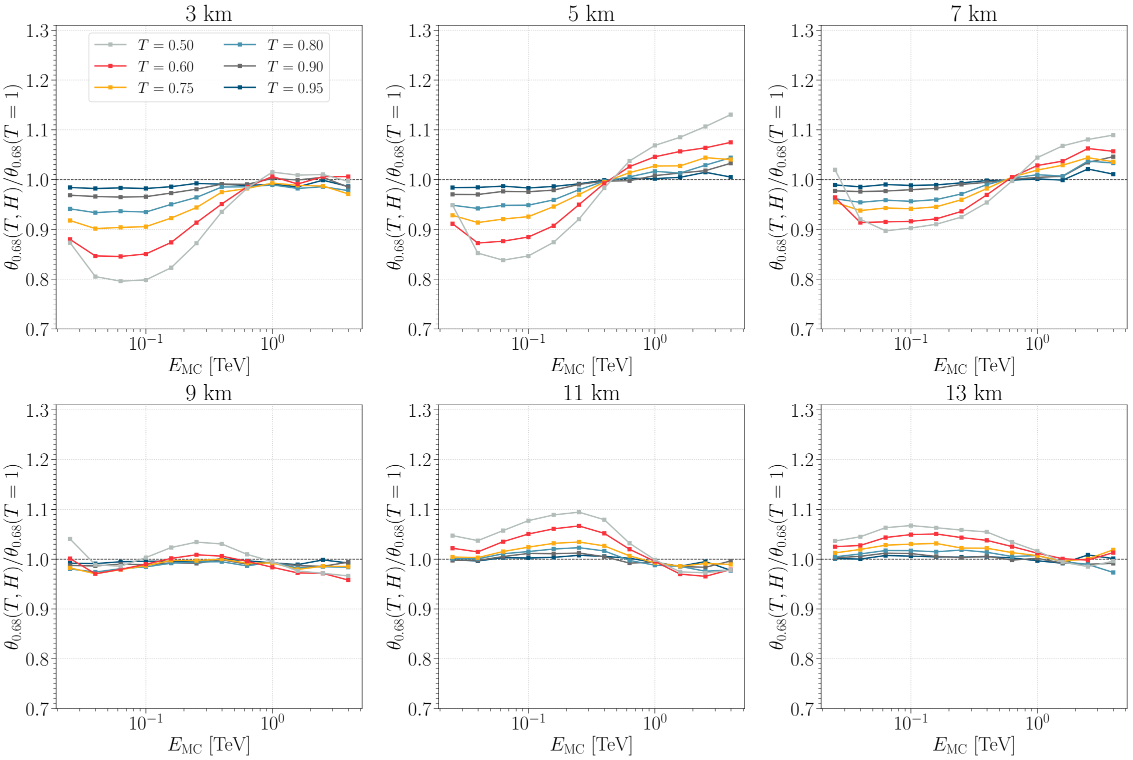

(b) 4 LSTs, transmission dependence of angular resolution ratio for fixed height

Figure 4.32: Angular resolution cloud-to-clear ratio for the layout of 4 LSTs for the case when adaptive MC simulations are used for DirLUT and RFs training.

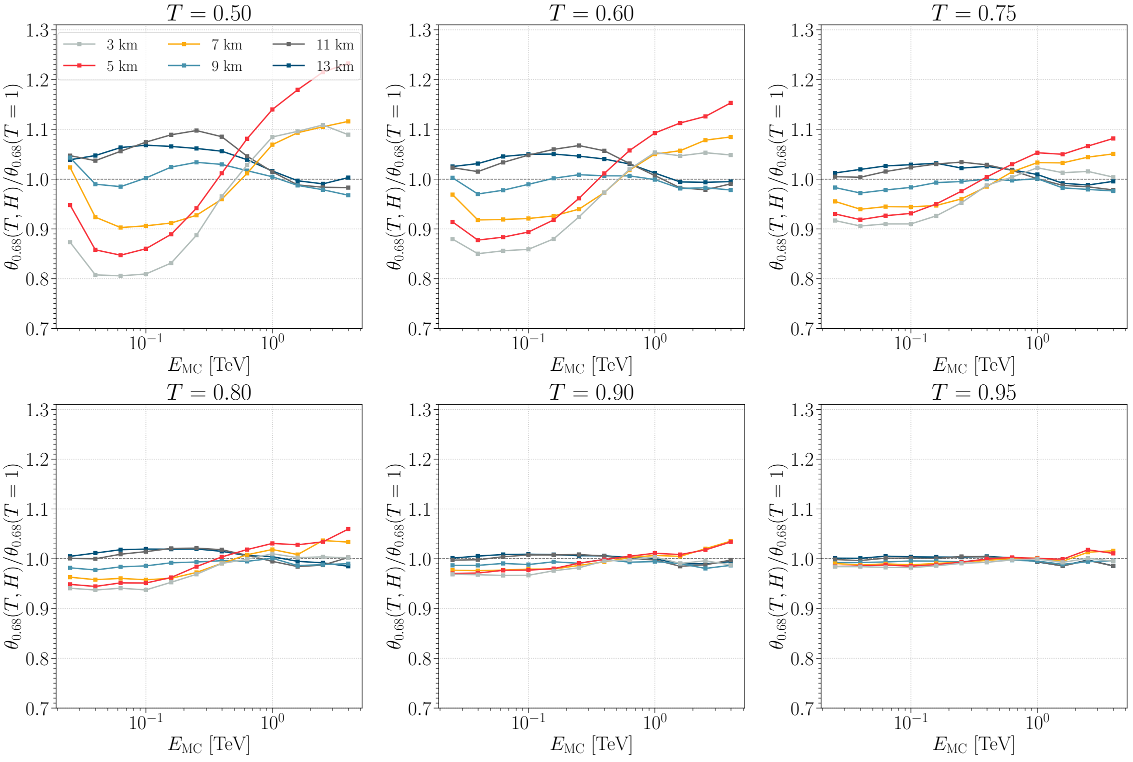

(a) 4 LSTs, height dependence of angular resolution ratio for fixed transmission

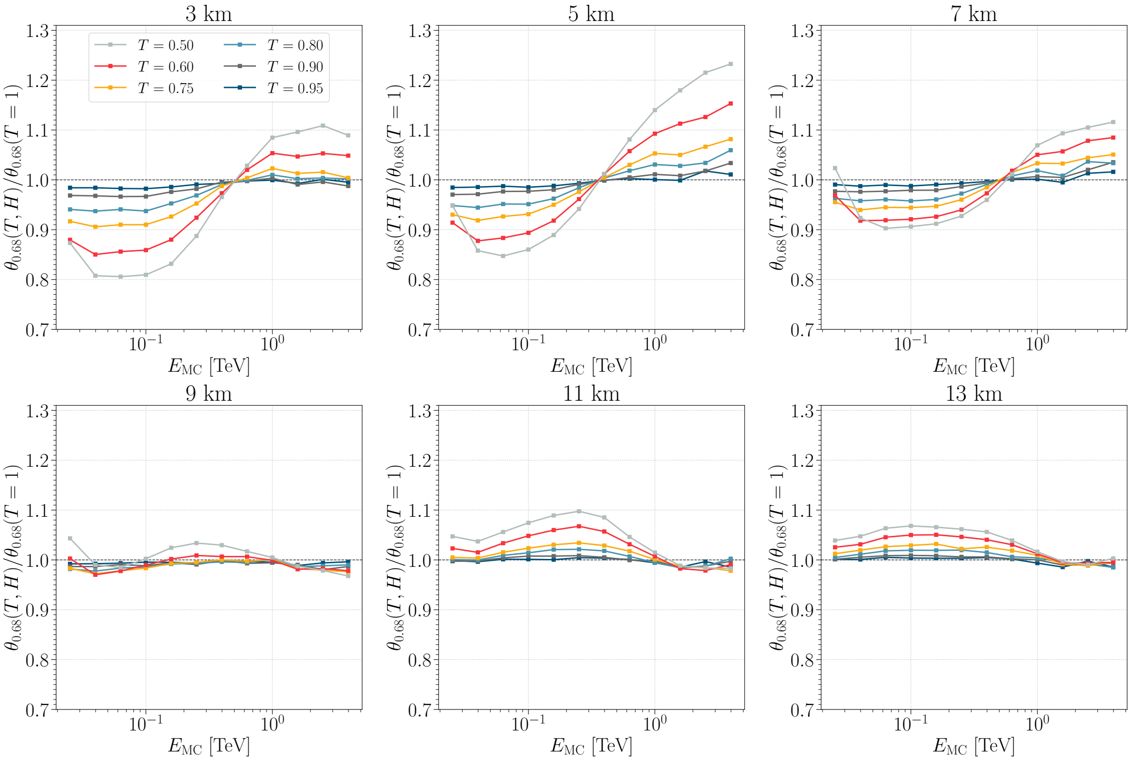

(b) 4 LSTs, transmission dependence of angular resolution ratio for fixed height

Figure 4.33: Angular resolution cloud-to-clear ratio for the layout of 4 LSTs for the case when standard MC simulations are used for DirLUT and RFs training.

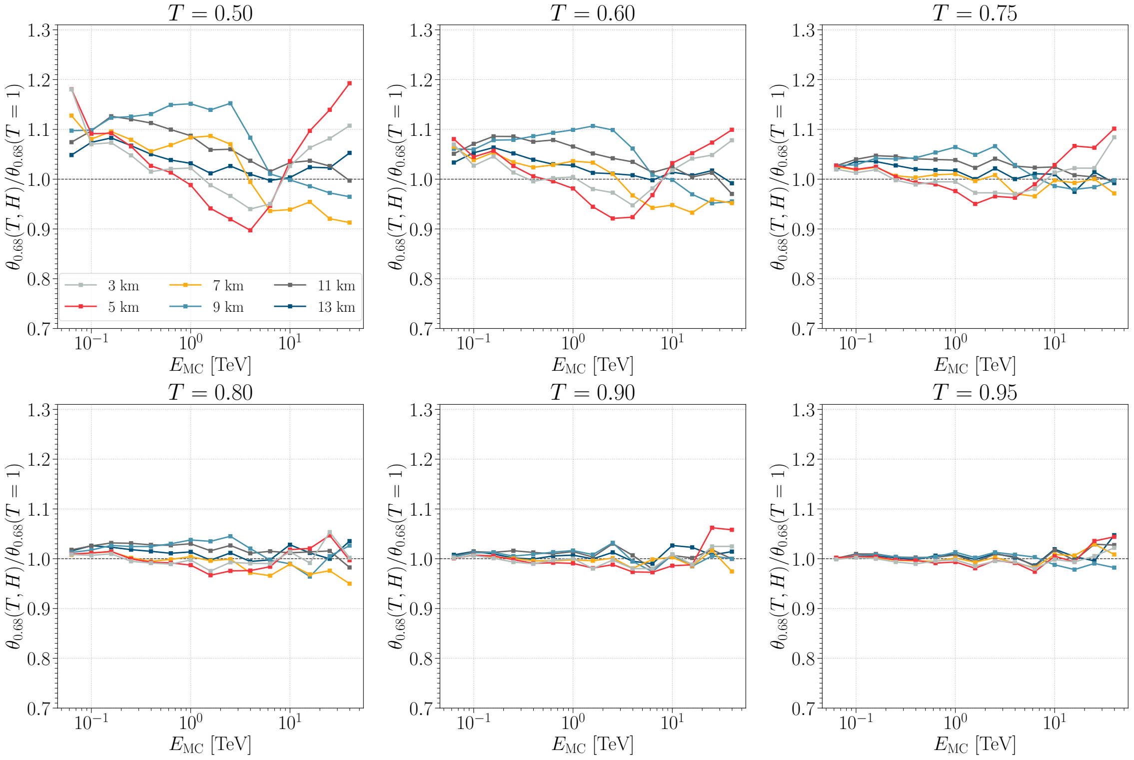

(a) 15 MSTs, height dependence of angular resolution ratio for fixed transmission

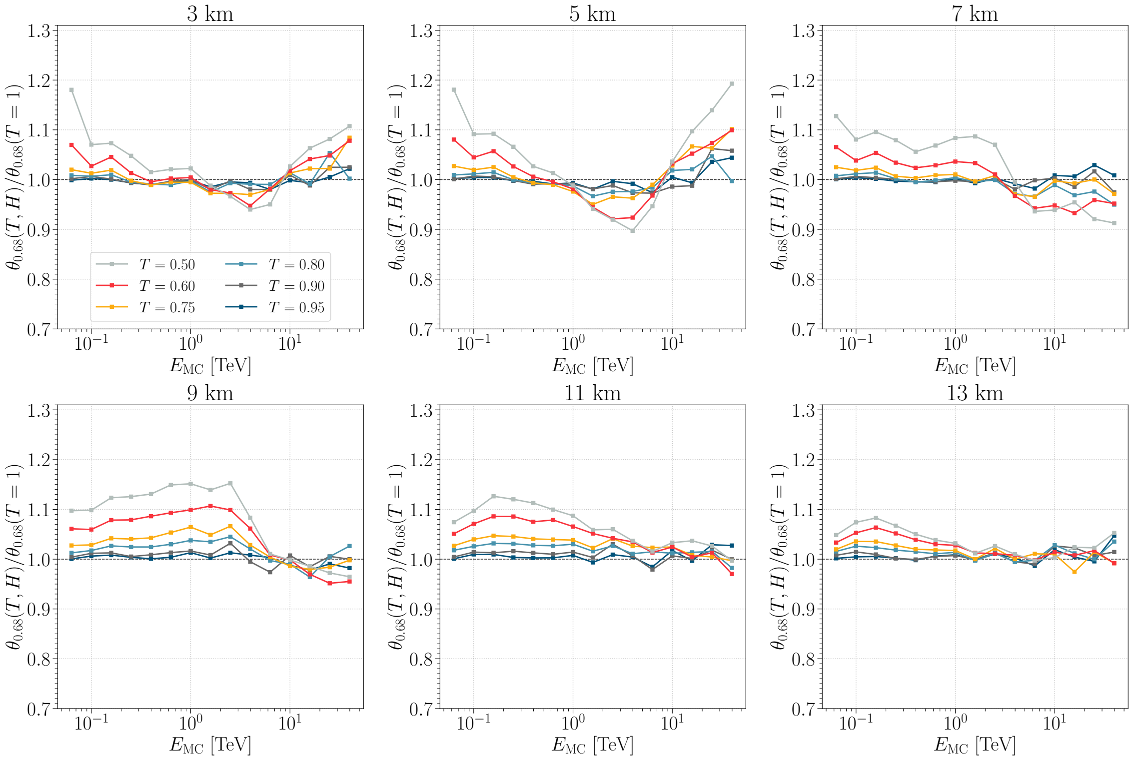

(b) 15 MSTs, transmission dependence of angular resolution ratio for fixed height

Figure 4.34: Angular resolution cloud-to-clear ratio for the layout of 15 MSTs for the case when adaptive MC simulations are used for DirLUT and RFs training.

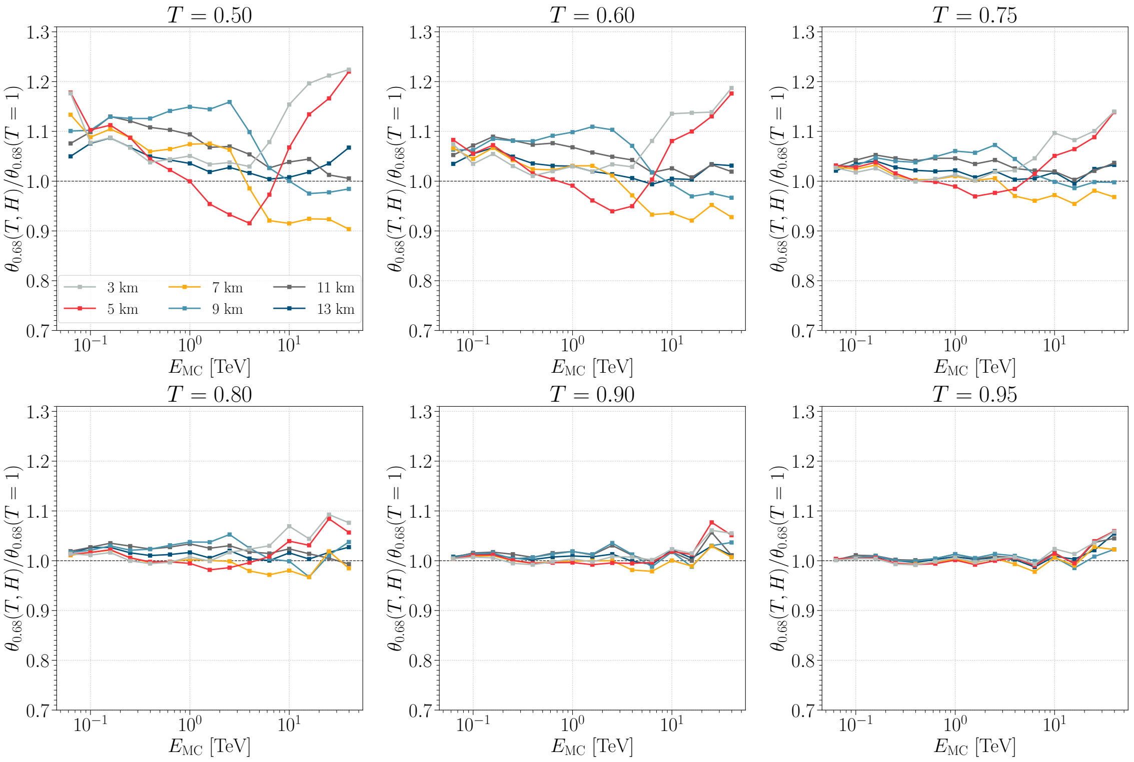

(a) 15 MSTs, height dependence of angular resolution ratio for fixed transmission

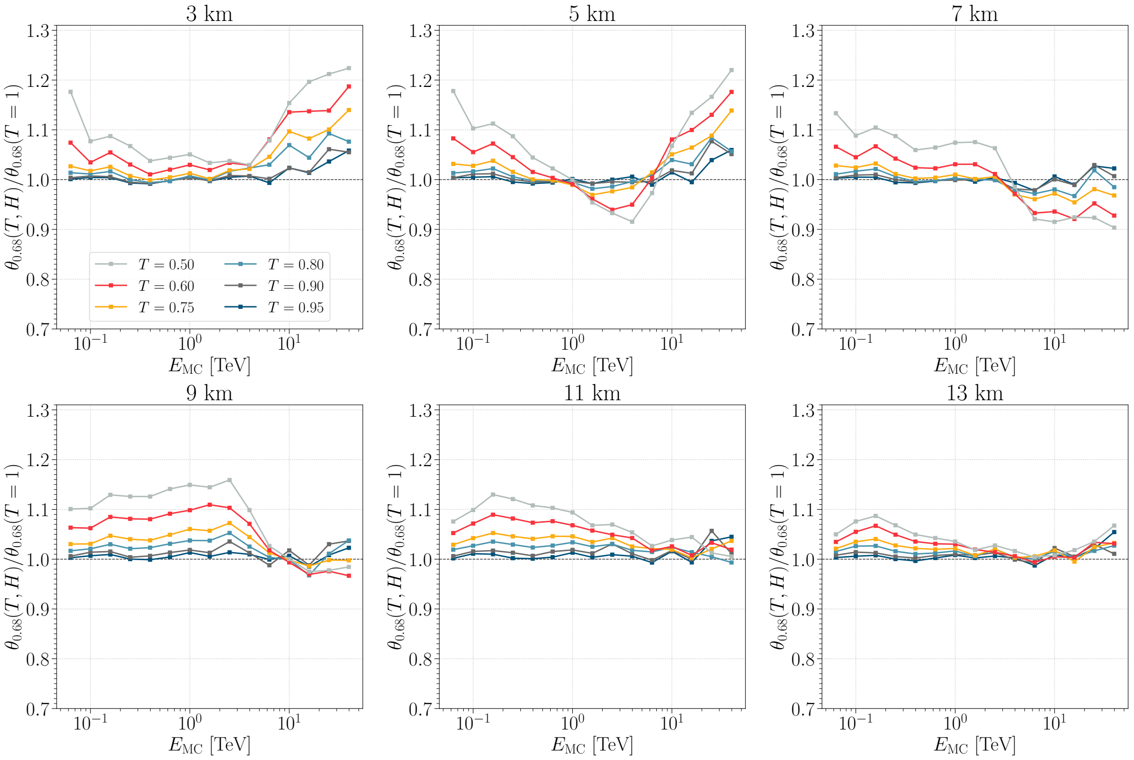

(b) 15 MSTs, transmission dependence of angular resolution ratio for fixed height

Figure 4.35: Angular resolution cloud-to-clear ratio for the layout of 15 MSTs for the case when standard MC simulations are used for DirLUT and RFs training.

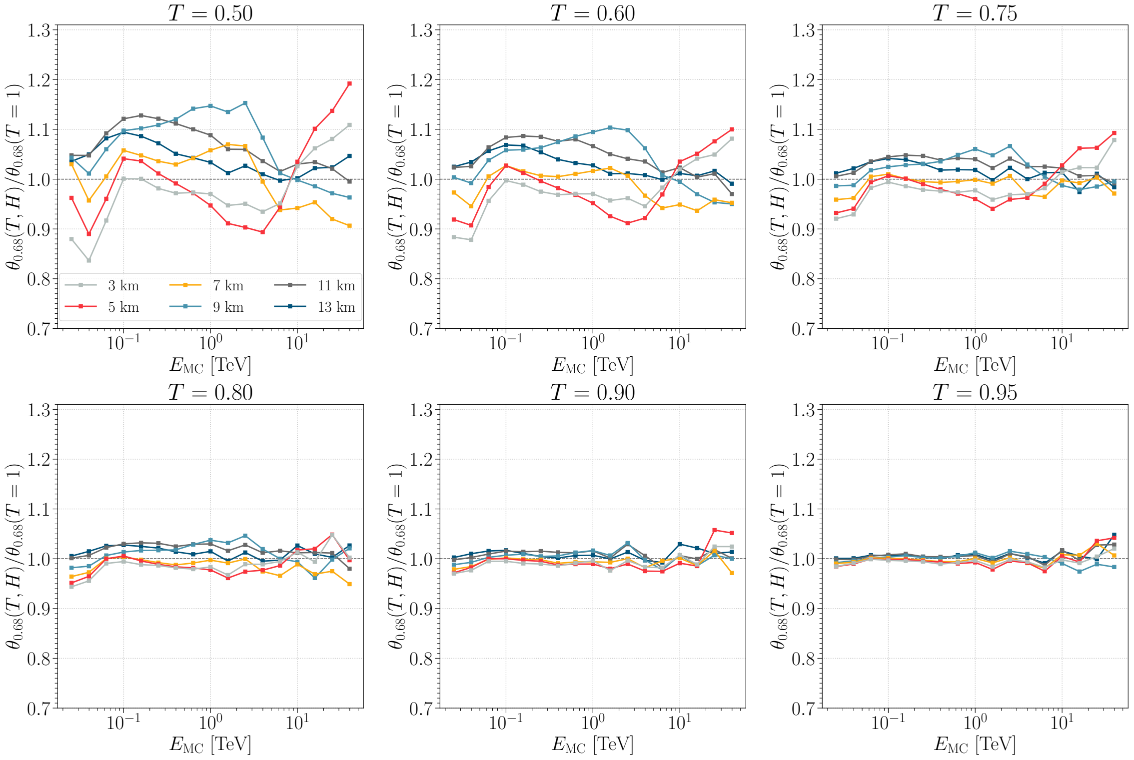

(a) CTAO-N, height dependence of angular resolution ratio for fixed transmission

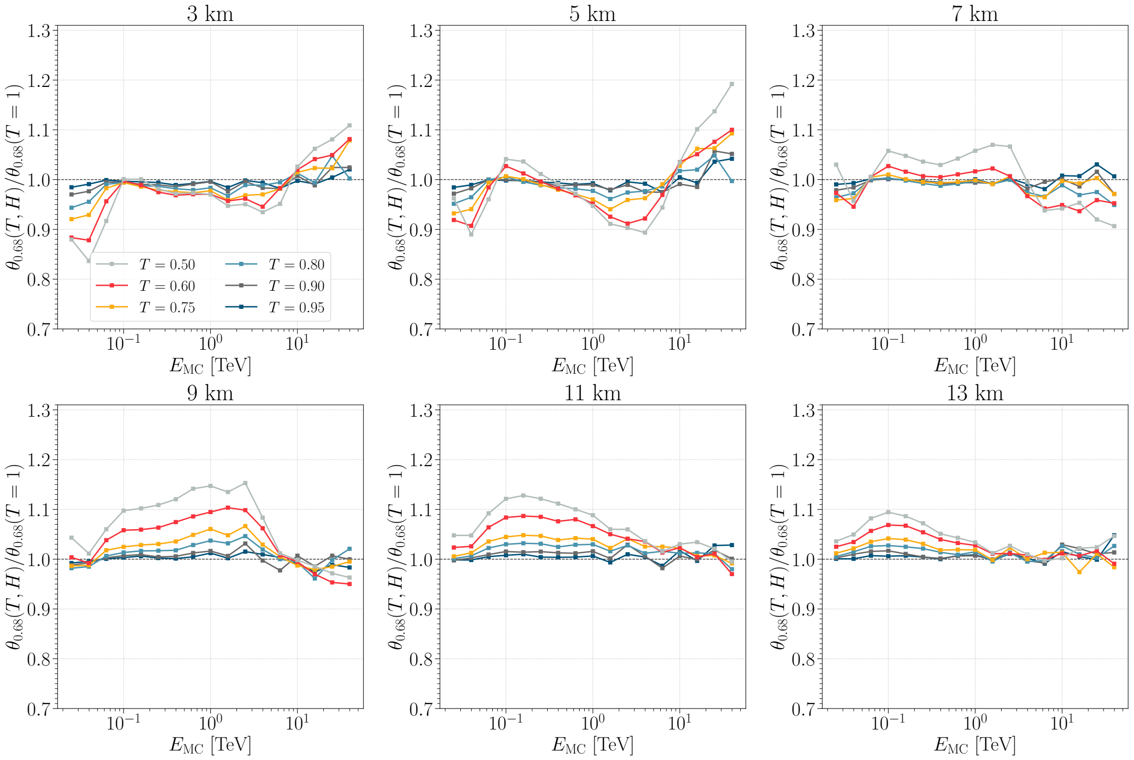

(b) CTAO-N, transmission dependence of angular resolution ratio for fixed height

Figure 4.36: Angular resolution cloud-to-clear ratio for CTAO-N for the case when adaptive MC simulations are used for DirLUT and RFs training.

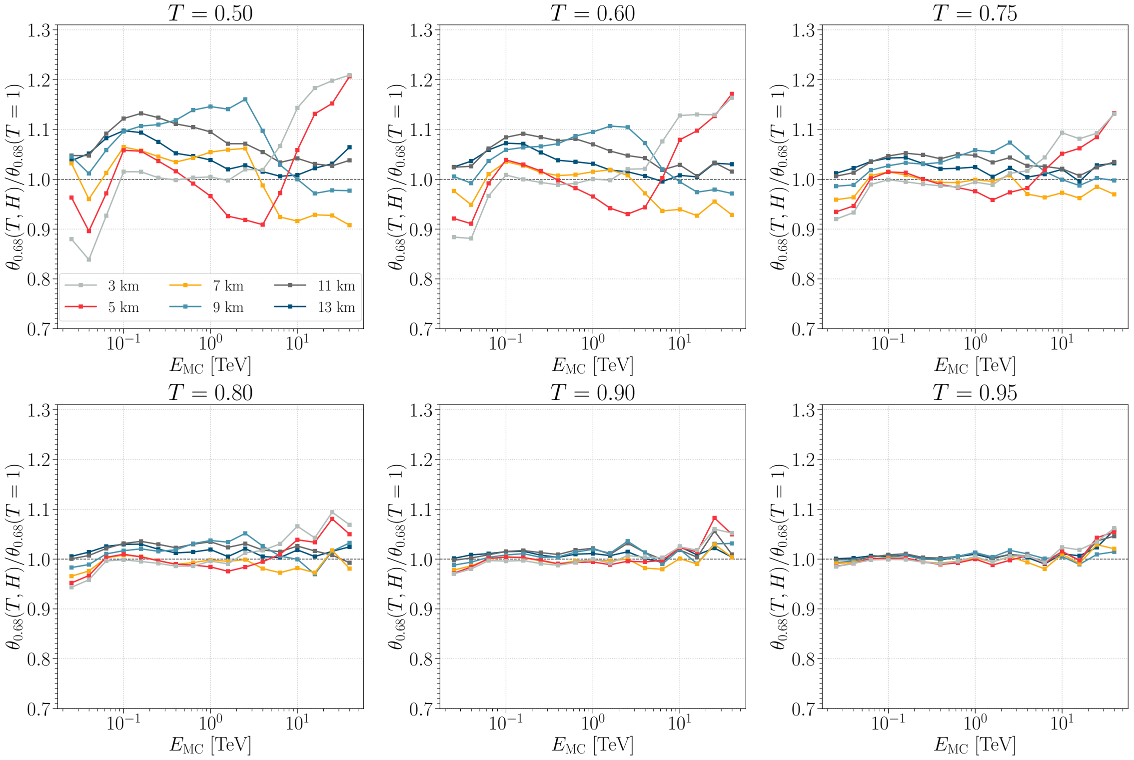

(a) CTAO-N, height dependence of angular resolution ratio for fixed transmission

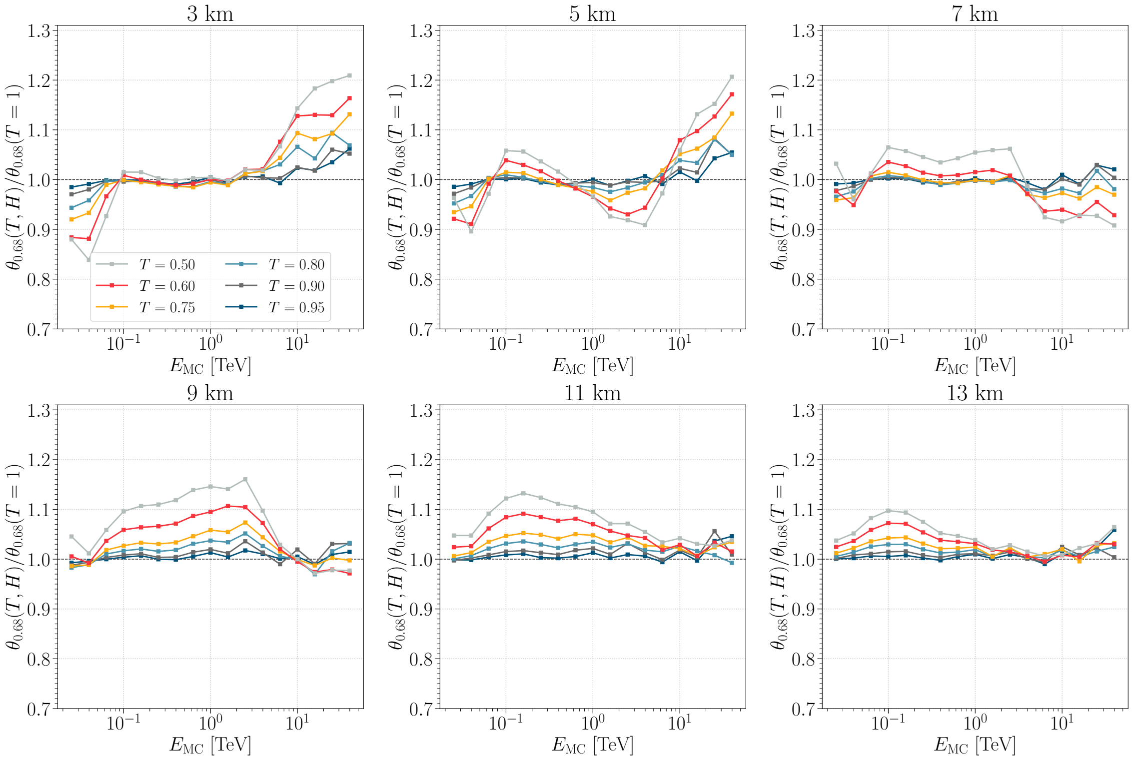

(b) CTAO-N, transmission dependence of angular resolution ratio for fixed height

Figure 4.37: Angular resolution cloud-to-clear ratio for CTAO-N for the case when standard MC simulations are used for DirLUT and RFs training.

Note also that the method used in the MARS/CHIMP chain to reconstruct the arrival direction (the crossing point method) is probably more robust to the effects of clouds than, for example, the *disp* method (Lessard et al., 2001) (see section 5.3 for an explanation). Clouds mainly influence the longitudinal distribution of the shower, while the direction of the main axis itself is in general affected by statistical fluctuations. In the crossing point method, the Hillas parameters are only used to fit the weights from different images, which leads to second-order effects of clouds on the obtained angular resolution even if the standard MC simulations are used. On the other hand, the disp-like methods reconstruct the direction of the source from each valid image using Hillas and timing parameters, leading to a first-order effect on the angular resolution. Therefore, one might expect poorer angular resolution with different reconstruction methods, see e.g. work of Żywucka et al. (2024).

4.7 Effective area

The effective area (describing the detection efficiency of a telescope) is the area of a perfect detector with a 100% detection efficiency which would collect the same rate of gamma rays as the real detector. Since the telescope is not able to detect all gamma rays, it is necessary to know the detection efficiency and reconstruct the actual number of gamma rays for the correct interpretation of the observed flux. In general, the effective area is defined as the geometric area around the telescope in which a gamma-ray shower produces a trigger, folded with the gamma-ray detection efficiency of all cuts used in the analysis:

$$A_{\mathrm{eff}} = \pi R_{\mathrm{max}}^2 \frac{N_{\mathrm{detected}}^{\gamma}}{N_{\mathrm{sim}}^{\gamma}}. \tag{4.14}$$

where $N_{\mathrm{detected}}^{\gamma}$ is the number of detected gamma-ray events surviving all cuts, $N_{\mathrm{sim}}^{\gamma}$ is the total number of simulated gamma-ray events, and R_{max} is the maximum simulated impact from the center of the array. Figure 4.38 shows the effective area as a function of the simulated energy E_{MC} for CTAO-N and the corresponding subarrays under cloudless conditions, after *hadronness* and θ^2 cuts applied. It is $\approx 10^5$ m^2 at 100 GeV and varies from $\approx 2 \cdot 10^5$ m^2 (LSTs) to $\approx 10^6$ m^2 (MSTs, CTAO-N) at 10 TeV. A small effective area below 100 GeV in the case of 15 MSTs is due to the poor sensitivity of these telescopes to low-energy air showers.

Subarray of 4 LSTs

The ratio of the effective area in the presence of clouds compared to the cloudless condition for the layout of 4 LSTs is shown in Figure 4.39. Due to the negative energy bias that arises when using standard MC simulations, the effective area is calculated as a function of E_{MC}. In the case where DirLUT and RFs are trained on the adaptive MC simulations, the largest effects are observed at low energies, where the effective area is limited by the hardware trigger and the *size* cut and is inherently small. At these energies, the detection efficiency is further reduced by the additional extinction of Cherenkov light due to the presence of clouds. At the highest energies, the effective area is greatly reduced due to the poor performance of the directional and *hadronness* estimators.

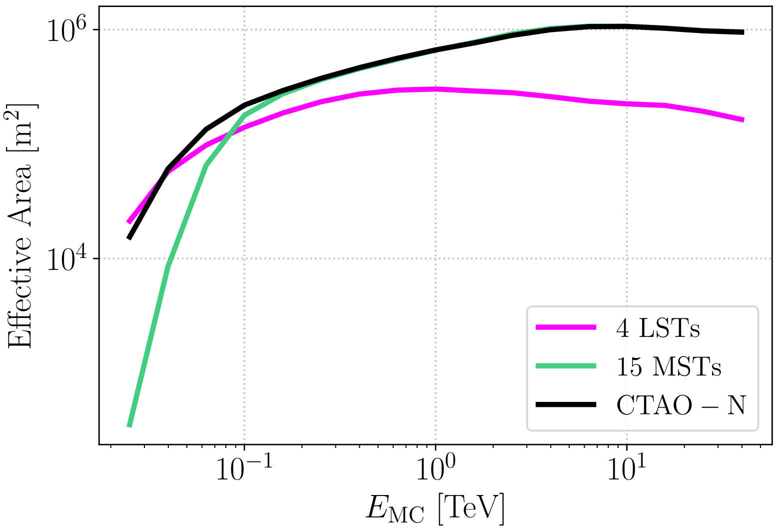

Figure 4.38: Effective area as a function of simulated energy for CTAO-N and the corresponding subarrays when clouds are not present in the atmosphere.

In addition, the effective area decreases at the highest energies due to image leakage. The effective area in the presence of clouds at 100 GeV is decreased between 10% and 55% compared to that in the clear atmosphere. At higher energies, the influence of clouds on the effective area is much smaller, less than 15% at 1 TeV. Clouds at intermediate altitudes, between 7 and 9 km, reduce the effective area at 100 GeV by up to 35% compared to cloudless conditions and $\lesssim$ 20% at energies above 1 TeV. In the presence of high clouds ($\geq$ 11 km), the effective area at 100 GeV is reduced by less than 10%. Clouds at low altitude with low transmission ($T \leq 0.60$) cause a reduction of up to $\approx$ 97% compared to cloudless conditions below the energy threshold, but $\lesssim$ 10% at energies above 1 TeV, depending on the cloud height. Clouds with high transmission ($T \geq 0.80$) behave similarly at a given height, reducing the effective area by up to 10% at 100 GeV and to less than 5% at energies above 1 TeV. The use of standard MC simulations when training DirLUT and RFs (Figure 4.40) leads to an additional reduction in the effective area compared to the case where adaptive MCs are used. This is particularly true for energies below 150 GeV, where the effective area decreases by a further 90% compared to adaptive MC simulations. At higher energies, a reduction of the effective area can also be observed, but the effects are rather small (on the order of a few percent).

Subarray of 15 MSTs

The effects of clouds on the effective area for a subarray of 15 MSTs (Figure 4.41) are similar to those for the case of 4 LSTs, although the factor of decrease is higher in the common energy range (80 GeV to 3 TeV) for the reasons explained in section 4.2.2. Below 200 GeV, there is a sharp decrease in the effective area, which is more than 90% in the worst case, where the cloud with $T = 0.50$ is at an altitude of 3 km. Above the energy threshold, high clouds above 9 km reduce the effective area by less than 10%, even at low transmission values, while in the case of lower clouds, the effective area is reduced by up to 30% above 1 TeV and by less than 20% above 10 TeV, depending on cloud transmission and base height. Similar to the case of 4 LSTs, the use of standard

MC simulations for the analysis does not lead to large changes in the obtained effective area for most of the energy range (Figure 4.42), but there is an additional reduction in effective area of up to 50% close to the energy threshold and for $T \leq 0.75$, depending on the cloud height.

CTAO-N array

In the case of the CTAO-N array (Figure 4.43), the effective area at lower energies is mainly determined by 4 LSTs, i.e. at energies $\lesssim 80$ GeV, the performance of CTAO-N is comparable to that of a subarray consisting of 4 LSTs, with the effective area decreasing by more than 90% in the worst case (cloud at 3 km altitude, $T = 0.5$). At energies ≥ 3 TeV, the performance of CTAO-N is equivalent to that of MSTs (decrease of up to 25% compared to the cloudless conditions). The use of standard MC simulations in the training of DirLUT and RFs (Figure 4.44) leads to an additional reduction of the effective area compared to the case where adaptive MCs are used. At energies below 150 GeV, the effective area decreases by a further 75% compared to adaptive MC simulations, depending on the transmission and the height of the cloud. At higher energies, the observed reduction in effective area is rather small (on the order of a few percent), although the effects increase with increasing energy, where large images deformed by the presence of clouds but trained with standard MC simulations do not survive *hadronness* and θ^2 cuts.

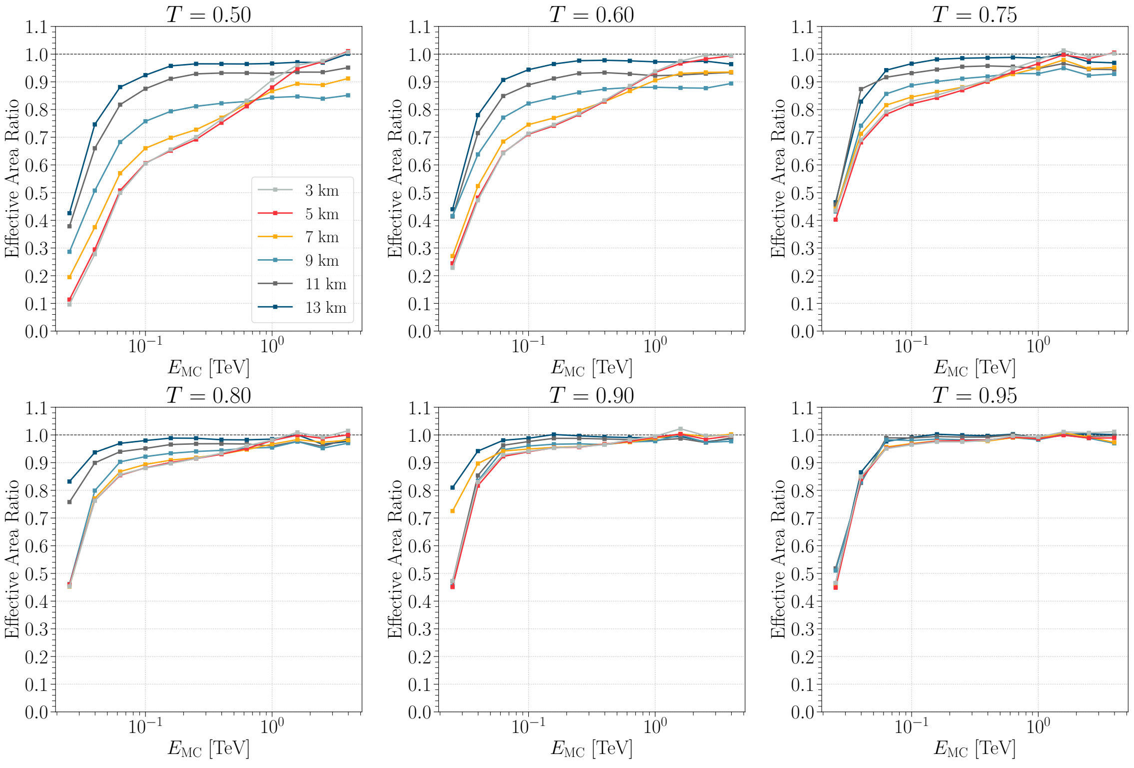

(a) 4 LSTs, height dependence of effective area ratio for fixed transmission

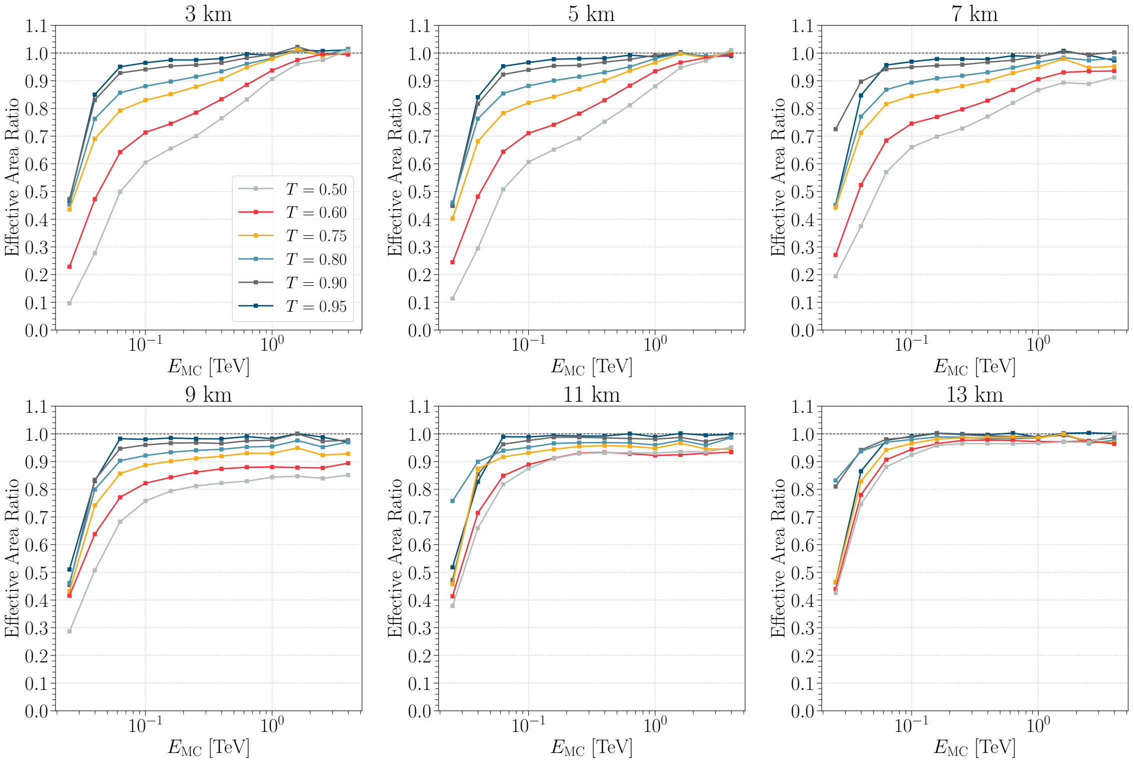

(b) 4 LSTs, transmission dependence of effective area ratio for fixed height

Figure 4.39: Effective area cloud-to-clear ratio for the subarray of 4 LSTs for the case when adaptive MC simulations are used for DirLUT and RFs training.

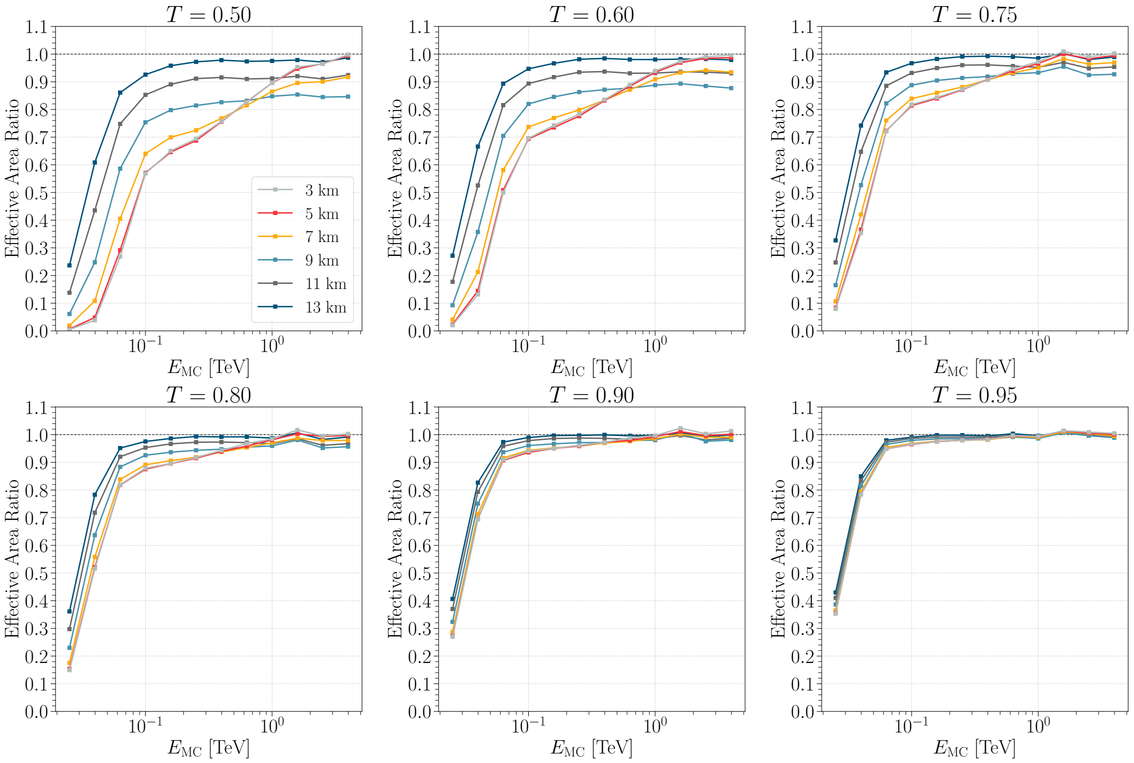

(a) 4 LSTs, height dependence of effective area ratio for fixed transmission

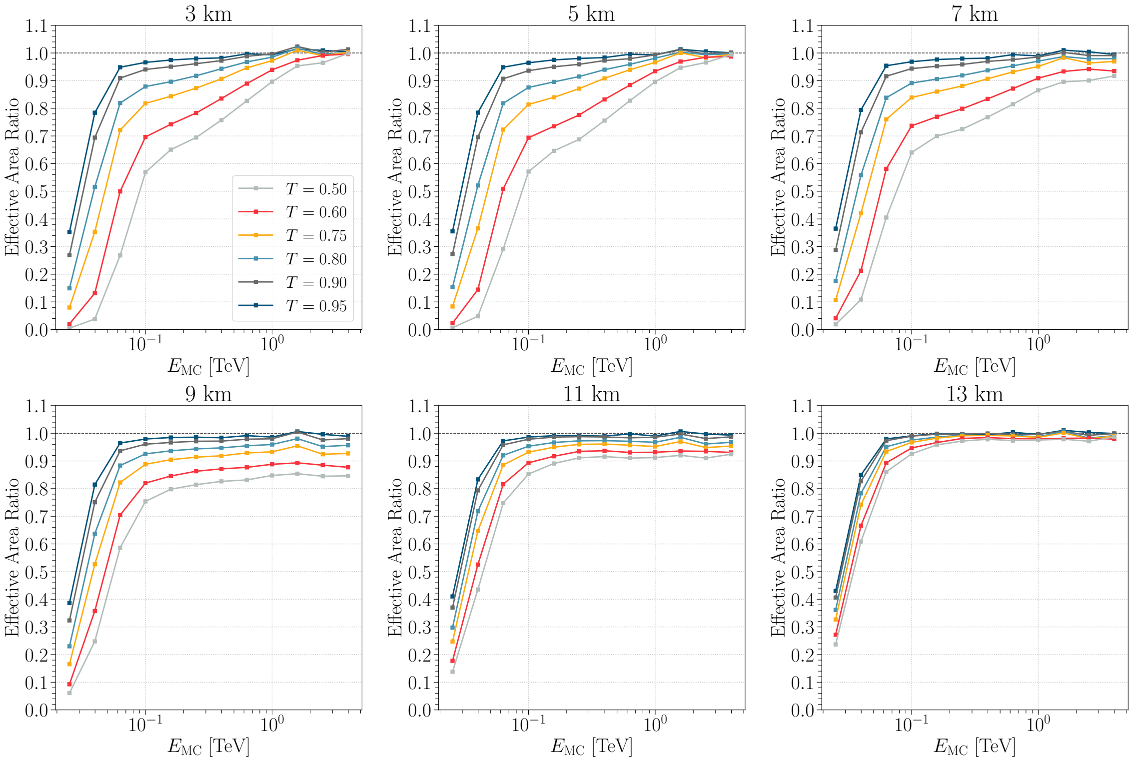

(b) 4 LSTs, transmission dependence of effective area ratio for fixed height

Figure 4.40: Effective area cloud-to-clear ratio for the subarray of 4 LSTs for the case when standard MC simulations are used for DirLUT and RFs training.

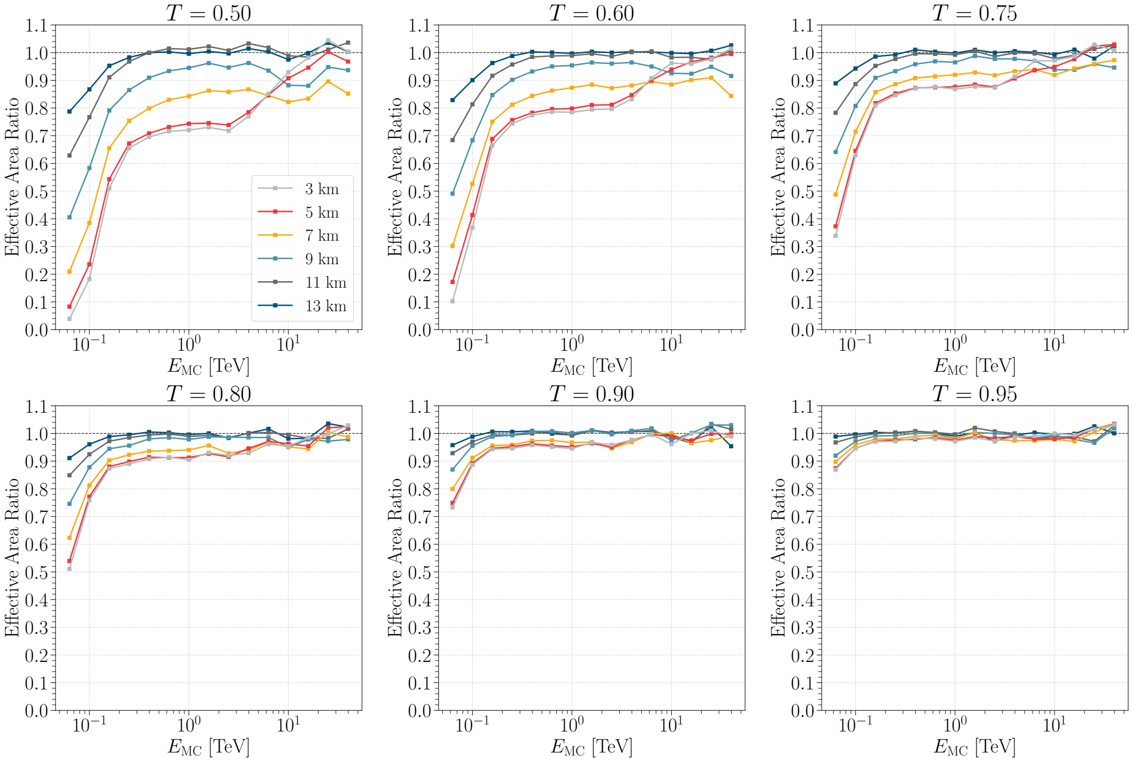

(a) 15 MSTs, height dependence of effective area ratio for fixed transmission

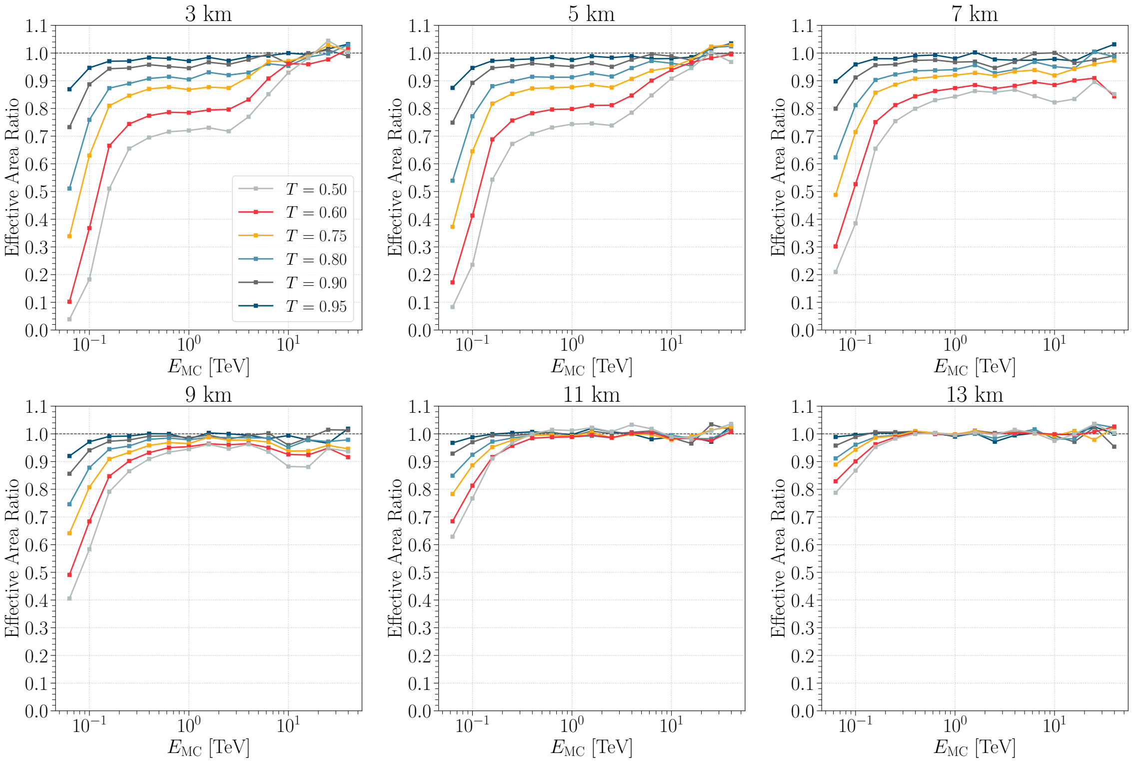

(b) 15 MSTs, transmission dependence of effective area ratio for fixed height

Figure 4.41: Effective area cloud-to-clear ratio for the subarray of 15 MSTs for the case when adaptive MC simulations are used for DirLUT and RFs training.

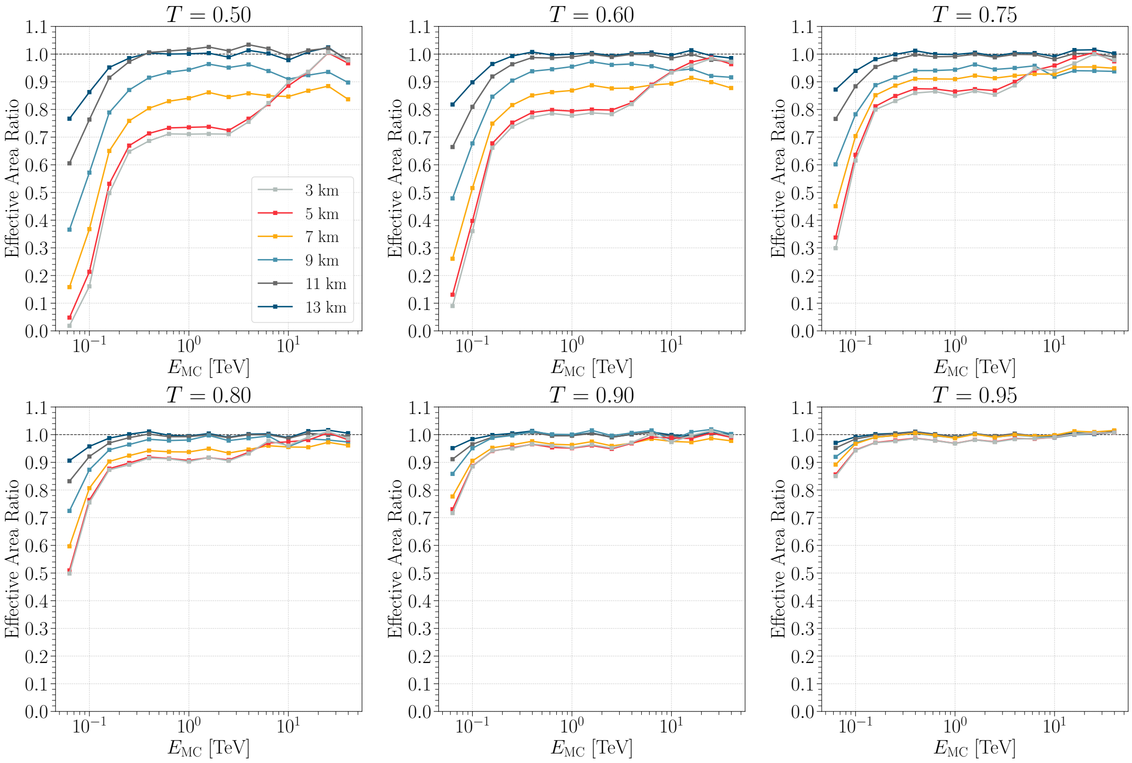

(a) 15 MSTs, height dependence of effective area ratio for fixed transmission

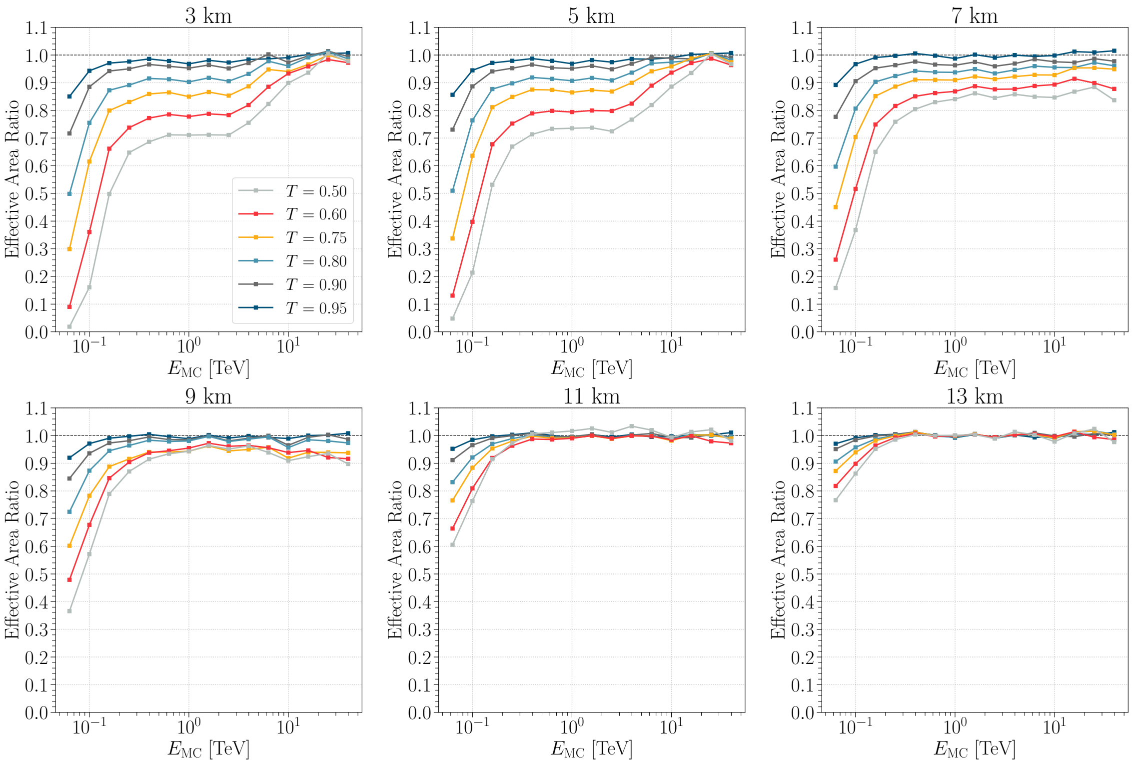

(b) 15 MSTs, transmission dependence of effective area ratio for fixed height

Figure 4.42: Effective area cloud-to-clear ratio for the subarray of 15 MSTs for the case when standard MC simulations are used for DirLUT and RFs training.

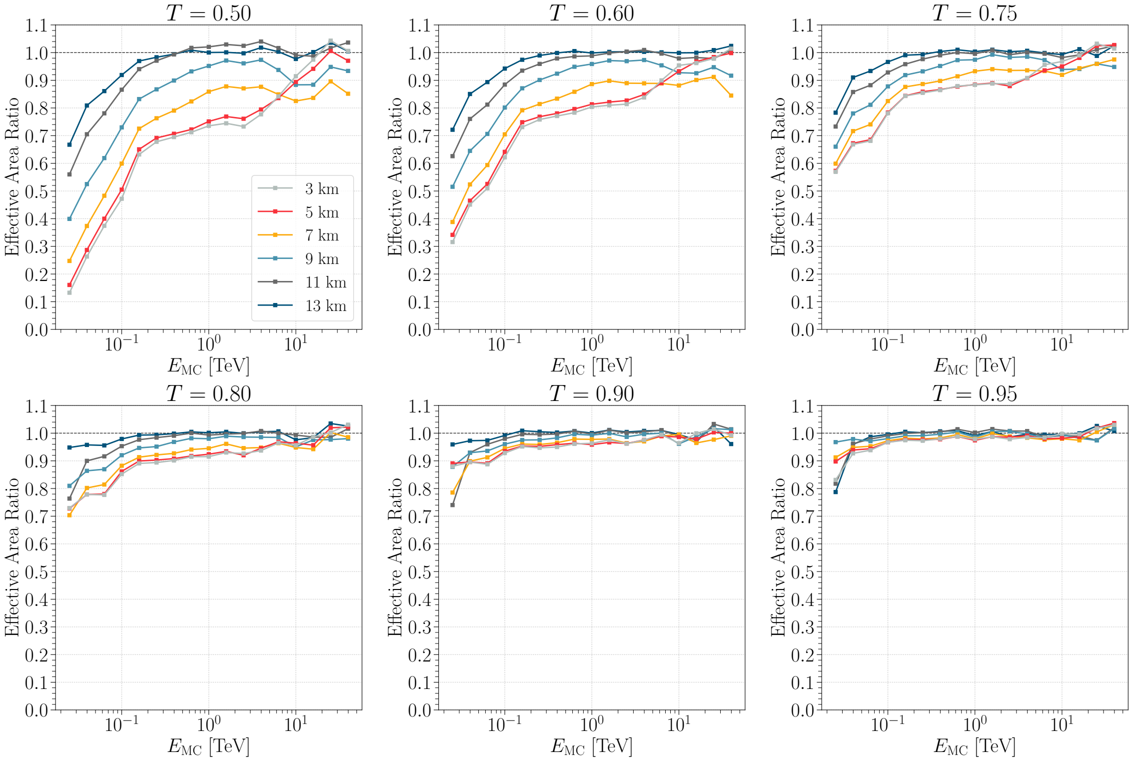

(a) CTAO-N, height dependence of effective area ratio for fixed transmission

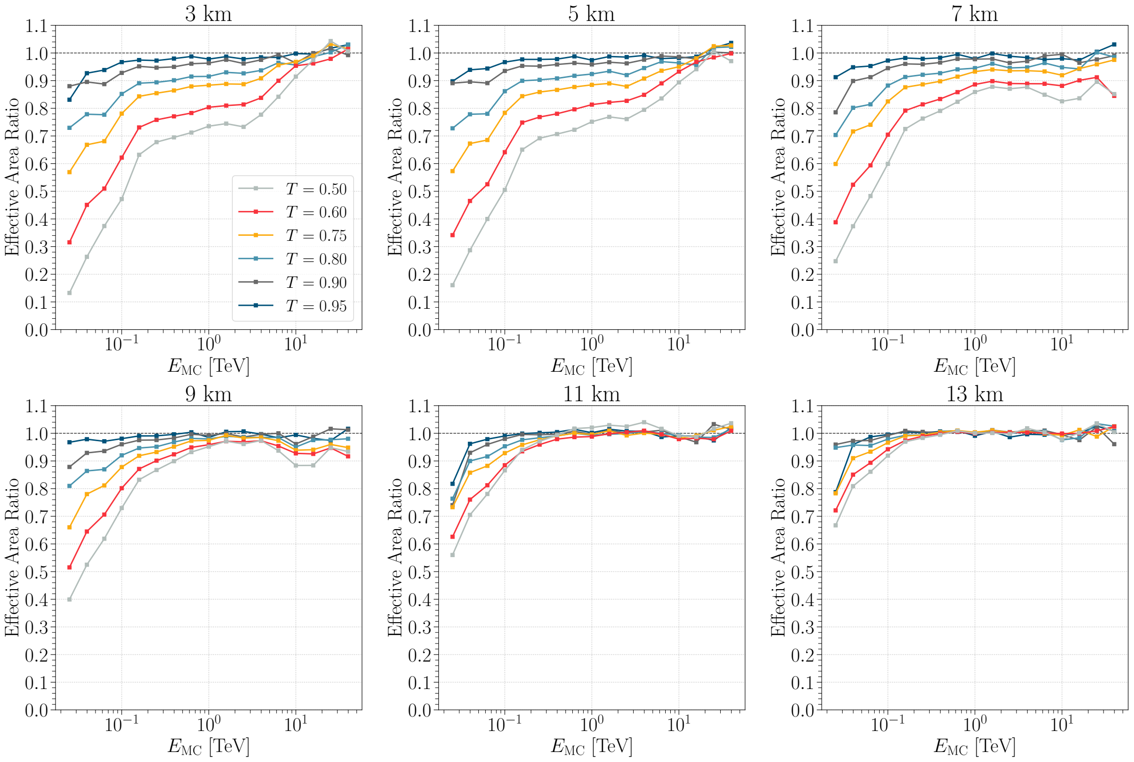

(b) CTAO-N, transmission dependence of effective area ratio for fixed height

Figure 4.43: Effective area cloud-to-clear ratio for CTAO-N for the case when adaptive MC simulations are used for DirLUT and RFs training.

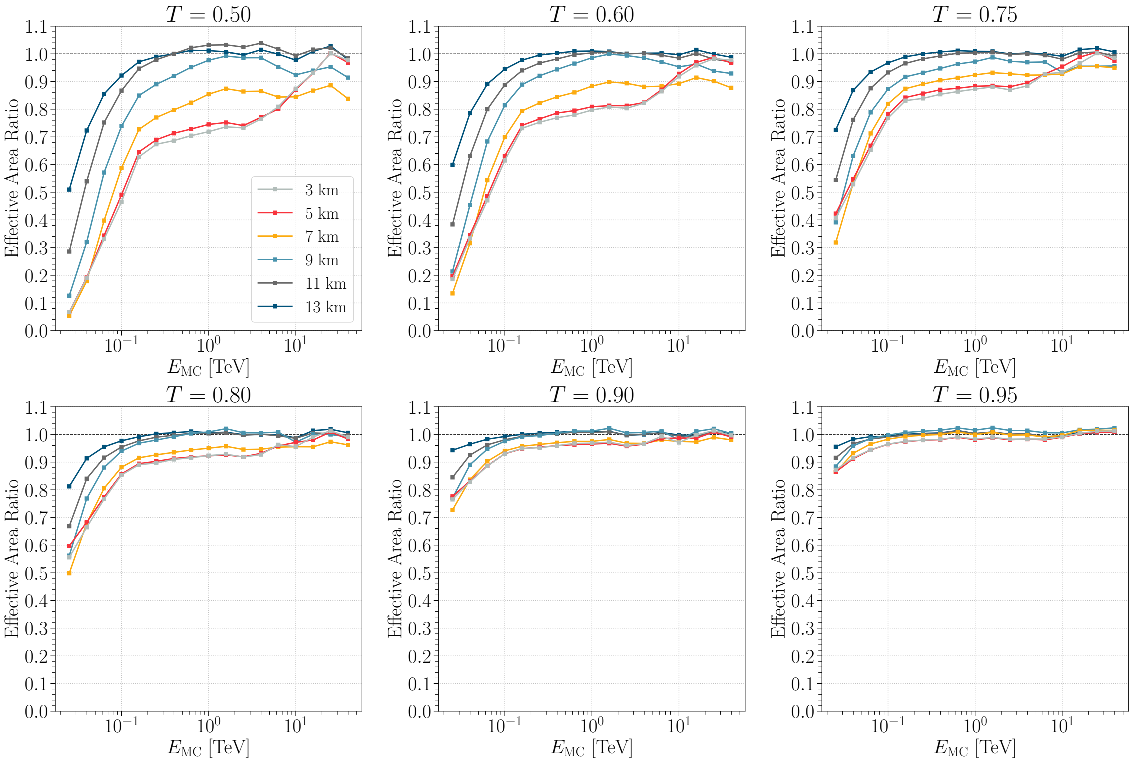

(a) CTAO-N, height dependence of effective area ratio for fixed transmission

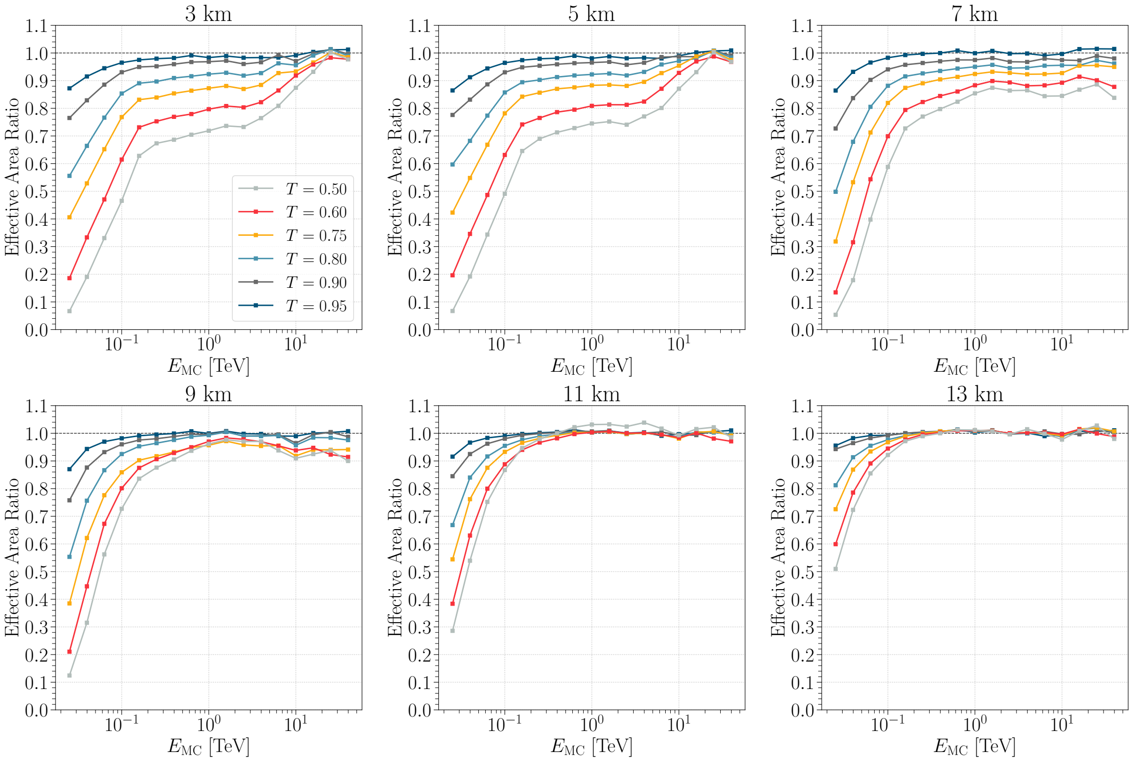

(b) CTAO-N, transmission dependence of effective area ratio for fixed height

Figure 4.44: Effective area cloud-to-clear ratio for CTAO-N for the case when standard MC simulations are used for DirLUT and RFs training.

4.8 Differential sensitivity

Differential energy flux sensitivity S is the minimum intrinsic flux that can be detected with a statistical significance of 5σ from a source with a power-law spectrum similar to the Crab Nebula in a defined observation time (usually 50 hours as a standard parameter to assess IACT performance). The differential sensitivity is calculated in non-overlapping logarithmic energy bins (five per decade), with a minimum number of 10 gamma-ray counts per energy bin and a signal count of more than 5% of the background counts.

To calculate the differential sensitivity, an observation is simulated and the statistical significance of the detection is calculated. First, the selection cuts are applied to the events in the ON region (i.e. the region where the potential gamma-ray signal could be detected) and to the events in the OFF region (i.e. the background region where the signal is not expected), resulting in N_{on} events in the on-source time t_{on} and N_{off} events in the off-source time t_{off}. In this way, the number of excess events is calculated as follows

$$N_{\mathrm{exc}} = N_{\mathrm{on}} - \alpha \cdot N_{\mathrm{off}}, \tag{4.15}$$

where $\alpha = \frac{t_{\mathrm{on}}}{t_{\mathrm{off}}}$ is the background normalization factor.

A statistical test is then performed to calculate the significance S of the detection of the observed source, expressed as the mean of the standard deviation σ. In the work of Li and Ma (1983) several ways of estimating the significance are discussed. If the significance is estimated as the ratio of the excess counts N_{exc} above the background to its standard deviation $\sigma(N_{\mathrm{exc}})$, then the significance is given as:

$$\Sigma = \frac{N_{\mathrm{exc}}}{\sigma(N_{\mathrm{exc}})} = \frac{N_{\mathrm{on}} - \alpha N_{\mathrm{off}}}{\sqrt{N_{\mathrm{on}} + \alpha^2 N_{\mathrm{off}}}}. \tag{4.16}$$

If one estimates the probability that the observed signals are due only to the background, then one must assume that all counts are due to the background and that there were no additional sources:

$$\Sigma = \frac{N_{\mathrm{on}} - \alpha N_{\mathrm{off}}}{\sqrt{\alpha (N_{\mathrm{on}} + N_{\mathrm{off}})}}. \tag{4.17}$$

However, for cases where $\alpha < 1$, it is obvious that equation (4.16) underestimates the significance, while equation (4.17) overestimates the significance. To obtain the most appropriate solutions, Li and Ma (1983) proceed with the maximum likelihood ratio method using Wilks' theorem (Wilks, 1938), i.e. assuming that if the null hypothesis is true and both N_{on} and N_{off} are not too small, the likelihood ratio is approximately distributed like a χ^2 distribution with one degree of freedom, resulting in the equation for significance calculation as follows:

$$\Sigma = \sqrt{2}\left[N_{\mathrm{on}} \ln\left(\frac{1+\alpha}{\alpha}\left(\frac{N_{\mathrm{on}}}{N_{\mathrm{on}} + N_{\mathrm{off}}}\right)\right) + N_{\mathrm{off}} \ln\left((1+\alpha)\left(\frac{N_{\mathrm{off}}}{N_{\mathrm{on}} + N_{\mathrm{off}}}\right)\right)\right]^{\frac{1}{2}}. \tag{4.18}$$

Simulated data are in the first step renormalized to achieve realistic physics spectra as CORSIKA events are generated following a power-law of index −2 to generate enough events above 10 TeV.

Gamma-ray production is weighted using the HEGRA Crab Nebula spectrum (Aharonian et al., 2004), proton production using the BESS cosmic-rays spectrum (Sanuki et al., 2000), while electrons are weighted using a parameterization of Fermi-LAT (Abdollahi et al., 2017) and H.E.S.S. (Aharonian et al., 2008, 2009) spectrum data. The first step is to calculate the flux normalization of the simulated events Φ_{sim} for a given observation time t. The number of simulated events N is calculated by integration of the differential flux (Nöthe, 2020):

$$N = \int_{E_{\min}}^{E_{\max}} \int_0^t \int_\Omega \int_A \Phi_{\mathrm{sim}} \left(\frac{E}{E_{\mathrm{ref}}}\right)^\gamma \mathrm{d}E\ \mathrm{d}t\ \mathrm{d}\Omega\ \mathrm{d}A = \frac{\Phi_{\mathrm{sim}} t \Omega A}{E_{\mathrm{ref}}^\gamma (\gamma+1)} (E_{\max}^{\gamma+1} - E_{\max}^{\gamma+1}), \tag{4.19}$$

which gives:

$$\Phi_{\mathrm{sim}} = \frac{E_{\mathrm{ref}}^\gamma (\gamma+1) N}{t \Omega A (E_{\max}^{\gamma+1} - E_{\max}^{\gamma+1})}. \tag{4.20}$$

The simulated area is calculated as:

$$A = \pi R_{\max}^2, \tag{4.21}$$

where $R_{\max}$ is the simulated maximum impact point with respect to CORSIKA (0, 0) coordinates. The solid angle is in the case of diffuse sources defined as:

$$\Omega = 2\pi(1 - \cos\Theta), \tag{4.22}$$

where Θ is the maximum simulated VIEWCONE angle, or $\Omega = 1$ in the case of point-like sources. The sample weight for i-th simulated event is finally calculated as the ratio of target and simulated energy spectrum (Nöthe, 2020):

$$w_i = \frac{\Phi_{\mathrm{target}}(E_i)}{\Phi_{\mathrm{sim}}(E_i)}. \tag{4.23}$$

The optimization of the sensitivity for a given observation time is achieved by applying optimal cuts for *hadronness*, θ and *multiplicity* in the energy range between 20 GeV and 200 TeV. The aim is to find a balance between the different ratios of surviving gamma-ray events after each cut and the efficiency (fraction of remaining gamma rays). The *hadronness* and θ^2 cuts are determined by calculating the sensitivity of multiple cuts for fixed decreasing efficiencies: 0.95, 0.90, 0.85, 0.80, 0.70, 0.60, 0.50, and in each energy bin each *multiplicity* cut is considered. The efficiency of a cut $\theta^2 < x$ is defined as the ratio of the number of events with $\theta^2 < x$ to the number of events with $\theta^2 < 1$, where 1 is loose cut for θ^2. The chosen maximum efficiency of the θ^2 cut is 0.8 to avoid too wide cuts that degrade the energy resolution. For each energy bin the multiplicity and efficiency cut providing the best sensitivity are selected. In this way, the analysis cuts in each bin have been optimized to achieve the best differential flux sensitivity. Note that in this section results are given for dynamic θ^2 and *hadronness* cuts to maximize sensitivity, while the previous results were given for fixed θ^2 cut.

A common problem in the calculation of differential sensitivity is the question of whether the

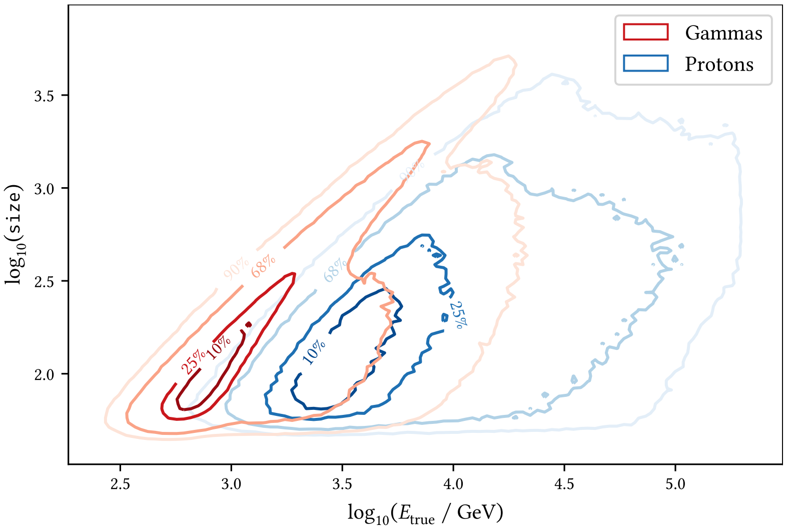

Figure 4.45: The *size* parameter as a function of primary (simulated) energy. The contours contain the indicated percentage of all events. Protons produce approximately one-fifth of the Cherenkov light produced by gamma rays of the same energy (Nöthe, 2020).

sensitivity should be calculated in the bins of estimated or true (simulated) energy since gamma rays and protons of the same energy produce different images in the Cherenkov camera (Figure 4.45). The calculation of the sensitivity in true energy bins for gamma rays and protons therefore uses a background model that is not realistic. Furthermore, the method does not apply to real data for which true energy is unknown. In contrast, calculating the sensitivity in estimated energy bins is feasible for both simulated and observed data and provides a more realistic background modeling within each bin. However, this approach also has disadvantages, as the performance of the energy estimator is limited and the introduced energy bias must be adequately accounted for in the calculations. Therefore, the reconstructed energy is corrected at the very end of the analysis chain after the selection of the gamma-like events. The correction consists of fitting a polynomial of 5th degree to the migration matrix, which is a simple and flexible function and a standard procedure in the MARS-CTA chain. The polynomial is then used to correct the estimated energy if there is an energy-dependent bias.

Figure 4.46 shows the differential flux sensitivity (multiplied by a square of the energy bin center, E^2) for CTAO-N and the corresponding subarrays under cloudless conditions. In the case of 4 LSTs, the differential sensitivity varies between $S = 6.13 \cdot 10^{-12}$ erg cm^{-2}s^{-1} at an energy of 40 GeV and $S = 1.25 \cdot 10^{-12}$ erg cm^{-2}s^{-1} at 10 TeV, while that of the subarray of 15 MSTs is between $S = 5.39 \cdot 10^{-12}$ erg cm^{-2}s^{-1} at an energy of 40 GeV and $S = 2.06 \cdot 10^{-13}$ erg cm^{-2}s^{-1} at 10 TeV. Above 100 GeV, MSTs have better sensitivity due to the larger effective area. In contrast, LSTs are more sensitive to lower energies, especially below 100 GeV. The combination of LSTs and MSTs can further increase the sensitivity below 5 TeV, while at higher energies the sensitivity is mainly determined by the performance of MSTs.

Similar to the effective area, the differential sensitivity is worsened by the presence of clouds. In general, the lower the height of the cloud base and the lower the transmission, the worse the flux sensitivity. This means that the flux sensitivity decreases in the presence of clouds, i.e. the

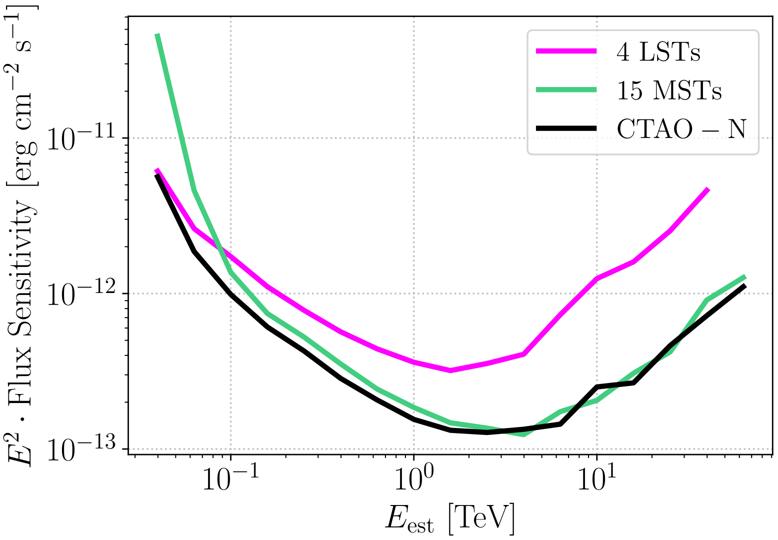

Figure 4.46: Flux sensitivity as a function of estimated (reconstructed) energy for CTAO-N and the corresponding subarrays when clouds are not present in the atmosphere.

telescopes detect weaker sources in the absence of clouds than in the presence of clouds in the atmosphere. To avoid any confusion, a decreased flux sensitivity means a higher value of differential sensitivity. At the highest energies, the flux sensitivity in the presence of high-transmission clouds is comparable to that in cloudless conditions, and there may be fluctuations in the data points where it appears that clouds may cause better sensitivity compared to the clear atmosphere. However, these data points are due to statistical uncertainties.

Subarray of 4 LSTs

Figure 4.47 shows the differential sensitivity ratio in the presence of clouds (at different heights, for adaptive MC simulations) compared to the clear atmosphere for a subarray of 4 LSTs. Below 100 GeV, the sensitivity decreases by more than a factor of 2 (1.5) compared to the case where no clouds are present in the atmosphere in the worst-case scenario (best-case scenario). At higher energies for $T \leq 0.75$, clouds above 11 km reduce the sensitivity by $\lesssim 20\%$, while clouds between 3 km and 9 km reduce the sensitivity between 20% and 40%. At higher transmission values ($T \geq 0.8$), the differences between the individual heights are small and the decrease in differential sensitivity is $\lesssim 10\%$. Above a few TeV, the sensitivity of LST telescopes is inherently worse than in the core energy range (100 GeV to 1 TeV), and thus the cloud-to-clear ratio increases again.

The use of standard MC simulations in the analysis chain (Figure 4.48) as a training sample leads to an additional deterioration of the flux sensitivity. In the presence of clouds at an altitude of ≤ 7 km and $T \leq 0.75$, the significant deterioration of the differential sensitivity compared to the cloudless conditions is visible over the entire energy range. For example, for $T = 0.5$ in the worst case at an energy of 40 GeV, the flux sensitivity is reduced by a factor of 2.5 compared to the cloudless conditions, which means an additional 50% decrease in flux sensitivity compared to the case where adaptive MC simulations are used. Above 1 TeV degradation of flux, sensitivity amounts up to 40% compared to the cloudless conditions. In the presence of higher clouds, the use of standard MC simulations additionally degrades the flux sensitivity below 400 GeV, while at higher energies the degradation is comparable to that when using adaptive MC simulations. For low clouds, the effects are visible over the entire energy range, while for medium clouds, the effects are most pronounced at lower energies, where clouds introduce significant energy bias comparable to the transmission of the cloud.

Subarray of 15 MSTs

The flux sensitivity for the array of 15 MSTs is also reduced in the presence of clouds (Figure 4.49). At the energy of 100 GeV (for $T \leq 0.75$), the sensitivity decrease varies from a factor of 1.15 for a cloud at a height of 13 km with $T = 0.75$ to a factor of 4 for a cloud at a height of 3 km with $T = 0.50$. Above 1 TeV the influence of clouds is below 40%. At higher transmission values ($T \geq 0.80$), the effects are small even with very low clouds (less than 20%, depending on the cloud base height and the transmission).

Similar to the case of the 4 LSTs, the use of standard MC simulations in the training sample leads to a further degradation of the flux sensitivity of the array of 15 MSTs (Figure 4.50). The effects are visible over the entire energy range for low clouds with $T \leq 0.75$ (up to factor of 4 at 100 GeV, and up to a factor of 1.1 above 1 TeV). For higher clouds (≥ 9 km), the use of standard MC simulations does not result in any additional degradation of the flux sensitivity, regardless of the transmission of the clouds. This can be explained by the fact that the energy bias for these cases is very low for MSTs, even lower than for LST telescopes.

CTAO-N array

Clouds have a similar influence on the sensitivity of CTAO-N (Figure 4.51) as on the sensitivity of 4 LSTs and 15 MSTs. The sensitivity in the low-energy range, where the number of detected events is inherently low, is reduced by a higher factor than at higher energies. Although a combination of LSTs and MSTs improves the differential sensitivity in the common energy range compared to the case of a single subarray, the influence of clouds with $T \leq 0.75$ is still large at energies below 2 TeV. Below 100 GeV, the decrease in sensitivity at $T \leq 0.75$ can be up to a factor of 3, depending on the energy, transmission value, and cloud base height. Above 1 TeV, the differential sensitivity decreases by up to 50%. At higher transmission values ($T \geq 0.80$), the effects of the clouds are $\lesssim 20\%$, even at the lowest energies, without strong differences between the individual base heights.

The use of standard MC simulations in the analysis chain (Figure 4.52) for the training of DirLUT and RFs in the case of CTAO-N leads to a significant additional degradation of flux sensitivity. For lower clouds (≤ 7 km) with lower transmission ($T \leq 0.75$), this introduces an additional reduction in flux sensitivity of up to 30% at 100 GeV and up to 15% at 10 TeV, depending on the transmission and the height of the cloud, compared to the case where adaptive MC simulations are used. For clouds above 7 km with $T \geq 0.80$, the differences between the obtained ratios for adaptive and standard MC simulations are on the order of a few percent.

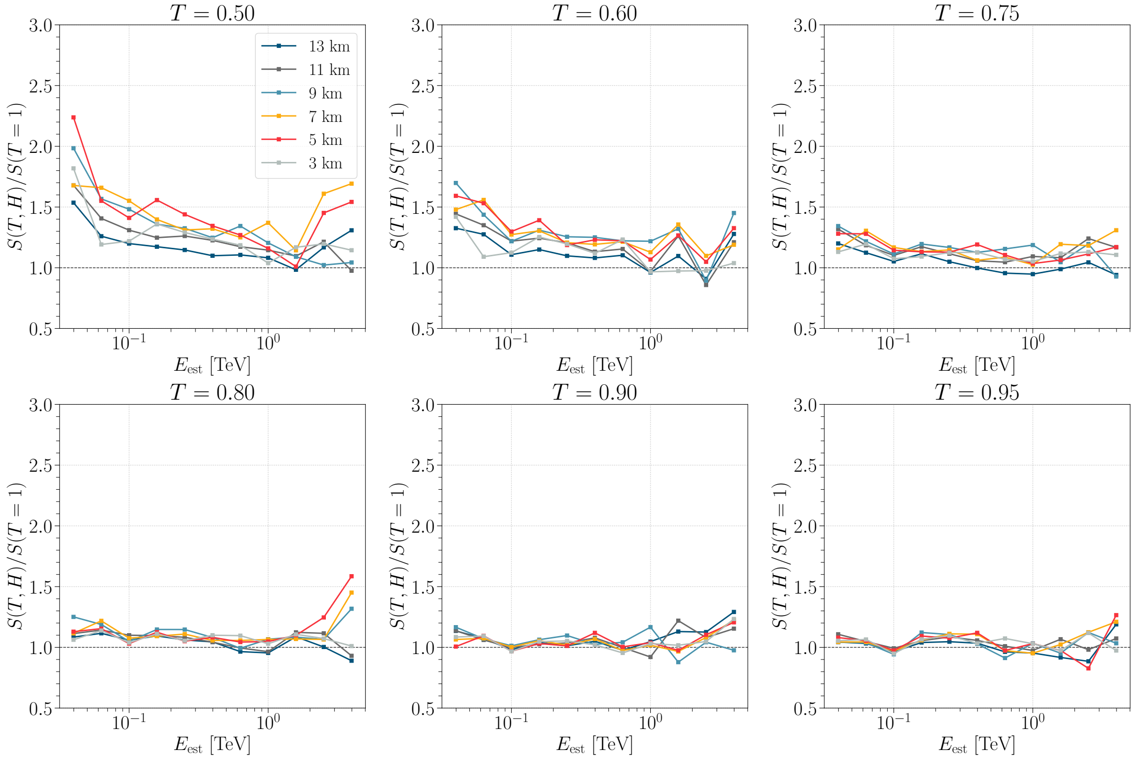

(a) 4 LSTs, height dependence of differential sensitivity ratio for fixed transmission

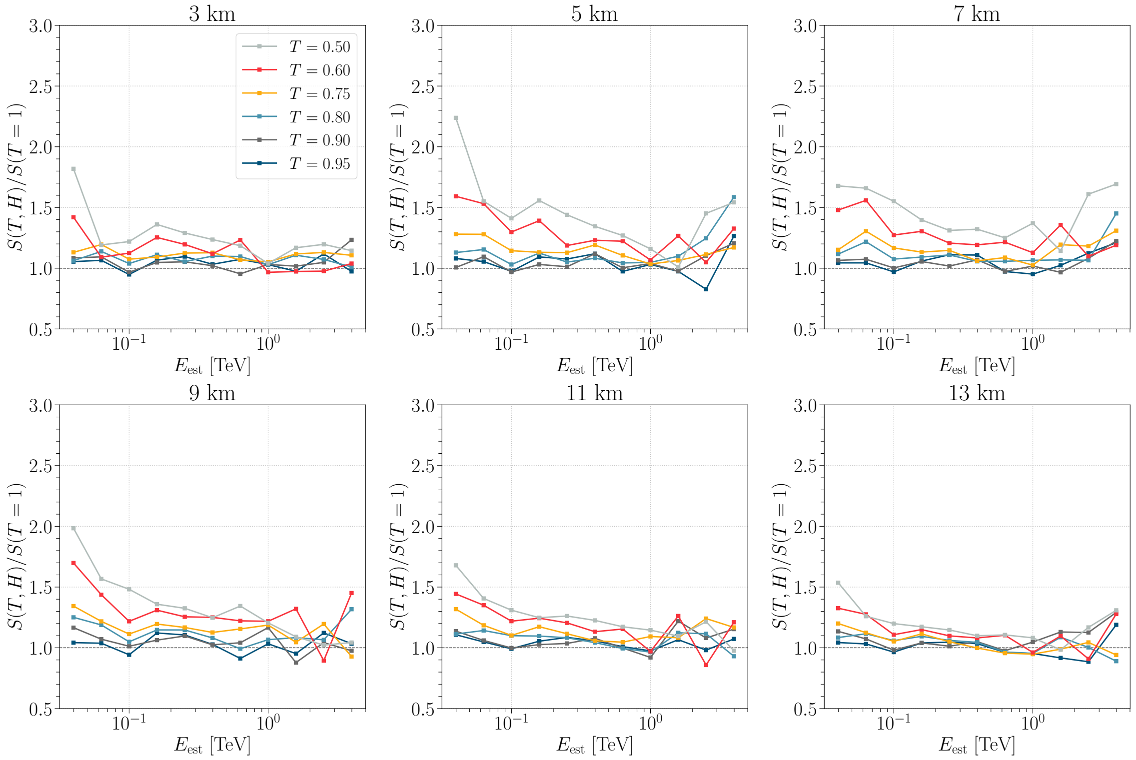

(b) 4 LSTs, transmission dependence of differential sensitivity ratio for fixed height

Figure 4.47: Differential sensitivity cloud-to-clear ratio for the subarray of 4 LSTs for the case when adaptive MC simulations are used for DirLUT and RFs training.

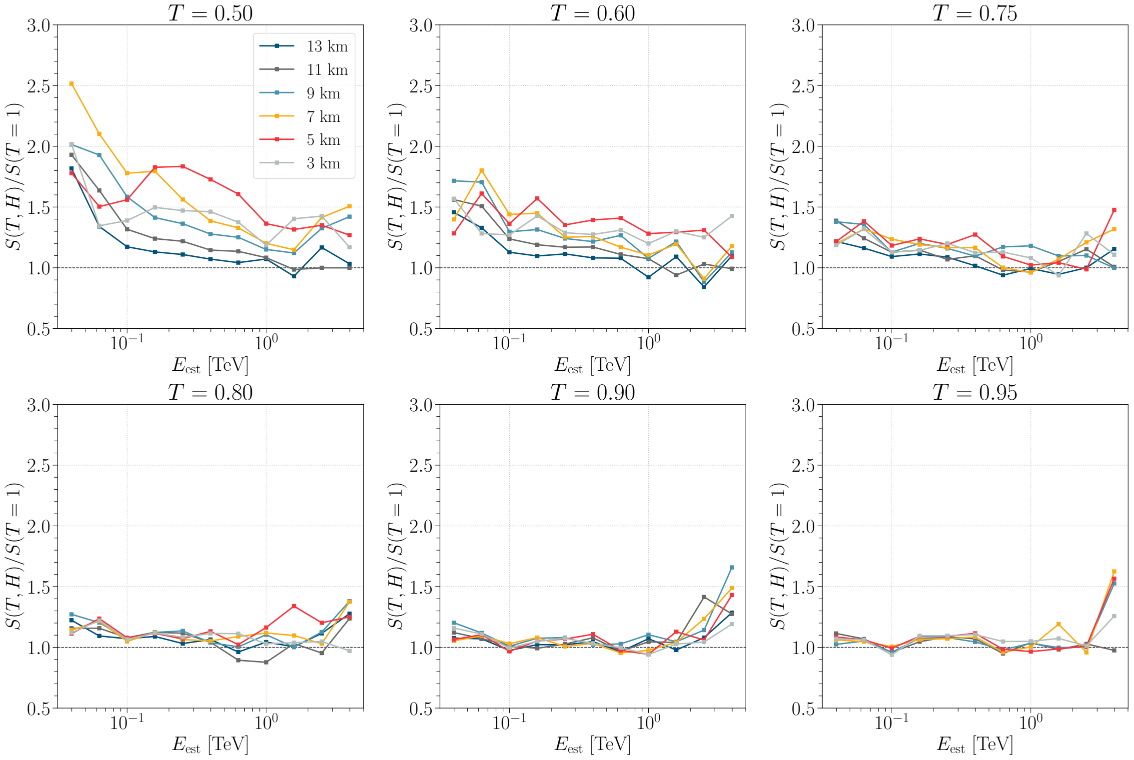

(a) 4 LSTs, height dependence of differential sensitivity ratio for fixed transmission

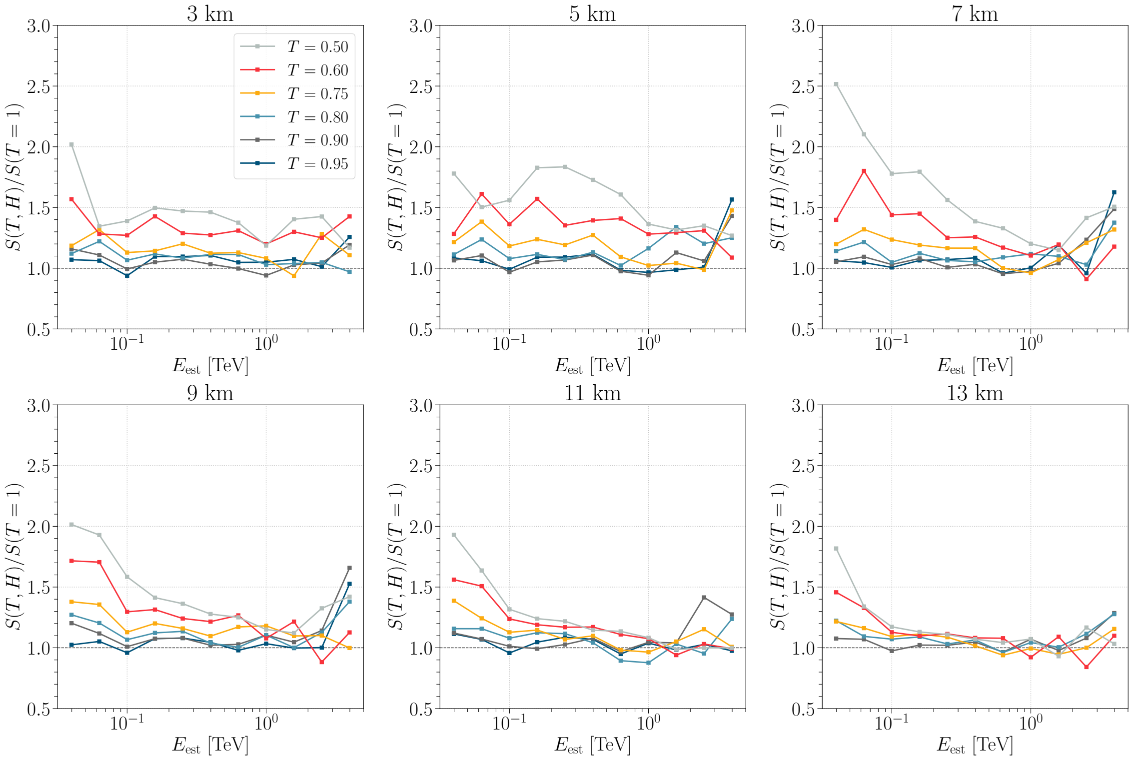

(b) 4 LSTs, transmission dependence of differential sensitivity ratio for fixed height

Figure 4.48: Differential sensitivity cloud-to-clear ratio for the subarray of 4 LSTs for the case when standard MC simulations are used for DirLUT and RFs training.

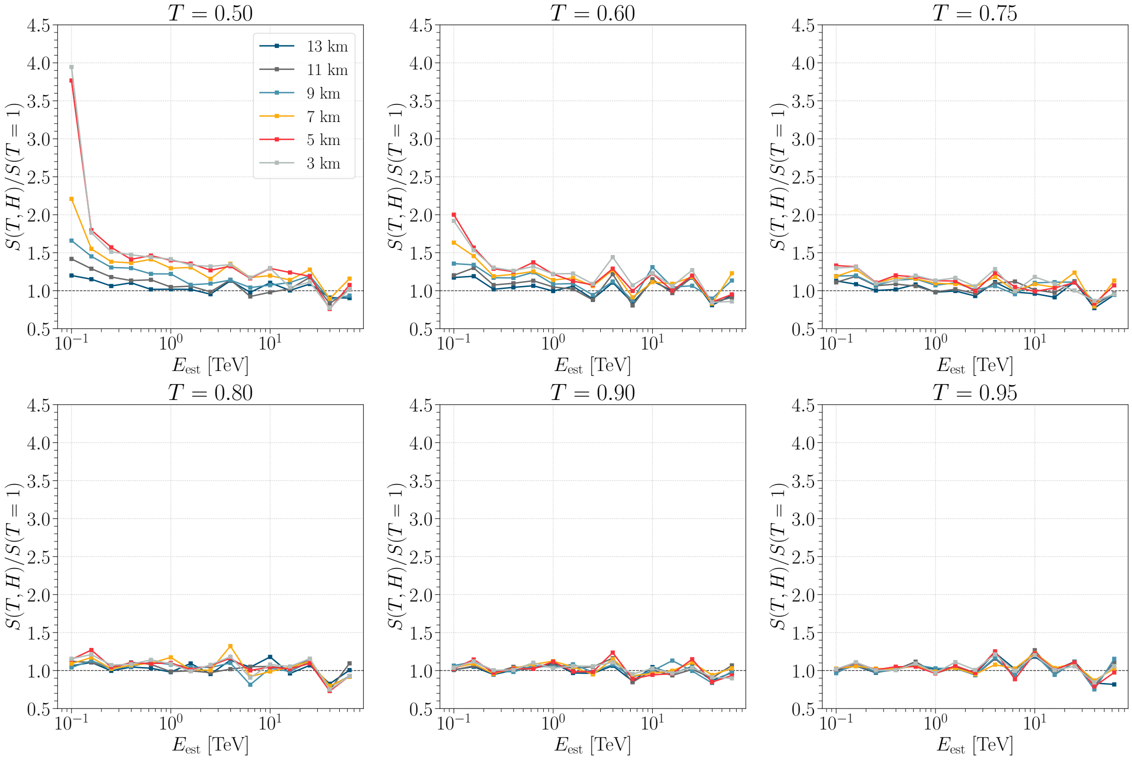

(a) 15 MSTs, height dependence of differential sensitivity ratio for fixed transmission

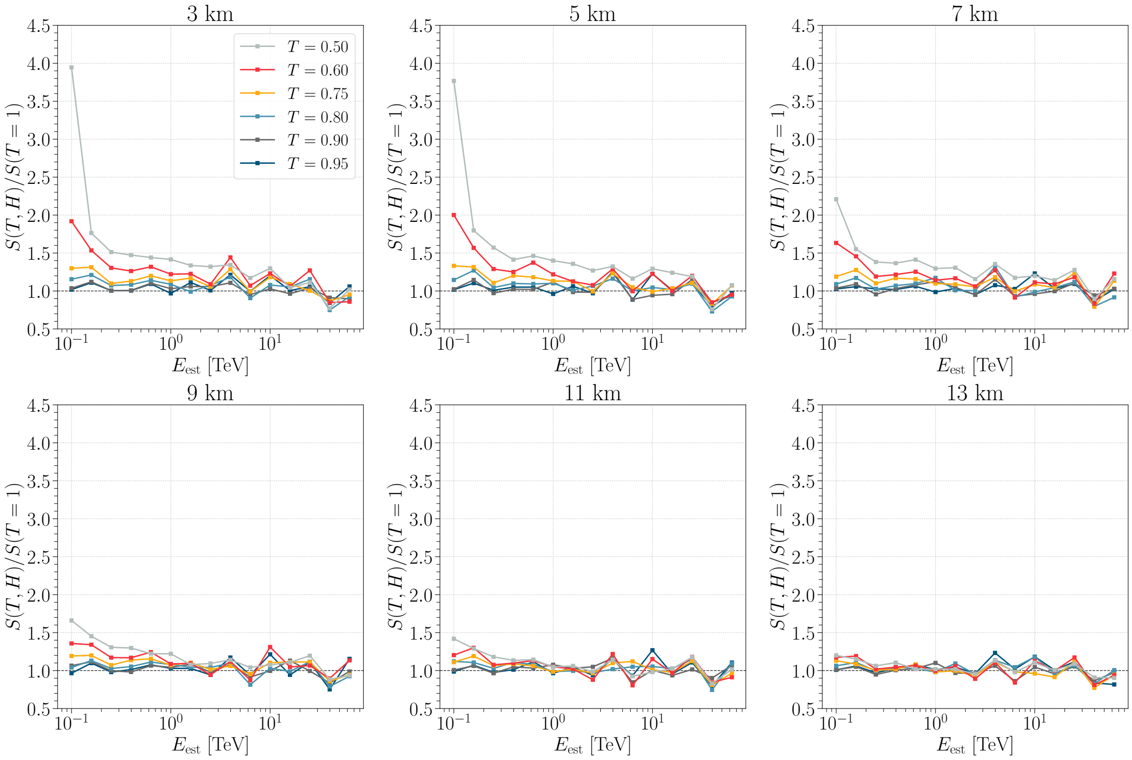

(b) 15 MSTs, transmission dependence of differential sensitivity ratio for fixed height

Figure 4.49: Differential sensitivity cloud-to-clear ratio for the subarray of 15 MSTs for the case when adaptive MC simulations are used for DirLUT and RFs training.

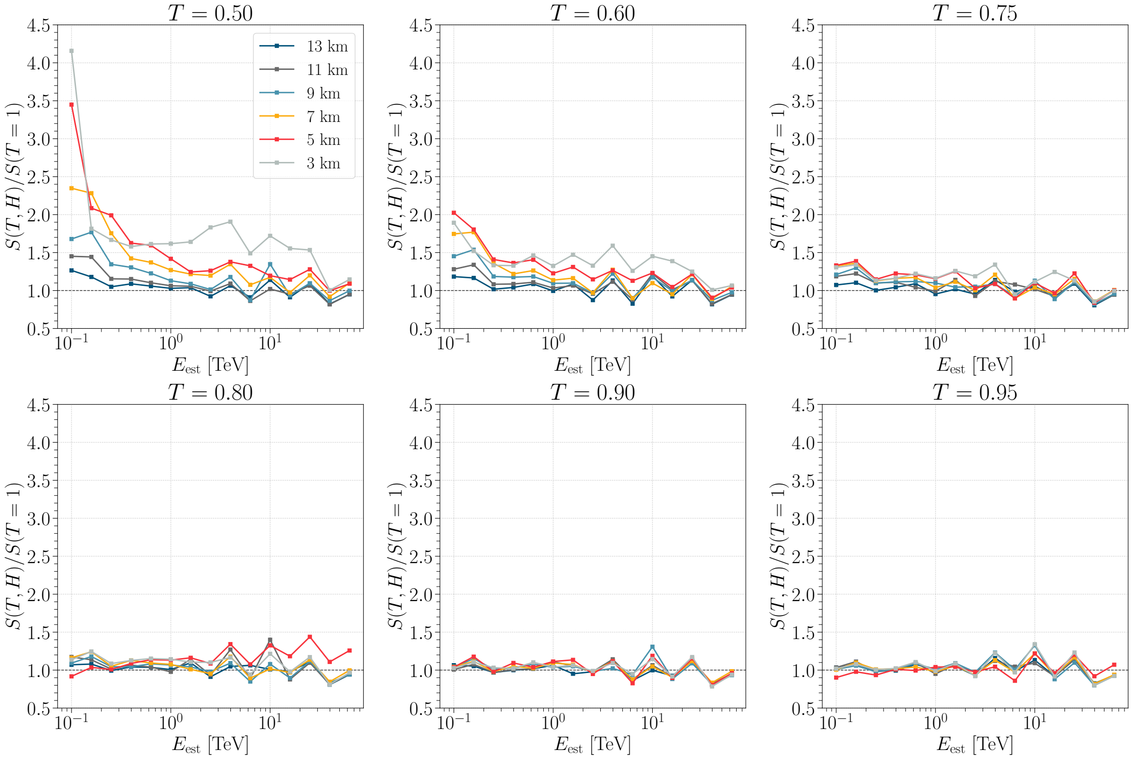

(a) 15 MSTs, height dependence of differential sensitivity ratio for fixed transmission

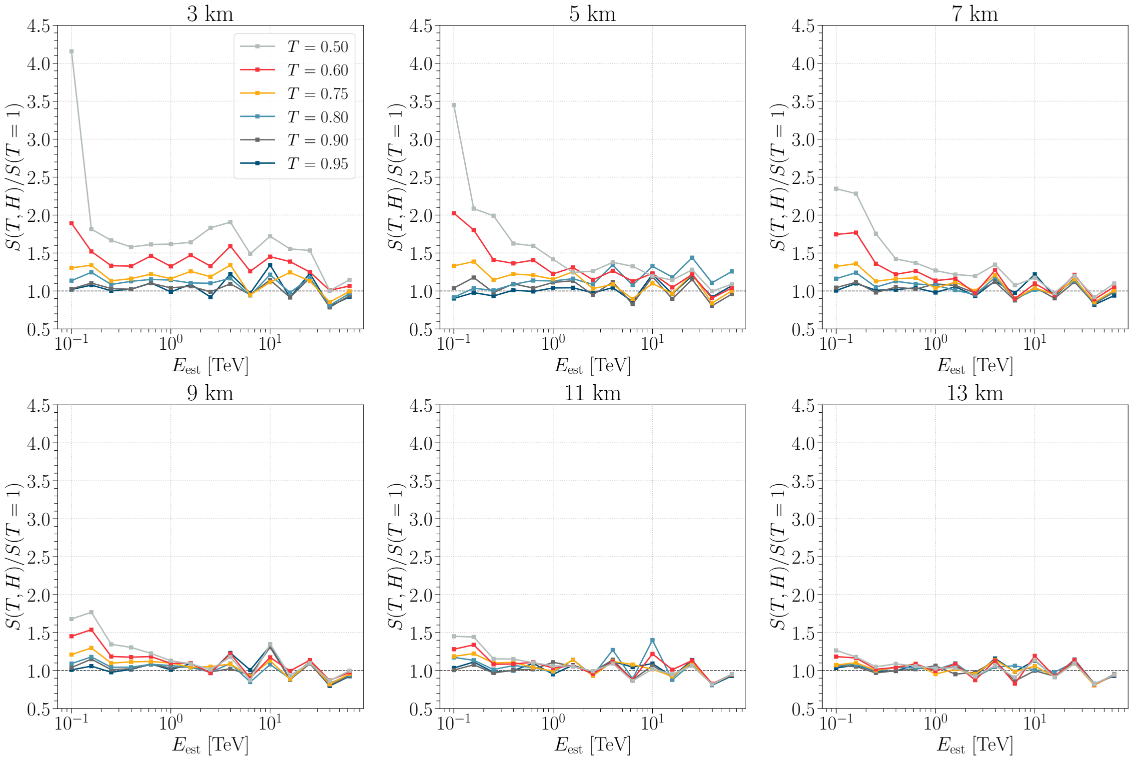

(b) 15 MSTs, transmission dependence of differential sensitivity ratio for fixed height

Figure 4.50: Differential sensitivity cloud-to-clear ratio for the subarray of 15 MSTs for the case when standard MC simulations are used for DirLUT and RFs training.

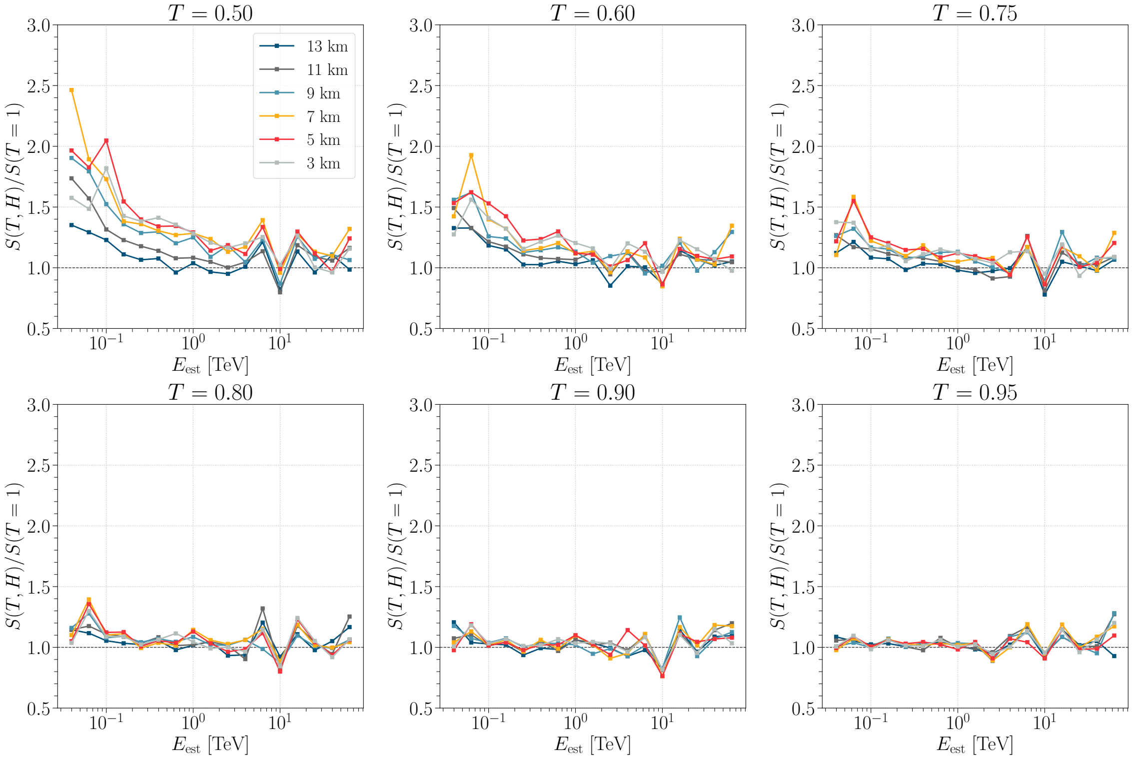

(a) CTAO-N, height dependence of differential sensitivity ratio for fixed transmission

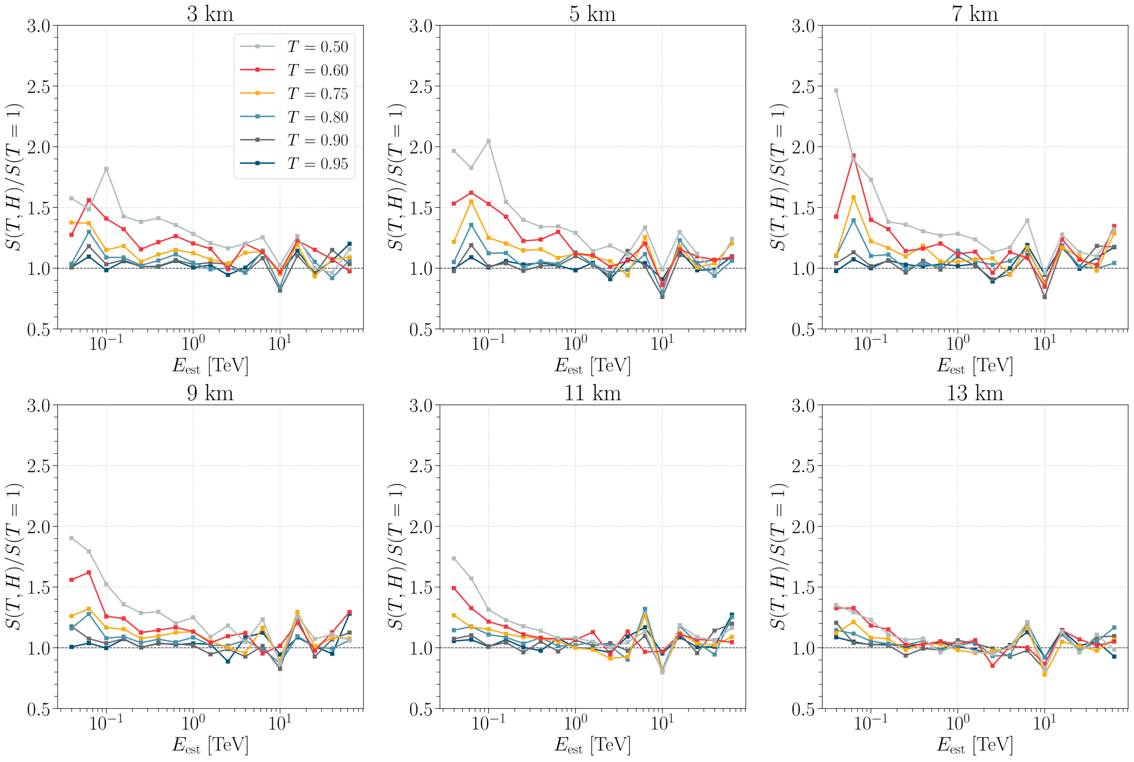

(b) CTAO-N, transmission dependence of differential sensitivity ratio for fixed height

Figure 4.51: Differential sensitivity cloud-to-clear ratio for CTAO-N for the case when adaptive MC simulations are used for DirLUT and RFs training.

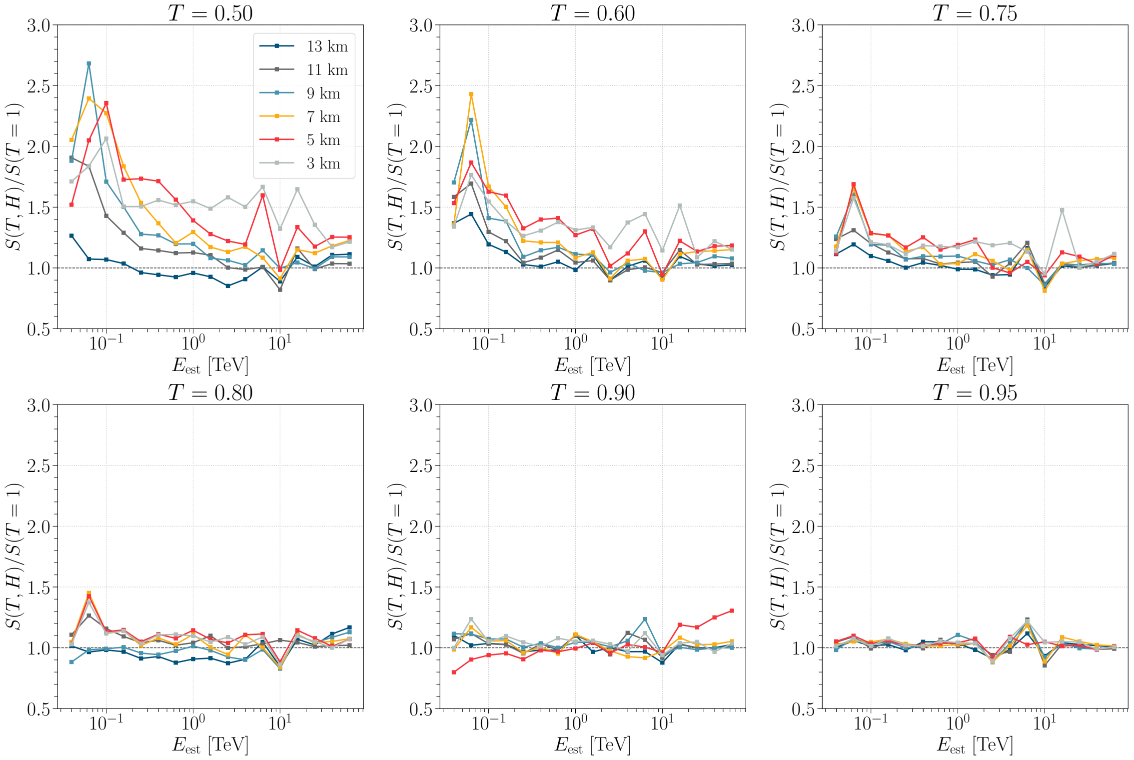

(a) CTAO-N, height dependence of differential sensitivity ratio for fixed transmission

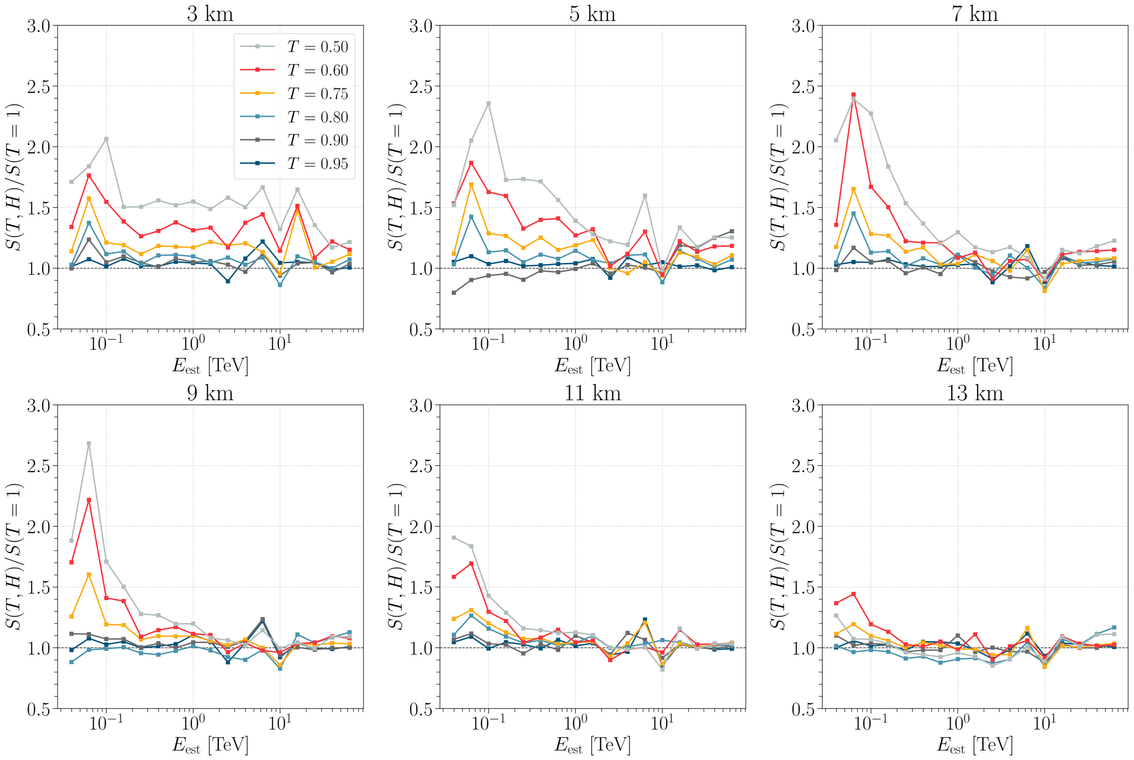

(b) CTAO-N, transmission dependence of differential sensitivity ratio for fixed height

Figure 4.52: Differential sensitivity cloud-to-clear ratio for CTAO-N for the case when standard MC simulations are used for DirLUT and RFs training.

4.9 Summary and conclusions

An extensive database of MC simulations (more than 700 TB of data) was produced to investigate the performance of CTAO-N and the corresponding subarrays of 4 LSTs and 15 MSTs in the presence of clouds with different base heights and vertical transmissions. The atmospheric transmission profiles were derived using the MODTRAN band model algorithm. The effects of clouds were evaluated by analyzing the simulated data and calculating the instrument response functions (IRFs) (energy bias, energy resolution, angular resolution, effective area, and differential sensitivity) for two different analyses: one in which the data were analyzed with adaptive MC simulations (which include clouds), and the other in which the data were analyzed with standard MC simulations (without clouds).

The presence of clouds has been shown to reduce the number of detected events, especially in the low energy regions where the number of detected events decreases even by an order of magnitude compared to the cloudless conditions. This significantly increases the energy threshold, by up to a factor of 2 depending on cloud properties. The use of adaptive Monte Carlo simulations exploits the energy bias and energy resolution comparable to that under cloudless conditions. However, the lost events cannot be recovered and reconstructed, so the effective area and thus the differential sensitivity are inevitably impaired even when using adaptive MC simulations. Observing weaker sources becomes more challenging when confronted with dense ($T \leq 0.75$) and low (≤ 7 km) cloud cover. In such conditions, the flux sensitivity of CTAO-N is decreased up to a factor of 3, compared to that achieved in clear atmospheric conditions.

The use of standard MC simulations in the training sample further degrades the performance of CTA and leads to a strong negative energy bias and degraded energy resolution. In such cases, both the effective area and the differential sensitivity are additionally reduced (even by 50% compared to the case of adaptive MC simulations). Nevertheless, for La Palma, where most of the clouds are located above 8 km a.s.l., the clouds are not of major importance when it comes to angular resolution, as the influence of the clouds on direction reconstruction is $\lesssim 10\%$, with no major differences between the standard and adaptive MC simulations.

Finally, one may wonder to what extent the standard MC simulations can be safely used to obtain the performance of an energy estimator that lies within the systematic uncertainties expected in the clear atmosphere. The answer to this question is not straightforward given the large number of variables (cloud transmission and height as well as gamma-ray energy), but can be given with some constraints. To answer this question, we evaluate the bias difference between the standard and adaptive MC simulations and compare it with the CTA requirement A-PERF-2050[2], which states that the systematic uncertainty in the measurement of the absolute intensity of Cherenkov light must be below 8%. Let us first focus on low and high clouds, where there are no strong energy-dependent effects, but the effects are similar over the entire energy range. For low clouds between 3 km and 5 km, the systematic uncertainties in the energy measurement are above 8% for $T < 0.95$, while in the case of $T = 0.95$ the systematic uncertainties amounts to $\lesssim 5\%$. In the case of high clouds at altitudes ≥ 11 km, the standard MC simulations can be safely used for energies

---

[2] `https://www.cta-observatory.org/wp-content/uploads/2019/04/CTA-SPE-SCI-00000-0001_Issue_1_SystemLevelSciencePerformanceReqs.pdf`

above 150 GeV regardless of the cloud transmission and over the whole energy range for $T \geq 0.8$. Below this energy and for $T \leq 0.75$ the effects of the clouds tend to be stronger and the systematic uncertainties increase above 8%.

Clouds at medium altitudes between 7 km and 9 km show strong energy-dependent effects, which makes it difficult to make a clear statement about when the standard MC simulations should be used and where one should generate adaptive MC simulations. For $T \geq 0.9$, the standard MC simulations show no systematic uncertainties above 8%, while for the rest of transmission values the standard MC simulations can be safely used only for energies above 10 TeV and 1 TeV for the clouds at 7 km and 9 km, respectively. For higher transmission values, one may safely use standard simulations to generate RF models for analyzing data taken in the presence of clouds.

CHAPTER 5

LST-1 and MAGIC joint observations of the Crab Nebula in the presence of clouds

The method of adaptive MC simulations presented in the previous chapter is not only suitable for studying the performance of Cherenkov telescopes under different atmospheric conditions, but can also be used to analyze the real data. Such MC simulations could be used to build RF models to classify the parent particle of the detected air shower and estimate its energy and direction. To test such an approach, a suitable atmospheric transmission profile needs to be recorded during data acquisition, e.g. with a LIDAR system. Since the CTA Raman LIDAR is currently in the commissioning phase, we opted to test the method using real data obtained through joint observations of the Crab Nebula with LST-1 and MAGIC telescopes. The spatial distance between LST-1 and the MAGIC telescopes is approximately 100 m and corresponds to the average size of the Cherenkov light pool. This enables joint, stereoscopic observations and an improvement in the performance of the system compared to individual observations. An essential part of the MAGIC auxiliary system is the elastic micro-Joule LIDAR system, which is used to measure atmospheric transparency during observations with the MAGIC telescopes. The corresponding LIDAR measurements, employed for cloud scanning and identification, were used to generate atmospheric transmission profiles for the `sim_telarray` simulations. In this chapter, a comparative analysis between adaptive MC simulations (generated based on the knowledge of atmospheric conditions from LIDAR measurements) and the real data from the Crab Nebula, which is considered the brightest constant-flux VHE gamma-ray source and has been intensively studied for decades, is performed. The performance of the joint observations of LST-1 and MAGIC in the presence of clouds is also evaluated. The chapter concludes with a comprehensive spectral and temporal analysis of the Crab Nebula data, affirming that the method of adaptive MC simulations consistently delivers the expected results.

5.1 The MAGIC LIDAR

The operating principle of LIDAR is simple and generally consists of a light emitter, usually a pulsed laser, and a receiver. A laser beam is emitted in the target region of the sky, while the backscattered light is collected by the telescope of the LIDAR. This is usually followed by an optical analysis system that selects specific wavelengths or polarization states. The light is then

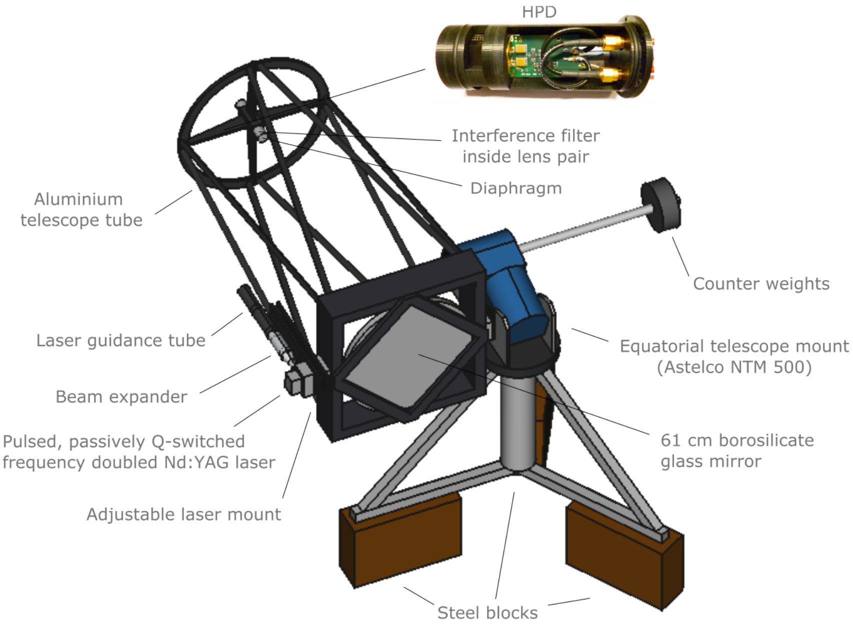

Figure 5.1: Basic LIDAR components. The MAGIC LIDAR system uses the commercial equatorial telescope mount NTM 500, a 61 cm borosilicate glass mirror, a frequency-doubled Nd:YAG laser characterized by a pulse energy of 25 μJ, and HPD detector with a quantum efficiency of more than 50% at a wavelength of 532 nm. The interference filter inside the lens pair is used for wavelength selection and reduces the light of the night sky background by more than a factor of 100 (Schmuckermaier et al., 2023).

focused onto a photosensor, where the received optical signal is converted into an electrical signal and analyzed using a LIDAR signal inversion algorithm.

The MAGIC elastic LIDAR (Fruck et al., 2022; Schmuckermaier et al., 2023) (Figure 5.1) uses a pulsed, passively Q-switched, frequency-doubled Nd:YAG laser with an output of 25 μJ. The laser operates at a wavelength of 523 nm and a repetition rate of 250 Hz. Although the laser beam is already highly collimated, its divergence is further reduced by a 20 × beam expander to the value of 12 mrad. This also ensures safety by reducing the light flux density. From the beam expander, the laser beam enters a guidance tube containing baffle rings to remove any remaining stray light. A hybrid photodetector (HPD) with a quantum efficiency of ≈ 50% at 532 nm is used for detection. The receiving setup also includes a borosilicate glass mirror positioned off-axis relative to the emitter with a focal length of 150 cm and a diameter of 61 cm. A lens parallelizes the backscattered light before the wavelength selection. The wavelength selection is achieved by an interference filter with a bandwidth of 3 nm, positioned between the lenses. The second lens focuses the light onto HPD. During standard operation, the LIDAR receives the pointing coordinates of the MAGIC telescopes and follows them with an offset of 5° so as not to interfere with the operations of the telescopes, while the measurements are performed every four minutes. The transmission profiles are extrapolated for MAGIC observation periods that extend up to 15 minutes beyond the time range covered by the LIDAR measurements. For details on the MAGIC LIDAR, the reader is referred to Fruck (2015); Fruck et al. (2022); Schmuckermaier et al. (2023).

The LIDAR equation

The emitted light pulse, which contains N_0 photons, is affected by scattering and absorption on its way through the medium. The backscattered light is recorded in the form of a photon count rate $\mathrm{d}N(t)/\mathrm{d}t$. The photon count rate received from a distance r depends on the performance of the LIDAR system, the geometry of the LIDAR system $G(r)$, the backscatter coefficient $\beta(r)$, the transmission $T(r)$ (Weitkamp, 2005), and the overall efficiency of the system C (including the optical transmission from the emitter to the receiver and the detection efficiency). The geometry factor G describes the overlap function of the laser beam with the FoV of the detector $O(r)$ and r^2:

$$G = \frac{O(r)}{r^2} \tag{5.1}$$

The dependence on r^{-2} results from the fact that the receiving detector area A is part of a spherical surface with radius r, which is centered in the scattering volume. Since the speed of light in the medium is known and constant, the photon count rate can be converted into the number of photons per distance. Everything together results in the final LIDAR equation in the form of:

$$\frac{\mathrm{d}N(r)}{\mathrm{d}r} = N_0 C O(r) \frac{A}{r^2} \beta(r) \exp\left(-2\int_0^r \alpha(r')\mathrm{d}r'\right). \tag{5.2}$$

The last term is the form of the Beer-Lambert law, which represents the transmission dependence of the photon count rate, where factor 2 stands for the forward and backward transmission and α is the extinction coefficient. Due to the short duration of the pulses (FWHM $\approx$ 1 ns), the number of photons can be calculated as a function of the distance by integration equation (5.2) over the digitization length l (Fruck, 2015):

$$N(r) = \int_{r-\frac{l}{2}}^{r+\frac{l}{2}} \mathrm{d}N(r') \approx N_0 C O(r) \frac{A}{r^2} l \beta(r) \exp\left(-2\int_0^r \alpha(r')\mathrm{d}r'\right). \tag{5.3}$$

However, the LIDAR equation in this form does not provide any information about the physical properties of the atmosphere, and therefore it is more common and convenient to introduce the logarithm of the range-corrected LIDAR return:

$$S(r) = \ln\left(N(r)r^2\right) = \ln\left(N_0 C A l\right) + \ln\beta(r) - 2\int_0^r \alpha(r')\mathrm{d}r', \tag{5.4}$$

which, expressed in differential form, results in:

$$\frac{\mathrm{d}S(r)}{\mathrm{d}r} = \frac{1}{\beta}\frac{\mathrm{d}\beta}{\mathrm{d}r} - 2\alpha. \tag{5.5}$$

The above equation has two variables, the backscatter coefficient and the extinction coefficient, and therefore it is not possible to extract the value of these variables from the return signal of a single-wavelength LIDAR without further assumptions or additional information. The most common methods to solve the LIDAR equations are the slope method (Leeuw and Kunz, 1993) and the Klett methods of forward and backward integration (Klett, 1981). Unfortunately, the slope

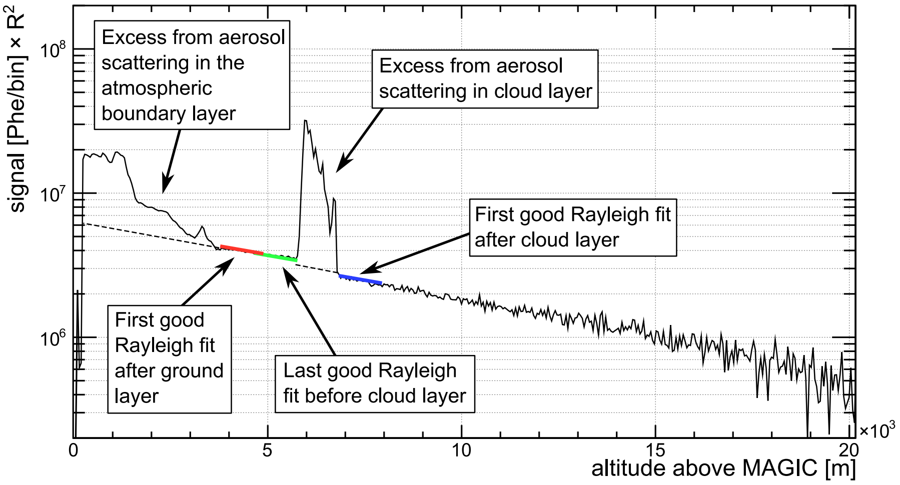

Figure 5.2: The LIDAR return signal shows the cloud between 5 and 7 km a.g.l. The excess below 2 km a.g.l. is due to aerosol scattering in the atmospheric boundary layer (Fruck, 2015).

method assumes a homogeneous atmosphere ($d\beta/dr = 0$), while the Klett method is only suitable for single-component atmospheres and LIDARs operating at near-IR wavelengths. At 532 nm, Mie scattering and Rayleigh scattering are two mechanisms with comparable influence and cannot be well described by a single power-law index used in the Klett method. To analyze the signals obtained with the MAGIC LIDAR system, a special method was developed (Fruck, 2015).

Inversion of the LIDAR signal

In the clear regions of the sky, where Rayleigh scattering predominates at 532 nm, the value of the LIDAR return decreases exponentially, which is due to the exponential decrease in density with increasing altitude, but also because of the attenuation of the light by the atmospheric molecules. However, the latter effect is of less importance due to the relatively high atmospheric transparency at 532 nm. As a result, the regions with clear air appear as straight line segments in the semi-logarithmic representation of the range-resolved LIDAR signal as a function of altitude (Fruck, 2015) (Figure 5.2). The excess up to an altitude of 2 km a.g.l. is due to aerosol scattering in the atmospheric boundary layer.

The MAGIC LIDAR algorithm uses a sliding window to fit a pure-Rayleigh barometric-density-profile model for the heights within the sliding windows (Fruck, 2015):

$$S_{\mathrm{mol}}(h) = C \cdot \exp \frac{h}{h_s} \tag{5.6}$$

where C is the scaling constant and h_s is the scale height of the barometric atmosphere model. By evaluating the quality of the fit with a reduced χ^2, regions of pure Rayleigh scattering can be identified. Sudden deterioration and subsequent improvements in the χ^2 value are then used to localize regions of excess aerosol scattering such as clouds or additional aerosol concentrations.

Any atmospheric contamination, e.g. by clouds or aerosols, introduces additional backscattering to the signal and leads to an increase in the magnitude of $S(r)$. The increase in backscattering

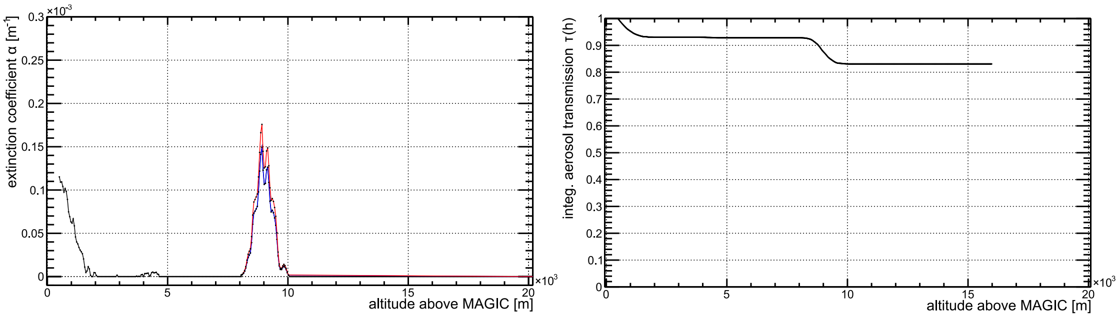

Figure 5.3: *Left:* The extinction coefficient is estimated by the extinction method (i.e. normalizing the backscattering excess of the cloud over the total backscattering, blue line) or by the LIDAR ratio method (i.e. scaling the backscattering excess with the LIDAR ratio, red line). *Right*: The transmission of the cloud layer (Fruck, 2015).

inevitably increases the total scattering cross section and thus also the extinction coefficient $\alpha(r)$. This leads to a decrease of $S(r)$ below the extrapolation of the previous straight fit from the region with clear air, at the latest when a second region with clear air is reached after the region with increased backscattering (compare green and blue line in Figure 5.2).

Identification of clouds and transmission measurements

The base of the cloud is positively detected if the value of the reduced χ^2 for the local fit is above 2.5 and there is a positive excess of the last bin over the fitted curve. The top of the cloud layer is positively detected if the value of the reduced χ^2 is greater than 1.5 and the first data point of the fit is below the last fit before the cloud, as clouds always reduce the amount of transmitted light.

Three methods for measuring transmission have been developed (Figure 5.3). In the first method, called the *extinction method*, the attenuation of light through the layer of a cloud is determined by comparing the scaling constant of the Rayleigh fit before (Figure 5.2, green line) and after the cloud (Figure 5.2, blue line). Assuming that the light is attenuated twice within the cloud layer (in the forward and backward direction), the relationship between the scaling constants is as follows (Fruck, 2015):

$$C_2 = C_1 \cdot T_{\mathrm{aer}}^2. \tag{5.7}$$

The transmission of the cloud layer is calculated as the square root of the ratio of the scaling constants after and before the cloud layer:

$$T_{\mathrm{aer}}^2 = \sqrt{\frac{C_2}{C_1}}. \tag{5.8}$$

The aerosol extinction coefficient is obtained by calculating the excess of $S(h)$ over the Rayleigh fit:

$$\overline{S}_{\mathrm{mol}}(h) = \frac{C_1 + C_2}{2} \cdot \exp\frac{h}{h_s}, \tag{5.9}$$

$$\alpha_{\text{aer}}(h) = \sqrt{\frac{C_2}{C_1}} \frac{S(h) - \overline{S}_{\text{mol}}(h)}{\int_{h_1}^{h_2} \left(S(h) - \overline{S}_{\text{mol}}(h)\right) \mathrm{d}h}. \tag{5.10}$$

The second approach, called the *LIDAR ratio method*, assumes a known and constant value of the LIDAR ratio within the cloud layer. The LIDAR ratio, K, is the ratio between the extinction coefficient and the backscatter coefficient. The aerosol extinction coefficient is determined by calculating the backscattering excess over the Rayleigh fit as (Fruck, 2015):

$$\alpha_{\text{aer}}(h) = K \cdot \beta_{\text{mol}}(h) \frac{S(h) - \overline{S}_{\text{mol}}(h)}{\overline{S}_{\text{mol}}(h)} \tag{5.11}$$

The method is only suitable for optically thin clouds where the total transmission is close to one, i.e. the light near the top of the cloud is not strongly attenuated by the rest of the cloud on its way back to the detector, and in practice needs to be calibrated with the extinction method.

However, the main method used is an iterative Klett formalism (Fruck et al., 2022). The signal region between the estimated cloud top and the cloud base is inverted with the Klett algorithm, assuming an initial LIDAR ratio of $K = 33$ sr. The resulting aerosol extinction coefficients are then integrated over the cloud and compared to the previously calculated vertical OD of the cloud. Then the LIDAR ratio used is rescaled by the ratio between the two estimates of OD and the cloud part of the signal is inverted again. This procedure is repeated until both vertical OD estimates match, allowing an indirect measurement of the LIDAR ratio.

5.2 Data sample

The Crab Nebula data

The joint observations of LST-1 and MAGIC telescopes began in late 2019, shortly after the inauguration of the LST-1 telescope, and were mostly conducted under excellent atmospheric conditions ($T \geq 0.90$). However, some of the runs were carried out under conditions of reduced atmospheric transmission, allowing the study of the Crab Nebula in the presence of clouds. In June 2022, minor issues were identified with the MAGIC LIDAR, such as the mechanical resonance or loosened screws of the mirror, which led to a drop in intensity during the LIDAR repositioning. Therefore, the LIDAR data recorded after April 2022 is considered unreliable and observations from that period were not used in the study. For further analysis, only observations on dark nights (the moon is below the horizon) with a zenith distance (Zd) of less than 50° were considered, as larger zenith angles inherently reduce the density of the Cherenkov light pool and significantly decrease the trigger yield even in the clear atmosphere. Since the MAGIC sum trigger is not yet implemented in `sim_telarray`, only data recorded with the standard MAGIC stereo trigger were used. All data acquisition was done in wobble mode, i.e. the telescopes were pointing with an offset of 0.4° from the center of the Crab Nebula. The data for which the pointing directions of the two systems differed by more than 0.1° were also excluded from the analysis.

Finally, a scan of the LIDAR measurements was performed using the MARS software to

base height [km]	thickness [km]	T	zenith range [°]
7.73	1.58	0.52	30.64 - 33.15
5.90	1.32	0.58	40.65 - 42.28
5.75	1.46	0.70	42.56 - 45.42
7.10	2.01	0.77	27.79 - 29.55
5.75	1.24	0.79	43.63 - 48.53

Table 5.1: Simulated cloud parameters. The base heights are given in km above ground level.

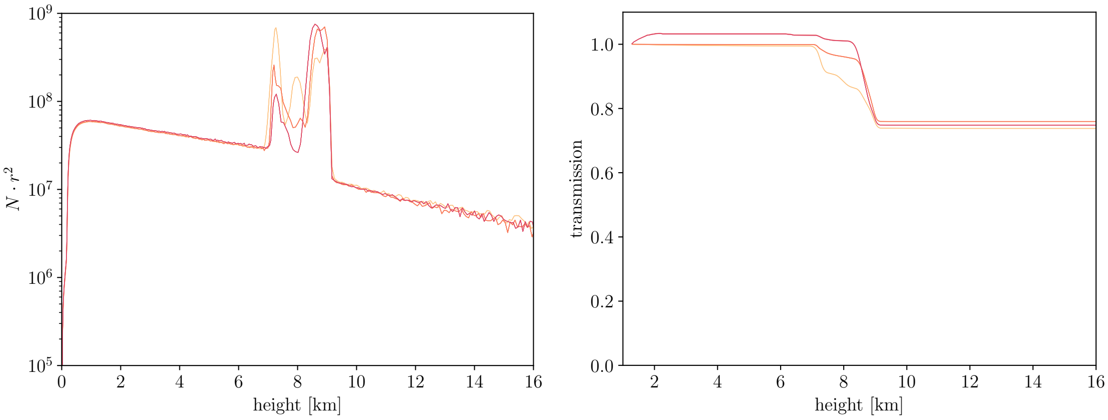

(a) range-corrected LIDAR return signal

(b) transmission profile

Figure 5.4: The results of the LIDAR measurements (the MAGIC run 5095078) from the night of March 11, 2021, show a cloud layer between ≈ 7 km and ≈ 9 km with an average transmission of $T = 0.77$.

discard the data recorded in the presence of increased aerosol concentrations, such as Calima, and only include the data taken in the presence of clouds. In addition, observational runs with highly variable atmospheric transmission (e.g. due to clouds crossing the FoV) were excluded due to the complexity, CPU overhead and duration of the MC simulations. Given the limitation of available data, time and CPU resources, five observational runs from March 2021 with relatively stable atmospheric transmission were selected (i.e. for which the standard deviation of the transmission distribution within the run is smaller than 0.05, as higher transmission variations in the case of low clouds with low transmission can lead to significant differences in the performance of the energy estimator, as shown in Chapter 4). The reduction in available runs resulted in a total of only ≈ 1.3 hours of observations available for analysis. However, this is still enough data to reconstruct the correct spectrum of the Crab Nebula. Although normally the low-zenith data ($Zd < 30°$) are analyzed separately from the data in the middle zenith range ($30° \leq Zd < 50°$) to achieve the lowest possible energy threshold, due to the limited and small number of runs, such a distinction is not made here and all data are combined.

MC simulations

Suitable atmospheric transmission profiles for `sim_telarray` were created with MODTRAN (Berk, Bernstein and Robertson, 1987) band model algorithm on the basis of the LIDAR measurements. For this purpose, the basis of the atmospheric model (i.e. clear sky transmission) was adapted

	E_{min} (TeV)	E_{max} (TeV)	VIEWCONE (deg)	CSCAT (m)
gamma (train)	$5 \cdot \cos^{-2.5}(Zd)$	$50 \cdot \cos^{-2.5}(Zd)$	0 - 2.5	$900 \cdot \cos^{-0.5}(Zd)$
proton (train)	$10 \cdot \cos^{-2.5} Zd$	$\max(100 \cdot \cos^{-2.5} Zd,\ 200)$	$0 - 8 \cdot \cos^{0.5}(Zd)$	$1500 \cdot \cos^{-0.5}(Zd)$
gamma (test)	$5 \cdot \cos^{-2.5}(Zd)$	$50 \cdot \cos^{-2.5}(Zd)$	0.3999 - 0.4001	$700 \cdot \cos^{-0.5}(Zd)$

Table 5.2: Input parameters of generated MC samples: energy range, spectral index, the offset angle from the camera center, and the maximum simulated impact parameter. The zenith-wise scaling is done following the approach of Abe et al. (2023a) .

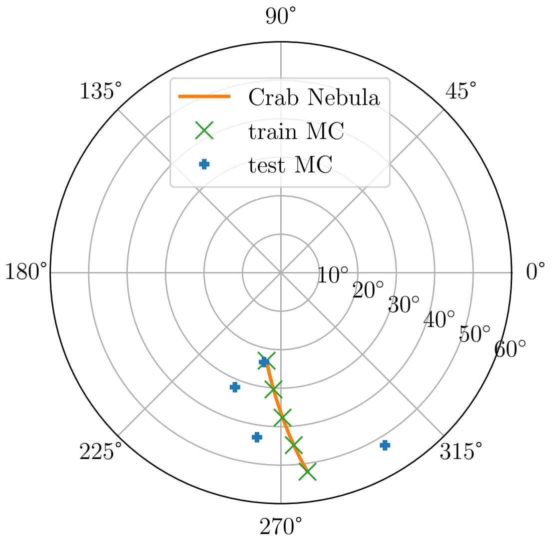

Figure 5.5: The pointing directions (azimuth, zenith) of the test and training samples. The training samples are used to create RF models for the reconstruction of events, while the test samples are used to calculate IRFs. The radial distance indicates the zenith, while the polar coordinate indicates the azimuth of the pointing direction.

to the default model used in the LSTProd2[1] settings for `sim_telarray` simulations of the joint observations. Namely, the tropical atmosphere with navy maritime extinction and the standard air mass character of the extinction model is used. This aerosol model consists of a sea salt component and a continental component (representing the rural aerosol, with larger, dust-like particles eliminated (Carr, 2005)). The relative amounts of the oceanic and continental components were adjusted to describe an aerosol distribution of the open ocean with a minor continental influence. Both the current wind speed and the 24-hour average wind speed were set to 0.1 m s^{-1}. The rest of the setup is the same as in section 2.4.6. The optical depth (transmission), the base height and the thickness of the clouds were determined on the basis of the LIDAR measurements. Due to the small variations in the obtained transmission from a subrun to a subrun ($\lesssim 0.05$, as more variable runs are excluded from the analysis), the mean values are calculated as a subrun duration weighted average to apply larger weights for longer subruns. The mean base height and top height are calculated in the same way. The simulated cloud parameters are listed in Table 5.1, while Figure 5.4 shows range-corrected LIDAR return signal and transmission profiles for selected runs.

MC simulations were performed with the CORSIKA code (Heck et al., 1998) version 7.741

---

[1] `https://github.com/cta-observatory/lst-sim-config`

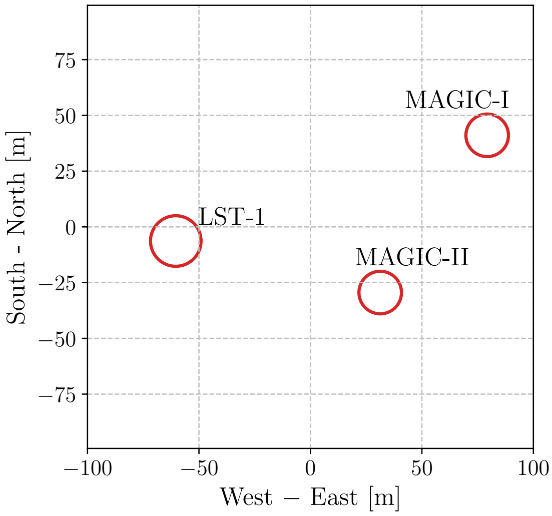

Figure 5.6: The positions of the telescopes.

and `sim_telarray` (Bernlöhr, 2014b) with the LSTProd2 settings (Abe et al., 2023a). The training samples (used to generate RF models) were simulated at fixed pointing coordinates along the path of the Crab Nebula in the sky in the bins of $\cos(Zd)$. The pointing directions for the test sample were chosen in a triangular grid layout in the $\cos(Zd)$ and $\sin(\delta)$ bins, where δ is the angle between the pointing direction and the geomagnetic field, in order to account for the effects of air mass, which is inversely proportional to $\cos(Zd)$, and geomagnetic field on the shape of the Cherenkov image, following the approach of Abe et al. (2023b) (Figure 5.5). All showers were generated with a spectral index of −2 and then reweighted in the analysis according to particle type. The gamma rays and protons for the training sample were simulated with a maximum offset from the camera center of 2.5° and 10°, respectively, to allow reconstruction of the sources in the FoV. The test sample gamma rays were simulated following the wobble mode, i.e. with an average offset of 0.4° from the camera center. The details of the CORSIKA input parameters can be found in Table 5.2. Note that the energy range, the maximum offset from the camera center and the maximum impact parameter have been scaled with respect to Zd according to the approach of Abe et al. (2023a). The layout of the telescopes is shown in Figure 5.6.

5.3 Data analysis

In their independent operations, LST-1 and the MAGIC telescopes use different analysis software. In the analysis of the MAGIC data ROOT-based C++ software MARS (Moralejo et al., 2009; Zanin, 2013) is used, which has been already extensively described in Chapter 4. The output of the such analysis is given in the ROOT containers. On the other hand, the LST-1 data is analyzed with Python-based library called `cta-lstchain`[2] (López-Coto et al., 2020) which heavily relies on the `ctapipe`[3] library (Kosack et al., 2022). The processed data of LST-1 telescope is stored in HDF5 files. In the case of joint observations, the signal extraction and calibration are done

---

[2] https://github.com/cta-observatory/cta-lstchain

[3] https://github.com/cta-observatory/ctapipe

by the telescope's respective analysis chain, while the image cleaning and the rest of the higher-level analysis are performed with special Python library `magic-ctapipe`[4] (MCP) dedicated to the analysis of the data taken in the joint observations of LST-1 and MAGIC telescopes (Abe et al., 2023a). Note, however, that other Python modules are used for specific task, such as `pyirf`[5] (Nöthe et al., 2023) for the calculation of IRFs or `gammapy`[6] (Deil et al., 2018; Donath et al., 2023) for flux estimation.

Signal extraction and calibration, image cleaning

LST-1 signal extraction is performed with `cta-lstchain` by the local peak window sum algorithm, i.e. extractor which sums the signal in a given time window around the peak of the waveform (8 samples, 1 sample $\approx$ 1 ns). The calibration is done by the means of F-factor method (Mirzoyan, 1997; Kobayashi et al., 2022). The image cleaning is done with MCP using the two-level time-constrained absolute image cleaning, where pixels are divided into core and boundary pixels depending on the charge (the thresholds are, respectively, 8 phe and 4 phe). In the first step, the threshold in the core pixels with a large level of noise is increased in such a way that the default threshold value is modified to the value of $\langle Q_{\text{ped}} \rangle + 2.5 \cdot \sigma_{Q_{\text{ped}}}$ (if the obtained value is greater than the default 8 phe), where $\langle Q_{\text{ped}} \rangle$ is the mean and $\sigma_{Q_{\text{ped}}}$ is the standard deviation of the reconstructed charge in the pixel computed from interleaved pedestal events (Abe et al., 2023b). The pixels with a charge above the core threshold and with at least two other neighboring pixels above the core threshold are selected and form the core of the image. The pixels with a charge above the boundary threshold (4 phe) and at least one core pixel are selected as boundary pixels. The pixel is kept as a part of the image if it has at least one neighboring pixel with a signal arrival time within 2 ns of the arrival time in that particular pixel.

In MARS, the signal extraction is performed with the sliding window algorithm where the largest sum of five consecutive time slices is searched over the entire range of readout slices for each pixel. The signal calibration is done with the F-factor method (Mirzoyan, 1997; Aleksić et al., 2016a). After the image extraction and calibration, the MAGIC ROOT files are converted to HDF5 format. The image cleaning is done with the sum cleaning algorithm implemented in MCP chain. In this procedure, the signal is searched in compact groups of 2, 3, or 4 neighboring pixels for which the sum of signals is calculated (Aleksić et al., 2016a). If this sum is above a certain threshold and within a given time interval these pixels are considered to belong to the shower image. The signal is clipped before the summations ensuring that after-pulses or strong NSB fluctuations do not dominate the summed pixels. Finally, a two-level absolute image cleaning with core and boundary charge thresholds is applied to pixels surviving sum cleaning (in the standard procedure thresholds are set to 6 and 3.5 phe for core and boundary pixels, respectively).

Events matching and stereo reconstruction

Cleaned images are parameterized to the Hillas parameters, whereupon the Event Coincidence algorithm is applied. As the LST-1 and MAGIC trigger and readout systems operate independently,

---

[4] `https://github.com/cta-observatory/magic-cta-pipe`

[5] `https://github.com/cta-observatory/pyirf`

[6] `https://gammapy.org`

they record air shower events at distinct trigger rates and with individual timestamps (Ohtani et al., 2022; Abe et al., 2023a). Despite this, both systems are equipped with GPS clocks that assign timestamps to each event. Consequently, in an offline analysis, a coincidence algorithm can be applied to identify events triggering both systems based on these timestamps. Two key parameters are utilized for this purpose. The first parameter, the time offset, compensates for timestamp differences between the systems arising from the telescope array's geometry or other systematic reasons. For this study, the time offset is searched in an interval from 0 to -10 μs. The algorithm systematically applies a range of time offset values to LST timestamps, scanning within the specified start and stop values. The final offset value is selected as a weighted average within the coincidence distribution. The second parameter is the half-width of the coincidence window, representing half of the time interval defined by LST-1 events and set to 300 ns. MAGIC-stereo events triggering both telescopes and falling within this coincidence window are identified as coincident events. Finally, the stereo reconstruction is performed. Quality cuts in this stage correspond to image intensity greater than 50 phe, a width greater than 0 m and a maximum angular difference between LST-1 and the average MAGIC pointing direction of less than 0.1°. The *intensity* parameter was used as a weight in the stereoscopic reconstruction of the events to obtain the averaged parameters.

Generation of Random Forest models

A Python library named `scikit`[7] (Pedregosa et al., 2011) is used to build RF models to classify the parent particle of the detected air shower and estimate its energy and direction. To reconstruct the arrival direction of the parent particle, the stereo *disp* RF method is used (Lessard et al., 2001; Aleksić et al., 2016a; Abe et al., 2023a). The *disp* parameter is the distance between the image center of gravity and the position of the source. The principle of the *disp* method is to reconstruct the *disp* parameters for all Cherenkov images and then determine the position of the incident direction on the main image axis at the distance *disp* from the image center of gravity. However, two directions fulfill this condition, each on the opposite side of the image. Therefore, from all possible combinations of pairs of possible directions of arrival from individual images, the one that gives the lowest dispersion of reconstructed positions is selected. The dispersion is quantified with the parameter *disp_diff_mean*, which is defined as the sum of the angular distances of the reconstructed directions from all pairs of telescopes divided by the number of these pairs. Note that only events with mean difference between the individual disp values smaller than 0.22° are used for stereoscopic reconstruction to improve the angular resolution and background rejection.

The RF models for energy and parent particle classification (i.e. gamma-hadron separation) are generated in a similar way as in MARS. All three RF regressors use the following parameters as input: *intensity*[8], *width*, *length*, *slope*, *skewness*, *kurtosis*, *time_gradient*, *h_max*, *impact*, *leakage_intensity_width_2* (fraction of signal pixels in the two outermost rings of pixels), *alt_tel* (telescope altitude pointing), and *alt_az* (telescope azimuth pointing). The *disp* and energy RF regressors use 150 estimators and a maximum tree depth of 50 and the squared error as the criterion for the best cut selection. The RF regressor for parent particle classification uses 100 estimators

---

[7] `https://scikit-learn.org/`

[8] The *intensity* parameter is the MCP analog of the *size* parameter in MARS, i.e. the total charge in the camera expressed in photoelectrons.

and a maximum tree depth of 100, using the Gini index as the best-cut selection criterion.

5.4 Comparison of Monte Carlo simulations with the Crab Nebula data

Since MC simulations are used to generate the RF models used in the analysis, they must be as similar as possible to the real data. To ensure that the MC simulations correctly reproduce the observed data, the data are compared with the simulations. The distribution of the image and stereo parameters for the observed (real) data is obtained by subtracting the distribution calculated with respect to a control region from the on-source distribution. The acceptance for background events is the same in both regions and is above 1% (Abe et al., 2023b). Therefore, subtracting the on-source distribution from the off-source distribution gives the distribution of θ^2 for the gamma-ray excess events. The gamma-ray MC simulations are reweighted to the log-parabola spectrum measured by Aleksić et al. (2015) (from spectral index -2 to spectral index -2.6). To allow a finer comparison of the distribution shapes, the overall MC distribution is normalized to the distribution of the excess data. The normalization factor is a free parameter resulting from a χ^2 test for the best fit between the distributions, following the approach of Abe et al. (2023b).

Figure 5.7 shows the telescope-wise comparison between MC simulations and excess data for the basic image parameters. Since *length*, *width* and *intensity* are used to generate the RF models, any *gammaness*[9] cut would lead to a bias of the distribution, resulting in a more MC-like distribution of excess events. Therefore, only a soft $\theta < 0.2°$ cut is applied. Both *length* and *width* reproduce the shape of the distribution of excess events. The *intensity* of the excess events is also well reproduced, although the values for LST-1 values are slightly shifted to higher values compared to the MC distribution. However, this is consistent with the distributions observed in the work of Abe et al. (2023a). Since *intensity* is the parameter that is most strongly influenced by the clouds, it can be concluded that the overall MC simulations of the *intensity* parameter accurately reflect the distribution of the real data, which in turn is reflected in the excellent agreement of the *gammaness* distributions. Therefore, the generated MC simulations can be safely used in the analysis.

Figure 5.8 shows a comparison of the average parameters: the height of the shower maximum, *gammaness* and θ^2. In addition to the θ cut already mentioned, the global *gammaness* cut < 0.6 is also applied when calculating the average parameters. All three parameters fairly reproduce the shape of the distribution of the excess events. However, the θ^2 distribution shows an increased tail for higher angular distances. This was also observed in the work of Abe et al. (2023a,b) and is most likely due to the mispointing of the telescopes on the arcminute scale.

5.5 Performance parameters

To evaluate the performance of the joint observations with LST-1 and the MAGIC telescopes, IRFs are calculated. These metrics are derived from the gamma-ray MC test sample (or excess data in the case of the flux sensitivity in this work) and are given as a function of true or reconstructed energy, depending on the metric in question. A global *intensity* cut > 50 phe is initially applied.

---

[9] In the MCP analysis, *gammaness* is used instead of *hadronness*. The closer the value of *gammaness* is to 1, the more gamma-like the event is, and the closer it is to 0, the more hadron-like the event is. In contrast, MARS uses the definition where *hadronness* of 0 indicates a gamma-like event.

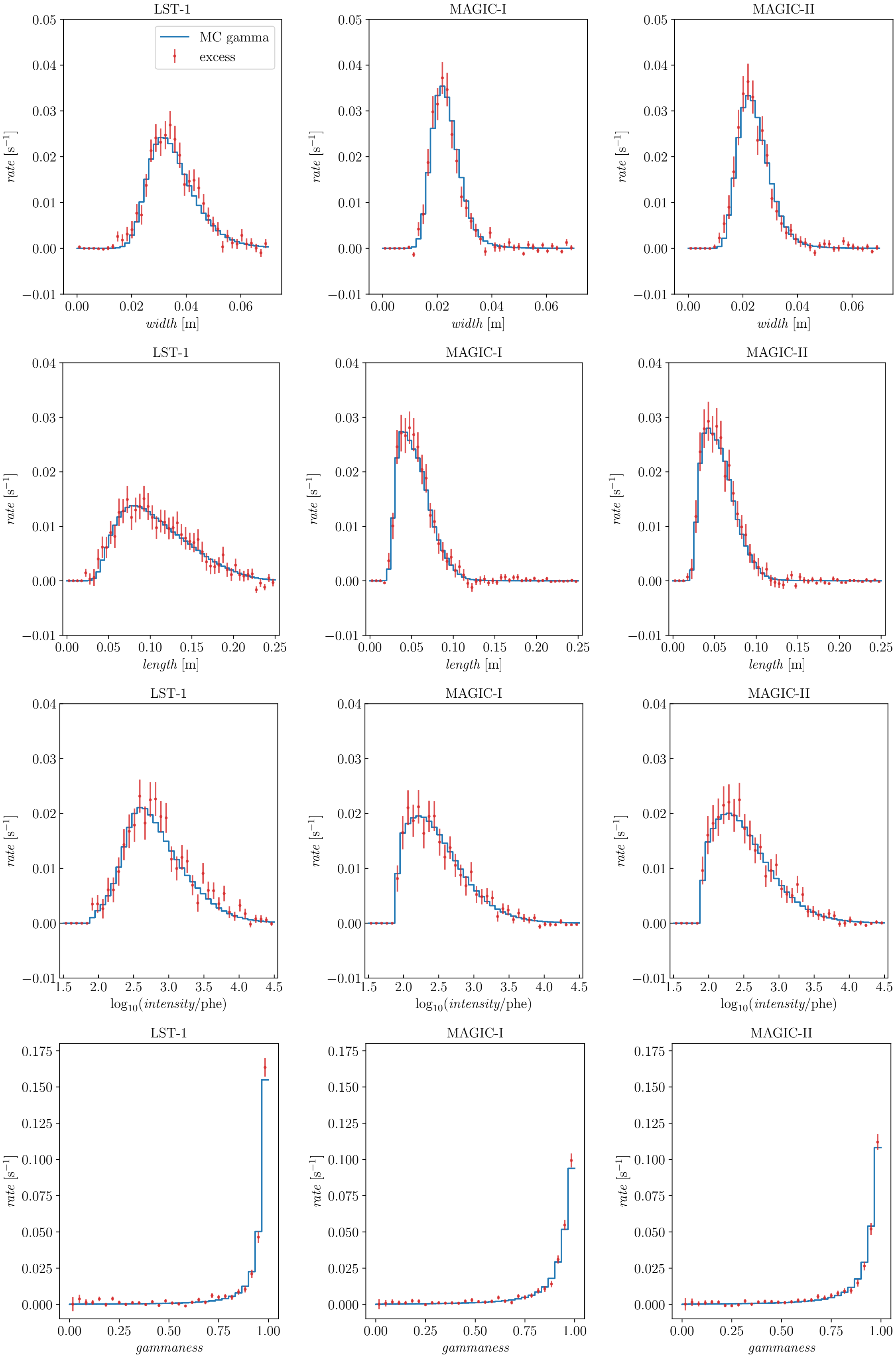

Figure 5.7: Comparison of basic image parameters between MC simulations and excess data from Crab Nebula observations. Gamma-ray MC distributions are normalized to match the excess data distributions.

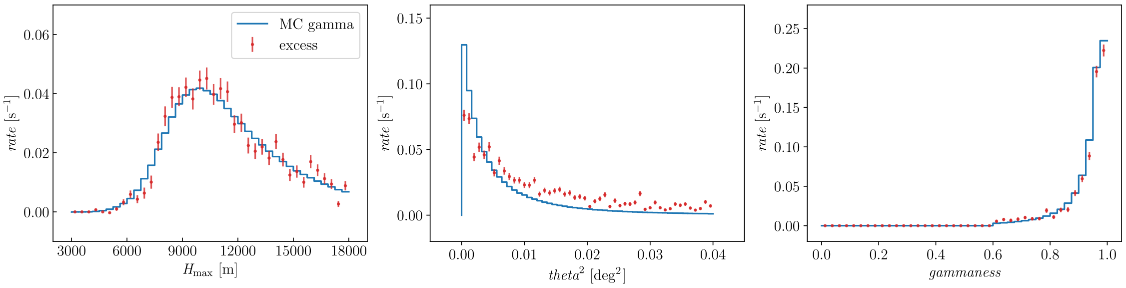

Figure 5.8: Comparison of the telescope-averaged parameters between MC simulations and excess data from Crab Nebula observations. Gamma-ray MC distributions are normalized to match the excess data distributions.

An energy-dependent *gammaness* cut is then applied to keep 90% of the gamma rays within a certain energy bin. For the calculation of energy threshold, energy resolution (bias), effective area and flux sensitivity, also a fixed $\theta < 0.2^\circ$ cut is applied to the selected gamma-ray events. Most of the parameters were calculated in the same way as in Chapter 4. Note, however, that some of the metrics are calculated in a different way to make it easier to compare the results with the work of Abe et al. (2023a). These differences, if any, are listed in the text.

Energy threshold

The energy threshold is calculated as the mean of a Gaussian fit to the true (simulated) energy distribution reweighted to obtain the Crab Nebula spectrum measured by Aleksić et al. (2015). The energy threshold of the analysis at the level of the stereoscopic reconstruction is shown in Figure 5.9. In the clear atmosphere it corresponds to ≈ 71 GeV for low zenith observations, which is slightly higher than 60 GeV reported by Abe et al. (2023a) (probably due to different test nodes used, here only 23.63°, while in the publication an additional node at 10.00° is used) and increases to ≈ 102 GeV for mid-zenith observations. The presence of clouds further increases the energy threshold to ≈ 92 GeV and ≈ 137 GeV for low and medium zenith values, respectively.

Energy bias and resolution

The energy resolution is defined as a 68% containment of the distribution of the relative difference between the estimated and true gamma-ray energy calculated using the approach of Abe et al. (2023a). In the first step, the relative difference between the estimated and the true energy is calculated for each bin of the true energy. The median of this distribution gives the energy bias for a given bin of true energy. Next, the difference between the energy bias and the 16% quantile of the distribution is calculated, as well as the difference between the energy bias and the 84% quantile. Finally, the energy resolution is calculated as the inverse of variance weighted average of the differences calculated in the previous step.

In a clear atmosphere, the energy bias (Figure 5.10, dashed lines) varies from 16% at 90 GeV to the point where there is basically no bias at energies above 300 GeV. This is consistent with the data from Abe et al. (2023a). As for the observations in the presence of clouds, larger differences compared to the energy bias in the clear atmosphere are only visible for energies below 300 GeV,

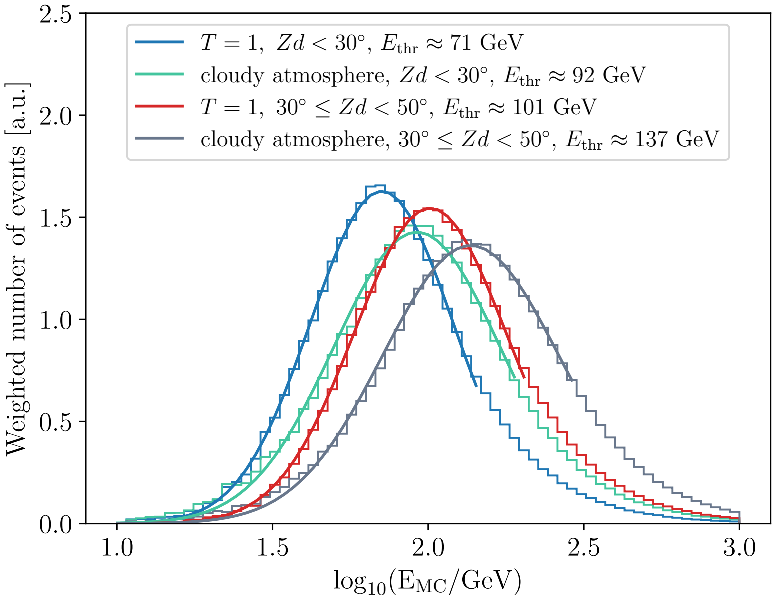

Figure 5.9: The energy threshold in the clear atmosphere and the presence of clouds for low-zenith and mid-zenith observations. The energy thresholds in the cloudy atmosphere are given for all cloud-affected observations combined. The histograms show the energy distribution of the events, while the solid lines represent the Gaussian fit to this distribution.

where the threshold effects dominate and the loss of Cherenkov photons is strongest. Above 300 GeV, the energy bias in the presence of clouds is comparable to that in the clear atmosphere. As expected, higher zenith angles degrade the energy reconstruction and overestimate the energy at 100 GeV by $\approx 37\%$. Above 300 GeV the reconstructed energy is underestimated up to 10% in a clean atmosphere and up to 14% in the presence of clouds.

The energy resolution (Figure 5.10, solid lines) in the clear atmosphere varies between 12% and 25% depending on the energy and zenith range, which is consistent with the values reported by Abe et al. (2023a) (Figure 5.10, black solid line). In the presence of clouds, the energy resolution increases from 30% at 100 GeV to 25% at 10 TeV for observations in at medium zeniths compared to that in a clear atmosphere. This increase is smaller for low zenith angles and at the highest energies, ranging from 30% at 100 GeV to 10% at 10 TeV.

Angular resolution

The influence of the clouds on the angular resolution (Figure 5.11a) is small and below 10%, which is consistent with the conclusion from the previous chapter. As expected, the energy resolution is worst near the energy threshold ($\approx 0.15°$) and improves with increasing energy down to $\approx 0.05°$ at 3 TeV. This is consistent with values reported by Abe et al. (2023a).

Effective area

The effective area after the application of *gammaness* and θ cuts is shown in Figure 5.11b. As can be seen from the figure, the effective area depends on the gamma-ray energy and the zenith angle of the incident direction (but also on the applied selection cuts). Below ≈ 300 GeV down to the energy

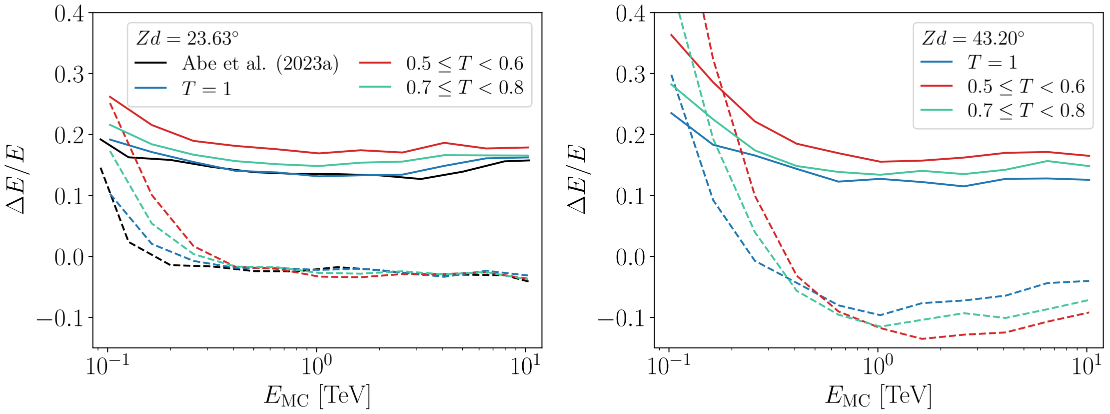

Figure 5.10: Energy bias (dashed lines) and resolution (solid lines) for a clear atmosphere and two different transmission ranges (from 0.5 to 0.6 and from 0.7 to 0.8) for a low zenith angle of 23.63° (*left*) and a medium zenith angle of 43.20° (*right*).

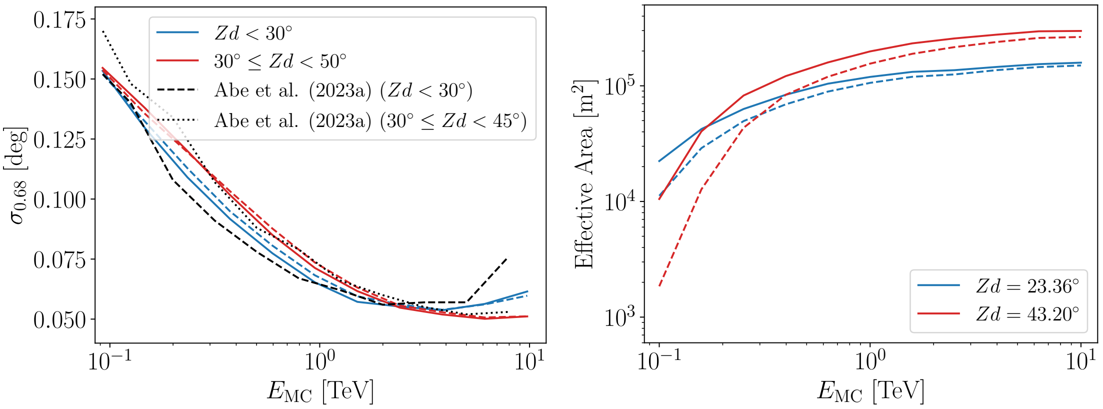

(a) angular resolution

(b) effective area

Figure 5.11: a) Angular resolution and b) effective area for observation in a clear atmosphere (solid lines) and for observation with clouds (dashed) lines. The values are given for the whole transmission range of the clouds.

threshold, the effective area decreases rapidly. In this energy range, the differences between the observations without clouds (Figure 5.11b, solid lines) and those with clouds (Figure 5.11b, dashed lines) are largest (up to 90% at 100 GeV), which is due to the increase of the energy threshold by additional light absorption. The effective area eventually reaches a plateau at higher energies, where the differences tend to be smaller. Above 10 TeV, the effective area in the presence of clouds is reduced by less than 5% for a zenith angle of 32.63° and ≈ 10% for a zenith angle of 43.20° compared to observations in a clear atmosphere.

Differential sensitivity

Differential sensitivity is calculated according to the standard definition, i.e. as the minimum flux from a point-like source required to achieve a statistical significance of 5σ in 50 hours of observation. In this work, the calculation of the sensitivity is based entirely on the Crab Nebula data under the assumption that the background can be calculated from control regions with the same acceptance as the signal region, allowing a reliable background estimation. Significance is calculated using equation (4.18), requiring at least 10 excess events counts in each energy bin and at least 5% above the background counts.

To improve the use of available events, the k-fold cross-validation (Raschka, 2018) based approach of Abe et al. (2023a) is used. In general, the sample is divided into k folds of approximately equal size. Each fold is used exactly once as a validation set, while the $k-1$ remaining folds form the training set. The trained model is then validated with the retained fold (the test set) to obtain an evaluation metric (in this case *gammaness* and θ cuts). These steps are repeated k times, using each of the k folds exactly once as validation data. In this work, k is set to four, i.e. every fourth event is in a different subsample. Then, both *gammaness* and θ cuts, optimized with the remaining three samples to achieve the best sensitivity, are applied to each subsample. Then all subsamples are stacked again and the sensitivity is calculated for the whole sample without being biased by the choice of cuts.

At energies below 0.4 TeV, where the background is abundant, only one control region is used to estimate the background (at an angular distance of 180° from the signal region) to minimize systematic uncertainties. Beyond this threshold, five different control regions are used for background estimation. This strategy prevents overlap between the control regions. In addition, for energies above 0.6 TeV, where the background is scarce and a high angular resolution leads to an optimal small angular distance from the source, a wider cut of 0.2° is implemented for the control region and the number of events is scaled to the actual θ cut to improve the background statistics (Abe et al., 2023a).

The differential sensitivity of the joint observations with LST-1 and MAGIC telescopes is shown in Figure 5.12. For low zenith observations, the sensitivity is systematically reduced across the energy range, by a factor of ≈ 4 at ≈ 120 GeV or less at higher energies compared to the sensitivity in the clean atmosphere reported in the work of Abe et al. (2023a). In the mid-zenith region, the sensitivity at ≈ 120 GeV is reduced by a factor of ≈ 7 compared to the sensitivity at the same energy reported by Abe et al. (2023a). Note, however, that the analyzed low zenith data are rare, which explains the larger error bars. Furthermore, the low-zenith data are only affected by one type of clouds, namely those with a relatively high transmission of 0.77, while the mid-zenith data are also affected by clouds with a lower transmission (see the reported zenith ranges in Table 5.1). The performance of all combined data (the entire zenith range) is generally better than the performance of the mid-zenith observations alone, but still worse than that of the observations without clouds.

5.6 Spectral analysis

To evaluate the performance of the adaptive MC simulation, a spectral and temporal analysis of the Crab Nebula data is performed. Given that the data is taken before August 2021 the intensity cut of 80 phe is applied to LST-1 images due to unstable trigger settings, following the approach of Abe et al. (2023b), and 50 phe to MAGIC images. For low-zenith observations at 30 GeV this cut reduces only 10% of events more compared to the standard cut of LST-1 images of 50 phe (Abe et al., 2023a).

The spectral analysis was performed with `gammapy`, the standard analysis tool for CTA. The

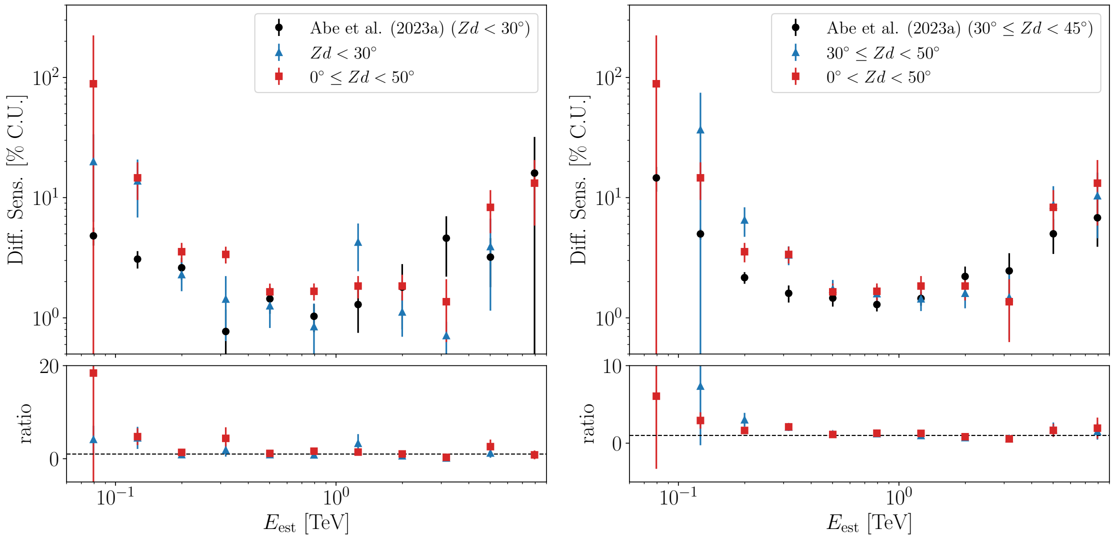

Figure 5.12: Different sensitivity for observations at low (*left*) and medium zeniths (*right*). The lower panels show the ratio compared to the differential sensitivity in a clean atmosphere reported by Abe et al. (2023a). Horizontal dashed lines represent the ratio value of 1. Missing points are due to a lack of statistics. Note the different y-axis scales in the bottom panels.

spectral analysis begins with the creation of a `gammapy` DataStore object containing a list of gamma-ray events described by their arrival time, energy and direction, and then binned by energy. Next, the signal and the background control regions are defined. To define the signal region, the `astropy` class `CircleSkyRegion` is used in the case of global theta cuts, or the class `PointSkyRegion` in the case of dynamic theta cuts. The reflected background regions for the background estimation are defined on the opposite side of the signal region. Then the `SpectrumDataset` object is used to create the main dataset for spectral fitting. It combines the binned counts, the background and IRFs. A safe mask and a fit mask can be added to exclude bins during the analysis. Next, the `SpectrumDatasetMaker` object is used to create new datasets containing the number of events, the number of excess and background events, the exposure and the background normalization factor. Finally, a spectral shape is defined, which is adopted in the forward folding (Albert et al., 2007) method to extract the source spectrum. For this purpose, the joint Poissonian maximum likelihood fitting is performed on the observed counts assuming the previously defined spectral model. The predicted number of events is given by the forward folding of a source model through IRFs (de Naurois, 2012; Donath et al., 2023):

$$N_{\text{pred}}(p,E;\hat{\theta})\mathrm{d}p\mathrm{d}E = t_{\text{obs}}\int_{E_{\text{true}}}\mathrm{d}E_{\text{true}}\int_{p_{\text{true}}}\mathrm{d}p_{\text{true}}R(p,E|p_{\text{true}},E_{\text{true}})\Phi(p_{\text{true}},E_{\text{true}};\hat{\theta}), \quad (5.12)$$

where:

$$R(p,E|p_{\text{true}},E_{\text{true}}) = E_{\text{disp}}(E|p_{\text{true}},E_{\text{true}})\cdot \mathrm{PSF}(p|p_{\text{true}},E_{\text{true}})\cdot A_{\text{eff}}(p_{\text{true}},E_{\text{true}}). \quad (5.13)$$

$E_{\text{disp}}(E|p_{\text{true}},E_{\text{true}})$ is the energy dispersion (matrix), i.e. the probability of reconstruction of the gamma ray for a given true energy E_{true} and true direction p_{true} with energy E, $\mathrm{Bkg}(p,E)$

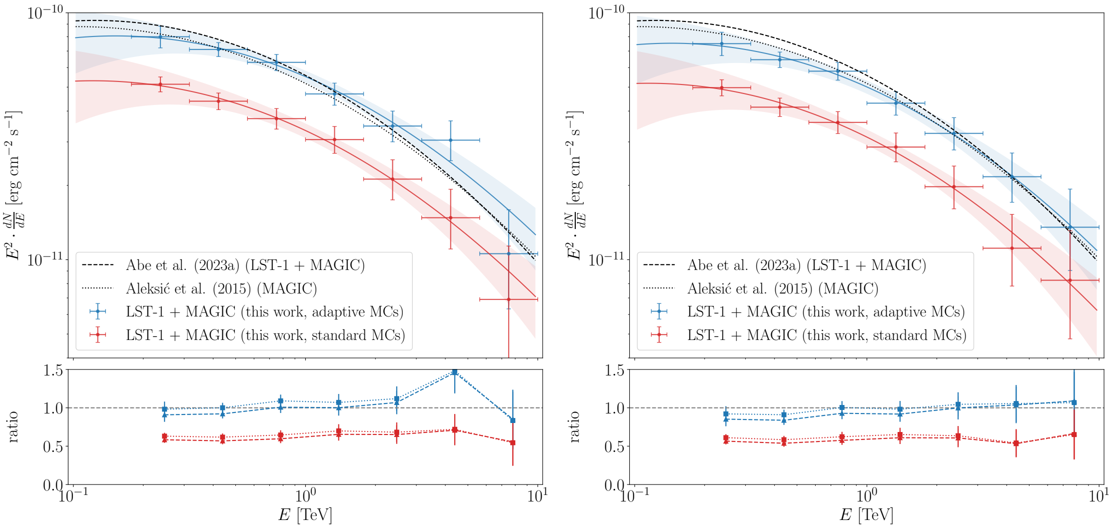

(a) γ-ness cut: 80% efficiency, θ cut: $< 0.2°$ **(b)** γ-ness cut: 80% efficiency, θ cut: 75% efficiency

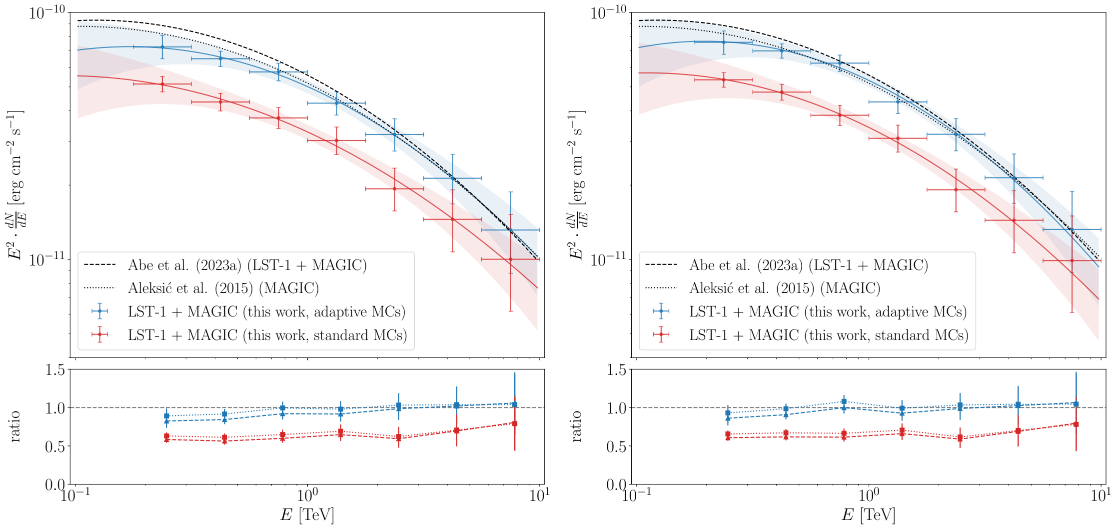

(c) γ-ness cut: 90% efficiency, θ cut: 75% efficiency **(d)** γ-ness cut: 90% efficiency, θ cut: 90% efficiency

Figure 5.13: *Upper panels*: Spectral energy distribution of the Crab Nebula up to 10 TeV, measured with LST-1 and the MAGIC telescopes for different applied cuts. The solid lines represent the best fit to the flux points, while the shaded areas show the statistical uncertainty of the fit. The black dashed and dotted lines show the reference spectra reported by Abe et al. (2023a) and Aleksić et al. (2015), respectively. *Bottom panels*: Ratio of the reconstructed flux to the reference flux reported by (Aleksić et al., 2015) (squares, dotted line) and Abe et al. (2023a) (triangles, dashed line).

is the background as a function of the reconstructed direction p and the reconstructed energy E, $\mathrm{PSF}(p|p_{\mathrm{true}}, E_{\mathrm{true}})$ is the point spread function, i.e. the probability density of the measurement of a direction p for the true direction p_{true} and the true energy E_{true}, $A_{\mathrm{eff}}(p_{\mathrm{true}}, E_{\mathrm{true}})$ is the effective collection area and t_{obs} is the observation time. $\Phi(p_{\mathrm{true}}, E_{\mathrm{true}}; \hat{\theta})$ is an analytical model used to describe the radiation intensity of gamma-ray sources as a function of the true energy E_{true} and the true position p_{true}, where $\hat{\theta}$ is a set of adjustable spectral model parameters (Donath et al., 2023).

The resulting spectral energy distribution (SED) of the Crab Nebula, fitted to the log-parabola

	$f_0 \left[\frac{10^{-11}}{\text{TeV cm}^2\text{ s}}\right]$	α	β	*gammaness*	θ
Aleksić et al. (2015)	3.23 ± 0.03	2.47 ± 0.01	0.24 ± 0.01		
Abe et al. (2023a)	3.48 ± 0.09	2.49 ± 0.03	0.118 ± 0.017		
standard MCs	2.14 ± 0.14	2.46 ± 0.07	0.105 ± 0.053	90%	90%
adaptive MCs	3.31 ± 0.19	2.45 ± 0.06	0.137 ± 0.052	90%	90%
standard MCs	2.05 ± 0.14	2.43 ± 0.06	0.089 ± 0.054	90%	75%
adaptive MCs	3.13 ± 0.19	2.42 ± 0.06	0.120 ± 0.052	90%	75%
standard MCs	2.08 ± 0.14	2.44 ± 0.06	0.105 ± 0.540	90%	$< 0.2°$
adaptive MCs	3.44 ± 0.19	2.40 ± 0.05	0.107 ± 0.048	90%	$< 0.2°$
standard MCs	1.96 ± 0.14	2.46 ± 0.07	0.107 ± 0.058	80%	75%
adaptive MCs	3.13 ± 0.19	2.42 ± 0.06	0.109 ± 0.052	80%	75%

Table 5.3: Best-fit parameters to the differential photon spectrum of the Crab Nebula for adaptive and standard MC simulations (for different dynamic/global cuts applied) and reference spectra. Note that the log-parabola spectrum reported by (Aleksić et al., 2015) is given as a function of a logarithm with base 10 ($\log_{10}$), while in other cases as a function of logarithm with base e, which explains different curvature parameter.

spectral shape:

$$\frac{\mathrm{d}N}{\mathrm{d}E} = f_0 \cdot \left(\frac{E}{E_0}\right)^{-\alpha-\beta\cdot\ln\frac{E}{E_0}}, \tag{5.14}$$

where $E_0 = 1$ TeV, f_0 is the flux normalization, α is the photon index and β is the curvature parameter, is shown in Figure 5.13. Due to the low statistics, four bins per energy decade are used instead of the standard five bins per decade. The energy threshold is clearly shifted to higher energies compared to the reference spectra, not only because of the presence of clouds, but also because most of the data were taken in the mid-zenith region. In the case where standard MC simulations (without clouds) are used to generate RF models and IRFs, the spectrum is significantly underestimated even at the highest energies, from $\approx 40\%$ at 138.91 GeV to 20% at 7.81 TeV compared to the reference spectrum (Abe et al., 2023a) for the standard *gammaness* 90% efficiency cut and the 75% efficiency θ, although the differences are slightly smaller compared to the spectrum reported by (Aleksić et al., 2015) and for loose cuts.

When adaptive MC simulations with clouds are used to generate RF models and IRFs, a proper Crab Nebula spectrum (Figure 5.13, blue dots) is reconstructed which agrees well with the reference spectra. A slightly worse agreement is observed in the case of the global $\theta < 0.2°$ cut for the highest energies, where such a cut is too loose, but the agreement is, on the other hand, improved for lower energies. In case of a larger discrepancy between the excess data and the MC simulation, looser selection cuts always lead to an overestimation of the fluxes. In contrast, too tight cuts would lead to an underestimated spectrum. Note, however, that the differences between the spectra obtained with adaptive MC simulations and the reference spectra reported by Abe et al. (2023a) are comparable to those between the individual reference spectra, about 10% at 138.91 GeV and less than 5% at the highest energies, showing that the generated MC simulations realistically represent the real atmospheric conditions during data taking. The θ cut efficiency 90% seems a good comprise for both the low-energy and the high-energy end of the spectrum.

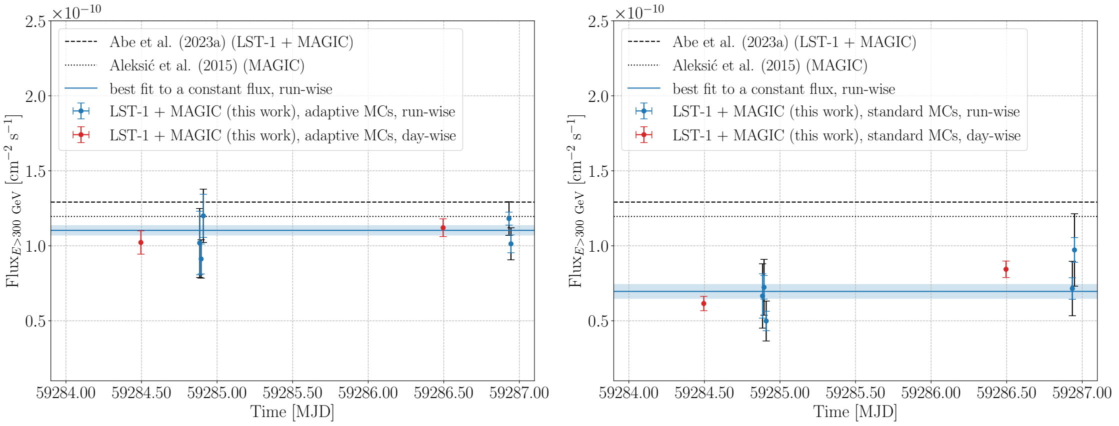

(a) adaptive MC simulations **(b)** standard MC simulations

Figure 5.14: Integrated fluxes above 300 GeV of the Crab Nebula for run-wise binned data (blue points) and daily binned data (red points). The gammaness 90% efficiency cut and θ 90% efficiency cut were applied to the data. The run-wise data were fitted to a constant flux. The black error bars show the statistical uncertainties added in quadrature with the systematic uncertainties.

The resulting spectral fit parameters for different applied cuts are shown in Table 5.3. The most important factors for quantifying the spectrum in the presence of clouds are the flux normalization and the spectral index, which are mainly determined by the low-energy part of the spectrum where the statistics of the event are high. However, it is precisely this part of the spectrum that is most strongly influenced by the cloud. As can be seen from Table 5.3, both parameters are mostly well reproduced when the adaptive MC simulations are used. Note, however, that when using standard MC simulations, the spectral index increases, i.e. the spectra become steeper. The curvature parameter is strongly influenced by the events with the highest energies where the statistics are inherently scarce, but the Cherenkov light yield is high and therefore this parameter is also well reproduced even in the case where standard MC simulations are used to generate RF models and IRFs. This is consistent with the results of LIDAR-based data correction in the work of (Schmuckermaier et al., 2023).

The light curve (LC) is the flux integrated above a certain energy threshold in the bins of time. To calculate LC, the number of excess events is determined separately for each time interval. The temporal evolution of the observed flux above 300 GeV is calculated with the `gammapy` module `LightCurveEstimator`. As in other publications on the Crab Nebula (Aleksić et al., 2015; Abe et al., 2023a,b, e.g.), the resulting LC (binned day-wise and run-wise, Figure 5.14a) is not consistent with a constant fit. Note, however, that in the case of the adaptive MC simulations, the flux fitted to a constant value of:

$$F_{>300\ \mathrm{GeV}} = (1.10 \pm 0.03_{\mathrm{stat}}) \cdot 10^{-10}\ \mathrm{cm}^{-2}\ \mathrm{s}^{-1}$$
$$\chi^2/\mathrm{NDF} = 9.84/4,\ p\mathrm{-value} \simeq 4.33 \cdot 10^{-2}$$

is consistent with the values reported by Aleksić et al. (2015) (7% underestimation) and Abe et al. (2023a) (14% underestimation), which seems reasonable given the differences in the zenith range of the MC simulations compared to the continuous real data, and other differences in conditions during data taking not caused by clouds (i.e. the systematic uncertainties are not included). However, the rather good value of the reduced χ^2 is due to two facts: The atmospheric profiles are tailored individually for each run and the data are concentrated around the same date. Note that the fit is performed only for run-wise data, as daily binned data consists of only two flux points. To obtain a fit probability of 0.5, an additional 8.74% of the systematic uncertainties must be added in quadrature to the statistical uncertainty. In contrast, there is a stronger observed variability of the flux when the standard MC simulations are used (Figure 5.14b):

$$\begin{aligned} F_{>300\ \mathrm{GeV}} &= (6.95 \pm 0.36_{\mathrm{stat}}) \cdot 10^{-11}\ \mathrm{cm}^{-2}\ \mathrm{s}^{-1} \\ \chi^2/\mathrm{NDF} &= 20.71/4,\ p\mathrm{-value} \simeq 3.62 \cdot 10^{-4}. \end{aligned}$$

This is expected as all runs were analyzed with the same standard MC simulations and no run-wise tailored MC simulations are used. Here, additional systemic uncertainties of 23.31% must be assumed to obtain a probability value of 0.5.

5.7 Summary and conclusions

This chapter focuses on the comparison of the adaptive MC simulations with Crab Nebula data obtained from joint observations of the LST-1 and MAGIC telescopes in the presence of clouds. The analysis aims to ensure that the MC simulations accurately reproduce the observed data. Various parameters, including basic image parameters and average parameters, are compared between MC simulations and the excess data, demonstrating good agreement and validating the use of MC simulations for further analysis.

Performance parameters such as energy threshold, energy bias and resolution, angular resolution, effective area and differential sensitivity are evaluated. For low zenith observations, the sensitivity is systematically reduced at energies up to 1 TeV, by a factor of 4 at the energy threshold or less at higher energies, compared to the sensitivity in the clean atmosphere. Despite these effects, the performance remains at an acceptable or even comparable level to clear sky observations.

The chapter concludes with a spectral analysis of the Crab Nebula data. Here, the results are compared when standard MC simulations and adaptive MC simulations with clouds are used to generate RF models. The adaptive MC simulations provide realistic spectral parameters and the obtained spectrum agrees well with the reference spectra. On the contrary, in the case where standard MC simulations are used to generate RF models, the spectrum is significantly underestimated even at the highest energies, up to $\approx 40\%$.

Summary and conclusions

To investigate the effects of clouds on the reconstruction of gamma-ray-induced air showers with CTA telescopes, an extensive database of MC simulations was generated. Atmospheric transmission profiles in the presence of clouds, which are required for MC simulations, were modeled using the MODTRAN band model algorithm. The effects of clouds were evaluated by analyzing the simulated data and calculating instrument response functions for two different analyses, depending on the type of MC simulations used to build the RF models: adaptive MC simulations including clouds and standard MC simulations for a clear atmosphere.

The study has shown that the presence of clouds significantly reduces the number of detected events, especially in the low-energy range (up to 90% compared to observations in a clear atmosphere), which significantly increases the energy threshold (by a factor of 2, depending on the cloud height, transmission and the zenith angle of the observation). The use of adaptive MC simulations leads to an energy bias and resolution comparable to that for a clear atmosphere. This suggests that the energy of a primary gamma-ray in the presence of clouds can be reconstructed with the same uncertainty as in a clear atmosphere. However, the lost events cannot be recovered and reconstructed, so the effective area and thus the differential sensitivity are inevitably impaired even if adaptive MC simulations are used. The observations of weaker sources become even more challenging when confronted with dense ($T < 75\%$) and low (≤ 7 km) cloud cover. Under such conditions, the differential sensitivity is reduced by up to a factor of 3 compared to that achieved in a clear atmosphere. The use of standard MC simulations in the sample to generate RF models further degrades the performance of CTAO-N and leads to a significant energy bias and degraded energy resolution. In such cases, the effective area and differential sensitivity are further decreased (even by another 50% compared to the case of adaptive MC simulations). However, for ORM, where most clouds are based above 8 km a.s.l. during observing conditions, clouds are not very important when it comes to angular resolution, as the influence of clouds on the direction reconstruction is $\lesssim 10\%$ and no significant differences between standard and adaptive MC simulations were observed.

To determine the reliability of standard Monte Carlo simulations for energy estimation in the cloudy atmosphere, it is necessary to evaluate the introduced biases compared to the biases in adaptive MC simulations as a function of cloud transmission, altitude and gamma-ray energy. An important benchmark is the CTA requirement A-PERF-2050, which sets a limit of 8% for the systematic uncertainty in the Cherenkov light intensity measurement. For low and high clouds (3-5 km and ≥ 11 km, respectively), where the effects of clouds are consistent over the energy range, the standard MC simulations perform well for energies above 150 GeV for low clouds with $T \geq 0.95$ and high clouds with $T \geq 0.75$, while for lower transmissions the systematic uncertainties increase above 8%. Clouds at medium altitudes (7-9 km) show strong energy-dependent effects, complicating the decision whether standard or adaptive MC simulations should be used. For $T < 0.9$, at low zenith angels, the standard MC simulations are reliable for energies above 1 TeV for clouds at 9 km and only above 10 TeV for cloud at 7 km. For higher transmission values, one may safely use standard simulations to generate RF models for analyzing data taken in the presence of such clouds.

The method of adaptive MC simulations was also tested on the Crab Nebula data taken during the joint observations of the LST-1 and MAGIC telescopes. The accompanying LIDAR measurements were used to identify clouds and model the atmospheric profiles required for the MC simulations. Several parameters, including Hillas parameters, were compared between MC simulations and real data showing good agreement. Basic parameters characterizing the response of the telescope were also calculated. The study has shown that for observations in the low zenith region, the sensitivity systematically decreases at energies up to 1 TeV, by a factor of 4 at the energy threshold or less at higher energies, compared to the sensitivity for a clean atmosphere. In the mid-zenith region, the sensitivity at the energy threshold is reduced by a factor of ≈ 7. Despite these effects, the overall performance of the telescope remains at an acceptable level with respect to the CTA requirements or even at a level comparable to observations in a clean atmosphere. The adaptive MC simulations provide realistic spectral parameters and the resulting spectrum agrees well with the reference spectra.

Please note, however, that such an approach requires large CPU resources. In the best case, different MC simulations have to be generated daily or even on a run-by-run basis, and in many cases classical correction methods can provide a comparable performance. Nevertheless, adaptive MC simulations are an unavoidable tool in cases where highly variable sources with a variability timescales shorter than the timescale of the variable cloud cover are observed, e.g. clouds passing through the FoV. In such a case, it would be very difficult to distinguish between the effects of the clouds and the intrinsic variability of the source, and the classical correction method would fail to recover the correct spectrum. On the other hand, when observing sources with constant flux at low to medium zeniths (or variable sources with steady aerosol ground layers, such as Calima), the classical correction methods (see Appendix A) can also provide a reliable analysis of the data and recover correct SEDs. Due to the duration of MC simulations and limited CPU resources, the adaptive MC simulations approach is not intended to be part of the standard analysis pipeline, but simulations should be performed on demand in cases where correction is not feasible. For the given observation, the only non-standard MC input in such a case would be a corresponding atmospheric transmission profile derived from, e.g. LIDAR measurements or isotropic background events (see Appendix B). Finally, it is important to highlight that the impact of clouds becomes particularly significant for very distant sources. Gamma rays of higher energies from those sources are more susceptible to attenuation by extragalactic background light, leading to a cutoff in the observed spectrum. As a result, the low-energy part of the spectrum remains unchanged and that is exactly the part of the spectrum with a low yield of Cherenkov light most strongly affected by clouds.

APPENDIX A

A novel Cherenkov image correction method

In addition to my research for doctoral thesis, I have collaborated intensively on the development of a novel method for correcting IACT data taken in the presence of clouds (see Żywucka et al. (2024) for details). As mentioned earlier, adaptive MC simulation can be very time consuming and require extensive CPU resources, while existing correction methods (e.g. Fruck and Gaug (2015); Sobczyńska et al. (2020); Schmuckermaier et al. (2023)) often prioritize limiting systematic errors without optimizing overall performance. Therefore, we wanted to develop a method that corrects Cherenkov data already at the image level. By correcting the data already at the image level, it is possible to improve event reconstruction without the need for adaptive MC simulations. It should be noted again that in some cases the correction methods are not feasible.

In the new method, each pixel in the camera is associated with a specific Cherenkov light emission height by using a simple geometric model, i.e. based on the parameters of the shower geometry (Figure A.1, the blue ellipse represents the air shower):

$$\xi = \arctan\left(\frac{I\cos Zd}{H}\right). \tag{A.1}$$

where ξ is the offset angle from the primary gamma ray direction corresponding to the height H (measured a.g.l.), Zd is the zenith angle of the observations (which corresponds to the zenith angle of the air shower) and I is the preliminary reconstructed impact parameter (to obtain preliminary parameters, the uncorrected images must first be cleaned and parameterized). The model assumes $I \ll H$ and allows a pixel-wise correction of the charge in the camera. Finally, the charge in the pixel is scaled by $\frac{1}{T^{\cos Zd}}$ (where T is the vertical transmission at height H) when the light is emitted above the cloud, while for the Cherenkov photons emitted below the cloud the charge in the pixels remains unchanged. The corrected images are cleaned and parameterized and undergo a stereo reconstruction. An example of a corrected image is shown in Figure A.2. It is evident that after the correction the charge in the corrected image is at the level of the image charge in the cloudless atmosphere. The performance of the proposed method (in terms of effective area and flux sensitivity) is comparable to that of adaptive MC simulations for most of the simulated cases ($T \gtrsim 0.6$), but at the cost of increased systematic uncertainties. However, the adaptive MC simulations still exploit better angular resolution and energy resolution, providing a smaller energy bias. For details and results, the reader is referred to Żywucka et al. (2024).

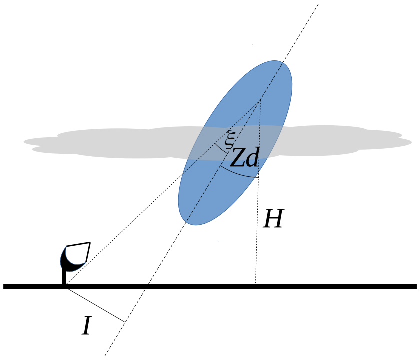

Figure A.1: The geometric model used in the method (Żywucka et al., 2024).

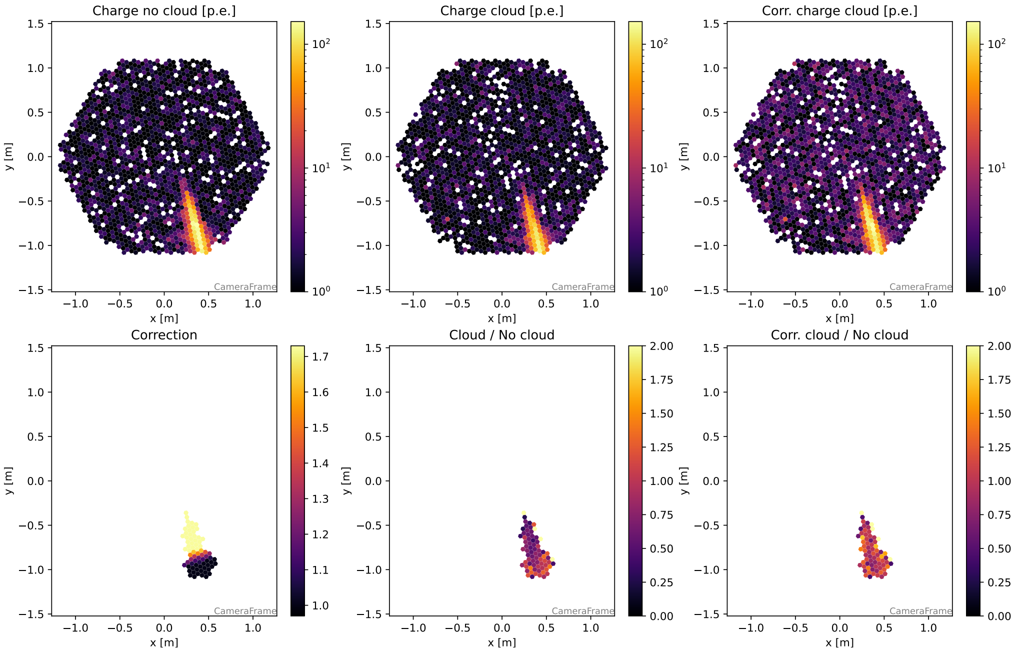

Figure A.2: Example of the images of the same event in the cloudless atmosphere (*left*), in the presence of clouds (*middle*) and after correction (*right*). The lower panels show only pixels that survived the cleaning (Żywucka et al., 2024). A 1 km thick cloud with the base at 7 km a.g.l. and $T = 0.6$ was simulated.

I contributed to this project by modeling atmospheric profiles including clouds with MODTRAN and simulating MC files with CORSIKA and `sim_telarray`, and also performed some parts of the low-level and high-level analysis. I was also actively involved in writing the draft of the paper and in correcting the draft after the internal review by the LST Collaboration and the CTA Consortium. This work was in a large portion done during my stay at the University of Łódź in Poland.

APPENDIX B

Estimation of the atmospheric absorption profile with isotropic background events

The second cloud-related project in which I was actively involved is the new method for determining the transmission profile from the isotropic background events detected with IACTs (Sitarek et al., 2024). According to the method presented in Appendix A, each pixel is associated with a particular Cherenkov light emission height. The method is based on a construction of the sum of the longitudinal distributions of the observed Cherenkov light from the isotropic background (containing mainly protons). These reconstructed distributions are compared between the cloudless and the cloudy atmosphere, and the ratio is directly interpreted as a measure of cloud transmission.

We tested a number of possible systematic errors that could affect the method. The study confirmed that helium and heavier nuclei (Figure B.1a), minor changes in the optical reflectivity or optical point spread function due to aging of the telescopes (up to 10% and 8%, respectively), the azimuth dependence, and the level of the background light have a negligible impact on the performance of the method and provide correctly reconstructed cloud parameters. The total vertical transmission of the cloud is accurately reconstructed for all simulated clouds and all presented scenarios. Although there is a slight bias in the estimation of the base cloud height, it remains within 0.75 km for low zenith observations. However, the method shows poorer performance when it comes to estimating the geometric thickness of clouds, especially those thinner than 3 km. This is due to the width of the distribution of the angular offset ξ for a given emission height (see Sitarek et al. (2024) for explanation). The main limitation of the method is the zenith angle of the observation (Figure B.1b). Due to the significant variations in the distribution of emission heights of the detected Cherenkov light, only the data taken at the same zenith angle can be compared. Since this is impractical, we proposed a scaling method to mitigate the bias caused by the different zenith distributions (see Sitarek et al. (2024) for details).

The proposed method achieves typical statistical and systematic accuracy within a few percent. The aggregated profiles of the emitted Cherenkov light can be reconstructed with a statistical accuracy of $\lesssim 5\%$ with only a 5-minute exposure. Although the method cannot completely replace LIDAR measurements (and is also not suitable for measuring the transmission of low layers of increased aerosols, such as a Calima), it allows independent and continuous monitoring of atmospheric transmission without the need for additional and specialized auxiliary instruments.

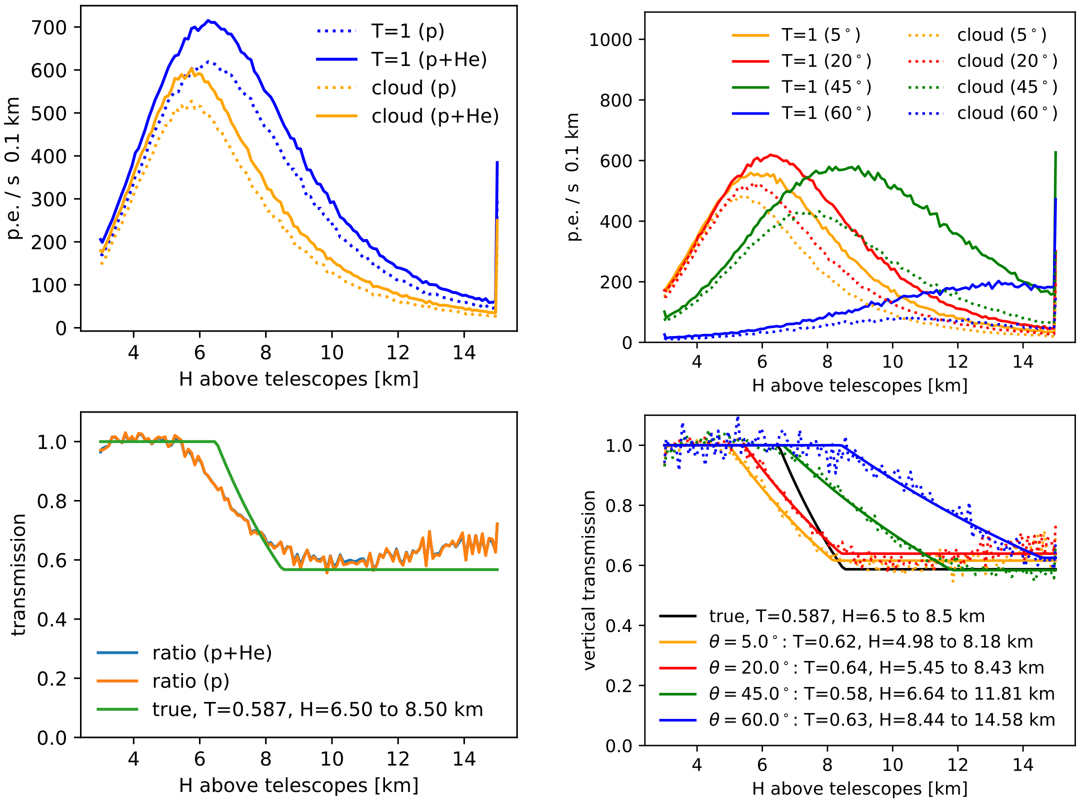

(a) **(b)**

Figure B.1: **a)** Top: the aggregated longitudinal distribution of the observed Cherenkov light from proton-induced air shower for the cloudless atmosphere (dotted blue line) and in the presence of a 2 km thick cloud with $T = 0.587$ based at 6.5 km a.g.l. (dotted orange line). Solid lines show a contribution of both protons and helium. *Bottom*: the ratios of these distributions compared to the simulated transmission profile of (green solid line). **b)** Top: the aggregated longitudinal distribution of the observed Cherenkov light from proton-induced air shower for the cloudless atmosphere (solid lines) and in the presence of a 2 km thick cloud with $T = 0.587$ based at 6.5 km a.g.l. (dotted lines) for different zenith angles θ. *Bottom*: the ratios of these distributions compared to the simulated transmission profile (black solid line) (Sitarek et al., 2024).

The obtained transmission profiles can be used directly in the correction method or as input for modeling the atmospheric profiles with MODTRAN needed for adaptive MC simulations.

I contributed to this project by modeling atmospheric profiles including clouds with MODTRAN and simulating MC files with CORSIKA and `sim_telarray`. I was also actively involved in writing the draft of the paper and in correcting the draft after the review process.

Bibliography

[1] Aab, A., Abreu, P., Aglietta, M., Ahn, E. J. et al. (2015). Muons in air showers at the Pierre Auger Observatory: Mean number in highly inclined events. *Physical Review D*, 91 (3), doi: 10.1103/physrevd.91.032003.

[2] Abdalla, H., Adam, R., Aharonian, F., Ait Benkhali, F. et al. (2019). A very-high-energy component deep in the γ-ray burst afterglow. *Nature 2019 575:7783*, 575 (7783), 464–467, doi: 10.1038/s41586-019-1743-9.

[3] Abdalla, H., Aharonian, F., Ait Benkhali, F., Angüner, E. O. et al. (2018). The starburst galaxy NGC 253 revisited by H.E.S.S. and Fermi-LAT. *Astronomy & Astrophysics*, 617, A73, doi: 10.1051/0004-6361/201833202.

[4] Abdollahi, S., Ackermann, M., Ajello, M., Atwood, W. B. et al. (2017). Cosmic-ray electron-positron spectrum from 7 GeV to 2 TeV with the Fermi Large Area Telescope. *Physical Review D*, 95 (8), 082007, doi: 10.1103/PHYSREVD.95.082007/FIGURES/19/MEDIUM.

[5] Abe, H., Abe, K., Abe, S., Acciari, V. A. et al. (2023a). Performance of the joint LST-1 and MAGIC observations evaluated with Crab Nebula data. *Astronomy & Astrophysics*, 679, doi: 10.1051/0004-6361/202346927.

[6] Abe, H., Abe, K., Abe, S., Aguasca-Cabot, A. et al. (2023b). Observations of the Crab Nebula and Pulsar with the Large-sized Telescope Prototype of the Cherenkov Telescope Array. *The Astrophysical Journal*, 956 (2), 80, doi: 10.3847/1538-4357/ACE89D.

[7] Abramowitz, M., Stegun, I. A., and Romer, R. H. (1988) Handbook of mathematical functions with formulas, graphs, and mathematical tables.

[8] Abramowski, A., Acero, F., Aharonian, F., Akhperjanian, A. G. et al. (2012). Spectral analysis and interpretation of the γ-ray emission from the starburst galaxy NGC 253*. *The Astrophysical Journal*, 757 (2), 158, doi: 10.1088/0004-637X/757/2/158.

[9] Abreu, L. W. and Anderson, G. P. (1996). The MODTRAN 2/3 report and LOWTRAN 7 model. *Contract*, 19628 (91-C), 132.

[10] Acciari, V. A., Aliu, E., Arlen, T., Aune, T. et al. (2009). A connection between star formation activity and cosmic rays in the starburst galaxy M82. *Nature 2009 462:7274*, 462 (7274), 770–772, doi: 10.1038/nature08557.

[11] Acciari, V. A., Ansoldi, S., Antonelli, L. A., Arbet Engels, A. et al. (2019). Teraelectronvolt emission from the γ-ray burst GRB 190114C. *Nature 2019 575:7783*, 575 (7783), 455–458, doi: 10.1038/s41586-019-1750-x.

[12] Acharya, B. S., Actis, M., Aghajani, T., Agnetta, G. et al. (2013). Introducing the CTA concept. *Astroparticle Physics*, 43, 3–18, doi: 10.1016/J.ASTROPARTPHYS.2013.01.007.

[13] Acharyya, A., Agudo, I., Angüner, E. O., Alfaro, R. et al. (2019). Monte Carlo studies

for the optimisation of the Cherenkov Telescope Array layout. *Astroparticle Physics*, 111, 35–53, doi: 10.1016/J.ASTROPARTPHYS.2019.04.001.

[14] ACTIS, M., AGNETTA, G., AHARONIAN, F., AKHPERJANIAN, A. ET AL. (2011). Design concepts for the Cherenkov Telescope Array CTA: An advanced facility for ground-based high-energy gamma-ray astronomy. *Experimental Astronomy*, 32 (3), 193–316, doi: 10.1007/S10686-011-9247-0/FIGURES/29.

[15] ADAMCZYK, K. AND SOBCZYŃSKA, D. (2017). Cloud transmission and its impact on the Cherenkov light density at high energies. *AIP Conference Proceedings*, 1792 (1), 80013, doi: 10.1063/1.4969034/885488.

[16] AHARONIAN, F., AKHPERJANIAN, A., BEILICKE, M., BERNLOHR, K. ET AL. (2004). The Crab Nebula and Pulsar between 500 GeV and 80 TeV: Observations with the HEGRA Stereoscopic Air Cerenkov Telescopes. *The Astrophysical Journal*, 614 (2), 897–913, doi: 10.1086/423931/FULLTEXT/.

[17] AHARONIAN, F., AKHPERJANIAN, A. G., ANTON, G., BARRES DE ALMEIDA, U. ET AL. (2009). Probing the ATIC peak in the cosmic-ray electron spectrum with H.E.S.S.. *Astronomy & Astrophysics*, 508 (2), 561–564, doi: 10.1051/0004-6361/200913323.

[18] AHARONIAN, F., AKHPERJANIAN, A. G., AYE, K. M., BAZER-BACHI, A. R. ET AL. (2005). Discovery of the binary pulsar PSR B1259-63 in very-high-energy gamma rays around periastron with HESS. *Astronomy & Astrophysics*, 442 (1), 1–10, doi: 10.1051/0004-6361:20052983.

[19] AHARONIAN, F., AKHPERJANIAN, A. G., BARRES DE ALMEIDA, U., BAZER-BACHI, A. R. ET AL. (2008). Energy spectrum of cosmic-ray electrons at TeV energies. *Physical Review Letters*, 101 (26), 261104, doi: 10.1103/PhysRevLett.101.261104.

[20] ALBERT, J., ALIU, E., ANDERHUB, H., ANTORANZ, P. ET AL. (2008a). FADC signal reconstruction for the MAGIC telescope. *Nuclear Instruments and Methods in Physics Research Section A: Accelerators, Spectrometers, Detectors and Associated Equipment*, 594 (3), 407–419, doi: 10.1016/J.NIMA.2008.06.043.

[21] ALBERT, J., ALIU, E., ANDERHUB, H., ANTORANZ, P. ET AL. (2008b). Implementation of the Random Forest method for the Imaging Atmospheric Cherenkov Telescope MAGIC. *Nuclear Instruments and Methods in Physics Research Section A: Accelerators, Spectrometers, Detectors and Associated Equipment*, 588 (3), 424–432, doi: 10.1016/J.NIMA.2007.11.068.

[22] ALBERT, J., ALIU, E., ANDERHUB, H., ANTORANZ, P. ET AL. (2007). Unfolding of differential energy spectra in the MAGIC experiment. *Nuclear Instruments and Methods in Physics Research Section A: Accelerators, Spectrometers, Detectors and Associated Equipment*, 583 (2-3), 494–506, doi: 10.1016/J.NIMA.2007.09.048.

[23] ALEKSIĆ, J., ALVAREZ, E. A., ANTONELLI, L. A., ANTORANZ, P. ET AL. (2012). Performance of the MAGIC stereo system obtained with Crab Nebula data. *Astroparticle Physics*, 35 (7), 435–448, doi: 10.1016/J.ASTROPARTPHYS.2011.11.007.

[24] ALEKSIĆ, J., ANSOLDI, S., ANTONELLI, L. A., ANTORANZ, P. ET AL. (2016a). The major upgrade of the MAGIC telescopes, Part II: A performance study using observations of the Crab Nebula. *Astroparticle Physics*, 72, 76–94, doi: 10.1016/J.ASTROPARTPHYS.2015.02.005.

[25] ALEKSIĆ, J., ANSOLDI, S., ANTONELLI, L. A., ANTORANZ, P. ET AL. (2016b). The major upgrade of the MAGIC telescopes, Part I: The hardware improvements and the commissioning of the system. *Astroparticle Physics*, 72, 61–75, doi: 10.1016/J.ASTROPARTPHYS.2015.04.004.

[26] ALEKSIĆ, J., ANSOLDI, S., ANTONELLI, L. A., ANTORANZ, P. ET AL. (2015). Measurement of

the Crab Nebula spectrum over three decades in energy with the MAGIC telescopes. *Journal of High Energy Astrophysics*, 5-6, 30–38, doi: 10.1016/J.JHEAP.2015.01.002.

[27] ALIU, E., ANDERHUB, H., ANTONELLI, L. A., ANTORANZ, P. ET AL. (2008). Observation of pulsed γ-rays above 25 GeV from the crab pulsar with MAGIC. *Science*, 322 (5905), 1221–1224, doi: 10.1126/SCIENCE.1164718.

[28] AMANS, J. P., BERGE, D., BONANNO, G., BOSE, R. B. ET AL. (2021) The Small-Sized Telescopes for the Southern Site of the Cherenkov Telescope Array. in *37th International Cosmic Ray Conference (ICRC2021)*, ICRC2021, 728: Sissa Medialab Srl, doi: 10.22323/1.395.0728.

[29] AMBROSI, G., AWANE, Y., BABA, H., BAMBA, A. ET AL. (2013) The Cherenkov Telescope Array Large Size Telescope. in *33rd International Cosmic Ray Conference*, 776.

[30] AMENOMORI, M., BAO, Y. W., BI, X. J., CHEN, D. ET AL. (2019). First Detection of Photons with Energy beyond 100 TeV from an Astrophysical Source. *Physical Review Letters*, 123 (5), 051101, doi: 10.1103/PHYSREVLETT.123.051101/FIGURES/5/MEDIUM.

[31] ARFKEN, G. B., WEBER, H. J., AND HARRIS, F. E. (2011) *Mathematical methods for physicists: a comprehensive guide*: Academic press.

[32] ARONS, J., SCHARLEMANN, E. T., ARONS, J., AND SCHARLEMANN, E. T. (1979). Pair formation above pulsar polar caps: structure of the low altitude acceleration zone.. *ApJ*, 231, 854–879, doi: 10.1086/157250.

[33] AXFORD, W. I. (1981). The acceleration of cosmic rays by shock waves. *Annals of the New York Academy of Sciences*, 375 (1), doi: 10.1111/j.1749-6632.1981.tb33702.x.

[34] BARRETO, A., CUEVAS, E., GARCIÁ, R. D., CARRILLO, J. ET AL. (2022). Long-term characterisation of the vertical structure of the Saharan Air Layer over the Canary Islands using lidar and radiosonde profiles: Implications for radiative and cloud processes over the subtropical Atlantic Ocean. *Atmospheric Chemistry and Physics*, 22 (2), 739–763, doi: 10.5194/ACP-22-739-2022.

[35] BASS, S. (1998). Microscopic models for ultrarelativistic heavy ion collisions. *Progress in Particle and Nuclear Physics*, 41, 255–369, doi: 10.1016/s0146-6410(98)00058-1.

[36] BECQUEREL, H. (1896). Sur les radiations émises par phosphorescence. *Comptes Rendus de l'Académie des sciences*, 122, 420–421.

[37] BELL, A. R. (2013). Cosmic ray acceleration. *Astroparticle Physics*, 43, 56–70, doi: 10.1016/J.ASTROPARTPHYS.2012.05.022.

[38] BENN, C. R. AND ELLISON, S. L. (1998). Brightness of the night sky over La Palma. *New Astronomy Reviews*, 42 (6-8), 503–507, doi: 10.1016/S1387-6473(98)00062-1.

[39] BERGSTRÖM, L. AND GOOBAR, A. (2006) *Cosmology and particle astrophysics*: Springer Science & Business Media.

[40] BERGSTRÖM, L., GOOBAR, A., AND JAFFE, A. H. (2001). Cosmology and Particle Astrophysics . *American Journal of Physics*, 69 (3), doi: 10.1119/1.1336841.

[41] BERINGER, J., ARGUIN, J. F., BARNETT, R. M., COPIC, K. ET AL. (2012). Review of Particle Physics. *Physical Review D*, 86 (1), 010001, doi: 10.1103/PhysRevD.86.010001.

[42] BERK, A., ANDERSON, G. P., ACHARYA, P. K., BERNSTEIN, L. S. ET AL. (2005) MODTRAN 5: a reformulated atmospheric band model with auxiliary species and practical multiple scattering options: update. in Shen, S. S. and Lewis, P. E. eds. *Algorithms and Technologies for Multispectral, Hyperspectral, and Ultraspectral Imagery XI*, 5806, 662 – 667: SPIE, doi: 10.1117/12.606026.

[43] BERK, A., BERNSTEIN, L., AND ROBERTSON, D. (1987) MODTRAN: A moderate resolution model for LOWTRAN. Technical Report, Spectral Sciences, Inc. Burlington, MA.

[44] Bernlöhr, K., Barnacka, A., Becherini, Y., Blanch Bigas, O. et al. (2013). Monte Carlo design studies for the Cherenkov Telescope Array. *Astroparticle Physics*, 43, 171–188, doi: 10.1016/J.ASTROPARTPHYS.2012.10.002.

[45] Bernlöhr, K. (2000). Impact of atmospheric parameters on the atmospheric Cherenkov technique. *Astroparticle Physics*, 12 (4), 255–268, doi: 10.1016/S0927-6505(99)00093-6.

[46] Bernlöhr, K. (2008). Simulation of imaging atmospheric Cherenkov telescopes with CORSIKA and sim_telarray. *Astroparticle Physics*, 30 (3), 149–158, doi: 10.1016/j.astropartphys.2008.07.009.

[47] Bernlöhr, K. (2014a) *eventio – a machine-independent hierarchical data format and its programming interface*, `https://www.mpi-hd.mpg.de/hfm/~bernlohr/sim_telarray/Documentation/eventio_en.pdf`.

[48] Bernlöhr, K. (2014b) Simulations of detector arrays and the impact of atmospheric parameters. in *International Workshop on Atmospheric Monitoring for High-Energy Astroparticle Detectors*.

[49] Bertone, G., Buchmuller, W., Covi, L., and Ibarra, A. (2007). Gamma-Rays from Decaying Dark Matter. *Journal of Cosmology and Astroparticle Physics* (11), doi: 10.1088/1475-7516/2007/11/003.

[50] Bielajew, A. F., Hirayama, H., Nelson, W. R., and Rogers, D. W. O. (1994) History, overview and recent improvements of EGS4. Technical Report, P00024420.

[51] Biland, A., Garczarczyk, M., Anderhub, D., Danielyan, V. et al. (2008) The Active Mirror Control of the MAGIC Telescope. in *Proceedingsofthe30thInternationalCosmicRayConference*, 1343–1356, Merida, Mexico: Universidad Nacional Autonoma de Mexico.

[52] Bose, D., Chitnis, V. R., Majumdar, P., and Acharya, B. S. (2021). Ground-based gamma-ray astronomy: history and development of techniques. *The European Physical Journal Special Topics 2021 231:1*, 231 (1), 3–26, doi: 10.1140/EPJS/S11734-021-00396-3.

[53] Carr, S. B. (2005) The aerosol models in MODTRAN: Incorporating selected measurements from Northern Australia. Technical Report, DSTO Defence Science and Technology Organisation, Edinburgh South Australia.

[54] Castro-Almazán, J. A. and Muñoz-Tuñón, C. (2018). Climatological Study for the Cherenkov Telescope Array North Site at the Canary Islands I: Temperature, Precipitation, and Relative Humidity. *Publications of the Astronomical Society of the Pacific*, 130 (993), 115002, doi: 10.1088/1538-3873/AADF77.

[55] Cerruti, M., Zech, A., Boisson, C., and Inoue, S. (2015). A hadronic origin for ultra-high-frequency-peaked BL Lac objects. *Monthly Notices of the Royal Astronomical Society*, 448 (1), 910–927, doi: 10.1093/MNRAS/STU2691.

[56] Cheng, K. S., Ho, C., Ruderman, M., Cheng, K. S. et al. (1986). Energetic Radiation from Rapidly Spinning Pulsars. I. Outer Magnetosphere Gaps. *ApJ*, 300, 500, doi: 10.1086/163829.

[57] Chernyakova, M. and Malyshev, D. (2020). Gamma-ray binaries. *Proceedings of Multifrequency Behaviour of High Energy Cosmic Sources - XIII — PoS(MULTIF2019)*, 362, 045, doi: 10.22323/1.362.0045.

[58] Chowdhury, D., Vempati, S. K., and Jog, C. J. (2011). Results from PAMELA, ATIC and FERMI: Pulsars or dark matter?. *Pramana 2011 76:1*, 76 (1), 1–22, doi: 10.1007/S12043-011-0019-1.

[59] Clough, S. A., Iacono, M. J., and Moncet, J.-L. (1992). Line-by-line calculations of atmospheric fluxes and cooling rates: Application to water vapor. *Journal of Geophysical Research: Atmospheres*, 97 (D14), 15761–15785.

[60] Collett, E. (2005) *Field guide to polarization*: SPIE, 134.

[61] Compagnino, A. A., Mineo, T., Maccarone, M. C., Catalano, O. et al. (2022). Evaluating the night sky background directly from the signal images detected by the ASTRI telescopes. *Exper. Astron.*, 53 (3), 1017–1035, doi: 10.1007/s10686-021-09830-9.

[62] Cortina, J. (2005). Status and First Results of the Magic Telescope. *Astrophysics and Space Science 2005 297:1*, 297 (1), 245–255, doi: 10.1007/S10509-005-7627-5.

[63] de Coulomb, C. A. (1785). Troisième mémoire sur l'électricité et le magnétisme. *Académie Royale des sciences*, 612–638.

[64] Crookes, W. (1879). On electrical insulation in high vacua. *Proceedings of the Royal Society of London*, 28 (190-195), 347–352, doi: 10.1098/rspl.1878.0139.

[65] Curie, P., Curie, M. P., and Bémont, G. (1898). Sur une nouvelle substance fortement radioactive, contenue dans la pechblende. *Comptes Rendus Hebdomadaires des Séances de l'Académie des Sciences*, 127.

[66] Curtis, A. R. (1952). Contribution to a discussion of "A statistical model for water vapor absorption," by R. M. Goody.. *Quart. J. Roy. Meteorol. Soc.* (78), 638–640.

[67] Daugherty, J. K., Harding, A. K., Daugherty, J. K., and Harding, A. K. (1982). Electromagnetic cascades in pulsars.. *ApJ*, 252, 337–347, doi: 10.1086/159561.

[68] Dazzi, F., Lazaro, D. H., López, M., Nakajima, D. et al. (2016). Performance studies of the new stereoscopic Sum-Trigger-II of MAGIC after one year of operation. *Proceedings of Science*, 236, 984, doi: 10.22323/1.236.0984.

[69] De Angelis, A. and Mallamaci, M. (2018). Gamma-ray astrophysics. *The European Physical Journal Plus 2018 133:8*, 133 (8), 1–18, doi: 10.1140/EPJP/I2018-12181-0.

[70] De Angelis, A. and Pimenta, M. (2018) *Introduction to particle and astroparticle physics: multimessenger astronomy and its particle physics foundations*: Springer.

[71] Deil, C., Zanin, R., Lefaucheur, J., Boisson, C. et al. (2018). Gammapy - A prototype for the CTA science tools. *Proceedings of Science*, 301, 766, doi: 10.22323/1.301.0766.

[72] Deleglise, G., Geffroy, N., and Lamanna, G. (2013) Large Size Telescope camera support structures for the Cherenkov Telescope Array. in *33rd International Cosmic Ray Conference*, 535.

[73] Delgado, C., Blanch, O., Diaz, C., Hamer, N. et al. (2013) Mechanics and cooling system for the camera of the Large Size Telescopes of the Cherenkov Telescope Array (CTA). in *33rd International Cosmic Ray Conference*, 371.

[74] Dermer, C. D. and Powale, G. (2013). Gamma rays from cosmic rays in supernova remnants. *Astronomy & Astrophysics*, 553, A34, doi: 10.1051/0004-6361/201220394.

[75] Dermer, C. D. and Schlickeiser, R. (1993). Model for the High-Energy Emission from Blazars. *ApJ*, 416, 458, doi: 10.1086/173251.

[76] Devin, J., Bregeon, J., Vasileiadis, G., and Gallant, Y. (2019). Impact of H.E.S.S. Lidar profiles on Crab Nebula data. *EPJ Web of Conferences*, 197, 01001, doi: 10.1051/EPJCONF/201919701001.

[77] Di Pierro, F., Arrabito, L., Larriva, A. B., Berti, A. et al. (2021). Monte Carlo Studies of Combined MAGIC and LST1 Observations. *Proceedings of Science*, 358, 659, doi: 10.22323/1.358.0659.

[78] Díaz-Castro, F. J. (1998). Adaptation of streetlighting on La Palma. *NewAR*, 42 (6-8), 509–513, doi: 10.1016/S1387-6473(98)00063-3.

[79] Donath, A., Terrier, R., Remy, Q., Sinha, A. et al. (2023). Gammapy: A Python package for gamma-ray astronomy. *Astronomy & Astrophysics*, 678, A157, doi: 10.1051/0004-6361/202346488.

[80] Dowling, D. R. and Radke, L. F. (1990). A Summary of the Physical Properties of Cirrus Clouds. *Journal of Applied Meteorology and Climatology*, 29 (9), 970–978, doi: 10.1175/1520-0450(1990)029.

[81] Drescher, H. J., Bleicher, M., Soff, S., and Stöcker, H. (2004). Model dependence of lateral distribution functions of high energy cosmic ray air showers. *Astroparticle Physics*, 21 (1), 87–94, doi: 10.1016/J.ASTROPARTPHYS.2003.10.007.

[82] Dubovik, O., Sinyuk, A., Lapyonok, T., Holben, B. N. et al. (2006). Application of spheroid models to account for aerosol particle nonsphericity in remote sensing of desert dust. *Journal of Geophysical Research: Atmospheres*, 111 (D11), doi: https://doi.org/10.1029/2005JD006619.

[83] Dubus, G. (2015). Gamma-ray emission from binaries in context. *Comptes Rendus Physique*, 16 (6-7), 661–673, doi: 10.1016/J.CRHY.2015.08.014.

[84] Elsasser, W. M. (1938). Mean Absorption and Equivalent Absorption Coefficient of a Band Spectrum. *Physical Review*, 54 (2), 126, doi: 10.1103/PhysRev.54.126.

[85] Fermi, E. (1949). On the Origin of the Cosmic Radiation. *Physical Review*, 75 (8), 1169, doi: 10.1103/PhysRev.75.1169.

[86] Ferrari, A., Ranft, J., Sala, P. R., and Fassò, A. (2005) *FLUKA: A multi-particle transport code (Program version 2005)*: Cern.

[87] Fesefeldt, H. (1985). Report PITHA-85/02. *RWTH Aachen*, 647, 27.

[88] Frank, I. and Tamm, I. (1937). Coherent visible radiation of fast electrons passing through matter. *Compt.Rend.Acad.Sci.URSS*, 14 (3), 109–114, doi: 10.3367/UFNR.0093.196710O.0388.

[89] Fréville, H., Chami, M., and Mallet, M. (2020). Analysis of the Transport of Aerosols over the North Tropical Atlantic Ocean Using Time Series of POLDER/PARASOL Satellite Data. *Remote Sensing 2020, Vol. 12, Page 757*, 12 (5), 757, doi: 10.3390/RS12050757.

[90] Fruck, C. (2015) *The Galactic Center resolved with MAGIC and a new technique for Atmospheric Calibration* Ph.D. dissertation, Technischen Universitat Munchen, Munchen, Germany.

[91] Fruck, C. and Gaug, M. (2015). Atmospheric monitoring in MAGIC and data corrections. *EPJ Web Conf.*, 89, 2003, doi: 10.1051/epjconf/20158902003.

[92] Fruck, C., Gaug, M., Hahn, A., Acciari, V. et al. (2022). Characterizing the aerosol atmosphere above the Observatorio del Roque de los Muchachos by analysing seven years of data taken with an GaAsP HPD-readout, absolutely calibrated elastic LIDAR. *Monthly Notices of the Royal Astronomical Society*, 515 (3), 4520–4550, doi: 10.1093/MNRAS/STAC1563.

[93] Fu, Q. (1996). An Accurate Parameterization of the Solar Radiative Properties of Cirrus Clouds for Climate Models. *JCli*, 9 (9), 2058–2082, doi: 10.1175/1520-0442(1996)009.

[94] Gaisser, T. K., Engel, R., and Resconi, E. (2016) *Cosmic rays and particle physics*: Cambridge University Press, 1–444, doi: 10.1017/CBO9781139192194.

[95] Gallo, F., Sanchez, K. J., Anderson, B. E., Bennett, R. et al. (2023). Measurement report: Aerosol vertical profiles over the western North Atlantic Ocean during the North Atlantic Aerosols and Marine Ecosystems Study (NAAMES). *Atmospheric Chemistry and Physics*, 23 (2), 1465–1490, doi: 10.5194/ACP-23-1465-2023.

[96] Gámez, C., Gutiérrez, M., Martínez, J. S., and Masip, M. (2020). High energy muons in extensive air showers. *Journal of Cosmology and Astroparticle Physics*, 2020 (01), 57, doi: 10.1088/1475-7516/2020/01/057.

[97] García-Gil, A., Muñoz-Tuñón, C., and Varela, A. M. (2010). Atmosphere Extinction at the ORM on La Palma: A 20 yr Statistical Database Gathered at the Carlsberg Meridian Telescope. *Publications of the Astronomical Society of the Pacific*, 122 (895), 1109–1121, doi: 10.1086/656329/XML.

[98] García, J. R., Dazzi, F., Häfner, D., Herranz, D. et al. (2013) Status of the new Sum-Trigger system for the MAGIC telescopes. in *33rd International Cosmic Ray Conference*, 666.

[99] Garrido, D., Gaug, M., Doro, M., Font, L. et al. (2013) Influence of Atmospheric Aerosols on the Performance of the MAGIC Telescopes. in *International Cosmic Ray Conference*, 33 of International Cosmic Ray Conference, 2909, `https://articles.adsabs.harvard.edu/pdf/2013ICRC...33.2909G`.

[100] Gaug, M., Blanch, O., Dorner, D., Doro, M. et al. (2013) Atmospheric Monitoring for the MAGIC Telescopes. in *1st Atmospheric Monitoring for High Energy Astroparticle Detectors (AtmoHEAD) workshop*, doi: 10.48550/arxiv.1403.5083.

[101] Ghisellini, G., Tavecchio, F., and Ghirlanda, G. (2009). Jet and accretion power in the most powerful Fermi blazars. *Monthly Notices of the Royal Astronomical Society*, 399 (4), 2041–2054, doi: 10.1111/J.1365-2966.2009.15397.X/2/M{_}MNRAS0399-2041-MU6.GIF.

[102] Godson, W. L. (1953). The evaluation of infrared radiative fluxes due to atmospheric water vapor. *Quart. J. Roy. Meteorol. Soc.* (79), 367–379.

[103] Goody, R. M. (1952). A statistical model for water-vapour absorption. *Quarterly Journal of the Royal Meteorological Society*, 78 (338), 638–640, doi: 10.1002/QJ.49707833820.

[104] Goody, R. M. and Yung, Y. L. (1989). Atmospheric Radiation: Theoretical Basis (2nd ed.). *Atmospheric Radiation: Theoretical Basis (2nd ed.)*, 482–484.

[105] Goudie, A. S. and Middleton, N. J. (2001). Saharan dust storms: nature and consequences. *Earth-Science Reviews*, 56 (1-4), 179–204, doi: 10.1016/S0012-8252(01)00067-8.

[106] Greisen, K. (1960). Cosmic Ray Showers. *https://doi.org/10.1146/annurev.ns.10.120160.000431*, 137 (3474), 913, doi: 10.1146/ANNUREV.NS.10.120160.000431.

[107] Greisen, K. (1966). End to the Cosmic-Ray Spectrum?. *Physical Review Letters*, 16 (17), 748, doi: 10.1103/PhysRevLett.16.748.

[108] Grieder, P. K. F. (2010). Extensive air showers. High energy phenomena and astrophysical aspects. Vol. 1 and 2. A tutorial, reference manual and data book.

[109] Guberman, D., Cortina, J., García, R., Herrera, J. et al. (2015). Using UV-pass filters for bright Moon observations with MAGIC. *PoS*, ICRC2015, 1237, doi: 10.48550/ARXIV.1509.02048.

[110] Hahn, J., De Los Reyes, R., Bernlöhr, K., Krüger, P. et al. (2014). Impact of aerosols and adverse atmospheric conditions on the data quality for spectral analysis of the H.E.S.S. telescopes. *Astroparticle Physics*, 54, 25–32, doi: 10.1016/J.ASTROPARTPHYS.2013.10.003.

[111] Harding, A. K., Stern, J. V., Dyks, J., and Frackowiak, M. (2008). High-Altitude Emission from Pulsar Slot Gaps: The Crab Pulsar. *The Astrophysical Journal*, 680 (2), 1378–1393, doi: 10.1086/588037/FULLTEXT/.

[112] Hassan Collado, T. (2015) *Sensivity studies for the Cherenkov Telescope Array* Ph.D. dissertation, Universidad Complutense de Madrid, Facultad de Ciencias Físicas, Madrid.

[113] Hassan, T., Arrabito, L., Bernlöhr, K., Bregeon, J. et al. (2017). Monte Carlo performance studies for the site selection of the Cherenkov Telescope Array. *Astroparticle Physics*, 93, 76–85, doi: 10.1016/J.ASTROPARTPHYS.2017.05.001.

[114] Hayashida, M., Noda, K., Teshima, M., Barres De Almeida, U. et al. (2016). The

Optical system for the Large Size Telescope of the Cherenkov Telescope Array. *Proceedings of Science*, 236, 927, doi: 10.22323/1.236.0927.

[115] Heck, D. and Pierog, T. (2012) Extensive Air Shower Simulation with CORSIKA: A User's Guide. Technical Report, Karlsruher Institut für Technologie, Karlsruhe.

[116] Heck, D., Knapp, J., Capdevielle, J. N., Schatz, G. et al. (1998). CORSIKA: A Monte Carlo code to simulate extensive air showers. *Report fzka*, 6019 (11).

[117] Heitler, W. (2010) *The quantum theory of radiation*: Dover Publications, 3rd edition.

[118] Henyey, L. G. and Greenstein, J. L. (1941). Diffuse radiation in the Galaxy.. *ApJ*, 93 (3733), 70–83, doi: 10.1086/144246.

[119] Hess, V. F. (1912). Observations in low level radiation during seven free balloon flights. *Phys. Zeit*, 13, 1084–1091.

[120] Hess, V. F. (1913). The origins of penetrating radiation. *Phys. Zeit*, 14, 612–617.

[121] Hidalgo, S. L., Muñoz-Tuñón, C., Castro-Almazán, J. A., and Varela, A. M. (2021). Canarian Observatories Meteorology; Comparison of OT and ORM using Regional Climate Reanalysis. *Publications of the Astronomical Society of the Pacific*, 133 (1028), 105002, doi: 10.1088/1538-3873/AC2A6C.

[122] Hillas, A. M. (1984). The Origin of Ultra-High-Energy Cosmic Rays. *https://doi.org/10.1146/annurev.aa.22.090184.002233*, 22 (1), 425–444, doi: 10.1146/ANNUREV.AA.22.090184.002233.

[123] Hillas, A. M. (1985) Cerenkov Light Images of EAS Produced by Primary Gamma Rays and by Nuclei. in *19th International Cosmic Ray Conference*, 3 of International Cosmic Ray Conference, 445.

[124] Hinton, J. A. (2004). The Status of the H.E.S.S. Project. *New Astronomy Reviews*, 48 (5-6), 331–337, doi: 10.1016/j.newar.2003.12.004.

[125] Hirotani, K. (2008). High Energy Emission from Rotation-Powered Pulsars: Outer-gap vs. Slot-gap Models. *Science*, 322 (5905), 1221–1224, `http://arxiv.org/abs/0809.1283`.

[126] Holder, J. (2006). The first VERITAS telescope. *Astropart. Phys.*, 25, 391–401, doi: 10.1016/j.astropartphys.2006.04.002.

[127] Hu, Y. X., Stamnes, K., Hu, Y. X., and Stamnes, K. (1993). An Accurate Parameterization of the Radiative Properties of Water Clouds Suitable for Use in Climate Models. *JCli*, 6 (4), 728–742, doi: 10.1175/1520-0442(1993)006.

[128] Ishio, K. and Paneque, D. (2022). A novel energy reconstruction method for the MAGIC stereoscopic observation. doi: 10.48550/arXiv.2212.03592.

[129] Ishio, K. (2020) *Improvement in the gamma-ray energy reconstruction of MAGIC and impact on the spectral analysis of the first Gamma Ray Burst detected at TeV energies* Ph.D. dissertation, Fakultat fur Physik der Ludwig–Maximilians–Universitat Munchen, Munich, doi: 10.5282/EDOC.27600.

[130] James, F. (1990). A review of pseudorandom number generators. *Computer Physics Communications*, 60 (3), 329–344, doi: 10.1016/0010-4655(90)90032-V.

[131] James, F. and Roos, M. (1975). Minuit - a system for function minimization and analysis of the parameter errors and correlations. *Computer Physics Communications*, 10 (6), 343–367, doi: 10.1016/0010-4655(75)90039-9.

[132] Kamata, K. and Nishimura, J. (1958). The Lateral and the Angular Structure Functions of Electron Showers. *Progress of Theoretical Physics Supplement*, 6, 93–155, doi: 10.1143/PTPS.6.93.

[133] Kinne, S., Schulz, M., Textor, C., Guibert, S. et al. (2006). An AeroCom initial assessment - Optical properties in aerosol component modules of global models. *Atmospheric Chemistry and Physics*, 6 (7), 1815–1834, doi: 10.5194/ACP-6-1815-2006.

[134] Klein, O. and Nishina, T. (1929). Über die Streuung von Strahlung durch freie Elektronen nach der neuen relativistischen Quantendynamik von Dirac. *Zeitschrift für Physik*, 52 (11-12), 853–868, doi: 10.1007/BF01366453/METRICS.

[135] Klett, J. D. (1981). Stable analytical inversion solution for processing lidar returns. *Applied Optics, Vol. 20, Issue 2, pp. 211-220*, 20 (2), 211–220, doi: 10.1364/AO.20.000211.

[136] Kobayashi, Y. (2022) *First detection of the very-high-energy gamma rays from the recurrent nova RS Ophiuchi with the Large Size Telescope prototype of the Cherenkov Telescope Array* Ph.D. dissertation, The University of Tokyo, Graduate School of Science, Tokyo, Japan.

[137] Kobayashi, Y., Okumura, A., Cassol, F., Katagiri, H. et al. (2022). Camera Calibration of the CTA-LST prototype. *Proceedings of Science*, 395, 720, doi: 10.22323/1.395.0720.

[138] Kokhanovsky, A. (2004). Optical properties of terrestrial clouds. *Earth-Science Reviews*, 64 (3-4), 189–241, doi: 10.1016/S0012-8252(03)00042-4.

[139] Kosack, K., Nöthe, M., Watson, J., Jacquemier, J. et al. (2022) cta-observatory/ctapipe: v0.15.0 – 2022-05-23. doi: 10.5281/zenodo.6572720.

[140] Kratz, D. P., Mlynczak, M. G., Mertens, C. J., Brindley, H. et al. (2005). An intercomparison of far-infrared line-by-line radiative transfer models. *Journal of Quantitative Spectroscopy and Radiative Transfer*, 90 (3-4), 323–341, doi: 10.1016/J.JQSRT.2004.04.006.

[141] Krennrich, F., Bond, I., Boyle, P., Bradbury, S. et al. (2004). VERITAS: the Very Energetic Radiation Imaging Telescope Array System. *New Astronomy Reviews*, 48 (5-6), 345–349, doi: 10.1016/J.NEWAR.2003.12.050.

[142] Kubo, H., Paoletti, R., Awane, Y., Bamba, A. et al. (2013) Development of the Photomultiplier-Tube Readout System for the CTA Large Size Telescope. in *33rd International Cosmic Ray Conference*, 206.

[143] Laken, B. A., Parviainen, H., García-Gil, A., Muñoz-Tuñón, C. et al. (2016). Thirty Years of Atmospheric Extinction from Telescopes of the North Atlantic Canary Archipelago. *Journal of Climate*, 29 (1), 227–240, doi: 10.1175/JCLI-D-14-00600.1.

[144] Leeuw, G. d. and Kunz, G. J. (1993). Inversion of lidar signals with the slope method. *Applied Optics, Vol. 32, Issue 18, pp. 3249-3256*, 32 (18), 3249–3256, doi: 10.1364/AO.32.003249.

[145] Lessard, R. W., Buckley, J. H., Connaughton, V., and Le Bohec, S. (2001). A new analysis method for reconstructing the arrival direction of TeV gamma rays using a single imaging atmospheric Cherenkov telescope. *Astroparticle Physics*, 15 (1), 1–18, doi: 10.1016/S0927-6505(00)00133-X.

[146] Li, T. P. and Ma, Y. Q. (1983). Analysis methods for results in gamma-ray astronomy.. *ApJ*, 272, 317–324, doi: 10.1086/161295.

[147] Liou, K. N. (2002) *An Introduction to Atmospheric radiation*, San Diego, California, USA: Elsevier Science, 2nd edition.

[148] Lombardi, G., Zitelli, V., Ortolani, S., Pedani, M. et al. (2008). Astronomy & Astrophysics El Roque de Los Muchachos site characteristics III. Analysis of atmospheric dust and aerosol extinction. *A&A*, 483, 651–659, doi: 10.1051/0004-6361:20078372.

[149] Lopez-Coto, R., Abe, H., Aguasca, A., Agudo, I. et al. (2022). Physics Performance of the Large Size Telescope prototype of the Cherenkov Telescope Array. *Proceedings of Science*, 395, 806, doi: 10.22323/1.395.0806.

[150] López-Coto, R., Baquero, A., Bernardos, M. I., Cassol, F. et al. (2020) lstchain: An Analysis Pipeline for LST-1, the First Prototype Large-Sized Telescope of CTA. in *30th Astronomical Data Analysis Software and Systems*, 532, 357, Granada, Spain: Astronomical Society of the Pacific.

[151] de Los Reyes, R., Hahn, J., Bernlöhr, K., Krüger, P. et al. (2013) Influence of Aerosols from Biomass Burning on the Spectral Analysis of Cherenkov Telescopes. in *International Cosmic Ray Conference*, 33 of International Cosmic Ray Conference, 2980, doi: 10.48550/arXiv.1309.3106.

[152] Maghrabi, A. H. (2007) *Ground based measurements of atmospheric infrared radiation from clear and cloudy skies.* Ph.D. dissertation, Univeristy of Adelaide, Adelaide, Australia, `https://digital.library.adelaide.edu.au/dspace/handle/2440/39513`.

[153] Maraschi, L., Ghisellini, G., and Celotti, A. (1992). A Jet Model for the Gamma-Ray–emitting Blazar 3C 279. *ApJL*, 397, L5, doi: 10.1086/186531.

[154] Maraschi, L. and Tavecchio, F. (2003). The Jet-Disk Connection and Blazar Unification. *The Astrophysical Journal*, 593 (2), 667–675, doi: 10.1086/342118/FULLTEXT/.

[155] Matricardi, M. (2007) An inter-comparison of line-by-line radiative transfer models. Technical Report, European Centre for Medium Range Weather Forecasts, Berkshire, England.

[156] Matthews, J. (2005). A Heitler model of extensive air showers. *Astropart. Phys.*, 22, 387–397, doi: 10.1016/j.astropartphys.2004.09.003.

[157] Mazin, D., Cortina, J., and Teshima, M. (2017). Large size telescope report. *AIP Conference Proceedings*, 1792 (1), 46, doi: 10.1063/1.4969022/885358.

[158] Mazuk, S. and Lynch, D. K. (2002) New Cirrus Models for MODTRAN4. I: Models Derived from the Standard and Subvisual Models. Technical Report, Los Angeles, `https://apps.dtic.mil/sti/citations/ADA400673`.

[159] Min, Q., Joseph, E., and Duan, M. (2004). Retrievals of thin cloud optical depth from a multifilter rotating shadowband radiometer. *Journal of Geophysical Research: Atmospheres*, 109 (D2), doi: https://doi.org/10.1029/2003JD003964.

[160] Mirzoyan, R. (1997). On the Calibration Accuracy of Light Sensors in Atmospheric Cherenkov Fluorescence and Neutrino Experiments. *ICRC*, 7, 265.

[161] Mirzoyan, R. (1998). Cherenkov light observations with the HEGRA detector at the Roque de los Muchachos observatory. *New Astronomy Reviews*, 42 (6-8), 547–551, doi: 10.1016/S1387-6473(98)00070-0.

[162] Moralejo, A., Gaug, M., Carmona, E., Colin, P. et al. (2009) MARS, the MAGIC Analysis and Reconstruction Software. in *31st International Cosmic Ray Conference*.

[163] Munar-Adrover, P. and Gaug, M. (2019). Studying molecular profiles above the Cherenkov Telescope Array sites. *EPJ Web Conf.*, 197, 1002, doi: 10.1051/epjconf/201919701002.

[164] National Geophysical Data Center (1992). U.S. standard atmosphere (1976). *Planetary and Space Science*, 40 (4), 553–554, doi: 10.1016/0032-0633(92)90203-Z.

[165] de Naurois, M. (2012) *Very High Energy astronomy from H.E.S.S. to CTA. Opening of a new astronomical window on the non-thermal Universe* Ph.D. dissertation, Ecole Polytechnique.

[166] de Naurois, M. and Mazin, D. (2015). Ground-based detectors in very-high-energy gamma-ray astronomy. *Comptes Rendus Physique*, 16 (6-7), 610–627, doi: 10.1016/J.CRHY.2015.08.011.

[167] Nelson, W. R., Hirayama, H., and Rogers, D. W. O. (1985) EGS4 code system. Technical Report, Stanford Linear Accelerator Center, Menlo Park, CA (USA).

[168] Nolan, S. J., Pühlhofer, G., and Rulten, C. B. (2010). Detailed studies of atmospheric calibration in imaging Cherenkov astronomy. *Astroparticle Physics*, 34 (5), 304–313, doi: 10.1016/J.ASTROPARTPHYS.2010.08.009.

[169] Nöthe, M., Kosack, K., Nickel, L., Peresano, M. et al. (2023). ctapipe - Prototype Open Event Reconstruction Pipeline for the Cherenkov Telescope Array. *PoS*, ICRC2023, 703, doi: 10.22323/1.444.0703.

[170] Nöthe, M. (2020) *Monitoring the High Energy Universe - Open, Reproducible, Machine Learning Based Analysis for the First G-APD Cherenkov Telescope* Ph.D. dissertation, Technische Universität Dortmund, Fakultät Physik, Dortmund, Germany.

[171] Nozaki, S., Blanch, O., Delgado, C., Gliwny, P. et al. (2020). The readout system based on the ultra-fast waveform sampler DRS4 for the Large-Sized Telescope of the Cherenkov Telescope Array. *Journal of Physics: Conference Series*, 1468 (1), 012104, doi: 10.1088/1742-6596/1468/1/012104.

[172] Ohtani, Y., Berti, A., Depaoli, D., Di Pierro, F. et al. (2022). Cross-calibration and combined analysis of the CTA-LST prototype and the MAGIC telescopes. *Proceedings of Science*, 395, 724, doi: 10.22323/1.395.0724.

[173] Olivera-Nieto, L., Mitchell, A. M. W., Bernlöhr, K., and Hinton, J. A. (2021). Muons as a tool for background rejection in imaging atmospheric Cherenkov telescope arrays. *Eur. Phys. J. C*, 81 (12), 1101, doi: 10.1140/epjc/s10052-021-09869-0.

[174] Ostapchenko, S. (2006). QGSJET-II: results for extensive air showers. *Nuclear Physics B - Proceedings Supplements*, 151 (1), 147–150, doi: 10.1016/j.nuclphysbps.2005.07.027.

[175] Pacini, D. (1912). La radiazione penetrante alla superficie ed in seno alle acque. *Il Nuovo Cimento*, 3 (1), 93–100, doi: 10.1007/BF02957440.

[176] Pacini, D. (1909). Sulle radiazioni penetranti. *Rend. Acc. Lincei*, 18, 123.

[177] Pacini, D. (1911). La radiation pénétrante sur la mer. *Radium (Paris)*, 8 (8), 307–312.

[178] Palatiello, M., Iori, M., Cassol, F., Cauz, D. et al. (2021). Performance of the INFN Camera calibration device of the first Large Size Telescope in the Cherenkov Telescope Array. *Proceedings of Science*, 358, 757, doi: 10.22323/1.358.0757.

[179] Pavletić, L., Gaug, M., Fruck, C., Hahn, A. et al. (2022). Elastic LIDAR Monitoring of the Night-sky Brightness over Roque de los Muchachos Observatory. *Journal of Physics: Conference Series*, 2398 (1), 012016, doi: 10.1088/1742-6596/2398/1/012016.

[180] Pedregosa, F., Varoquaux, G., Gramfort, A., Michel, V. et al. (2011). Scikit-learn: Machine Learning in Python. *Journal of Machine Learning Research*, 12 (85), 2825–2830, `http://jmlr.org/papers/v12/pedregosa11a.html`.

[181] Penndorf, R. (1957). Tables of the Refractive Index for Standard Air and the Rayleigh Scattering Coefficient for the Spectral Region between 0.2 and 20.0 μ and Their Application to Atmospheric Optics. *JOSA, Vol. 47, Issue 2, pp. 176-182*, 47 (2), 176–182, doi: 10.1364/JOSA.47.000176.

[182] Picozza, P. and Sparvoli, R. (2011). Understanding cosmic rays and searching for exotic sources with PAMELA. *Astrophys.Space Sci.Trans.*, 7 (2), 85–91, doi: 10.5194/ASTRA-7-85-2011.

[183] Pierro, F. D. (2023). Status of the Large-Sized Telescope of the Cherenkov Telescope Array.. *Journal of Physics: Conference Series*, 2429 (1), 012020, doi: 10.1088/1742-6596/2429/1/012020.

[184] Plass, G. N. (1958). Models for Spectral Band Absorption*. *JOSA, Vol. 48, Issue 10, pp. 690-703*, 48 (10), 690–703, doi: 10.1364/JOSA.48.000690.

[185] Ptitsyna, K. and Troitsky, S. (2008). Physical conditions in potential sources of ultra-high-energy cosmic rays: Updated Hillas plot and radiation-loss constraints. *Physics-Uspekhi*, 53 (7), 691–701, doi: 10.3367/UFNe.0180.201007c.0723.

[186] Ptuskin, V., Zirakashvili, V., and Seo, E. S. (2010). Spectrum of galactic cosmic rays

accelerated in supernova remnants. *The Astrophysical Journal*, 718 (1), 31, doi: 10.1088/0004-637X/718/1/31.

[187] Ranft, J. (1995). Dual parton model at cosmic ray energies. *Physical Review D*, 51 (1), 64, doi: 10.1103/PhysRevD.51.64.

[188] Raschka, S. (2018). Model evaluation, model selection, and algorithm selection in machine learning. *arXiv preprint arXiv:1811.12808*.

[189] Rossi, B. and Greisen, K. (1941). Cosmic-Ray Theory. *Reviews of Modern Physics*, 13 (4), 240, doi: 10.1103/RevModPhys.13.240.

[190] Ruderman, M. A. and Sutherland, P. G. (1975). Theory of pulsars: polar gaps, sparks, and coherent microwave radiation.. *ApJ*, 196, 51–72, doi: 10.1086/153393.

[191] Saito, T., Delgado, C., Blanch, O., Artero, M. et al. (2021). Commissioning of the camera of the first Large Size Telescope of the Cherenkov Telescope Array. *Proceedings of 37th International Cosmic Ray Conference — PoS(ICRC2021)*, 395, doi: 10.22323/1.395.0718.

[192] Salby, M. L. (2012) *Physics of the Atmosphere and Climate*, New York: Cambridge University Press.

[193] Sanuki, T., Motoki, M., Matsumoto, H., Seo, E. S. et al. (2000). Precise Measurement of Cosmic-Ray Proton and Helium Spectra with the BESS Spectrometer. *The Astrophysical Journal*, 545 (2), 1135–1142, doi: 10.1086/317873/FULLTEXT/.

[194] Schmuckermaier, F., Gaug, M., Fruck, C., Moralejo, A. et al. (2023). Correcting Imaging Atmospheric Cherenkov Telescope data with atmospheric profiles obtained with an elastic light detecting and ranging system. *Astronomy & Astrophysics*, 673, A2, doi: 10.1051/0004-6361/202245787.

[195] Serrano, D., Marín, M. J., Núñez, M., Utrillas, M. P. et al. (2015). Wavelength dependence of the effective cloud optical depth. *Journal of Atmospheric and Solar-Terrestrial Physics*, 130-131, 14–22, doi: 10.1016/J.JASTP.2015.05.001.

[196] Shayduk, M., Hengstebeck, T., Kalekin, O., Pavel, N. A. et al. (2005). A New Image Cleaning Method for the MAGIC Telescope. *ICRC*, 5, 223.

[197] Sherman, A. A. (1970). Translation of an historic paper. On a new, strongly radioactive substance, contained in pitchblende: by M.P. Curie, P. Curie and M.G. Bémont; presented by M. Becquerel.. *Journal of Nuclear Medicine*, 11 (6), 269–270.

[198] Shettle, E. and Fenn, R. (1976). Models of the atmospheric aerosols and their optical properties. *AGARD Conf Proc*, -1.

[199] Sicard, M., Nadzri Md Reba, M., Tomás, S., Comerón, A. et al. (2010). Results of site testing using an aerosol, backscatter lidar at the Roque de los Muchachos Observatory. *MNRAS*, 405 (1), 129–142, doi: 10.1111/J.1365-2966.2010.16468.X/2/MNRAS0405-0129-F12.JPEG.

[200] Sitarek, J., Sobczyńska, D., Szanecki, M., Adamczyk, K. et al. (2018). Nature of the low-energy, γ-like background for the Cherenkov Telescope Array. *Astropart. Phys.*, 97, 1–9, doi: 10.1016/j.astropartphys.2017.10.005.

[201] Sitarek, J. (2022). TeV Instrumentation: Current and Future. *Galaxies*, 10 (1), 21, doi: 10.3390/galaxies10010021.

[202] Sitarek, J., Gaug, M., Mazin, D., Paoletti, R. et al. (2013). Analysis techniques and performance of the Domino Ring Sampler version 4 based readout for the MAGIC telescopes. *Nucl.Instrum.Meth.A*, 723, 109–120, doi: 10.1016/J.NIMA.2013.05.014.

[203] Sitarek, J., Pecimotika, M., Żywucka, N., Sobczyńska, D. et al. (2024). Estimation of the atmospheric absorption profile with isotropic background events observed by Imag-

ing Atmospheric Cherenkov Telescopes. *Journal of High Energy Astrophysics*, 42, 87–95, doi: 10.1016/J.JHEAP.2024.03.003.

[204] SOBCZYŃSKA, D., ADAMCZYK, K., SITAREK, J., AND SZANECKI, M. (2020). An analysis method for data taken by Imaging Air Cherenkov Telescopes at very high energies under the presence of clouds. *Astroparticle Physics*, 120, 102450, doi: https://doi.org/10.1016/j.astropartphys.2020.102450.

[205] SOBCZYNSKA, D. AND BEDNAREK, W. (2014). Influence of clouds on the parameters of images measured by IACT at very high energies. *J. Phys. G*, 41 (12), 125201, doi: 10.1088/0954-3899/41/12/125201.

[206] SOBCZYNSKA, D., BENDAREK, W., SOBCZYNSKA, D., AND BENDAREK, W. (2013). Images of Gamma-ray Shower in Cherenkov Telescopes in Presence of Clouds. *ICRC*, 33 (July), 2905, `https://ui.adsabs.harvard.edu/abs/2013ICRC...33.2905S/abstract`.

[207] STANEV, T. (2010) *High energy cosmic rays*: Springer Science & Business Media.

[208] STOTTS, L. B. AND SCHROEDER, J. (2019) *Atmospheric Modeling Using PcModWin/MODTRAN®*, Bellingham, Washington USA: SPIE PRESS.

[209] SZANECKI, M., SOBCZYŃSKA, D., NIEDŹWIECKI, A., SITAREK, J. ET AL. (2015). Monte Carlo simulations of alternative sky observation modes with the Cherenkov Telescope Array. *Astroparticle Physics*, 67, 33–46, doi: 10.1016/J.ASTROPARTPHYS.2015.01.008.

[210] TSAI, Y. S. (1974). Pair production and bremsstrahlung of charged leptons. *Reviews of Modern Physics*, 46 (4), 815, doi: 10.1103/RevModPhys.46.815.

[211] UDO, S. O. AND AKPAN, A. E. (2002). Band models approach in atmospheric transmission function calculation - A review. *Global Journal of Pure and Applied Sciences*, 8 (3), 371–380.

[212] VALORE, L., ARAMO, C., DINELLIB, B. M., DI PIERRO, F. ET AL. (2018). The ARCADE Raman Lidar and atmospheric simulations for the Cherenkov Telescope Array. *Proceedings of Science*, 301, 763, doi: 10.22323/1.301.0763.

[213] VARELA, A. M., VÁZQUEZ RAMIÓ, H., VERNIN, J., MUÑOZ-TUÑÓN, C. ET AL. (2014). European Extremely Large Telescope Site Characterization III: Ground Meteorology. *Publications of the Astronomical Society of the Pacific*, 126 (938), 412–431, doi: 10.1086/676135/XML.

[214] VRASTIL, M. (2017). Overview of Atmospheric Simulation Efforts in CTA. *EPJ Web of Conferences*, 144, 01014, doi: 10.1051/EPJCONF/201714401014.

[215] WAGNER, R. M. (2006) *Measurement of very high energy gamma-ray emission from four blazars using the MAGIC telescope and a comparative blazar study* Ph.D. dissertation, Technische Universität München, Fakultät für Physik, Munich, Germany.

[216] WEEKES, T. C. (2003) *Very High Energy Gamma-Ray Astronomy*: CRC Press, 1st edition.

[217] WEEKES, T. C., CAWLEY, M. F., FEGAN, D. J., GIBBS, K. G. ET AL. (1989). Observation of TeV Gamma Rays from the Crab Nebula Using the Atmospheric Cerenkov Imaging Technique. *Astrophysical Journal*, 342, 379, doi: 10.1086/167599.

[218] WEFEL, J. P. (2001). The ATIC experiment: first balloon flight. *ICRC*, 6, 2111, `https://t.ly/ULCFH`.

[219] WEITKAMP, C. (2005) *Lidar. Range-Resolved Optical Remote Sensing of the Atmosphere*: Springer Science & Business Media.

[220] WERNER, K. (1993). Strings, pomerons and the VENUS model of hadronic interactions at ultrarelativistic energies. *Physics Reports*, 232 (2-5), 87–299.

[221] WILKS, S. S. (1938). The Large-Sample Distribution of the Likelihood Ratio for Testing Composite Hypotheses. *Ann. Math. Stat.*, 9 (1), 60–62, doi: 10.1214/AOMS/1177732360.

[222] WILSON, C. T. R. (1901). On the ionisation of atmospheric air. *Proceedings of the Royal Society of London*, 68 (442-450), 151–161, doi: 10.1098/rspl.1901.0032.

[223] WOOD, M., JOGLER, T., DUMM, J., AND FUNK, S. (2016). Monte Carlo studies of medium-size telescope designs for the Cherenkov Telescope Array. *Astroparticle Physics*, 72, 11–31, doi: 10.1016/J.ASTROPARTPHYS.2015.04.008.

[224] ZANIN, R. (2013) MARS, the MAGIC analysis and reconstruction software. in *33rd International Cosmic Ray Conference*, 773.

[225] ZARIĆ, D. (2022) *Very large zenith angle observations of VHE gamma-ray sources by IACT telescopes and development of the system for their precision pointing* Ph.D. dissertation, University of Zagreb, Faculty of Physics, Zagreb.

[226] ZARIĆ, D., CIKOTA, S., FIASSON, A., GODINOVIĆ, N. ET AL. (2021). Pointing System for the Large Size Telescopes Prototype of the Cherenkov Telescope Array. *Proceedings of Science*, 358, 829, doi: 10.22323/1.358.0829.

[227] ZATSEPIN, G. T. AND KUZ'MIN, V. A. (1966). Upper limit of the spectrum of cosmic rays. *JETP Lett.*, 4, 78–80, `http://jetpletters.ru/ps/1624/article_24846.pdf`.

[228] ŻYWUCKA, N., SITAREK, J., SOBCZYŃSKA, D., PECIMOTIKA, M. ET AL. (2024). A novel image correction method for cloud-affected observations with Imaging Atmospheric Cherenkov Telescopes. *Astronomy & Astrophysics*, 685, A165, doi: 10.1051/0004-6361/202449304.